Imperial College London

Department of Earth Science & Engineering

Using Full-Waveform Inversion to recover sub-surface physical properties at the Hikurangi margin

Author:
Melissa C. Gray

February 2020

Supervisors:
Dr. Rebecca Bell & Professor Joanna Morgan

Submitted in part fulfilment of the requirements for the degree of Doctor of Philosophy and the Diploma of Imperial College London

Copyright Declaration

The copyright of this thesis rests with the author and is made available under a Creative Commons Attribution Non-Commercial No Derivatives licence. Researchers are free to copy, distribute or transmit the thesis on the condition that they attribute it, that they do not use it for commercial purposes and that they do not alter, transform or build upon it. For any reuse or redistribution, researchers must make clear to others the licence terms of this work.

Melissa C. Gray

Department of Earth Science and Engineering
Imperial College London
February 2020

Declaration of Originality

I declare that this thesis titled, **Using Full-Waveform Inversion to recover sub-surface physical properties at the Hikurangi margin**, and the work presented in it are my own, performed under the supervision of Rebecca E. Bell and Joanna V. Morgan at the Department of Earth Science and Engineering, Imperial College London. All published and unpublished material used in the thesis has been given full acknowledgement. This thesis has not been previously submitted in whole or in part for a degree or any other qualification at this University or any other institution.

Melissa C. Gray

Department of Earth Science and Engineering
Imperial College London
February 2020

Abstract

The discovery of new slip modes at subduction zones since 2000 raises some interesting questions about how subduction megathrust faults behave. The Hikurangi margin offshore North Island New Zealand is the perfect natural laboratory to study different types of seismic behaviour, including slow-slip events (SSEs), as the margin experiences some of the shallowest (<2kmbsf) well documented SSEs worldwide. Theories to explain why some margins slip aseismically rather than in large stick-slip events often invoke the presence of high fluid pressure, conditionally stable frictional conditions (perhaps related to variations in lithology) and/or the subduction of ocean floor relief. As a plate boundary fault that undergoes slow slip has not yet been drilled it is currently difficult to directly test these hypotheses. Seismic reflection images allow us to investigate key areas at subduction margins, including the incoming section, trench and accretionary wedge, but these techniques often require extensive pre-processing and give limited information on lithology and fluid presence as they principally tell us about impedance contrasts rather than an individual physical property. Full-Waveform Inversion (FWI) is a relatively new technique which uses the wave equation to generate synthetic seismic data, and iteratively updates a starting model to improve the match between the synthetic and observed data, with the aim of producing high-resolution models of subsurface physical properties including P-wave velocity. This technique has become standard practice in the oil industry for imaging shallow hydrocarbon reservoirs in mostly sedimentary settings, and is being increasingly applied to academic datasets acquired across various geological settings including subduction zones.

The aims of this research are twofold. Firstly, to test whether full-waveform inversion is a plausible technique at the Hikurangi margin for improving models of key features, and secondly to determine what these recovered physical properties imply about the margin, and whether this affects seismicity. In the first science chapter, 2D FWI is applied to a 2D marine streamer dataset collected across the Hikurangi margin to recover a high-resolution model of P-wave velocity. While a previous, conventional velocity model created using pre-stack depth migration produced an adequate starting model, including variable velocities in the water column, precisely located seafloor

depths, and smoothing of abrupt boundaries needed to be carried out before FWI modelling. FWI modelling showed great improvement in model resolution compared to previous velocity modelling across the margin, resolving features to fault-block scale. Low-velocity-zones along faults in the model are identified as potential fluid conduits, which may be pathways for fluid release from the subduction interface at depth. Part way through this project a new 3D seismic experiment was funded by NERC (NZ3D-FWI). The second science chapter describes performing a suite of 3D synthetic FWI tests to optimise the location of the onshore seismometer array, to ensure that 3D FWI had the potential to recover high-resolution images of the principal targets of the survey: the subduction interface, a proposed subducting seamount, and the source region of shallow SSEs at Hikurangi. By investigating three potential land receiver layouts, the synthetic testing concluded with the selection of the optimal land-receiver layout which was used in the experiment. In the final year of the PhD, the margin was drilled as part of International Ocean Discovery Program (IODP) Expedition 372 and 375. Physical property data were acquired from logging-while drilling (LWD), wireline logging, and direct measurements made on the core. The third and final science chapter of this project uses physical property measurements from the IODP expeditions and derives relationships between P-wave velocity and other physical properties. These relationships are then used to transform the 2D FWI P-wave velocity model into models of porosity, S-wave velocity, Vp/Vs, bulk modulus and shear modulus. These models are used to examine whether sediments are over- or under- compacted in the incoming section and wedge, provide estimates of porosity within fault zones and elastic moduli within the accretionary wedge.

The model reveals the shallow structure of the overriding plate down to depths of ∼2km below the sea floor, including the fault plumbing system above the the origination zone of the SSEs. Hanging walls within the accretionary wedge appear more compacted than footwalls, and low velocity and corresponding low compaction and high porosity within the fault zones suggest they are acting as fluid pathways. Based on drilling data, the incoming section is composed of clastics, pelagics and volcaniclastics, and the FWI model is used to track these lithologies away from the drill site towards the trench. Sediment compaction estimates suggest that the different lithologies experience lateral compression that starts at ∼5.3-8km seaward of the trench. Pelagics which have been incorporated into the wedge appear to be under-compacted, likely due to their low permeability, while clastics appear over-compacted, suggesting that they are well drained. Porosity estimates indicate that ∼33% of fluid has been expelled from the clastic sediments and ∼20% from the pelagic layer across the Pāpaku frontal thrust. In the derived porosity model, 45% of initial fluid is released in the 5km section seaward of the wedge, and this rises to ∼62% at 25km landward from the trench. Shear modulii estimates suggest a low shear modulus of (1-4GPa) within the wedge, which is an important input parameter for tsunami modelling in the region, which has previously been modelled with much higher (7GPa) rigidity. New data for 3D FWI modelling at Hikurangi has now been collected, which will allow the work in this thesis to be extended both deeper and in

3D, in order to further investigate the physical properties at Hikurangi and their role in seismicity at the margin. Overall, the research in this thesis highlights that FWI is a promising method for producing high-resolution models at subduction zones, and using newly acquired data specifically for FWI, these models have the potential to produce a high-resolution characterisation of the SSE source zone below Hikurangi.

Acknowledgements

First and foremost I would like to thank my supervisors Becky Bell and Jo Morgan. Not only are they incredible scientists and mentors, but also amazing women who will always be role models to me. Thank you both so much for everything you have done - I can't even begin to express my gratitude toward you both. I honestly could not have asked for better supervisors.

I would also like to express thanks to all the people in the scientific community who helped me to complete this project. I would like to thank the FULLWAVE group at Imperial, in particular Mike Warner, Tenice Nangoo, Jack Ashley, Tatiana Kalinicheva and Lluis Guash for the invaluable help with data processing, coding and general PhD support. Thank you to Dr. Gail Christeson and Professor Saskia Goes for agreeing to read and review this work as part of my PhD viva. Thanks must also go to the crews and science parties of the three research cruises I was fortunate enough to take part in, especially to the P.I.s Emilee Hooft, Jenny Collier, Becky Bell and Nathan Bangs for letting me take part is such amazing experiences both offshore and on.

Someone once told me that doing a PhD was 'character-building' and I have to say they really weren't exaggerating! To all my friends that I have made along the way I wish to extend thanks, for always encouraging and believing in me. To my Imperial colleagues that have become lifelong friends - Naomi, Roan, Jack and Miriam - thank you for keeping me sane! I have been lucky enough to have always been surrounded by strong, inspiring women throughout my life, and to thank you all individually would take up more pages than I have. Particularly I would like to thank my childhood friends Tamara Dolsingh and Dr. Alex Amon for bossing their respective fields, there are too many letters after your names to add in here! To the women who put up with living with me throughout my academic journey, Rachael, Becky, Sophie and Lulu, thank you for being my family away from home.

I would like to sincerely thank my family, Nicola, Geoff and Bethany Gray for always telling me I can - I'm finally no longer a student, Dad! And finally to John, for always making me smile no matter what - you're the best.

Contents

Copyright Declaration i

Declaration of Originality iii

Abstract v

Acknowledgements viii

Table of Contents vii

List of Figures xi

List of Tables xx

1 Introduction 1
1.1 Subduction zones and their seismic behaviour . . . 1
1.2 Slow slip events (SSEs) . . . 5
1.3 Geophysical imaging at subduction zones . . . 6
1.4 Hikurangi Megathrust . . . 9
1.4.1 Tectonic setting and seismic behaviour . . . 9
1.4.2 Proposed hypotheses for variable slip behaviour along the margin . . . 10
1.4.2.1 Fluid pressure plays a role in controlling slip behaviours at subduction zones . . . 10
1.4.2.2 Subduction of sediments causes high pressured fluids in the SSE region of Hikurangi . . . 12
1.4.2.3 Subducting seamounts encourage SSEs . . . 12
1.4.2.4 In SSEs, the slip along the plate interface is distributed over a thicker shear zone than in stick-slip regions . . . 13
1.5 FWI at Hikurangi . . . 13
1.6 Aims and Objectives . . . 14
1.6.1 Aim 1: To determine whether the application of FWI is feasible at subduction zones 15
1.6.1.1 Objective 1.1: To apply 2D FWI to line 05CM-04 across the Hikurangi margin . . . 15
1.6.1.2 Objective 1.2: To use determine the optimal survey design for 3D FWI data collection at subduction zones . . . 15
1.6.2 Aim 2: To investigate the physical properties of the incoming section and overriding plate and interpret them in terms of the seismic behaviour of the north Hikurangi margin . . . 15
1.6.2.1 Objective 2.1: To assess the geological significance of high-resolution P-wave velocity anomalies . . . 15
1.6.2.2 Objective 2.2: To use IODP drilling measurements to transform P-wave velocity models into other physical properties to assess subduction margin processes . . . 15
1.7 Thesis Outline . . . 16

2 Theory 18
2.1 Introduction . . . 18
2.1.1 FWI code . . . 18
2.1.2 Amplitude balancing . . . 19
2.2 Seismic Wave Equation . . . 19
2.3 The Forward Problem . . . 20
2.4 The Inverse Problem . . . 21
2.5 Calculating the Residual . . . 22
2.6 Method of Steepest Descent . . . 23
2.6.1 Calculating the Unscaled Model Update (Gradient) . . . 24
2.6.2 Scaling the Model Update - Calculating the Step Length . . . 25
2.7 Stability Criteria . . . 27
2.7.1 Low Kernel . . . 27
2.7.2 High Kernel . . . 28

2.7.3 Downfalls of FWI . . . 28
2.7.3.1 Convergence to a local minimum . . . 28
2.7.3.2 Cycle-skipping . . . 28
2.8 Implementing FWI . . . 29
2.8.1 Time Domain vs. Frequency Domain FWI . . . 29
2.8.1.1 Frequency Domain . . . 30
2.8.1.2 Time Domain . . . 30
2.8.2 Implementing FWI successfully . . . 31
2.8.2.1 Long Offsets . . . 31
2.8.2.2 Low Frequencies . . . 31
2.8.2.3 Wide Azimuths . . . 32
2.8.2.4 Good Starting Model . . . 32

3 Methods **33**
3.1 Introduction . . . 33
3.1.1 Using FWI at Hikurangi . . . 34
3.2 Dataset . . . 34
3.3 FWI Workflow . . . 34
3.4 Implementing the Workflow . . . 38
3.4.1 Step 1. The dataset was preprocessed in preparation for FWI. . . . 38
3.4.2 Step 2. A source wavelet was extracted from the field data. . . . 39
3.4.2.1 Directly extracting the source wavelet from the data . . . 39
3.4.2.2 Predicting the source wavelet using Weiner filtering . . . 43
3.4.3 Step 3. Selecting a starting velocity model . . . 44
3.4.4 Step 4. Modifying the starting velocity model . . . 44
3.4.4.1 Smoothing . . . 47
3.4.4.2 Choosing accurate ocean velocities . . . 48
3.4.4.2.1 Using NMO to estimate ocean velocities . . . 48
3.4.4.2.2 A constant ocean velocity of 1500m/s . . . 51
3.4.4.2.3 Using simplified velocities from the World Ocean Database (WOD) 51
3.4.4.2.4 Using complete velocities from the World Ocean Database (WOD) 52
3.4.4.3 Adjusting the sea floor . . . 52
3.4.4.3.1 Using minimum ocean velocities to pick the sea bed . . . 54
3.4.4.3.2 Picking the sea bed based on a receiver gather . . . 54
3.4.4.3.3 Using swath bathymetry data . . . 54
3.4.4.3.4 Final sea bed location adaptation . . . 55
3.4.5 Step 5. The adequacy of the source wavelet and starting velocity model . . . 55
3.4.6 Step 6. Inversion strategies were tested and a final inversion scheme selected . . . 57
3.4.6.0.5 Muting the data . . . 57
3.4.6.0.6 Inverting in increasing frequency blocks . . . 57
3.4.6.0.7 Inverting in increasing offsets of the data . . . 59
3.4.6.0.8 Adjusting for computational power . . . 59
3.4.6.0.9 Final inversion scheme . . . 59
3.4.7 Step 7. The dataset was inverted using the selected inversion scheme, with regular quality assurance to check for cycle skipping . . . 60
3.5 Quality Assurance of the model . . . 61
3.5.1 Quality Assurance techniques . . . 61
3.5.1.1 Monitoring the gradient of the objective function . . . 61
3.5.1.2 Comparing the model with the PSDM seismic seflection Image . . . 62
3.5.1.3 Comparrison between the real data and synthetic shot gathers . . . 62
3.5.1.4 Comparison with logging-while drilling (LWD) and wireline sonic data . . . 63
3.6 Assessing further improvements to he model . . . 63
3.6.1 Inverting for all offsets up to 12km . . . 63
3.6.2 Extending the mute from 2 seconds to 5 seconds. . . . 64
3.6.3 Using different versions of the FULLWAVE code . . . 64
3.6.4 Increasing offset at each frequency band with different smoothing parameters. . . . 64
3.7 Raytracing was computed to determine maximum target depths. . . . 65
3.8 3D synthetic testing for key targets . . . 66
3.9 Transforming the model using IODP results . . . 67

4 2D FWI at Hikurani with streamer data **69**
4.1 Abstract . . . 69
4.2 Introduction . . . 70
4.3 Geological Setting . . . 73
4.3.1 Seismic character of the north Hikurangi margin and seamount subduction . . . 73
4.3.2 Character of the Plate Interface and Accretionary Wedge . . . 74
4.3.3 Incoming Sedimentary Section . . . 75
4.4 Datasets . . . 76
4.5 Method and data analysis . . . 76
4.5.1 Implementing the workflow . . . 78
4.5.2 Raytracing was computed to determine maximum target depths. . . . 86
4.6 Results . . . 87

4.6.1 Quality Assurance . . . 87
4.6.1.1 Comparison with the PSDM Seismic Reflection Image . . . 87
4.6.1.2 Comparison of Real Data with Synthetic Shot Gathers . . . 89
4.6.1.3 Comparison with LWD and wireline Sonic Logs . . . 91
4.6.1.4 Quality Assurance: Summary . . . 92
4.6.2 Observations from the FWI velocity model . . . 93
4.6.2.1 The Overriding Plate . . . 93
4.6.2.2 The Toe of the wedge . . . 93
4.6.2.3 The Incoming Section . . . 95
4.7 Discussion . . . 98
4.7.1 Lithology of the Incoming Section . . . 98
4.7.2 Low-Velocity Zones, Faults, and Fluid Flow . . . 98
4.7.3 Relation to SSEs . . . 99
4.8 Conclusion . . . 100
4.9 Acknowledgements . . . 101

5 Aims, design and configuration of NZ3D-FWI 102
5.1 Abstract . . . 102
5.2 Introduction . . . 103
5.2.1 Additional notable features at Hikurangi associated with the subduction zone . . . 104
5.2.2 Motivation for the NZ3D-FWI Experiment . . . 106
5.2.3 Hypotheses for the generation of SSEs . . . 106
5.2.3.1 Elevated fluid pressures exist in zones of slow slip leading to transitional frictional stability. . . . 107
5.2.3.2 Rheological heterogeneity exists in zones of slow-slip. . . . 107
5.2.3.3 SSEs occur within thickened shear zones, compared to narrow faults that host large earthquakes. . . . 108
5.3 Method . . . 109
5.3.1 Creation of a 3D Hikurangi volume and application of checkerboard testing. . . . 110
5.3.1.1 Creating a start model . . . 110
5.3.1.2 Determine the wavefield coverage and maximum depth of penetration using ray-tracing. . . . 111
5.3.1.3 Adding the checkerboard to generate a true model. . . . 112
5.3.1.4 Propagating the source wavefield through the true model. . . . 114
5.3.1.5 Generating a synthetic field dataset for different receiver geometries . . . 116
5.3.1.6 Choosing an inversion scheme and running FWI. . . . 117
5.3.1.6.1 Computing power . . . 117
5.3.1.6.2 Inversion parameters . . . 118
5.3.1.7 Subtracting the resulting velocity model from the start model to determine how well the checkerboard is resolved. . . . 119
5.4 Results . . . 121
5.4.1 General checkerboard recovery. . . . 121
5.4.2 Target areas along the décollement . . . 121
5.4.3 Shallow targets . . . 123
5.4.3.1 Additional checkerboard and receiver geometry. . . . 123
5.4.3.2 Recovery of shallow targets . . . 127
5.4.3.3 Recovery of deeper targets with heterogeneities in the shallow model. . . . 132
5.5 Discussion . . . 136
5.6 Choosing a layout . . . 137
5.7 Deployments . . . 139
5.7.1 Gisborne Array . . . 140
5.7.2 Waiamata Valley Array . . . 141
5.8 Instrumentation . . . 141
5.8.1 Energy Sources . . . 141
5.8.1.1 Active source - Airgun array . . . 141
5.8.1.2 3.2.1.2. Passive sources local, regional, and global earthquakes . . . 144
5.8.2 Onshore instruments and site design . . . 147
5.8.2.1 6TD broadband instrument . . . 147
5.8.2.2 CUBE3 . . . 148
5.8.2.3 GSX . . . 149
5.8.3 Offshore Instruments . . . 150
5.8.3.1 Ocean Bottom Seismometers (OBS) . . . 150
5.8.3.2 Hydrophone streamer . . . 150
5.9 Data . . . 151
5.9.1 Examples of active source data . . . 152
5.9.2 Examples of passive source data . . . 152
5.10 Conclusion . . . 156

6 Physical properties at Hikurangi 157
6.1 Abstract . . . 157
6.2 Introduction . . . 158
6.3 Datasets . . . 159
6.3.1 Seismic data . . . 159
6.3.2 Logging data . . . 161

6.3.3 Core Data . . . 161
6.4 Method . . . 162
6.4.1 Vp difference model . . . 166
6.4.2 Porosity Model . . . 168
6.4.3 Vs, Vp/Vs, bulk modulus and shear modulus . . . 173
6.5 Results . . . 177
6.5.1 Velocity difference and porosity models . . . 177
6.5.1.1 Velocity difference model . . . 177
6.5.1.2 Porosity model . . . 179
6.5.1.3 Porosity and velocity differences on the overriding plate . . . 180
6.5.1.4 Porosity and velocity differences in the Hikurangi Trough and toe of the wedge . . . 180
6.5.2 Vs, Vp/Vs, shear and bulk modulii calculations . . . 182
6.5.3 Error analysis . . . 185
6.6 Discussion . . . 193
6.6.1 How far from the trench do incoming sediments first feel the effects of compression? 193
6.6.2 How much fluid is expelled across the margin? . . . 197
6.6.2.1 Dewatering estimates within the wedge . . . 197
6.6.2.2 Dewatering estimates across individual faults . . . 198
6.6.2.3 Comparison of fluid expelled at other subduction zones . . . 200
6.6.3 Can models of estimated elastic moduli improve modelling of tsunami generation? 202
6.7 Conclusions . . . 205
6.A Appendix . . . 206

7 Conclusions **209**
7.1 Aim 1 . . . 209
7.1.1 Objective 1.1: To apply 2D FWI to line 05CM-04 . . . 209
7.1.2 Objective 1.2: To use synthetic 3D FWI to optimise the 3D survey . . . 210
7.2 Aim 2 . . . 210
7.2.1 Objective 2.1: To assess the geological significance of high-resolution P-wave velocity anomalies. . . . 210
7.2.2 Objective 2.2: To use IODP drilling measurements be used to transform the model into other physical properties . . . 211
7.3 Future Work . . . 213

Bibliography **215**

List of Figures

1.1 Map showing worldwide seismicity at subduction zone interfaces. This figure is taken from Berryman et al. (2015) and has been reproduced from Heuret et al. (2011). The rupture area of the Mw $\geq$ 8.0 subduction interface events (1900 - 2007) is represented by red and black ellipses. Red crosses are used here to indicate Mw $\geq$ 8.0 events that did not have available rupture area data. Coloured dots represent, by each 1° of trench, the number of Mw $\geq$ 5.5 subduction interface events (1976 - 2007). Subduction velocities (Heuret and Lallemand, 2005) are represented by blue arrows 2

1.2 Schematic of a subduction zone showing the oceanic plate subducting beneath the continental plate, highlighting the trench and accretionary wedge. Image taken from USGS (https://www.usgs.gov/media/images/subduction-fault-zone-diagram Date taken: 18/07/2016) 3

1.3 Moment (M_0) vs duration (t) of seismic and aseismic slip events and proposed scaling relationships. Dashed and dotted lines denote representative stress drops and rupture propagation velocities for the different event types. SSEs have several orders of magnitude lower stress drops (∼50kPa) than earthquakes (∼5MPa). Image taken from Bürgmann (2018) based on data from Peng and Gomberg (2010). 4

1.4 The locations of some slow-slip around the globe. The yellow stars mark the locations of tremor triggered by regional and teleseismic earthquakes. Regions where ETS events have been observed are marked by black boxes. Image from Peng and Gomberg (2010). 5

1.5 FWI has been used to image the megasplay fault system at Nankai by Kamei et al. (2012). (A) Shows the location of the study area at Nankai. (B) Shows the starting model and (B) the final result of acoustic inversion de-trended by the 3rd order polynomial which best fit the original 2D traveltime tomography. Image from Kamei et al. (2012). 8

1.6 (a) Is the regional map of New Zealand showing plate boundaries, highlighting line 05CM-04 which is shown in detail in (d). (b) shows a more detailed map of the north island, highlighting the change in geodetic plate coupling. Line 05CM-04 is again highlighted as are the 1947 Offshore Poverty Bay (along line 05CM04) and Tolaga Bay tsunami earthquakes (Bell et al., 2014) represented by yellow stars. Green contours represent total slip in mm detected in SSEs on the Hikurangi subduction interface since 2002 and dashed black lines show depth contours to the subduction interface. GISB represents the location on a cGPS site, shown in (c). Image taken from Wallace and Beavan (2010). (c) shows the east component of cGPS time series from GISB, highlighted in (b). Eastward (positive) jumps denote SSEs, and major SSEs since 2002 have been highlighted in green. Image adapted from Wallace et al. (2016). (d) shows the reflection seismic profile along line 05CM-04, highlighting the frontal thrust, estimated plate interface and proposed subducting seamount (Bell et al., 2014) based on magnetic data. Image adapted from Bell et al. (2014). 11

2.1 Representation of the local minima problem in FWI. Due to the non-linearity of the problem, forward modelling $\mathbf{G}(\mathbf{m}) = \mathbf{u}$ produces spurious local minima, represented by the red points. Choosing an inaccurate starting model, for example point B, can cause the local gradient method to push the model to converge to a local minima. Choosing a more accurate starting mode, for example point A, allows the inversion to converge to the true global minimum shown in blue 29

2.2 Schematic of cycle-skipping in FWI 29

3.1 Location map of the Hikurangi margin (inset) where the Pacific plate subducts beneath the Australian plate at a rate of 50mm/yr. The large map shows the location of the 05CM survey. Bold black lines show 2D lines used in analysis by Barker et al. (2009), and line 05CM-04, the dataset used in this thesis, is highlighted in red. A 2D line recorded by an earlier survey, the NIGHT survey is also shown. Red vectors show long-term estimates of convergence between the rotating east coast margin relative to the Pacific plate in mm/yr (Wallace et al., 2004). Boxed brown text shows the approximate sediment thicknesses on the downgoing plate at the Hikurangi Trough, which increases as we move south. Earthquake epicentres from the GeoNet catalog within a 3-20km depth range are shown by grey dots. Image from Barker et al. (2009). 35
3.2 Examples of two shot gathers of the raw data, detailed in Table 4.1. The signal-to-noise ratio is quite low, with a lot of contamination from swell noise. 36
3.3 (a) shows an example shot gather from the 05CM-04 dataset after bandpass filtering. (b) is a zoom-in of the red box highlighted in A at the end of the streamer where the tail-buoy noise is seen. The purple line tracks one such reflection created by the tail-buoy, and displays it as the purple line in (c) on the F-K spectrum. All such reflections from the tail-buoy lie in a similar position across all shot gathers in the dataset. The black triangle is the selection of data in the F-K spectrum which will be cut out from the data, however, much of the usable low-frequency data also lies within the triangle. 39
3.4 (a) shows an example shot gather after bandpass filtering, containing tail-buoy noise at the end of the streamer (11-12m along streamer).(b) shows the same shot gather after removing the tail-buoy noise. (c) shows this difference between (a) and (b), which is the tail-buoy noise which has been successfully removed using the mask, keeping all usable low-frequency data in the rest of the shot gather. 40
3.5 (a) and (b) shows two example shot gathers within the dataset, at different ocean depths (a) in the shallow ocean nearer onshore, and (b) in the deeper basin further offshore). (c) and (d) show the same two shot gathers after the application of the F-X deconvolution. We can see that a lot of the background noise has been removed and the signal to noise ratio greatly improved, however some noise still remains. 41
3.6 An example of a single shot gather through the pre-processing steps. (a) is the raw shot gather contaminated by swell noise. (b) is the shot gather after F-K filtering and (c) is the shot gather after F-K filtering and F-X deconvolution. The signal-to-noise ratio is greatly improved and the data is ready for inversion 42
3.7 (a) shows the initial source wavelet that was extracted by stacking 6 near offset traces in parts of the model with deeper seafloor depths, muted from 1500 ms. This source wavelet was used to create forward modelled synthetic data, indicated by a red star, which I could directly compare, trace-by-trace, to the real data. Note that the shape and arrival time of the real and predicted data are different for both the direct arrival and seafloor reflection. 43
3.8 (a) The original source wavelet $\mathbf{w_1}$, a bandpass filtered spike. (b) The predicted data $\mathbf{p_1}$ on the left, and the same trace from the field data $\mathbf{d}$ on the right. (c) The final source wavelet $\mathbf{w_2}$ after application of the matching filter $\mathbf{f}$ to $\mathbf{w_1}$. (d) Side-by-side comparison of the predicted, $\mathbf{p_2}$ (indicated by a red star), and observed data, $\mathbf{d}$, for a single shot gather of the 2D seismic data used in this study. We note that the real and synthetic data match well, with matching shapes and arrival times 45
3.9 (a) Velocity model produced using PSDM by Barker et al. (2018). (b) and (c) show two shots gathers, with synthetic data generated using the PSDM model (highlighted in pink) interleaved with the observed data. The figure shows a poor match for both the direct water wave arrivals and seafloor reflections. (d), (e), (f) and (g) show zoomed in plots of data from within the boxes shown in (b) and (c). From these more detailed views, we can see that the arrivals are not well matched and are cycle skipped. 46
3.10 The PSDM velocity model produced by Barker et al. (2018) where rock velocities below the seabed were smoothed to remove all abrupt changes below the sea-floor except the seabed itself. 47
3.11 A source-receiver pair showing the distance the wave travels to and from the reflector (t x v) compared to the horizontal distance between the source and receiver (x), used in the derivation of the travel-time equation (equation 33.6). 49
3.12 (a) a common mind-point (CMP) showing a single reflection. (b) The same reflection after the successful application of an NMO correction the gather is flattened. (c) The same gather shown in (a), by the NMO velocity used is too low, causing the gather to be overcorrected and curve upwards, and (d) The same gather shown in (a), but the NMO velocity used is too high, causing the gather to be undercorrected and curve downwards. From Yilmaz (1987). 49

3.13 Four CMP gathers from the 05CM-04 dataset before (a) and after (b) the application of an NMO correction of 1500 m/s. The first two gathers from the shallower, landward part of the data are undercorrected, the deeper CMP gather is overcorrected, and the deepest seaward gather is flattened. This process was carried out over many CMP gathers with a variety of NMO velocities until a model was made which flattened CMP gathers across the model. 50
3.14 Ocean velocity vs depth based on XBT data from NOAA from the Hikurangi margin at the same time of year as the 05CM-04 survey. The solid line is the velocities calculated by equation 3.7 using data from the XBTs, and the dashed line is the projection of the velocity deeper than the XBT measurements based on a linear trend (Howe et al., 1987). 52
3.15 Different ocean velocities tested for the start model (a) shows the original ocean velocities found by Barker et al. (2018) using PSDM techniques. (b) Shows the velocities determined using NMO testing. (c) shows a constant ocean velocity of 1500 m/s. (d) shows a 3-layered ocean model based on XBT data from NOAA and (e) shows the final ocean velocity used which is based on the full data from XBTs. 53
3.16 Different sea floor bathymetries tested in the start model. (a) is the original seafloor bathymetry used by Barker et al. (2018) based on PSDM. (b) Is the seafloor bathymetry found by using the minimum ocean velocity from the model shown in Fig 3.9(a). (c) shows the seafloor bathymetry picked from the nearest offset receiver gather over all shots. (d) is the bathymetry from the fine-gridded dataset provided by Stuart Henrys (GNS) and (e) is the final seafloor bathymetry I used which is the bathymetry data (d), edited near the onshore part of the model (∼0-10km horizontal distance), on the slope (∼45-55m horizontal distance) and far offshore (∼81-89m horizontal distance) for best matching synthetic gathers. (f) shows all the seafloor tests overlaid on one figure to better discern differences in the sea floor depths. 56
3.17 (a)) Plot of the final modified starting model for full-waveform inversion (FWI). (b) and (c) show two shot gathers, with synthetic data generated using the starting model (highlighted in pink) interleaved with the observed data. The figure shows a good match for both the direct water wave arrivals and seafloor reflections, and a reasonable match for some later arrivals and longer-offset refractions. (d), (e), (f) and (g) show zoomed in plots of data from within the boxes shown in (b) and (c). From these more detailed views, we can see that some of the later arrivals and longer offset data are not well matched and may be cycle skipped. 58
3.18 The gradient of the objective function at each iteration. A decrease in the gradient indicates the inversion is converging, however it is not an especially useful tool as we don't know whether it is converging to a local or global minima. 61
3.19 PSDM image of line 05CM-04 migrated using the tomography velocity model by Barker et al. (2018), displayed with root mean square (RMS) normalisation. 62
3.20 Paraxial ray tracing through the starting model at 4 locations along line 05CM-04. The black lines show the rays being recorded by the 12-km long streamer. There is good ray coverage in the uppermost 1.5-2 km of the sub-seafloor, with some rays penetrating down to 3.5 km depth. 66
3.21 (a) shows the location of the IODP drill sites on a bathymetry map of the area. Black line represents line 05CM-04. (b) shows the locations and depths of the same drilling sites on a depth converted seismic image of line 05CM-04. Structurat interpretation is modified from Barker et al. (2018), star represents the projected location of the March 1947 tsunami earthquake. VB = volcanic cone and VE = vertical exaggeration. Figures from Wallace et al. (2019) 67

4.1 (a) Regional map of New Zealand showing plate boundaries. Red lines show the 2D multichannel seismic lines 05CM-04 (used in this study) and 05CM-38 (Barker et al., 2009). The blue box shows the location of (b), the larger map, in which the colour scale is offshore bathymetry across the Hikurangi margin, based on 25-m gridded swath data. The black dots represent the drill sites, where borehole velocity measurements were taken on IODP Expedition 372 at U1519, U1518 and U1520. The red stars show the location of the 1947 Offshore Poverty Bay (along line 05CM-04) and Tolaga Bay tsunami earthquakes (Bell et al., 2014).(c) Reflection seismic section of 2D line 05CM-04. The dashed line shows the location of the proposed subducting seamount from Bell et al., (2014) based on magnetic data, and the red star shows the location of the March 1947 tsunami earthquake event offshore Poverty Bay. The red lines represent three IODP drill sites. The different lithology types based on interpretations from the literature are shown as well as the location of the frontal thrust in the near surface, the variable reflectivity of the subduction interface, and the Tūranganui Knolls. After Bell et al. (2014) 72

4.2 (a) Raw shot gather; the data are dominated by swell noise. (b) The same shot gather after bandpass and F-K filters have been applied to remove swell noise. The shot gather is much cleaner, however there is still a large amount of random noise across the gather. (c) The same shot gather after the application of F-X deconvolution to the gather shown in (b). While the data still contain some noisy traces, the majority of swell noise has been removed. 79
4.3 (a) The original source wavelet $\mathbf{w}_1$, a bandpass filtered spike (b) The predicted data $\mathbf{p}_1$ on the left, and the same trace from the field data $\mathbf{d}$ on the right. (c) The final source wavelet $\mathbf{w}_2$ after application of the matching filter $\mathbf{f}$ to $\mathbf{w}_1$. (d) Side-by-side comparison of the predicted, $\mathbf{p}_2$ (indicated by a red star), and observed data, $\mathbf{d}$, for a single shot gather of the 2D seismic data used in this study. 81
4.4 (a) PSDM velocity model by Barker et al., (2018). Panels (b) and (c) show filtered shot gathers at the two points labelled on the model. 83
4.5 (a) Plot of the smoothed PSDM model from Barker et al. (2019) used here as the starting model for full-waveform inversion (FWI). (b) and (c) show the same two shots gathers as in Fig. 4.4, with synthetic data generated using the starting model (highlighted in pink) interleaved with the observed data. The figure shows a good match for both the direct water wave arrivals and seafloor reflections, and a reasonable match for some later arrivals and longer-offset refractions. (d), (e), (f) and (g) show zoomed in plots of data from within the boxes shown in (b) and (c). From these more detailed views, we can see that some of the later arrivals and longer offset data are not well matched and may be cycle skipped. 84
4.6 Paraxial ray tracing through the starting model at 4 locations along the line. The black lines show the rays being recorded by the 12-km long streamer. There is good ray coverage in the uppermost 1.5-2km of the sub-seafloor, with some rays penetrating down to ∼3.5km depth. 87
4.7 (a) Final P-wave velocity model recovered after 160 iterations of FWI. The white dashed line indicates the extent of the model that we consider to be reasonably well constrained: the area below this line is likely to suffer from poor wavefield coverage (b) Final P-wave FWI velocity model overlain on the PSDM seismic image from Barker et al. (2018). Three areas of interest, i, ii and ii have been highlighted for discussion in the text. Thin white vertical lines show the location of three drill holes (U1519, U1518 and U1520) where LWD and wireline (U1520 only) data were collected during IODP Expeditions 372 and 375 (Pecher et al., 2018; Wallace et al., 2019) 88
4.8 (a) The final P-wave velocity model produced by FWI. (b) and (c) show the same two shots gathers as Figure 4.5, with the observed and synthetic data interleaved. In this figure the synthetic data (highlighted in pink) are generated using the final FWI velocity model shown in (a). (d), (e), (f) and (g) show zoomed in plots of data from within the boxes shown in (b) and (c), at the same streamer positions as in Figure 4.5. These plots show that there is an improvement in the match between the synthetic and observed data, in comparison to the synthetics shown in Figure 4.5. 90
4.9 P-wave velocity at the IODP Expedition 372 drill sites: (a) 1519; (b)1518; and (c) 1520. Blue lines show LWD data, green line shows wireline data collected at 1520 on Expedition 375. Yellow and purple lines are the velocities through the starting and FWI velocity models, within a region that extends 100 m either side of the drill site. Red rectangle in B shows the location of the fault identified in Pecher et al. (2019). 91
4.10 Detailed view of the PSDM seismic image from (Barker et al., 2018) and the overlay of the velocity model onto the PSDM seismic image shown in Figure 4.7, showing the location of site U1519. This is the overriding plate and a synform has been highlighted, labelled 1, as well as three faults labelled 2, 3 and 4, as well as smaller anomalies labelled a, b and c, which corresponds to shallow gas anomalies associated with the BSR (Navalpakam et al., 2012) 94
4.11 Detailed view of the PSDM seismic image from Barker et al. (2018) and the overlay of the velocity model onto PSDM seismic image shown in Figure 4.7ii and the location of site U1518. This is the toe of the dcollement where and 3 faults have been highlighted labelled 5, 6 and 7 (Barker et al., 2018) as well as potential inversion artefacts labelled d and e. A package of material of approximately the same velocity has been traced across fault 6, highlighted by the dashed white lines. 96
4.12 Detailed view of PSDM seismic image from Barker et al. (2018) and the overlay of the velocity model onto the PSDM seismic image shown in Figure 4.7iii. This is the Hikurangi Trough on the incoming plate, where well U1520 is located. The final model shows two dome-like features of higher velocity, labelled 8, a low velocity feature labelled 9 and an area of onlapping labelled 10. The velocity inversion west of U1520 highlighted as 9 does correspond to a strong reflector in the PSDM seismic image, however, as the well did not penetrate this zone, we cannot say for sure whether this feature is real or an artefact of the inversion. Nevertheless, synthetic shot gathers in the region match well with real field data, indicating that this feature could be real. 97

5.1 (a) Regional map of New Zealand showing plate boundaries between the Australian and Pacific plates. The red line shows the 2D multichannel seismic line 05CM-04 used in chapters 3 and 4. The blue box shows the location of (b), the larger map, in which the colour scale is bathymetry across the Hikurangi margin, based on 25-m gridded swath data. Grey contours show culmulative slow slip from 2002 - 2012 in mm and yellow dashed line shows the location of the boundary between coupled (east of the line) and uncoupled (west of the line) plate boundary behaviour, both from Wallace et al. (2012). The black dots represent the IODP drill sites, where LWD core and wireline (1520 only) measurements were taken on Expeditions 372 and 375. The red stars show the location of the 1947 Offshore Poverty Bay (along line 05CM-04) and Tolaga Bay tsunami earthquakes (Bell et al., 2014). The black dashed boxes show the proposed location for the NZ3D-FWI experiment, and the purple dashed circle shows the region in which evidence for mud volcanism was noted on a scouting trip of the area. (c) Reflection seismic section of 2D line 05CM-04. overlain onto the final FWI P-wave velocity model from chapter 4, showing the depth to which P-wave velocities are constrained by turning rays. The black dashed line shows the location of the proposed subducting seamount from Bell et al., (2014) based on magnetic data, and the red star shows the location of the March 1947 tsunami earthquake event offshore Poverty Bay. The white dashed line shows the approximate location of the plate interface where SSEs are known to occur (Wallace et al., 2016), and the HRZ is shown, where strong reflectivity is seen in reflection seismic images. 105
5.2 Cut-away image of the Start model showing the different sub-surface seismic velocities, plate interface and proposed subducting seamount. 111
5.3 Paraxial ray-trace tests through a 2D slice through the centre start model (Fig 5.2) at 3 different shot locations. Some of the key targets of the 3D-FWI experiment are shown including the plate interface, HRZ and subducting seamount. Receivers will record data from depths of ∼19km. 113
5.4 Schematic of the checkerboard used in the synthetic testing. The numbers represent the velocity difference between the checkerboard and the background velocity model in Fig 5.2. 114
5.5 Cut-away diagram of the 3D checkerboard which will be added to the Start Model (Fig 5.2). The checkerboard lied along the top of the picked décollement. 115
5.6 Cutaway image of the 3D true model the start model (Fig 5.2) with the checkerboard (Fig 5.5) added to it. 115
5.7 The source wavelet used to create the synthetic forward modelled seismic data to be used in the inversion. It is a Ricker wavelet of amplitude 1 shifted to start at 350ms. 116
5.8 Bird's eye view of the 9000 offshore shots used in the synthetic FWI testing. 116
5.9 The arrangement of OBS and land receivers for the Regular Grid geometry shown in both birds eye view and across the entire 3D model. 117
5.10 The arrangement of OBS and land receivers for the Dense Grid geometry shown in both birds eye view and across the entire 3D model. 118
5.11 Schematic overview of the methods outlined in this section and how the results are calculated. 120
5.12 (a) The location of the slice taken through the model. (b) The original checkerboard. With perfect model resolution this is what we should resolve after FWI. Note that as the slice had to be picked along flat planes, topography of the checkerboard due to the addition of the seamount along the décollement causes some parts of the model to contain missing checks. (c) Results of the checkerboard test for the regular grid land receiver layout and (d) Results of the checkerboard test for the dense grid receiver land receiver layout. 122
5.13 The slice extracted from the checkerboard shown in Fig 5.12, and (b), highlighting deeper target areas the subducting seamount, the HRZ and the region of the plate coupling transition outlined in Fig 5.1. 122
5.14 (a) Zoom-in of the true checkerboard along the picked slice (Fig 5.13(a)) at the key target of the subducting seamount shown by the black dashed outline. The results of the checkerboard test for the regular grid land receiver layout (b) and dense grid land receiver layout (c) at the seamount. White boxes highlight areas where the checkerboard structure is not fully resolved and a smearing effect between checks is seen. 124
5.15 (a)Zoom-in of the true checkerboard along the picked slice (Fig 5.13(a)) at the key target of the HRZ. The results of the checkerboard test for the regular grid land receiver layout (b) and dense grid land receiver layout (c) at the HRZ. While checks are relatively well resolved in the offshore part of the model, there is poor recovery of the larger checks in the onshore part of the model. 125
5.16 Schematic of the checkerboard used in the synthetic testing of the shallow target in the area of the mud volcano system. The numbers represent the velocity difference between the checkerboard and the background velocity model in Fig 5.2. 126
5.17 (a) The location of the checkerboard which represents the mud volcano as well as the checkerboard along the décollement. Note the model has been rotated horizontally 180 degrees to show the shallow checkerboard in the onshore part of the model. (b) Zoom-in of the checkerboard, detailing the dimensions. 128
5.18 The arrangement of OBS and land receivers for the Combination Grid geometry shown in both birds eye view and across the entire 3D model. 129

5.19 The shallow checkerboard shown in Fig 5.18, highlighting the three slices where results are compared for the three land receiver layouts. Note slice 1 is taken vertically through the block while slices 2 and 3 are taken horizontally. 129
5.20 (a) Vertical slice 1 (Fig 5.19) through the actual checkerboard placed in the model. Results for the regular grid land receiver layout (b), dense grid land receiver layout (c) and combination grid land receiver layout (d) All three layouts poorly resolve the shallow checkerboard, with vertical anomalies shown, likely representing ray-paths in the inversion. 130
5.21 (a) Horizontal slice 2 (Fig 5.19) through the actual checkerboard placed in the model. Results for the regular grid land receiver layout (b), dense grid land receiver layout (c) and combination grid land receiver layout (d). Some resolution of structure and amplitude can be seen. 130
5.22 (a) Horizontal slice 3 (Fig 5.19) through the actual checkerboard placed in the model. Results for the regular grid land receiver layout (b), dense grid land receiver layout (c) and combination grid land receiver layout (d) All three layouts poorly resolve the shallow checkerboard, displaying several small, sharp anomalies. 131
5.23 (a) The location of the slice taken through the model. (b) The original checkerboard. With perfect model resolution this is what we should resolve after FWI. Note that as the slice had to be picked along flat planes, topography of the checkerboard due to the addition of the seamount along the décollement causes some parts of the model to contain missing checks. Results of the checkerboard test for the regular grid land receiver layout (c), dense grid receiver land receiver layout (d) and combination grid land receiver layout (E). White dashed boxes show the location of the marine shots. 133
5.24 (a) Zoom-in of the true checkerboard along the picked slice (Fig 5.23(a)) at the key target of the subducting seamount shown by the black dashed outline. The results of the checkerboard test for the regular grid land receiver layout (b), dense grid land receiver layout (c), and combination grid receiver layout (d) at the seamount. White boxes highlight areas where the checkerboard structure is not fully resolved and a smearing effect between checks is seen. 134
5.25 (a) Zoom-in of the true checkerboard along the picked slice (Fig 5.23(a)) at the key target of the HRZ. The results of the checkerboard test for the regular grid land receiver layout (b), dense grid land receiver layout (c), and combination grid land receiver layout (d) at the HRZ. While checks are relatively well resolved in the offshore part of the model, there is poor recovery of the larger checks in the onshore part of the model. 135
5.26 Crew and science party onboard the R/V Marcus G. Langseth for the NZ3D-FWI experiment. 140
5.27 Map of the Gisborne region showing land receiver deployment locations. The deployments consists of two main arrays, the Gisborne array composed of instruments spaced every ∼2km mostly made of CMT-6TD and GSX3 instruments, and the Waimata Valley array, more densely spaced every ∼500m and mostly composed of DATA-CUBE3 instruments. All instruments were deployed from December 2017- February 2018. Coordinate system is New Zealand Regional Grid. Image courtesy Bell et al., (submitted). 142
5.28 NZ3D land station locations in Waimata Valley array with instruments spaced every ∼ 500m. Instruments were deployed and recording between December 2017 February 2018. Coordinate system is New Zealand Regional Grid. Image courtesy Bell et al., (submitted). 143
5.29 (a) Airgun Source onboard the R/V Marcus G. Langseth (b) The R/V Marcus G. Langseth showing towed streamers in yellow and towed airgun sources in white stars. 144
5.30 Map showing the location of each shot point. The streamer data only recorded shots within the main rectangle. The land and OBS instruments (shown as white circles) additionally recorded shots around the corners. 145
5.31 (a) Regional earthquakes with magnitudes larger than Mw 3 which occurred during the NZ3D-FWI Waimata Array deployment (19/12/17 12/2/18) and (b) during the Gisborne Array deployment (19/12/17 10/10/18) Image courtesy Bell et al., (submitted). (c) Global earthquakes with magnitudes larger than 6 occurring between 19/12/17 - 10/10/18 during instrument deployment. 146
5.32 (a) local earthquakes which occurred during the NZ3D-FWI Waimata Array deployment (19/12/17 12/2/18) and (b) during the Gisborne Array deployment (19/12/17 10/10/18) Image courtesy Bell et al., (submitted) 147
5.33 (a)CMG-6TD instruments in the Gisborne field centre where a huddle test was carried out - this ensures all instruments are working and able to get a GPS lock (b) the CMG-6TD instrument. (c) and (d) show examples of CMG-6TD sites during the Gisborne Array deployment (19/12/17 10/10/18) including GPS, solar panel and fences. The instrument in (b) is buried beneath the tarpaulin. Image courtesy Bell et al., (submitted). 148
5.34 (a)the CUBE3 geophone in the ground ∼ 30cm below the surface, and the recorder in a plastic bag. (b) The CUBE3 recorder (image from www.gfz-potsdam.de). (c) An example of a CUBE3 site during the deployment (19/12/17 10/10/18). The plastic box is placed over the instruments to protect them from cattle. Image courtesy Bell et al., (submitted)). 149

5.35 (a)The GSX geophone in the ground ∼30cm below the surface alongside two batteries and yellow GSX recorder. (b) An example of a GSX site during the deployment (19/12/17 10/10/18). Two plastic boxes are placed over the instruments to protect them from cattle. Image courtesy Bell et al., (submitted). 150
5.36 (a)The OBS instruments on deck and (b) and being lowered overboard. Image courtesy GNS Science 151
5.37 (a) One of the 4km streamers on deck and (b) Compassbirds on deck 152
5.38 Receiver gathers for shot lines 1236 and 1244 for vertical components of CUBE3 stations BC03 and EC23. (a) and (c) show the receiver gathers from BC03 and EC23 respectively, while (b) and (d) show gathers in reduced time using a velocity of 7km/s. Data have been bandpassed filtered between 8 and 100 Hz. Image courtesy Bell et al., (submitted) 153
5.39 Receiver gathers for shot lines 1236 and 1244 for vertical components of CUBE3 stations BS28 and BS60. (a) and (c) show the receiver gathers fro BS28 and BS60 respectively, while (b) and (d) show gathers in reduced time using a velocity of 7km/s. Data have been bandpassed filtered between 8 and 100 Hz. Image courtesy Bell et al., (submitted) 154
5.40 (a)The 13th January, 2019 magnitude 3.5 Gisborne earthquake as recorded on all land instruments. (b) P-wave arrival times at all instruments in the array 155

6.1 (a) Regional map of New Zealand showing plate boundaries between the Australian and Pacific plates. The red line shows the 2D multichannel seismic line 05CM-04 used in this study (see chapter 4). The blue box shows the location of (b), the larger map, in which the colour scale is offshore bathymetry across the Hikurangi margin, based on 25-m gridded swath data. The black dots represent the drill sites, where LWD core and wireline (1520 only) measurements were taken on IODP Expeditions 372 and 375. The red stars show the location of the 1947 Offshore Poverty Bay (along line 05CM-04) and Tolaga Bay tsunami earthquakes (Bell et al., 2014). (c) Reflection seismic section of 2D line 05CM-04. The dashed line shows the location of the proposed subducting seamount from Bell et al. (2014) based on magnetic data, and the red star shows the location of the March 1947 tsunami earthquake event offshore Poverty Bay. The red lines represent three IODP drill sites. The different lithology types based on interpretations from the literature are shown as well as the location of the frontal thrust in the near surface, the variable reflectivity of the subduction interface, and the Tūranganui Knolls (after Gray et al. (2019)). 160
6.2 LWD and core data recovered at site U1519 on the overriding plate. Images from Wallace et al. (2019). 163
6.3 LWD and core data recovered at site U1518 near the trench.Images from Wallace et al. (2019). 164
6.4 LWD and core data recovered at site U1520 in the Hikurangi Trough.Images from Wallace et al. (2019). 165
6.5 General velocity vs depth trend based on LWD measurements through undeformed clastic (grey points) and pelagic sediments (black points) in the Hikurangi trough ever 0.1524m (0.5ft). Blue points represent the velocity of pelagic sediments averaged over 15m intervals. The blue line represents the clastic velocity-depth profile and the pink lines represent best-fit pelagic velocity-depth profiles for the unconstrained (dashed) and averaged (solid) pelagic values. The purple line shows the velocity profile extracted from the FWI model at the location of U1520 (b) shows a zoomed-in version of the area in (a) denoted by the red box 167
6.6 Cross-plots of porosity vs density from core data for U1519 (a), U1518(b) and U1520 (c), and corresponding density LWD data converted to porosity (black points) directly compared to porosity LWD data (pink points), for U1519 (d), U1518 (e), and U1520 (f). . 169
6.7 Cross-plot of porosity converted from density LWD data (detailed in Fig 6.6), vs velocity from LWD data for all three wells U1518-1520. Five best-fit relationships to the data based on different porosity-velocity models are plotted as coloured lines, for each lithology: clastic (a), pelagic (b), and volcaniclastic (c). 171
6.8 Differences between porosity models based on different best fit relationships between porosity and velocity data outlined in Fig 6.7 and Table 6.3. 174
6.9 Vp vs Vs measurements for clastic lithology taken from LWD data for (a) U1519, (b) U1518, (c) U1520, (d) all sites and (d) U1520. (e) Shows Vs vs Vp for pelagic lithology at 1520. Note the axes are reversed in order to fit relationships based on Greenberg and Castagna (1992). Standard equations from Castagna et al. (1985) and Greenberg and Castagna (1992) are shown in green while best fit relationships based on data are shown in purple (a, b and c) and pink (d and e). The relationships derived in (d) and (e) (equations displayed on graphs and shown in Tables 6.4 and 6.5) were used to convert Vp to Vs in the models. 176

6.10 (a) Vp model (from chapter 4), (b) porosity model across 05CM-04 based on the reciprocal relationship between Vp and porosity (Fig 6.7, Table 6.3) (c) Velocity anomaly model based on difference between (a) and the velocity vs depth trend for undeformed clastic and pelagic sediments from LWD and core data (Fig 6.5) (d) Velocity anomaly model based on difference between (a) and the velocity vs depth trend for undeformed sediments from the FWI model extracted at site U1520 (Fig 6.5). 178
6.11 Detailed models of P-wave velocity overlying PSDM seismic image (from chapter 4) (a), porosity (b) and velocity anomaly (c) of the overriding plate (Fig 6.10(i)). This part of the model contains three faults (faults 1, 2 and 3) with strong variations in properties between footwalls, hanging walls and along faults. 181
6.12 Detailed models of P-wave velocity overlying PSDM seismic image (from chapter 4) (a), porosity (b) and velocity anomaly (c) of Hikurangi trough and trench (Fig 6.10(ii)). This part of the model contains three faults (faults 4, 5 and 6) with the Pāpaku fault (fault 6) the frontalmost thrust fault at the trench, and fault 4 which was drilled by well U1518. . 183
6.13 (a) Final FWI Vp model (from chapter 4), (b) Vs model based on linear equation from Vp vs Vs cross-plots of wells U1519 and U1520 (Fig 6.9). (c) Vp/Vs ratio calculated by dividing (a) by (b), (d) Bulk modulus and (e) shear modulus models calculated using equations 6.6 and 6.7 respectively. 186
6.14 Site U1519. (a) Differences is possible density values. Black dots represent LWD density measurements, purple dots represent core density measurements, grey dots represent density values calculated from velocity LWD using Gardners relationship (equation 6.8). The blue line shows the density extracted from the P-wave FWI model converted to density using Gardners law. (b) shows the Vp measurements from LWD while the blue line shows Vp from the FWI model extracted at the drill site. (c) Black dots show Vs values calculated from Vp LWD measurements shown in (b) using the best-fit relationships derived in section 6.4.3 (Tables 6.4 and 6.5), as well as LWD Vs data shown in pink. The blue line shows the Vs profile extracted from the Vs model at the drill site. (d) Shows the porosity converted to desity from the LWD log as outlined in Section 6.3.2. Purple dots show the porosty from core measurements and the blue line shows the porosity profile extracted from the model at the well site. (e) and (f) show calculated bulk and shear modulii using density, Vp and Vs values from the logs shown using both calculated (black) and true (pink) Vs. Also shown in (d) and (e) are the calculated values of elastic modulii from well U1519 location in the models shown in Fig 6.13 using Gardners density, FWI derived Vp and Vs calculated from equations in Tables 6.4 and 6.5. 188
6.15 Site U1518. (a) Differences is possible density values. Black dots represent LWD density measurements, purple dots represent core density measurements, grey dots represent density values calculated from velocity LWD using Gardners relationship (equation 6.8). The blue line shows the density extracted from the P-wave FWI model converted to density using Gardners law. (b) Shows the Vp measurements from LWD in black and core in purple, while the blue line shows Vp from the FWI model extracted at the drill site. (c) Black and purple dots show Vs values calculated from Vp LWD and core measurements respectively shown in (b) using the best-fit relationships derived in section 6.4.3 (Tables 6.4 and 6.5), as well as LWD Vs data shown in pink. The blue line shows the Vs profile extracted from the Vs model at the drill site. (d) Shows the porosity converted to density from the LWD log as outlined in Section 6.3.2. Purple dots show the porosty from core measurements and the blue line shows the porosity profile extracted from the model at the well site. (e) and (f) show calculated bulk and shear modulii using density, Vp and Vs values from the logs shown. Also shown in (d) and (e) are the calculated values of elastic modulii from well U1518 location in the models shown in Fig 6.13 using Gardners density, FWI derived Vp and Vs calculated from equations in Tables 6.4 and 6.5. 189

6.16 Site U1520. (a) Differences is possible density values. Black dots represent LWD density measurements, purple dots represent core density measurements, grey dots represent density values calculated from velocity LWD using Gardners relationship (equation 6.8). The blue line shows the density extracted from the P-wave FWI model converted to density using Gardners law. (b) Shows the Vp measurements from LWD, purple dots show core Vp values, and grey dots show wireline Vp values, while the blue line shows Vp from the FWI model extracted at the drill site. (c) Black, purple, and grey dots show Vs values calculated from Vp LWD, core, and wireline measurements respectively shown in (b) using the best-fit relationships derived in section 6.4.3 (Tables 6.4 and 6.5), as well as LWD Vs data shown in pink. The blue line shows the Vs profile extracted from the Vs model at the drill site. (d) Shows the porosity converted to desity from the LWD log as outlined in Section 6.3.2. Purple dots show the porosty from core measurements and the blue line shows the porosity profile extracted from the model at the well site. (e) and (f) show calculated bulk and shear modulii using density, Vp and Vs values from the logs shown using both calculated (black) and true (pink) Vs. Also shown in (d) and (e) are the calculated values of elastic modulii from well U1519 location in the models shown in Fig 6.13 using Gardners density, FWI derived Vp and Vs calculated from equations in Tables 6.4 and 6.5. 190
6.17 (a) shows the velocity difference model in the Hikurangi Trough based on velocity profiles extracted from LWD and core data. (b) Shows the velocity difference model in the Hikurangi Trough based on the velocity profile extracted at U1520 from the FWI model.The dashed lines show the location where the profile in (c) was extracted, at 200mbsf. 194
6.18 Estimates of fluid released at 5km intervals landward of the trench at a depth of 250mbsf using porosity taken form the transformed model. 198
6.19 Zoom in of faults 1, 2, 3,5 and 6 in porosity model (a), (c) and velocity difference model (b), (d), highlighting where porosity measurements were taken for use in calculation of expelled fluid. 199
6.20 Comparison of fluid release at various subduction zones. 201
6.21 (A) Map showing where data from prism sediments are taken to compare to the Hikurangi transformed models. Blue lines show plate boundaries. Comparison between (B) bulk modulus and (C) shear modulus from margins shown in (A) calculated by Jeppson et al. (2018) using measured (open symbols) and calculated (closed symbols) S-waves, and profiles extracted from well locations from the transformed models shown in Fig 6.13(d) and (e).(D) shows bulk modulus from models above 100m which are too low for (C) (<0.1GPa) 203
6.22 Comparison of the standard Erickson and Jarrard equations with data collected at Hikurangi from all three well sites. 207
6.23 Comparison between porosity LWD measurements and porosity measurements converted from density LWD recordings. As the porosity LWD tool measures free hydrogen in the rock and assumes this is all within pores, the tool often overestimates density. 208

List of Tables

3.1 Details of the seismic line 05CM-04 collected across the Hikurangi margin. 37
3.2 Filters and their values applied to the dataset in order to remove swell noise 38
3.3 Parameters used in FWI of the dataset. 60

4.1 Parameters used in FWI of the dataset. 85

5.1 Details of parameters used in the FWI modelling for the 3D checkerboard testing. 119

6.1 Velocity-depth profiles used for modelling velocity differences between undeformed sediments in the Hikurangi Trough, and deformed sediments in the wedge. 168
6.2 Best-fit porosity-density relationships using core data at each well. 170
6.3 Porosity-velocity equations used in a linear least-squares best fit algorithm, and the associated best-fit parameters. 172
6.4 Parameters used by Castagna et al. (1985) to relate Vp to Vs, and the associated parameters found in this study. 175
6.5 Parameters used by Greenberg and Castagna (1992) to relate Vp to Vs, and the associated parameters found in this study. 175

Chapter 1

Introduction

1.1 Subduction zones and their seismic behaviour

Subduction plate boundary faults are responsible for producing some of the largest and most destructive earthquakes and tsunami on Earth, and are a global concern for society due to the proximity of many subduction zones to large cities. Seismic hazards are notoriously difficult to quantify and predict, therefore understanding the processes at work at these plate boundaries is extremely important. Averaged over the past 500 years, subduction margin earthquakes and their associated tsunami have killed on average approximately 100,000 people per year (Bilham, 2004). Recent examples include the 2011 Tōhuku-Oki Mw 9.0, Japan earthquake and tsunami which caused over 15,000 deaths, and the 2004 Mw 9.3 Sumatra-Andaman earthquake, which killed over 230,000 people (USGS, 2014). The Global Earthquake Model (GEM) Faulted Earth Subduction Characterisation Project (Berryman et al., 2015) aims to develop a global model of Earth's subduction zones in order to create a reference for hazard and risk modelling (Fig 1.1). Fig 1.1 not only highlights the proximity of large-scale subduction-zone seismic events to coastal cities, but also shows how variable the size and frequency of earthquakes in these regions can be.

Subduction zones cause the largest earthquakes on Earth due to the size and scale of the plate boundary faults between overriding and downgoing plates. A subduction zone occurs when two tectonic plates collide causing the denser, heavier plate to subduct beneath the lighter plate (Fig 1.2). The site of subduction is marked by a deep trench, and an accretionary wedge is formed as the overriding plate scrapes sediment off the upper crust of the downgoing plate (Moore, 1989; Silver and Reed, 1988; Westbrook and Smith, 1983).

The frictional response of materials at these subduction zones determines the way the fault slips. Faults have a complex frictional dependence on slip velocity, time, and slip distance. Velocity weakening behaviour is when frictional resistance to fault movement decreases faster than reduction of stress due to movement, and this produces 'stick-slip motion, where sliding occurs in sudden slips punctuated by

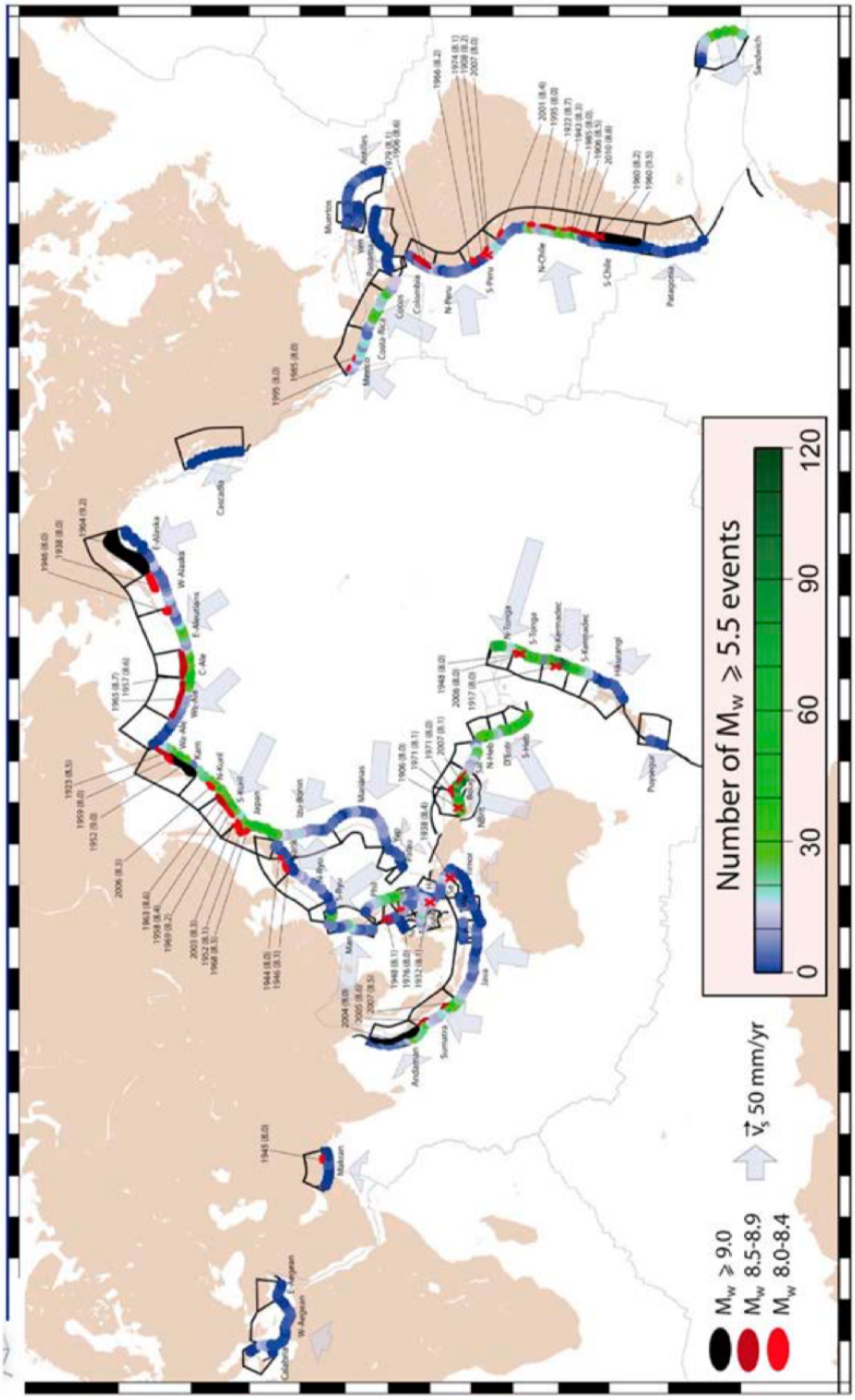


Figure 1.1: Map showing worldwide seismicity at subduction zone interfaces. This figure is taken from Berryman et al. (2015) and has been reproduced from Heuret et al. (2011). The rupture area of the Mw $\geq$ 8.0 subduction interface events (1900 - 2007) is represented by red and black ellipses. Red crosses are used here to indicate Mw $\geq$ 8.0 events that did not have available rupture area data. Coloured dots represent, by each 1° of trench, the number of Mw $\geq$ 5.5 subduction interface events (1976 - 2007). Subduction velocities (Heuret and Lallemand, 2005) are represented by blue arrows

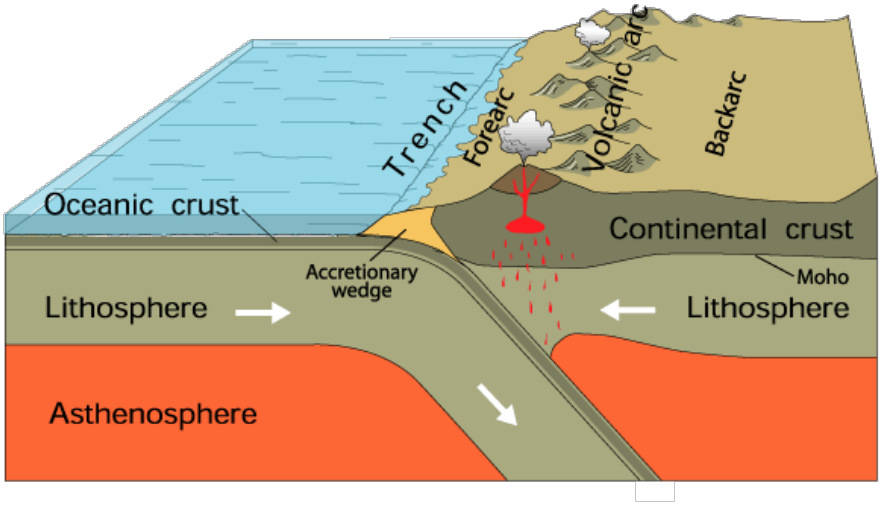


Figure 1.2: Schematic of a subduction zone showing the oceanic plate subducting beneath the continental plate, highlighting the trench and accretionary wedge. Image taken from USGS (https://www.usgs.gov/media/images/subduction-fault-zone-diagram Date taken: 18/07/2016)

periods of no motion as stress builds-up during the interseismic period (Marone et al., 1991; Wesson, 1988). As temperatures increase with depth, frictional behaviour transitions from velocity weakening to velocity strengthening, which occurs when the frictional resistance increases with sliding velocity and is believed to be responsible for the termination of earthquakes, causing plate motion to now be accommodated through stable sliding (Marone et al., 1991; Marone and Scholz, 1988; Savage, 1983). The region of velocity-weakening along the plate boundary fault is known as the seismogenic zone.

Over the last couple of decades, a large number of new fault slip modes have been discovered on subduction megathrust faults using geodetic and seismic data (Figs 1.3 and 1.4)(Peng and Gomberg, 2010). These types of slip go beyond the simple stick-slip or stable sliding categories, and include slow-slip events (SSEs) (Dragert et al., 2001; Obara et al., 2004; Wallace et al., 2004), low-frequency earthquakes (LFEs) (Katsumata and Kamaya, 2003; Shelly et al., 2006), very low- frequency earthquakes (VLFEs) (Ito et al., 2009; Obara and Ito, 2005) and episodic tremor and slip (ETS) (Obara, 2002; Rogers and Dragert, 2003; Saffer and Tobin, 2011) . In these types of slow-slip phenomena, slip does not reach dynamic velocities, and low-amplitude, low-frequency seismic waves radiate, if any at all (Peng and Gomberg, 2010)(Fig 1.3). The use of data from plate-boundary scale GPS networks recording continuously over the last ∼25 years have revealed the significance of these aseismic events along plate boundaries (Dragert et al., 2001; Hirose et al., 1999; Lowry et al., 2001; Peng and Gomberg, 2010; Wallace and Beavan, 2006).

The variability of the duration and magnitude of these slow slip modes reflect a suite of unique fault-slip characteristics. SSEs in particular have much lower slip rates, propagation velocities and stress drops with much longer event durations distinguishing them from earthquakes (Fig 1.3). Peng and Gomberg (2010) suggest the time required for particular slip event to release accumulated stress can be quantified in terms of the scaling between moment and duration, and therefore slip modes on faults should span a continuum (Fig 1.3) rather than separating into distinct fast or slow groupings as suggested by Ide

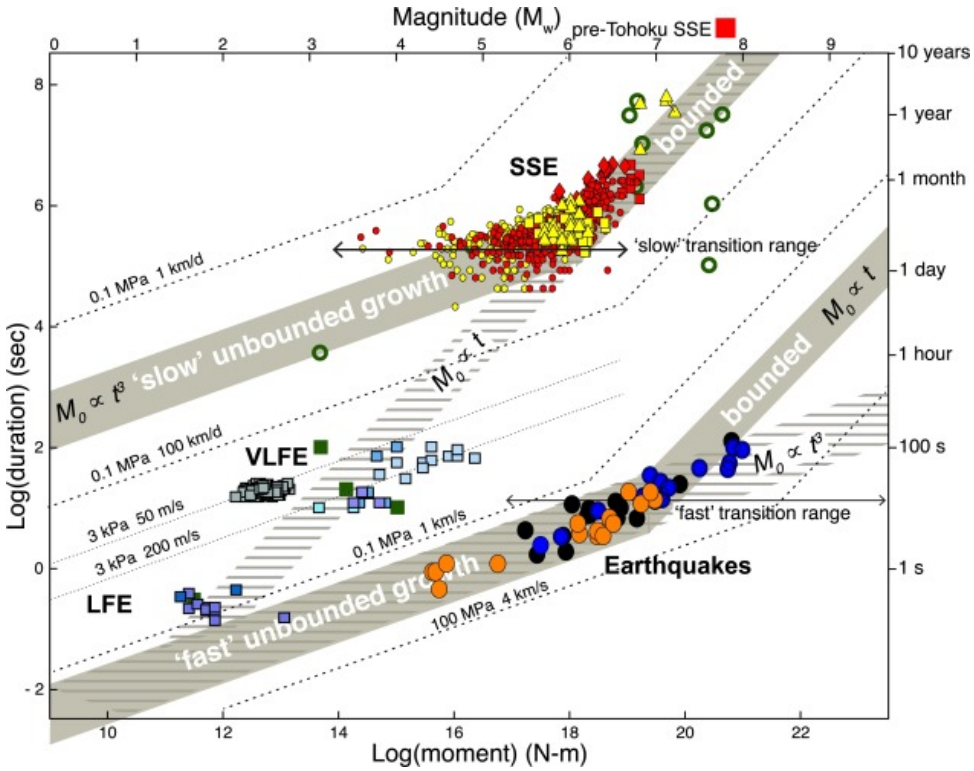


Figure 1.3: Moment (M_0) vs duration (t) of seismic and aseismic slip events and proposed scaling relationships. Dashed and dotted lines denote representative stress drops and rupture propagation velocities for the different event types. SSEs have several orders of magnitude lower stress drops (∼50kPa) than earthquakes (∼5MPa). Image taken from Bürgmann (2018) based on data from Peng and Gomberg (2010).

et al. (2007). This introduction of new seismic behaviours at subduction zones completely changes our understanding of how stress is released at these faults, and how faults accommodate relative plate motion. Gomberg et al. (2016), and Bürgmann (2018) show how slow slip-events occur with highly variable moment magnitudes and slip durations compared to 'regular' stick-slip events, slow slip spans a wide range of sizes, recurrence intervals and durations at all depths (Fig 1.3).

'Tsunami earthquakes' are another type of earthquake that can occur at subduction zones, which are often located near the trench and exhibit a relatively low surface wave magnitude, yet produce very large tsunamis (Kanamori, 1972). These earthquakes include the 1992 Nicaragua (McIntosh et al., 2007; Polet and Kanamori, 2000), the 1994 and 2006 Java earthquakes (Abercrombie et al., 2001; Ammon et al., 2006; Kopp et al., 2009), and, relevant to this thesis, the 1947 Offshore Poverty Bay and Tolaga Bay earthquakes over the Hikurangi subduction zone (Bell et al., 2014; Bilek and Lay, 1999b; Downes, 2001; Pelayo and Wiens, 1992; Power et al., 2008). These events are characterised by long source durations and lack of high frequency energy (Kanamori, 1972). Tsunami earthquakes have been attributed to shallow seamount asperities (Bell et al., 2014; Bilek et al., 2003; Hicks et al., 2012; Husen et al., 2002). These events are a particular hazard as the surface wave motion is relatively weak, nearby populations may not be given sufficient warning to self-evacuate to higher ground before the large tsunami reaches the coast (e.g. Bell et al. (2014)).

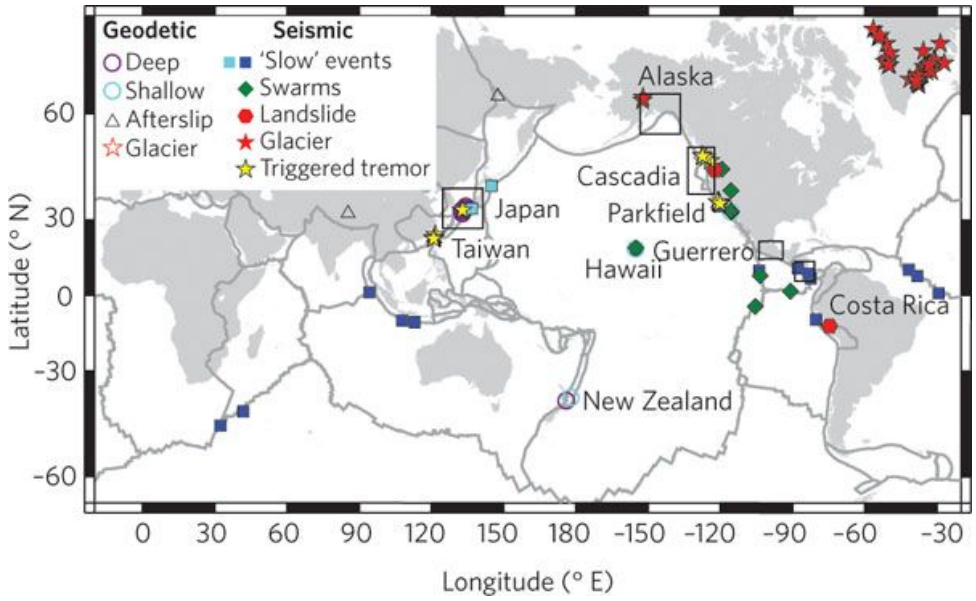


Figure 1.4: The locations of some slow-slip around the globe. The yellow stars mark the locations of tremor triggered by regional and teleseismic earthquakes. Regions where ETS events have been observed are marked by black boxes. Image from Peng and Gomberg (2010).

1.2 Slow slip events (SSEs)

Slow-slip events, or SSEs are described by transient fault slip episodes causing ∼10s of centimetres of slip over timescales of days to months; too slow to generate seismic waves yet faster than the rate of plate velocity (commonly of the order of a few cm/yr) (Bartlow et al., 2014; Wallace et al., 2012, 2014, 2016). Slow-slip events occur with highly variable moment magnitudes and slip durations compared to 'regular stick-slip motion, where stress is relieved through instantaneous rupture of locked faults. These relatively newly discovered slow-slip events rupture slowly enough that only low-frequency seismic waves are released, if any at all, and hence are not felt by people living above them (Fig 1.3). Since SSEs were first discovered, the list of subduction zones with documented occurrences of SSEs has continued to grow, and presently includes Cascadia (Dragert et al., 2001; Miller et al., 2002), central Japan at Boso (Ozawa et al., 2003), south west Japan at Nankai (Hirose et al., 1999; Ozawa et al., 2002; Obara et al., 2004) and Ryukyu (Heki and Kataoka, 2008; Nishimura, 2014), Mexico (Kostoglodov et al., 2003; Lowry et al., 2001), Alaska (Fu and Freymueller, 2013; Ohta et al., 2006; Wei et al., 2012), Costa Rica (Dixon et al., 2014; Jiang et al., 2012; Outerbridge et al., 2010), Ecuador (Vallée et al., 2013) and New Zealand (Douglas et al., 2005; Wallace and Beavan, 2010) (Fig 1.4).

SSEs occur at a range of depths, and fall into two broad categories, deep and shallow. Deep SSEs have been found to initiate between 25-45km depth along the plate interface (Dragert et al., 2001, 2004; Hirose et al., 1999). Shallow SSEs occur at depths less than 12km and will be the focus of this thesis. These slow-slip events are not constrained to any minimum depth along the decollement and shallow SSEs have not been seen to correlate with temperature (Saffer and Wallace, 2015). Fig 1.3 shows that slow-slip events span a continuum of seismic moments and durations rather than falling in one specific range.

SSEs occur at most subduction zones where the GPS networks are dense enough to detect them, and play an important role in strain accumulation and release (Peng and Gomberg, 2010; Saffer and Tobin, 2011). As these events significantly contribute to moment release at subduction zones, it is important to be able to quantify their size, and discover why they occur (Douglas et al., 2005).

The physical mechanisms responsible for the generation of SSEs remain poorly understood, and it is unclear as to whether SSEs have the potential to trigger larger earthquakes and tsunami. Resolving what controls how a plate boundary fault ruptures and releases stress during large stick-slip events and slow earthquakes is one of the most important current questions in seismology (Lay, 2009). The physical mechanisms responsible for SSE generation are not well constrained, but have been linked to temperature, fluid pressure and fault zone rheology. Based on numerical modelling, geophysical and geological data, discussed in section 1.3, the properties attributed to SSE generation are: (1) Velocity-strengthening material in the fault zones; and/or (2) Velocity-weakening patches along the fault which are smaller in size than a critical size necessary for earthquake nucleation; and/or (3) Large volumes of highly pressured fluids; and/or (4) Heterogeneous fault structure, roughness, and composition over a wide range of scales (Bürgmann, 2018).

1.3 Geophysical imaging at subduction zones

To understand why some faults experience SSEs where they do, understanding the fault structure and physical properties of slowly slipping fault segments is necessary. One of the reasons why slow slip mechanisms have not yet been constrained may be related to the fact that no wells have yet drilled a subduction margin slow slip zone to provide direct geological evidence. This is because well constrained source regions of SSEs are generally too deep for drilling to be technically viable. This has motivated many studies using a range of geophysical techniques as well as geological studies of exhumed fault zones. The most common type of investigation uses seismic imaging methods to provide information about seismic wave speeds and related elastic properties affected by differences in lithology, density and fluids in and near fault zones (Bürgmann, 2018). Seismic tomography has been used to image the San Andreas fault (e.g. Lewis et al. (2007); Li et al. (1997); Thurber et al. (1997)), Cascadia margin (e.g. Audet et al. (2009); Nedimović et al. (2003)), Nankai (e.g. Kodaira et al. (2004); Park et al. (2010); Tobin and Saffer (2009)), Costa Rica (e.g. Husen et al. (2003); Saffer et al. (2000); Tobin et al. (2001)) and Hikurangi (e.g. Barker et al. (2018); Eberhart-Phillips and Chadwick (2002)). Other techniques include using teleseismic receiver functions to recover low velocities and high Vp/Vs rations (e.g. Audet and Kim (2016); Eberhart-Phillips and Bannister (2015); Zhao et al. (2011)) high electric conductivity suggesting fluid presence (e.g. Wannamaker et al. (2014)), and fluid rich subducted sediment and high fluid pressure based on inferences from reflection seismic imaging (e.g. Bell et al. (2010); Kodaira et al. (2004); Tobin and Saffer (2009)). A unique geophysical signature of slow slip has been difficult to pin-point, with most studies aimed at detecting the presence of highly pressured fluids near the fault and thickness of the fault zone (Bürgmann, 2018). Unfortunately, many of these studies are limited in resolution (usually $\sim$

tens - hundreds of meters), and do not resolve the physical properties within the fault zone directly.

Fortunately, improvements in computing power have allowed for the advancement and application of a technique called Full-Waveform Inversion (FWI). FWI is a relatively new technology in which the full seismic waveform is inverted in order to obtain higher-resolution images of velocity than is possible using conventional travel-time tomography (Tarantola, 1984; Virieux and Operto, 2009). Full-waveform inversion is an iterative technique which predominantly uses the refracted wavefield, and utilises a series of linearised local inversions to update a starting model in a way that gradually improves the match between the predicted and observed data (Pratt, 1999). As computing power has advanced, using these theories published in the 80's and 90's is now feasible, and the petroleum industry now regularly uses 3D full-waveform inversion of seismic data to obtain high-resolution images of a variety of physical properties including S-wave velocity, attenuation, anisotropy and density, but is mostly used to produce high-resolution models of P-wave velocity (Guasch, 2012; Guasch et al., 2019; Lu et al., 2013; Sirgue et al., 2009, 2010; Warner et al., 2013; Vigh et al., 2014). The full theory behind FWI is detailed in chapter 2.

Although FWI has been applied successfully to a large number of datasets within the oil and gas industry in the imaging of relatively shallow hydrocarbon reservoirs (e.g. Houbiers et al. (2013); Jones et al. (2013); Sirgue et al. (2010); Warner et al. (2013)), it is only recently that the method is beginning to be applied to academic datasets, and to deeper targets including subduction zones (eg Calvert et al. (2011); Christeson et al. (2012); Kamei et al. (2012); Morgan et al. (2011, 2013), chapter 3). The main difference in the application to academic datasets is that, while within the oil industry FWI is primarily used to improve depth migration of reflectors, for longer and deeper academic datasets, the high resolution velocity model itself can often be used to test scientific hypothesis (Morgan et al., 2013).

Kamei et al. (2012) completed a 2D FWI study over the megasplay fault system of the central Nankai subduction zone using long offset ocean-bottom seismometer (OBS) data with spacing between 1 and 10km, to obtain 2D velocity images of the subducting plate. The results of the Nankai inversion showed a great improvement to the starting model (Fig 1.5A), showing lithological boundaries which corresponded to reflectors on seismic migration images. The subducting plate can be clearly discerned from the final result (Fig 1.5B). The results gave a good insight into the mechanics of the megasplay, with Kamei et al. (2012) concluding that the continuous low-velocity zone suggests pore-fluids may be transported from the inner wedge, to the transition zone, and to the surface, through fluid conduits associated with the megasplay fault system. This study is extremely promising for the use of FWI to recover physical properties at subduction zones.

I aim to investigate physical properties at the Hikurangi margin, East of North Island, New Zealand, which has been observed to undergo many SSE events for the past 17 years. Reflection seismic surveys have previously been carried out over this region , and industry-standard 2D streamer data was readily available for use at the start of my PhD in October 2015 (Bell et al., 2010; Davy et al., 2008). This data provides an excellent starting point for carrying out FWI along the 2D marine streamer line 05CM-

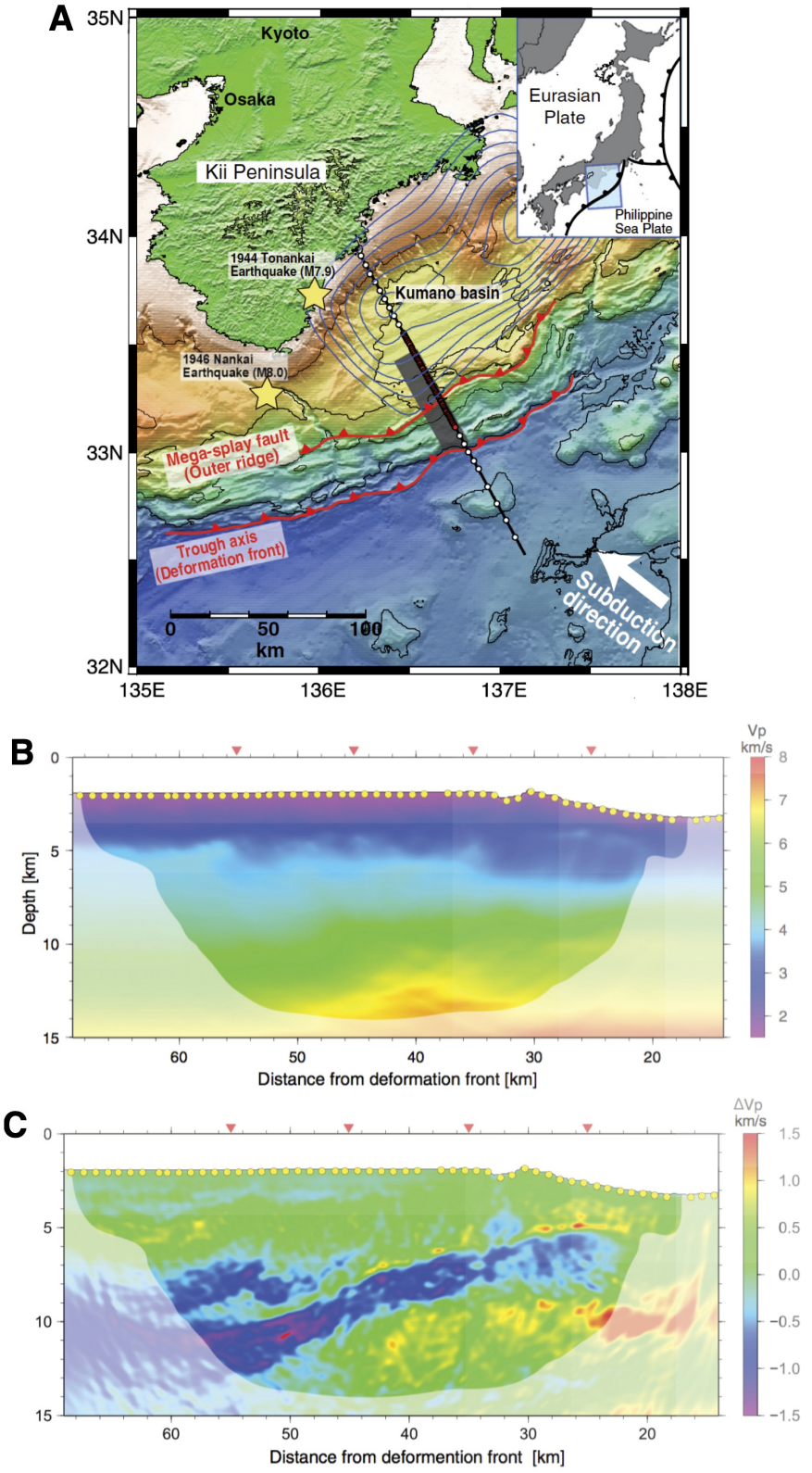


Figure 1.5: FWI has been used to image the megasplay fault system at Nankai by Kamei et al. (2012). (A) Shows the location of the study area at Nankai. (B) Shows the starting model and (B) the final result of acoustic inversion de-trended by the 3rd order polynomial which best fit the original 2D traveltime tomography. Image from Kamei et al. (2012).

04 (Fig 1.6). Velocity models are available based on Normal Move-Out (NMO) velocities, and some structure has been discerned from the reflection seismic images (Barker et al., 2009, 2018; Bell et al., 2010; PlazaFaverola et al., 2016). This 2D streamer data allows FWI imaging down to 2km below the seafloor, which will allow investigation of the incoming section which likely plays a key role in the slow slip mechanism and will allow me to investigate the hydrogeology of the wedge above the slow slip patch (chapter 4). Part way through the PhD drilling data was collected along the 2D profile and this was used to transform the velocity model and extend the results of drilling down to depths of 2 km and in 2D (chapter 6).

In addition, this thesis involved the design of a 3D seismic experiment to collect data that will allow the slow slip zone to be resolved using 3D FWI (chapter 5). The 3D active-source seismic dataset was funded by NSF, NERC, Japan and New Zealand and collected in 2017-2018, across northern Hikurangi. The experiment was designed optimally for use with FWI in order to invert for physical properties within the northern Hikurangi zone of slow slip, to determine why this plate boundary fault slips slowly in SSEs and tsunami earthquakes. This experiment will resolve fine-scale 3D elastic properties of the subduction interface experiencing SSEs and tsunami earthquakes for the first time and will be a key study in testing hypotheses of why slow slip and tsunami earthquakes occur and how the physical properties along the fault interface differ from subduction zone megathrusts which experience large, stick-slip earthquakes.

1.4 Hikurangi Megathrust

1.4.1 Tectonic setting and seismic behaviour

The Hikurangi margin is located at the boundary where the Pacific Plate subducts beneath the Australian Plate, along the east coast of the North Island, New Zealand (Fig 1.6). The plate motion is on the scale of <30 - ∼60mm/a, with a rate of ∼55mm/a offshore the town of Gisborne (Barker et al., 2009; DeMets et al., 1994; Walcott, 1987a; Wallace et al., 2004) with a separation between convergence near the trench, strike-slip motion near the crest of the forearc ridge and extension near the arc volcanoes (Barker et al., 2009; Walcott, 1984; Wallace et al., 2004). Several reflection seismic surveys have been carried out over the Hikurangi margin (eg Fig 1.6) (Barker et al., 2009; Bell et al., 2014; Douglas et al., 2005; Wallace et al., 2004), in order to determine structure of the margin. Continuous GPS data has also been used since 2002 to measure small changes in topography at the Earth's surface, and to record SSEs occurring at the margin (Douglas et al., 2005; Wallace et al., 2004; Wallace and Beavan, 2006) (Fig 1.6).

Most notably across the margin is a distinct change in geodetic coupling, discovered by Wallace et al. (2004) using a decade of GPS data (Fig 1.6). Interplate coupling is the ability of a fault between two plates to lock and accumulate stress (Wang and Dixon, 2004).There is a deep, interseismically coupled zone beneath the southern North Island which shallows quickly to the North-East, near Cape Turnagain. Beneath the North Island there is an abrupt transition zone, where the two plates become uncoupled, and the interface changes from coupled to creeping behaviour (Wallace et al., 2004). Along-strike, there

is an abrupt change in the downdip limit of interseismic coupling. The change cannot be explained by temperature profiles along the interface, as has been done at other subduction zones (Hyndman et al., 1995; McCaffrey and Goldfinger, 1995; Oleskevich et al., 1999). The coupling occurs at temperatures as low as 100°C despite the suggested temperatures of 350°C to mark the base of the frictionally unstable portion of the fault, and 450°C to mark the beginning of the free slipping behaviour (Liu and Rice, 2007; McCaffrey and Goldfinger, 1995; Oleskevich et al., 1999). Deeper SSEs (<15km), however, somewhat correlate with temperature, and occur in regions with temperatures in the range ∼350-450°C (Peacock, 2009; Peng and Gomberg, 2010). The cause of the change in coupling at Hikurangi is most likely due to a combination of interface temperatures, fluid pressure, structure of the upper and lower plates, and tectonic stress state of the upper plate (Fagereng and Sibson, 2010; Wallace et al., 2004, 2009).

Two tsunami earthquakes occurred at the northern Hikurangi margin in March and May of 1947 (Fig 1.6) (Bell et al., 2014; Doser and Webb, 2003), which had local magnitudes of only M_L 5.6 and 5.9. They caused abnormally large tsunami, compared to other earthquakes at comparable depths and magnitude, with run-up heights up to 10m, which have been attributed to unusually slow seismic rupture velocities (Bell et al., 2014; Downes, 2001). The margin is also known to host low frequency, long lasting slow slip events at a recurrence rate of between 1 and 2 years, which have been detected in the region via continuous GPS (cGPS) measurements since 2004 (Wallace et al., 2009, 2012, 2016), an example of which is shown in Fig 1.6, showing jumps in the cGPS data recorded at site GISB since 2004 during SSEs. Shallow SSEs at northern Hikurangi accommodate slip equivalent to that of an earthquake with moment magnitude of M6.3-6.8, and typically result in 1-3cm of horizontal surface displacement over 1 to 2 weeks. For the southern Hikurangi margin, the SSEs are larger (∼M7.0), longer lasting (>200 days) and deeper (25-60km depth) (Wallace et al., 2004, 2009; Wallace and Beavan, 2010; Wallace et al., 2012, 2016).

The updip extent of shallow offshore SSEs at northern Hikurangi is not well constrained by the land-based cGPS observations, but the recent addition of data from offshore absolute pressure gauges (APGs) indicates that these shallow SSEs extend to within 2km of the sea floor, and possibly all the way to the trench (Wallace et al., 2016). The SSEs at Hikurangi are the shallowest well documented SSEs in the world to date, making them more accessible to geophysical and geological investigations. The physical properties at Hikurangi which govern these seismic behaviours are not yet fully understood. Several hypotheses exist as to why SSEs occur at subduction zones, such as Hikurangi, and how these might be evidenced at the Hikurangi margin.

1.4.2 Proposed hypotheses for variable slip behaviour along the margin

1.4.2.1 Fluid pressure plays a role in controlling slip behaviours at subduction zones

Numerical models of subduction zones exhibiting SSE behaviour require low effective stress (Liu and Rice, 2005, 2007) and therefore low effective confining pressure (Peng and Gomberg, 2010). The most viable way to achieve these conditions is extremely high (∼99% lithostatic) pore fluid pressure. Analysis

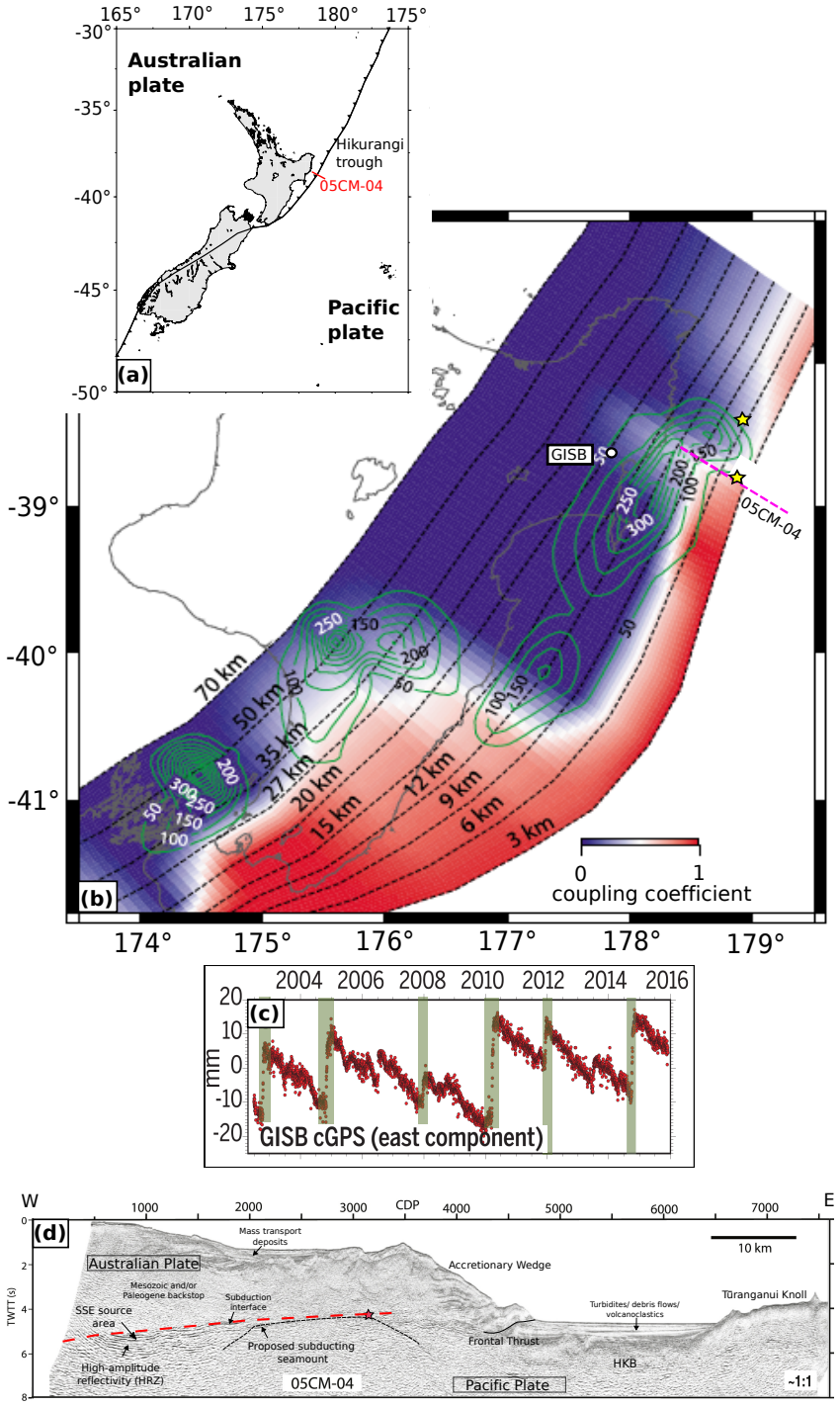


Figure 1.6: (a) Is the regional map of New Zealand showing plate boundaries, highlighting line 05CM-04 which is shown in detail in (d). (b) shows a more detailed map of the north island, highlighting the change in geodetic plate coupling. Line 05CM-04 is again highlighted as are the 1947 Offshore Poverty Bay (along line 05CM04) and Tolaga Bay tsunami earthquakes (Bell et al., 2014) represented by yellow stars. Green contours represent total slip in mm detected in SSEs on the Hikurangi subduction interface since 2002 and dashed black lines show depth contours to the subduction interface. GISB represents the location on a cGPS site, shown in (c). Image taken from Wallace and Beavan (2010). (c) shows the east component of cGPS time series from GISB, highlighted in (b). Eastward (positive) jumps denote SSEs, and major SSEs since 2002 have been highlighted in green. Image adapted from Wallace et al. (2016). (d) shows the reflection seismic profile along line 05CM-04, highlighting the frontal thrust, estimated plate interface and proposed subducting seamount (Bell et al., 2014) based on magnetic data. Image adapted from Bell et al. (2014).

of low-resolution tomographic images of elastic properties around SSE source regions reveal evidence of elevated fluid pressure (Audet et al., 2009; Matsubara et al., 2009; Peng and Gomberg, 2010; Song et al., 2009). In situ effective stress estimates along the subducting plate interface at Hikurangi imply the presence of excess fluids (Bell et al., 2010; Kitajima and Saffer, 2012; Kodaira et al., 2004), however presence of these fluids is still speculative without cores or high-resolution velocity models (Peng and Gomberg, 2010). Using FWI has the potential to produce high-resolution seismic velocity models in the region, allowing a detailed interpretation of the presence of fluids, characterised by low P-wave velocities (Audet and Schwartz, 2013; Shelly et al., 2006; Song et al., 2009). Current velocity models are only able to provide resolution at relatively long scale lengths (∼1-10km) (Barker et al., 2018), while reflection seismic imaging on line 05CM-04 resolves velocity structure on the scale of 500m at about 6km below the seafloor (bsf) and on a scale of 1km at 15kmbsf (Barker et al., 2009; Bell et al., 2010). Imaging has therefore not yet been able to resolve velocity structure within the narrow thicknesses along the decollement at which SSEs occur, or within the frontal thrusts or accretionary wedge.

1.4.2.2 Subduction of sediments causes high pressured fluids in the SSE region of Hikurangi

The origin of the fluids speculated to facilitate SSEs at subduction zones is still unclear. Studies show fluids from metamorphic dehydration reactions and early diagenesis are unlikely to provide the necessary fluids (Saffer and Wallace, 2015), as the pressures and temperatures at which these reactions occur are inconsistent with the locations of SSEs (Saffer and Tobin, 2011; Spinelli et al., 2006). When sediments are subducted, they undergo a relatively fast increase in overburden, and are unable to dewater quickly enough so that compaction equilibrium is maintained (Saffer and Wallace, 2015). Consequently, they have been observed to maintain an extremely high porosity, causing them to develop high pore fluid pressure (Saffer and Wallace, 2015). This rapid compaction in combination with the low permeability of marine sediments is the more likely origin of fluids in SSE regions (Saffer and Wallace, 2015). Dilatant strengthening, whereby frictional faults dilate during accretion at rates which prohibit draining, may also cause a decrease in permeability and subsequent increase in effective normal stress, which may limit dynamic rupture (Peng and Gomberg, 2010; Rubin, 2008; Segall and Bradley, 2009). In the context of the Hikurangi subduction zone, it would be useful to accurately determine the volume of sediment that has been subducted. By doing so, the amount of fluid originating from the subducted sediment can be estimated.

1.4.2.3 Subducting seamounts encourage SSEs

Subducting seamounts have been suggested to cause many different behaviours at subduction zones. Some literature suggests subducting seamounts cause large earthquakes by creating strongly contrasting conditions (Cloos, 1992; Scholz and Small, 1997), while other literature suggests they prevent large earthquakes and encourage aseismic creep (Saffer and Wallace, 2015). Seamount subduction occurs at

Hikurangi, with seamounts identified on the seafloor (e.g. Tūranganui Knoll, Fig 1.6) and on the plate interface as inferred from seismic reflection and magnetic data along the northern part of the margin (Barker et al., 2009, 2018; Barnes et al., 2010, 2018; Bell et al., 2010, 2014) (Fig 1.6). Subducting seamounts may create a heterogeneous stress field as they fracture the upper plate as they subside (Wang and Bilek, 2011). This fracturing can disrupt the spatial continuity of the plate interface, creating a mixture of velocity strengthening and velocity weakening zones (Saffer and Wallace, 2015). Subducting seamounts may also aid in the subduction of marine sediments, which may relate to elevation of fluid pressures along the decollement, enhancing the probability of SSEs. The subducting sediments dragged along with the seamount may also produce large (kilometre-scale) variations in lithology along the fault, producing a combination of slip behaviours (Bell et al., 2010; Saffer and Wallace, 2015; Wang and Bilek, 2014).

1.4.2.4 In SSEs, the slip along the plate interface is distributed over a thicker shear zone than in stick-slip regions

One hypothesis is that SSE and aseismic creep dominated subduction zones may be characterised by a thick (∼100's m - km) mixed, heterogeneous zone of fractured and sheared rocks (Fagereng and Sibson, 2010). In this zone, the slow observed displacement is due to steady deformation distributed within the fine-grained matrix (Fagereng and Sibson, 2010; Wang and Bilek, 2011). The heterogeneous zone will in turn produce a heterogeneous stress field, resulting in the subduction interface becoming a mosaic of lithologies which includes carbonates, basalt, clays and quartz (Fagereng and Sibson, 2010; Saffer and Wallace, 2015; Wang and Bilek, 2014). The heterogeneous structure is evidenced by seismic reflection images which show an interleaving zones of high and low amplitude reflectivity (Fig 1.6) (Bell et al., 2010; Saffer and Wallace, 2015). Each element in this mosaic has different properties making them stable or unstable, as well as velocity strengthening or velocity weakening. By maintaining this heterogeneous stress field, SSEs are believed to originate as the plate cannot rupture over large areas to produce a stick-slip event. Results from numerical models and lab experiments have been used to argue this theory (Ikari et al., 2013; Saito et al., 2013; Skarbek et al., 2012). As little is known about SSE and aseismic creep dominated subduction zones, the creeping segment of the San Andreas fault is used as a reference where drilling has exposed a wide, low-velocity damage zone (eg Thurber et al. (2004); Zoback et al. (2011)).

1.5 FWI at Hikurangi

As the data that existed at the start of the project only allow us to image to 2km with FWI, this does not include the source region for SSEs is along the decollement at depths of ∼10 - 15kmbsf (Wallace and Beavan, 2010). Much insight about SSE can, however, be gained without imaging the fault directly. The incoming section is critical as the plate boundary fault forms within it and the accretionary wedge provides clues as to the hydrogeology of above the plate interface. The main parts of the margin

investigated in this project include:

1. Incoming section

   The Hikurangi Trough represents the incoming sediment which will undergo subduction at the margin, and the plate boundary fault itself forms within this incoming section. As many theories of SSE generation are linked to high fluid pressures and the subduction of fluid-rich sediment, investigating the physical properties of the inputs into the subduction zone is important. The different lithologies and thickness of sediments entering the subduction zone may be able to provide insights into the seismicity at Hikurangi.

2. Accretionary Wedge

   The accretionary wedge is important, as shown by Wallace et al. (2017), who speculate that shallow subduction interfaces overlain by a low-velocity sedimentary wedge can be highly susceptible to dynamic triggering of slip events by regional earthquakes, both seismic and aseismic. This means that at Hikurangi, the wedge may be acting as a waveguide promoting the triggering of shallow SSEs. It is therefore important to understand the accretionary wedge at Hikurangi in detail. Various studies have also been able to estimate behaviours such as the amount of fluid released at subducting margins using physical properties such as porosity (e.g. Bangs et al. (1990); Han et al. (2017); Von Huene et al. (1998)). It would be useful to do similar analysis at Hikurangi.

3. Faults

   A study by Shaddox and Schwartz (2019) indicated that during a large plate boundary SSE at Hikurangi, fluids in overpressured sediments downdip of the subducting seamount (Bell et al., 2010), may migrate into the large fracture network on the overriding plate, triggering further slow-slip on these pre-existing faults. Imaging these faults within the accretionary wedge is therefore very important to understand what physical properties these faults exhibit, and whether they may be related to the seismic behaviour at the margin. As the updip extent of SSEs at Hikurangi has been found to be <2kmbsf and may propagate all the way through to the trench, it is important that the physical properties at frontal thrust faults at the margin are also investigated.

1.6 Aims and Objectives

This thesis has two primary aims:

1.6.1 Aim 1: To determine whether the application of FWI is feasible at subduction zones

1.6.1.1 Objective 1.1: To apply 2D FWI to line 05CM-04 across the Hikurangi margin

a) Prepare the 05CM04 streamer dataset, and associated PSTM velocity model for FWI.

b) Assess how effective the method is using a range of quality assurance methods and comparing the modelled results to real data, and determine what resolution can be obtained with this dataset.

1.6.1.2 Objective 1.2: To use determine the optimal survey design for 3D FWI data collection at subduction zones

a) Determine key targets for a 3D experiment at Hikurangi to recover velocity of the plate boundary zone.

b) Optimise the land receiver layout in order to best recover key targets using FWI to allow future imaging of the slow slip zone at depths of 10km.

1.6.2 Aim 2: To investigate the physical properties of the incoming section and overriding plate and interpret them in terms of the seismic behaviour of the north Hikurangi margin

1.6.2.1 Objective 2.1: To assess the geological significance of high-resolution P-wave velocity anomalies

a) Identify key differences between the starting and final velocity models.

b) Determine how velocity changes across features resolved by FWI including faults in the wedge, frontal thrusts and incoming section.

c) Evaluate how these velocity differences may affect seismicity at the margin.

1.6.2.2 Objective 2.2: To use IODP drilling measurements to transform P-wave velocity models into other physical properties to assess subduction margin processes

a) Develop relationships between modelled Vp and recovered Vp, porosity, Vs, and density measurements taken on IODP Expeditions 372 and 375.

b) Use these relationships to transform the FWI Vp model into models of potential compaction, porosity, Vs, Vp/Vs, bulk modulus and shear modulus.

c) Investigate how these properties vary in the incoming section, wedge and at faults to determine how these physical properties may affect seismic behaviour at Hikurangi.

1.7 Thesis Outline

The thesis is organised into seven chapters as follows:

Chapter 2: Theory of Full-Waveform Inversion (FWI).
This chapter describes the background mathematical theory of full-waveform inversion as well as some of the requirements for its successful application.

Chapter 3: Methods.
This chapter describes the approach used in the application of FWI to the 2D Hikurangi dataset, and for the physical property transforms. Details of the seismic dataset are provided, as well as a description of the challenges faced in the application of FWI to this dataset. This is followed by a description of how the starting model, source wavelet and inversion scheme were derived. This chapter also briefly introduces how the synthetic testing and model transformations are carried out. Further details of the adopted approach are provided later in the thesis, in their respective chapters.

Chapter 4: Imaging the shallow subsurface structure of the north Hikurangi subduction zone, New Zealand, using 2D Full-Waveform Inversion.
This chapter shows the high-resolution P-wave velocity model across the Hikurangi margin obtained using 2D, isotropic FWI of streamer data. This is followed by a description and interpretation of some of the recovered features. This chapter has been published in Gray et al. (2019), Journal of Geophysical Research: Solid Earth.

Chapter 5 : Aims, design and configuration of NZ3D-FWI: a large 3D seismic experiment at the Hikurangi margin.
In this chapter 3D FWI synthetic checkerboard tests are used to assess which acquisition geometries are best able to recover features in the target areas; the results of which were then used to design the NZ3D-FWI seismic experiment, as well as check for hazards prior to the two IODP drilling expeditions. Details of the instrumentation, chosen seismometer locations, and data acquisition are provided at the end of the chapter.

Chapter 6 : Using logging-while-drilling, wireline and core data to investigate physical properties at the Hikurangi margin based on the 2D Vp model created using Full-Waveform Inversion.

Physical property data, acquired during the two drilling expeditions using logging-while-drilling, wire-line logs and core samples, are used to derive relationships between Vp and a range of other physical measurements, including porosity, Vs, Vp/Vs, and elastic modulii. These relationships are then used to transform the 2D FWI velocity model into various physical properties models, which are evaluated in terms of their hydrological and lithological implications, and degree of compaction across the subduction zone.

Chapter 7: Conclusions.
This chapter summarises the main points of the research in relation to the original aims of the research outlined in this chapter.

All attempts have been taken to avoid repetition in this thesis, however, due to the inclusion of a published article there will inevitably be some replication of material.

Chapter 2

Theory

2.1 Introduction

This chapter details the theory behind Full-Waveform Inversion. It begins with the acoustic wave equation and details how the full wavelet is used during model inversion. It also discusses the common downfalls of FWI, and how to implement the theory successfully.

2.1.1 FWI code

The codes I used for FWI are know as FULLWAVE and were developed at Imperial College London over the last 15 years, building on 2D phase-only frequency-domain acoustic and viscoelastic codes developed at Imperial by Gerhard Pratt in the late 1990's, therefore only the acoustic wave equation is considered. The most important advance, in terms of the accuracy of models recovered by FWI, was the move from 2D to 3D. The second most important advance has been the capability to account for anisotropy. Acoustic anisotropic 3D FWI is now widely used within the petroleum sector; the sponsors of the FWI consortium at Imperial use the same codes and share experiences with the research group, helping with the continuous improvement and optimisation of the code. The current FWI code, which is a time-domain code, has the capability to account for elasticity, attenuation, density and anisotropy, to invert globally for attenuation and anisotropy, and to mitigate the amplitude effects of elasticity, density and attenuation when using the purely acoustic version of the code (Agudo et al., 2018; Calderón Agudo et al., 2018; da Silva et al., 2017, 2018, 2019; Debens, 2015; Guasch, 2012).

Here we use a 2D version of the 3D Imperial College time-domain code (Warner et al., 2013). The code uses both velocity and density contrasts to produce reflections, and the two models are coupled together using Gardners law to estimate density from Vp. The acoustic approximation of the wavefield is utilised, since there are no a priori constraints on anisotropy, S-wave velocity, attenuation or density. Given this approximation, we can expect there to be some inaccuracies in the recovered P-wave model; for example,

if anisotropy is not accounted for, FWI velocity models are stretched and the depths inaccurate. This was observed in the recent drilling of the Chicxulub impact crater, where FWI-determined (sub-horizontal) velocities obtained prior to drilling (Morgan et al., 2011) led to an overestimate in the vertical velocity within the sedimentary overburden and corresponding depth to the crater (Christeson et al., 2018).

2.1.2 Amplitude balancing

In industrial seismics, it is often straightforward to validate velocity models recovered using FWI using extensive well-log data, well-constrained anisotropy models, and reflector flatness in pre-stack depth migrated gathers. Using continual testing within Imperial's FWI research group over many years, a key finding is that one of the most important factors affecting the accuracy of final models recovered by FWI is the careful treatment of amplitudes, both within and between traces (Agudo et al., 2018; Calderón Agudo et al., 2018; da Silva et al., 2017, 2018, 2019; Debens, 2015; Guasch, 2012). To account for this, the code applies a stabilized, smooth, data-adaptive approach to amplitude matching and balancing, designed and optimized on the basis of performance, principally that measured in calibrated wells. Exhaustive testing of amplitude balancing schemes has been carried out based on a multitude of datasets from different settings provided by Imperial's industrial partners. The resultant amplitude treatment used in the current codes evolves adaptively as FWI proceeds and the model improves. This largely, but not completely, mitigates for amplitude changes that are related to attenuation, density, elasticity and short-wavelength changes in anisotropy, while largely, but not completely, retaining those amplitude affects that are related directly to the P-wave velocity model. The code will, by proxy, achieve this most effectively in the geological settings for which it has been optimized, and these are mostly sedimentary; the code has also been widely applied to basaltic sections in deep-water continental margins, and these igneous settings are somewhat analogous to those pertaining in the present study.

In the inversions shown here, we have normalised amplitudes between different time slices using stabilised amplitude matching that varies smoothly and slowly in both space and time independently for both observed and predicted data, and we have balanced trace amplitudes between predicted and observed data using a scheme that is sensitive to the similarity between the two datasets, and that is also stabilised and that varies smoothly in space (Warner et al., 2013). The former scheme largely removes amplitude effects associated with attenuation and divergence, and corrects for the differences between 2D and 3D spreading. The latter scheme largely removes amplitude-vs-offset effects related to un-modelled elasticity and density effects while retaining other amplitude variation with offset (AVO) effects. We are not trying to perfectly match changes in absolute amplitude with offset since, with an acoustic code, we cannot properly reproduce changes in amplitude.

2.2 Seismic Wave Equation

The wave equation is a fundamental equation describing the behaviour of waves in a medium. It is a second order, partial differential equation which involves derivatives of space and time. It can be

described most simply as the behaviour of sound in an acoustic, isotropic, inhomogeneous fluid medium with no attenuation or dispersion as:

$$\frac{1}{c^2}\frac{\partial^2 p}{\partial t^2} - \rho\nabla\cdot\left(\frac{1}{\rho}\nabla p\right) = s, \tag{2.1}$$

where p is pressure; c is the acoustic p-wave velocity; ρ is the density; and s is the source. Both pressure, p, and source,s, are functions of position (x, y, z) and time, whereas density, ρ, and velocity,c, are functions of position (x, y, z) only.

We can express the wave equation using a linear operator relating the wavefield, $\mathbf{p}$, and source, $\mathbf{s}$, by:

$$\mathbf{Ap} = \mathbf{s}, \tag{2.2}$$

Where $\mathbf{p}$ represents the pressure wavefield produced by $\mathbf{s}$ at all times and positions in the model and $\mathbf{A}$ is a matrix depending on the model parameters c and p, and the boundary conditions. $\mathbf{A}$ represents the operator

$$\frac{1}{c^2}\frac{\partial^2}{\partial t^2} - \rho\nabla\cdot\left(\frac{1}{\rho}\nabla\right). \tag{2.3}$$

2.3 The Forward Problem

The underlying theory of FWI begins with the forward modelling problem. The full seismic wavefield must be modelled, and the main issue in FWI is doing this efficiently, particularly for 3D datasets (Virieux and Operto, 2009). The full seismic wavefield can be described in the time-domain by the following partial differential equation:

$$\mathbf{M}(\mathbf{x})\frac{d^2\mathbf{u}(\mathbf{x},t)}{dt^2} = \mathbf{A}(\mathbf{x})\mathbf{u}(\mathbf{x},t) + \mathbf{s}(\mathbf{x},t), \tag{2.4}$$

where $\mathbf{M}$ and $\mathbf{A}$ are matrices containing parameters describing the mass and stiffness of the subsurface (Marfurt, 1984). The source term is shown here by $\mathbf{s}$ and the seismic wavefield by $\mathbf{u}$, which, for the acoustic case is usually a representation of pressure. The spatial coordinates and the time are denoted by $\mathbf{x}$ and t respectively. Equation 2.4 can be rewritten using the operator, $\mathbf{G}$, to obtain

$$\mathbf{G}(\mathbf{m}) = \mathbf{u}, \tag{2.5}$$

which is the generic wave equation. Here all the information about the subsurface from the matrices **M** and **A** are contained in a column vector **m**. Therefore, given the column vector, **u**, of the seismic wavefield, the operator **G** calculates how the seismic data describe a certain model of the subsurface (Dmowska, 2006; Pratt and Worthington, 1990; Tarantola, 2005; Virieux and Operto, 2009; Warner et al., 2013).

2.4 The Inverse Problem

In reality, after seismic acquisition is undertaken the data acquired can be described by **u**. This data is used to create a model of the subsurface parameters being investigated, most commonly, P-wave velocity. In order to obtain an accurate model, the inverse problem must be solved, which can be written as

$$\mathbf{m} = \mathbf{G^{-1}}\left(\mathbf{d}\right), \tag{2.6}$$

where **d** is the observed data, and **G** in this equation is different to **G** in equation 2.5. The main problem in solving this equation is that the operator **G** is non-linear with no true analytical inverse (Lailly, 1983; Tarantola, 1984; Warner et al., 2013). Instead, the problem is approached by calculating an approximate solution to equation 2.6, and improving the result iteratively towards a true solution. Each iteration consists of 3 main processes:

1. Forward propagating a wavefield through the initial model, **m** and calculating the difference between the predicted and observed wavefields (the residuals) at each receiver position. Back propagating these residuals back through the model.

2. Cross correlating the forward and back propagated wavefields at every point in the model to calculate an unscaled model update (the gradient).

3. Calculating the step-length to obtain a scaled model update. Once a scaled model update has been calculated, the model can be updated and the whole process repeated until a best fit model is found.

This process is not always straightforward as several problems are associated with the inverse problem. These include:

- Data are inexact and incomplete as they are acquired at discrete locations in space.

- Data contain noise from several sources.

- The operator **G** may not have an inverse $\mathbf{G^{-1}}$.

- The solution may be non-unique, or enough observed data may not exist to provide a single unique

solution, but rather several possible solutions.

- The problem is ill-posed, in that small variations in the data may cause large, uncontrolled perturbations in the solution.

2.5 Calculating the Residual

A synthetic wavefield is produced by propagating a source wavelet through the initial model, $\mathbf{m}_0$. Provided this initial model is sufficiently close to the true subsurface model, one iteration should produce a model update, $\delta\mathbf{m}$. This is added to the previous model, $\mathbf{m} = \mathbf{m}_0 + \delta\mathbf{m}$. The new model, m, should eventually converge to a solution which minimises the residual produced by subtracting the forward propagated predicted data from the observed data. A scalar term is defined to describe the misfit using the L_2 norm (Asnaashari et al., 2013; Virieux and Operto, 2009). This is equivalent to the sum of the squares of the residuals (Asnaashari et al., 2013), and is also known as the objective function:

$$f(\mathbf{m}) = \sum_{ns} \|\mathbf{W}_d(\mathbf{d}_{obs} - \mathbf{d}(\mathbf{m}))\|^2 = \sum_{ns} \frac{1}{2} \left\{ (\mathbf{d}_{obs} - \mathbf{d}(\mathbf{m}))^T \mathbf{W}_d^T \mathbf{W}_d (\mathbf{d}_{obs} - \mathbf{d}(\mathbf{m})) \right\}. \tag{2.7}$$

In equation 2.7, $\mathbf{d}_{obs}$ and $\mathbf{d}(\mathbf{m})$ are the observed and predicted data respectively, with $\mathbf{d}_{obs} - \mathbf{d}(\mathbf{m}) = \delta d$. $\mathbf{W}_d$ is a weighting matrix based on the covariance (Asnaashari et al., 2013). Other misfits may be used such as the L_1 norm or the phase residual, however the FULLWAVE code used at Imperial employs the L_2 norm as shown in equation 2.7 (Warner et al., 2013).

The objective function can be minimised with respect to the model parameters, $\mathbf{m}$, if the gradient is zero:

$$\nabla_{\mathbf{m}} f(\mathbf{m}) \equiv \frac{\partial f(\mathbf{m})}{\partial \mathbf{m}} \equiv \begin{bmatrix} \frac{\partial f}{\partial m_1} \\ \frac{\partial f}{\partial m_2} \\ \vdots \\ \frac{\partial f}{\partial m_M} \\ \cdot \end{bmatrix} = 0 \tag{2.8}$$

As FWI is a local iterative inversion scheme beginning from a model $\mathbf{m}_0$, we need to consider the objective function from this starting model $\mathbf{m}_0$ and a new model $\mathbf{m} = \mathbf{m}_0 + d\mathbf{m}$. Using a Taylor series expansion we can expand this differential as

$$f(\mathbf{m}) = f(\mathbf{m_0} + \delta\mathbf{m}) = f(\mathbf{m_0}) + \delta\mathbf{m}^T \left.\frac{\partial f(\mathbf{m})}{\partial \mathbf{m}}\right|_{\mathbf{m}=\mathbf{m_0}} + \frac{1}{2}\delta\mathbf{m}^T \left.\frac{\partial^2 f(\mathbf{m})}{\partial \mathbf{m}^2}\right|_{\mathbf{m}=\mathbf{m_0}} \delta\mathbf{m} + \mathcal{O}(\delta\mathbf{m}^3). \quad (2.9)$$

Minimising this equation to determine the model update $d\mathbf{m}$ gives:

$$\delta\mathbf{m} \approx -\mathbf{H}^{-1}\nabla_{\mathbf{m}} f(\mathbf{m}), \quad (2.10)$$

where $\mathbf{H}$ is the Hessian matrix. This is a square symmetric matrix formed by the zero-lag correlation between partial derivative wavefields. The diagonal terms represent the square of the amplitudes of the partial-derivative wavefield as they are calculate by the zero-lag autocorrelation (Virieux and Operto, 2009). The Hessian provides a measure of the local curvature of the M-dimensional error surface for the current model (Warner et al., 2012),

$$\mathbf{H} = \frac{\partial^2 f(\mathbf{m})}{\partial \mathbf{m}^2} \equiv \begin{bmatrix} \frac{\partial^2 f}{\partial m_1^2} & \frac{\partial^2 f}{\partial m_1 \partial m_2} & \cdots & \frac{\partial^2 f}{\partial m_1 \partial m_M} \\ \frac{\partial^2 f}{\partial m_2 \partial m_1} & \frac{\partial^2 f}{\partial m_2^2} & \cdots & \frac{\partial^2 f}{\partial m_2 \partial m_M} \\ \vdots & \vdots & \ddots & \vdots \\ \frac{\partial^2 f}{\partial m_M \partial m_1} & \frac{\partial^2 f}{\partial m_M \partial m_2} & \cdots & \frac{\partial^2 f}{\partial m_M^2} \end{bmatrix}. \quad (2.11)$$

2.6 Method of Steepest Descent

In practice, the Hessian is very large, and so, in order to reduce computational cost, an approximation to the diagonal elements of the Hessian is used, which makes equation 2.10 much more computationally feasible to calculate. To do this, we replace the inverse of the Hessian in equation 2.10 with a scalar, α, called the step length, such that

$$\delta\mathbf{m} = \alpha\frac{\partial f}{\partial \mathbf{m}} = -\alpha\nabla_{\mathbf{m}} f(\mathbf{m}). \quad (2.12)$$

This is an iterative process involving the following steps:

1. Evaluating the gradient $\nabla_{\mathbf{m}} f$ of the objective function for the starting model m0.
2. Finding the step length, α.
3. Obtaining a new model by calculating $\mathbf{m}_0 - \alpha\nabla_{\mathbf{m}} f$.

4. Replacing $\mathbf{m}_0$ with the new updated model.

5. Repeating until the objective function is sufficiently small.

In order to implement this work-flow, we need to calculate the gradient and determine the step length, (α).

2.6.1 Calculating the Unscaled Model Update (Gradient)

As models are large, calculating the gradient by perturbing each of the model parameters and calculating the change in the objective function is computationally expensive. A more efficient way to do this is by using the Jacobian matrix, $\mathbf{J}$, or the differential of the data with respect to the model parameters. We can then express the gradient as:

$$\nabla_{\mathbf{m}} f(\mathbf{m}) = \frac{\partial f(\mathbf{m})}{\partial \mathbf{m}} = \frac{\partial}{\partial \mathbf{m}} \left(\frac{1}{2} \delta \mathbf{d}^T \delta \mathbf{d} \right) = \left(\frac{\partial \mathbf{d}}{\partial \mathbf{m}} \right)^T \delta \mathbf{d} = \mathbf{J}^T \delta \mathbf{d}. \tag{2.13}$$

By differentiating the wave equation (2.1) with respect to the model parameters, and equating the gradient to zero we obtain:

$$\mathbf{J} = \frac{\partial \mathbf{p}}{\partial \mathbf{m}} = -\mathbf{A}^{-1} \frac{\partial \mathbf{A}}{\partial \mathbf{m}} \mathbf{p}. \tag{2.14}$$

For a dataset, $\mathbf{d}$,

$$\mathbf{d} = \mathbf{D}\mathbf{p}, \tag{2.15}$$

which is a subset of the full-wavefield $\mathbf{p}$, generated by a source $\mathbf{s}$ and extracted by the diagonal matrix $\mathbf{D}$, we can express the Jacobian, $\mathbf{J}$, as:

$$\mathbf{J} = \frac{\partial \mathbf{d}}{\partial \mathbf{m}} = \mathbf{D} \frac{\partial \mathbf{p}}{\partial \mathbf{m}} = -\mathbf{D}\mathbf{A}^{-1} \frac{\partial \mathbf{A}}{\partial \mathbf{m}} \mathbf{p}. \tag{2.16}$$

Substituting this into equation 2.13 gives

$$\mathbf{D}^T \delta \mathbf{p} = \delta \mathbf{d}. \tag{2.17}$$

We find the gradient can now be expressed as:

$$\nabla_{\mathbf{m}} f(\mathbf{m}) = -\mathbf{p}^T \left(\frac{\partial \mathbf{A}}{\partial \mathbf{m}} \right)^T \left(\mathbf{A}^{-1} \right)^T \delta \mathbf{d}. \tag{2.18}$$

This means that, in order to calculate the gradient, we first need to calculate the forward wavefield $\mathbf{p}$, analytically differentiate the operator $\mathbf{A}$ with respect to the model parameters, and compute the final term. This final term represents the back-propagation of the residual wavefield.

We can now write the final term as

$$\left(\mathbf{A}^{-1} \right)^T \delta \mathbf{d} = \delta \mathbf{p}, \tag{2.19}$$

and rearrange to

$$\mathbf{A}^T \delta \mathbf{p} = \delta \mathbf{d}. \tag{2.20}$$

This equation describes a wavefield $\delta \mathbf{p}$ generated by a virtual source propagated by the adjoint of the operator $\mathbf{A}$. Equation 2.20 is therefore a modification of the wave equation (equation 2.1) where the source is the data residuals. We can further simplify time-domain computations by designing $\mathbf{A}$ such that it is symmetrical in space and therefore self-adjoint, and such that $\mathbf{A}^T$ is equivalent to a back propagation in time and therefore:

$$\nabla_{\mathbf{m}} f(\mathbf{m}) = -\mathbf{p}^T \left(\frac{\partial \mathbf{A}}{\partial \mathbf{m}} \right)^T \delta \mathbf{p}. \tag{2.21}$$

Equation 2.21 represents the zero-lag temporal cross-correlation between the forward-propagated wavefield for a particular source with the back-propagated residual wavefield for all receivers of that same source, weighted by a function of the model and the modelling operator (Warner et al., 2013). This formulation greatly reduces computational cost by only requiring two forward modelling runs and one cross-correlation per source. We then need to multiply these terms together for all times and all sources, and sum the results together to produce a value corresponding to each model parameter, which typically results in one value at each grid point in the model. This will produce the unscaled model update.

2.6.2 Scaling the Model Update - Calculating the Step Length

While the gradient gives us the direction for the model update, we still do not know how much the model should be changed by. This is equivalent to converting the gradient vector calculated in equation 2.10 to the dimensions of the model (Pratt, 1999).

To obtain this we need to calculate the step-length. To do this, the model is perturbed by a small amount in the opposite direction to the gradient. By assuming a linear relationship between the changes in the model and changes in the residual we get:

$$\delta \mathbf{d}_\alpha = \delta \mathbf{d}_0 + \alpha \left(\mathbf{d}_1 - \mathbf{d}_0 \right) = \delta \mathbf{d}_0 + \alpha \left(\delta \mathbf{d}_1 - \delta \mathbf{d}_0 \right), \tag{2.22}$$

and differentiating the L_2 norm of this term with respect to α gives:

$$\alpha = \frac{\delta \mathbf{d}_0^T \mathbf{q}}{\mathbf{q}^T \mathbf{q}}, \tag{2.23}$$

where:

$$\mathbf{q} = \delta \mathbf{d}_0 - \delta \mathbf{d}_1. \tag{2.24}$$

Following the method of steepest descent, the next step is to obtain a new model using

$$\mathbf{m}_1 = \mathbf{m}_0 - \alpha \nabla_{\mathbf{m}} f. \tag{2.25}$$

This produces a scaled model update, and we can replace $\mathbf{m}_0$ with this new, updated model $\mathbf{m}_1$. This process can then be repeated n times until we obtain a model, $\mathbf{m}_n$, where the objective function (equation 2.7 is sufficiently small.

By following the FWI method, it is possible, in practice, to resolve subsurface properties to approximately a quarter of the seismic wavelength (Virieux and Operto, 2009), rather than a Fresnel width as with traditional traveltime tomography (Williamson, 1991). Traveltime tomography is similar to FWI in that it solves the non-linear seismic inverse problem to create stable velocity models, however assumes that that all frequencies travel at the same velocity (Luo and Schuster, 1991) and often uses the eikonal approximation to the wave equation to predict arrival times (Hole, 1992; Nolet, 1987), which limits the resolution. FWI, on the other hand, utilises the full-physics of the wavefield, hence improving resolution over traveltime tomography, often by an order of magnitude (Wu and Toksöz, 1987). FWI is also sensitive to short-wavelength features and velocity inversions in the subsurface, which traveltime tomography is not.

2.7 Stability Criteria

In order for the inversion to avoid numerical dispersion, there are stability conditions which should be met when applying FWI to a model. Numerical dispersion occurs when attempting to solve the acoustic wave equation (equation 2.1) with too few samples per wavelength (Fei and Larner, 1995). FULLWAVE at Imperial College, London, can be run on either the high-kernel, or the low kernel, which have different stability criteria. When running an inversion, we must be aware of the runtime, r, which can be estimated using the following equation:

$$r \propto n^4, \tag{2.26}$$

where n represents the number of gridpoints per kilometer in the model. The factor of 4 is due to the 3 space dimensions, (x, y, z) and the timestep, t.

2.7.1 Low Kernel

In order to avoid numerical dispersion when using the low kernel, the shortest wavelength in the velocity model needs to be sampled at a minimum of five gridpoints per wavelength (Levander, 1988). As the wavelength is proportional to velocity and inversely proportional to frequency, the grid spacing, δx, is limited by

$$\delta x < \frac{V_{min}}{5 f_{max}}. \tag{2.27}$$

The second stability condition details that the time-step interval, and states that the distance travelled by the wavefield per time-step should be less that half a grid cell for the highest velocity (Graves, 1996),

$$\delta t \leq \frac{\delta x}{2 V_{max}}. \tag{2.28}$$

Exceeding this limit can result in numerical anisotropy in the model. As the maximum grid spacing is determined by the minimum velocity, and the maximum time-step is determined by the maximum velocity (equations 2.27 and 2.28). Thus, the velocities of the model control the choice of appropriate grid spacing, δx, maximum inversion frequency, f_{max}, and the time sampling, δt, which all affect the computational cost.

2.7.2 High Kernel

The high kernel has been customised and optimised for industry datasets collected for FWI, and allows for a coarser mesh in the model. In order to avoid numerical dispersion when using the high kernel, the shortest wavelength in the velocity model needs to be sampled at a minimum of 2.62 gridpoints per wavelength. The grid spacing is therefore limited by

$$\delta x \lesssim \frac{V_{min}}{2.62 f_{max}}. \tag{2.29}$$

The time-step interval is still determined by the maximum model velocity as in equation 2.28, but in the high kernel, the distance travelled by the wavefield per time-step should be less than $\frac{2}{3}$ of a grid cell for the highest velocity:

$$\delta t \leq \frac{2\delta x}{3V_{max}}. \tag{2.30}$$

Overall, using the high kernel is better for models with coarser meshes and larger time sampling rates.

2.7.3 Downfalls of FWI

The ill-posed and highly non-linear nature of the inversion scheme can, however, can be unstable, which can lead to an inaccurate recovered velocity model. These include:

2.7.3.1 Convergence to a local minimum

For computational efficiency, the FWI method utilises localised iterative descent methods rather than a global search method. These local gradient methods could cause the inversion to converge to a local, rather than a global minimum in the error space. This is possible as a local minimum had a gradient of zero, but is not the lowest possible value of the objective function, which is the global minimum.. For example, figure 2.1 shows how two points in the model space, A and B, can converge to different minima despite being very close together.

2.7.3.2 Cycle-skipping

Cycle-skipping is the most common cause of convergence to a local minima. Cycle skipping occurs when the difference between the forward-modelled data and the observed data, $\delta\mathbf{d}$ is greater than half the period of the wavelength of the lowest frequency used in the observed data $\mathbf{d_{obs}}$ (Pratt, 1999; Sirgue and Pratt, 2004). This causes the FWI method to try and match traces to the wrong cycle, producing errors in the model. Cycle-skipping arises from the use of the Born approximation in calculating the gradient (equation 2.21) and the sinusoidal nature of waves (Beydoun and Tarantola, 1988).

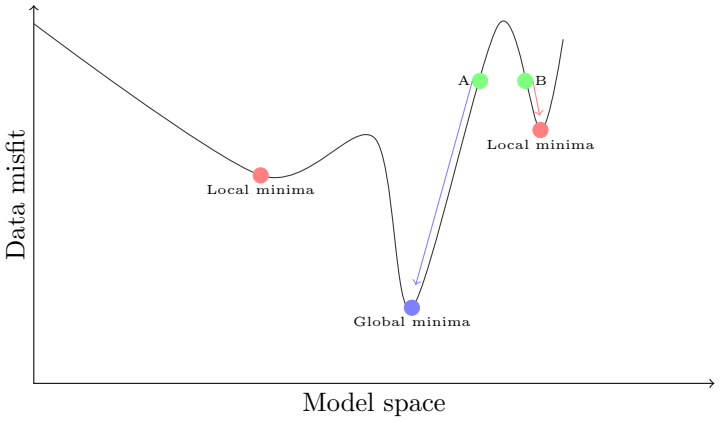


Figure 2.1: Representation of the local minima problem in FWI. Due to the non-linearity of the problem, forward modelling $\mathbf{G}(\mathbf{m}) = \mathbf{u}$ produces spurious local minima, represented by the red points. Choosing an inaccurate starting model, for example point B, can cause the local gradient method to push the model to converge to a local minima. Choosing a more accurate starting mode, for example point A, allows the inversion to converge to the true global minimum shown in blue

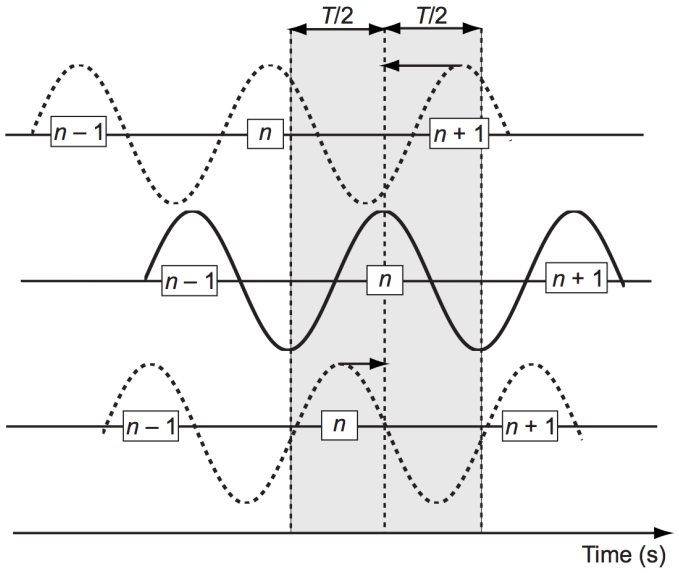


Figure 2.2: Representation of cycle-skipping in FWI. The solid black sinusoid represents a trace from the observed data as a function of time with a period T. The upper dashed sinusoid represents a predicted trace with peak, n, over half a cycle out-of-phase with a time delay greater than $T/2$. The FWI method would attempt to match the peak labelled $n+1$ to the observed data, as it is closer in time, hence producing an incorrect model. The lower dashed sinusoid represents a predicted trace which would not be cycle-skipped as the two traces are in-phase with a time delay less than $T/2$. This prediction would allow convergence to the global minimum (Virieux and Operto, 2009).

2.8 Implementing FWI

2.8.1 Time Domain vs. Frequency Domain FWI

While originally formulated in the time domain (Gauthier et al., 1986; Mora, 1988; Tarantola, 1984), the seismic inverse problem can also be formulated in the frequency domain (Pratt and Worthington, 1990; Pratt and Goulty, 1991; Pratt, 1999). Choosing to compute an FWI problem in the time or frequency

domain can affect several factors including computational memory usage, computation time and the inherent non-linearity of models used during inversion. Each domain has pros and cons which should be considered when formulating an inversion problem.

2.8.1.1 Frequency Domain

Inverting in the frequency domain is advantageous in computing the forward-modelling algorithm (Pratt, 1999). Forward-modelling in the frequency domain only requires a discrete number of frequency components of the source spectrum, which drastically reduces computational time in 2D FWI while still producing an un-aliased model image (Pratt, 1999). Computational efficiency is also improved as a limited number of frequencies are necessary for the inversion due to overlapping of wavenumber illumination in wide-aperture surveys (Pratt, 1999). In the frequency domain it is also easy to add attenuation to the model. Frequency domain FWI does, however, require large amounts of data to be stored in memory during inversion (Operto et al., 2004), and the need for a few select frequencies is strongly dependent on target depth and maximum offset (Sirgue and Pratt, 2004), this also makes it difficult to include anisotropy in the model.

2.8.1.2 Time Domain

Inverting in the time domain is relatively straightforward to achieve quickly and with less memory than frequency domain inversions in 3D (Vigh et al., 2009). Time domain inversions also theoretically produce better quality of image as they contain the full spectrum of frequency components and therefore a larger signal to noise ratio (Virieux and Operto, 2009). Quality control is much easier in the time domain with the ability to quickly and easily window, mute and process the raw field data in the time domain (Shipp and Singh, 2002), and including anisotropy in the model is straightforward. In the time domain, however, there is more numerical instability, as inverting low and high frequencies together can produce aliasing and cycle-skipping (Vigh et al., 2009), and low-frequency estimation may be difficult due to time derivatives in the gradient calculation (Sirgue and Pratt, 2004). We can circumvent this problem by inverting in stages, starting with low maximum frequencies in the inversion and gradually increasing the maximum frequency. Including attenuation in time domain inversions, however, is difficult.

Within the FWI community, there is an ongoing debate as to the best domain of inversion for FWI. The domain of choice often depends on the type of dataset which is being inverted, inversion aims, user preference and group expertise, with both time- and frequency-domain FWI being used by various research groups to produce sub-surface models (e.g. frequency domain inversion: Ben-Hadj-Ali et al. (2008); Brossier et al. (2009); Kamei et al. (2012); Operto et al. (2006); Plessix (2009); Sirgue et al. (2009); e.g. time-domain inversion: Calvert et al. (2011); Christeson et al. (2012); Morgan et al. (2011); Nangoo et al. (2012)).

Within the FULLWAVE research group at Imperial College London, the FWI code is written in the time-domain, due to the majority of datasets inverted within the group comprising large, 3D, multi-shot and multi-receiver geometries. The models in this thesis are, therefore, all calculated using the time-domain formulation of the FWI problem.

2.8.2 Implementing FWI successfully

Implementing FWI to create a velocity model better than that produced by other more conventional techniques requires some initial inputs. These initial inputs are important in producing a robust inversion scheme and mitigating the effects caused by the non-linearity of the process. The ingredients for implementing FWI successfully fall under four main headings, outlined below.

2.8.2.1 Long Offsets

Wide-angle data comprise mainly of transmitted, horizontally travelling, post-critical refracted waves and diving waves which allow for better illumination and a more accurate representation of the subsurface velocities. This is because the transmitted arrivals are more sensitive to subsurface velocity than the reflected wavefield. Short-offset seismic data, on the other hand, tend to be dominated by short-offset reflected energy, and fewer transmitted arrivals. Reflected arrivals are more difficult to invert as they increase the amount of local minima (Fig 2.1) and the chance of cycle-skipping (figure 2.2) due to the hyperbolic nature of reflections and the linear approximation made during FWI (Mora, 1988; Pratt, 1999; Tarantola, 1984).

2.8.2.2 Low Frequencies

Using low frequencies in FWI improves the stability of the inversion as the relationship between lower frequency components of the data and the model are inherently more linear than at higher frequencies. Lower frequency data therefore contain fewer local minima and a broader global minimum of the objective function (Warner et al., 2013). This implies that the low frequency data helps the inversion converge to a global minimum in the objective function and hence recover a model that more accurately represents the geology of the subsurface (Baeten et al., 2013; Plessix, 2006; Sirgue and Pratt, 2004; Warner et al., 2012; Gulanay).

Most towed-streamer seismic data contain usable frequencies as low as 3-5Hz, with lower frequencies often contaminated by swell noise, while ocean-bottom seismometer (OBS) data can contain usable frequencies down to 2Hz (Morgan et al., 2013). The frequency content of input data should not be too low, however, as this may introduce noise into the inversion, as shown by Warner et al. (2013).

As frequency is inversely proportional to period, we can avoid cycle-skipping in FWI by inverting from low frequency to high frequency. By gradually increasing the frequency range, shorter wavelength structure

is progressively introduced into the velocity model, and the predicted and true data remain less than half a cycle out of phase (Bunks et al., 1995; Plessix, 2006; Pratt, 1999; Sirgue and Pratt, 2004; Smithyman et al., 2009).

2.8.2.3 Wide Azimuths

Data collected with wide azimuthal geometries (wider than conventional towed-streamer datasets) provide better coverage of the subsurface, and are likely to lead to more accurately recovered velocity models (Mothi et al., 2013; Plessix, 2008; Sirgue et al., 2007). The wide azimuths allow for, better illumination (multiple crossing wavefields in many directions), and higher-fold data coverage, hence providing better access to low-wavenumber information within transmitted arrivals (Mothi et al., 2013; Shipp and Singh, 2002; Vigh et al., 2009). This is examined in detail by Sirgue and Pratt (2004) who show superior inversion results from wide-azimuth surveys in comparison to narrow azimuth data.

2.8.2.4 Good Starting Model

While having a good starting model is unrelated to data acquisition, it is fundamental in carrying out a successful FWI scheme. As outlined above, FWI utilises local optimization schemes, and therefore, the first local-descent direction of the objective function (equation 2.10) is calculated using the initial starting model (Virieux and Operto, 2009). For successful convergence, the initial model must therefore be in the vicinity of the global minimum in order to utilise FWI successfully, as shown in Fig 2.1. Small differences in the starting model can be crucial in causing the objective function to converge in the right direction, also shown in Fig 2.1, where the difference between two starting models, A and B is small, but A allows for convergence to the global minimum, while selecting B will cause incorrect convergence to a local minimum. It should also be noted that Fig 2.1 is a very simplified schematic of the local minima problem, and with real data there will be a vast number of local minima across many different model parameters. The starting model should predict travel times of seismic waves to within half a period of the dominant wavelength at the lowest usable frequency of the field data in order to reduce the probability of cycle-skipping and convergence to a local minima (Beydoun and Tarantola, 1988; Mora, 1988; Pratt, 1999; Smithyman et al., 2009; Vigh et al., 2009; Warner et al., 2013). A good starting model means that the inversion is more likely to converge to the global minimum, and lead to an overall more accurate resulting model.

Chapter 3

Methods

3.1 Introduction

This chapter describes the method used to create a high resolution P-wave velocity model using Full-waveform Inversion in detail (see Chapter 4 for results). It covers all steps from pre-processing of the raw data, ensuring an accurate starting model, using an appropriate inversion scheme and actually inverting the data. Please note that an abridged version of this chapter appears within the Methods section of Chapter 4 *Imaging the shallow subsurface structure of the Hikurangi subduction zone, New Zealand, using 2D Full-Waveform Inversion.*

I use FWI as it has the potential to produce high-resolution models of any physical property that influences the seismic wavefield (Pratt, 1999; Sirgue et al., 2010; Tarantola, 1984; Virieux and Operto, 2009; Warner et al., 2013). In practice, in most commercial applications, a robust model of P-wave velocity is recovered using three-dimensional acoustic, anisotropic FWI codes (Sirgue and Pratt, 2004; Warner et al., 2013). Although, accurate modelling of the seismic wavefield requires a three-dimensional elastic code that can account for changes in S-wave velocity, anisotropy, density and attenuation, this is normally prohibitively computationally expensive. In addition, the amplitudes of individual arrivals are sensitive to several physical properties, so multi-parameter inversions tend to be less robust due to cross-talk between individual parameters (Sirgue and Pratt, 2004; Virieux and Operto, 2009). Apart from applications focused on imaging the reservoir and drilling hazards in petroleum exploration, FWI has also been used to resolve the P-wave velocity structure of crustal-scale targets in a range of tectonic settings, including subduction zones (Calvert et al., 2011; Christeson et al., 2012; Kamei et al., 2012; Morgan et al., 2011).

3.1.1 Using FWI at Hikurangi

The Hikurangi dataset is quite large, the data are noisy, the target is a challengingly heterogenous, each inversion takes 3-4 days, and the QC is time-consuming. Inversions shown in this thesis paper took 18-20 months to produce, during which time an exhaustive suite of tests were performed with different starting models, different time windows, different offset sequences and frequencies, different smoothing, and different amplitude normalisations, which will be outlined in this chapter. The dataset being inverted is a 2D streamer dataset, and, given the significant variations in offline structure at Hikurangi, modelling a 3D world with a 2D dataset is likely to be the most significant contributor to any inaccuracies in our final Vp model (e.g. Kalinicheva et al. (2017)). Based on extensive testing detailed in this chapter, an inversion strategy was chosen based on a number of quality assurance tests. I am confident from these tests, and from similar experience within the research group using other datasets, that the final Vp model is close to the best that can be obtained with this dataset using 2D FWI, and that further additional inversions and testing would not lead to further significant improvement.

3.2 Dataset

This study utilised a 2D marine seismic dataset across the Hikurangi margin, where the Hikurangi Plateau, part of the Pacific Plate, is subducting beneath the east coast of New Zealands North Island (Australian plate) (Fig. 3.1).

The seismic line that I use to produce an FWI P-wave velocity model was acquired in May 2005 as part of the 05CM survey (Fig. 4.1), which was led by the New Zealand Government (see Barker et al. (2009); Multiwave (2005)). Line 05CM-04 is 90km long and was collected using a 12km long streamer by Multiwave Geophysical aboard the MV Pacific Titan. Data were recorded to 12s two-way time (TWT) with a shot spacing of 37.5m over 960 channels (Multiwave, 2005). Full details are shown in Table 4.1.

Line 05CM-04 is used as it crosses the deformation front, allowing imaging of the incoming plate,the décollement, the subduction interface and the accretionary wedge. It was also subject to various drilling and 3D experiment proposals, which were approved and carried out during my PhD research. The line had also been used to create a Pre-Stack Depth Migrated velocity model by Barker et al. (2018), making it the ideal dataset for this project.

An example of raw shot gathers from along this profile is shown in Fig. 3.2. The signal-to-noise ratio is quite low, with a lot of contamination from swell noise.

3.3 FWI Workflow

The FWI workflow that I use in this study follows Warner et al. (2013) and involves the following steps, which will be discussed in more detail below:

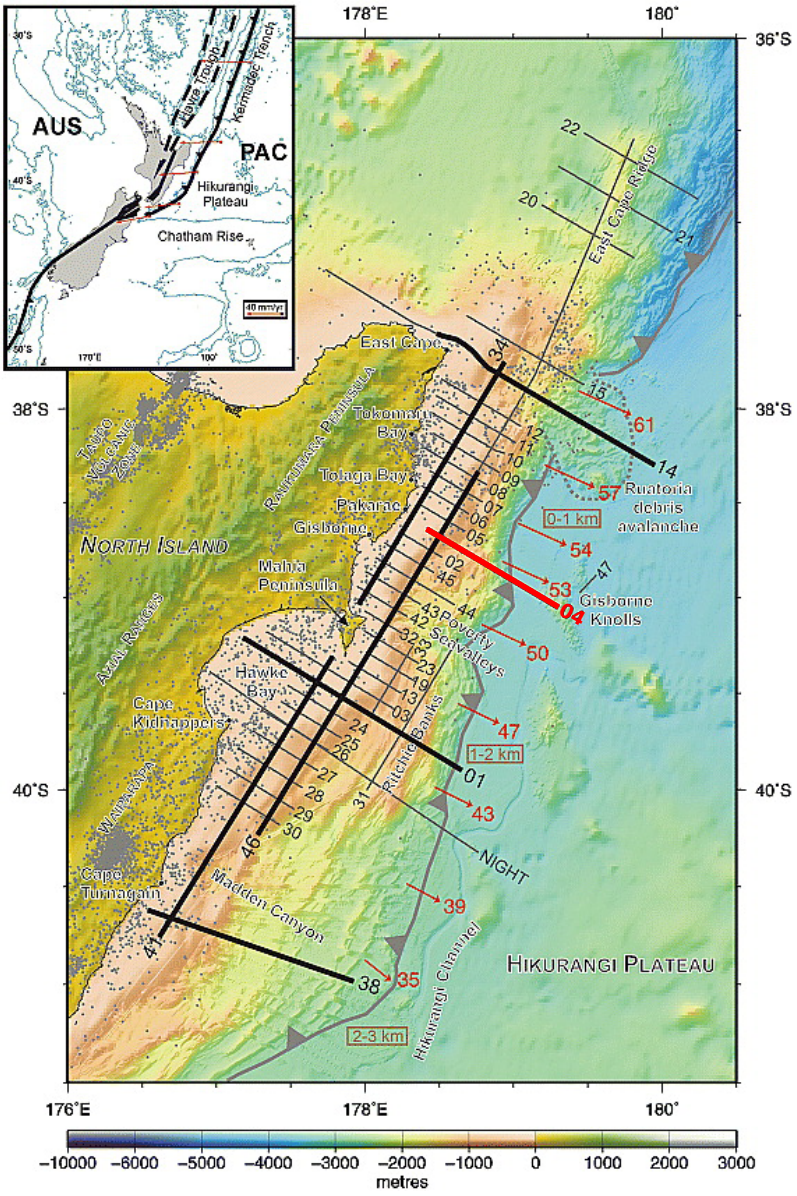


Figure 3.1: Location map of the Hikurangi margin (inset) where the Pacific plate subducts beneath the Australian plate at a rate of 50mm/yr. The large map shows the location of the 05CM survey. Bold black lines show 2D lines used in analysis by Barker et al. (2009), and line 05CM-04, the dataset used in this thesis, is highlighted in red. A 2D line recorded by an earlier survey, the NIGHT survey is also shown. Red vectors show long-term estimates of convergence between the rotating east coast margin relative to the Pacific plate in mm/yr (Wallace et al., 2004). Boxed brown text shows the approximate sediment thicknesses on the downgoing plate at the Hikurangi Trough, which increases as we move south. Earthquake epicentres from the GeoNet catalog within a 3-20km depth range are shown by grey dots. Image from Barker et al. (2009).

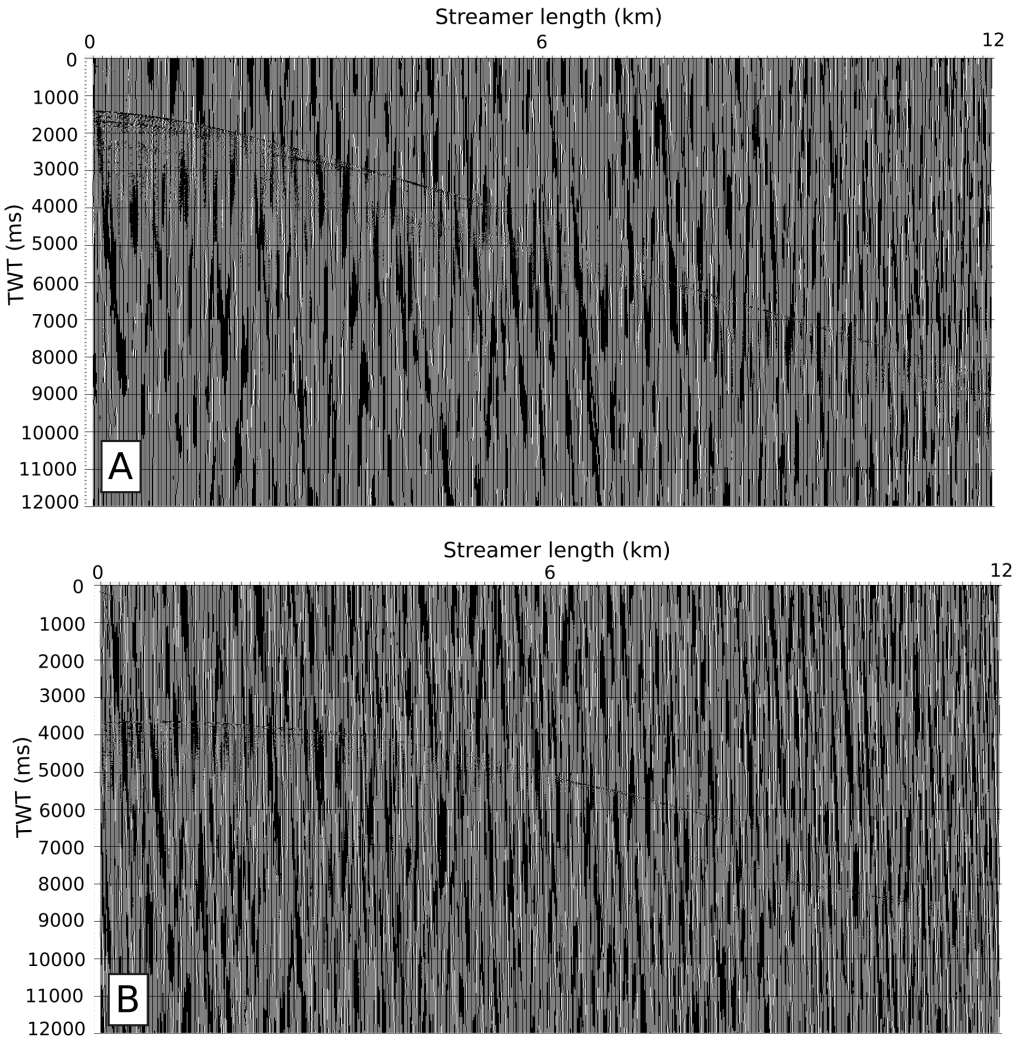


Figure 3.2: Examples of two shot gathers of the raw data, detailed in Table 4.1. The signal-to-noise ratio is quite low, with a lot of contamination from swell noise.

Table 3.1: Details of the seismic line 05CM-04 collected across the Hikurangi margin.

Property	Value
Number of shots	2375
Streamer length	12km
Number of channels	960
Length of line	89.062km
Initial sampling rate	2ms
Total recording time (TWT)	12s
Receiver spacing	12.5m
Shot spacing	37.5m
Shot-receiver spacing	160m
Streamer depth	7m
Source depth	6m

1. The dataset was preprocessed in preparation for FWI;
2. A source wavelet was extracted from the field data;
3. A starting velocity model was selected;
4. The starting model was modified;
5. The adequacy of the source wavelet and starting velocity model were quality checked by comparing the observed and predicted data;
6. Inversion strategies were tested and an inversion scheme selected;
7. The dataset was inverted using the selected inversion scheme, with regular quality assurance to check for cycle skipping.

Steps 4 and 6 are particularly important in order to avoid cycle skipping in the inversion (Asnaashari et al., 2013; Pratt, 1999; Tarantola, 1984; Warner et al., 2013). Cycle skipping occurs when arrivals within the synthetic and real datasets differ by more than half a cycle, causing the velocity model to converge to a local rather than global minimum, as outlined in the previous chapter (chapter 2) (Virieux and Operto, 2009). Ideally, to mitigate this problem FWI should start at low frequencies, since the travel times are easier to match within half a cycle for larger periods. The lower-frequency data improve the long-wavelength velocity structure, which means the predicted arrival times better match the observed, and the maximum frequency can then be gradually increased to introduce the finer-scale structure. As frequencies are increased, however, so too do computational costs due to the necessity of finer grids and smaller time-steps (equations 2.27 and 2.28), so frequencies need to be selected carefully based on the minimum and maximum subsurface velocity structure (Virieux and Operto, 2009; Warner et al., 2013).

3.4 Implementing the Workflow

3.4.1 Step 1. The dataset was preprocessed in preparation for FWI.

As noted in Chapter 2, FWI is more likely to be successful when the input data include low-frequency signals. The 2D seismic line used in this study, however, was contaminated with swell noise, as shown in the raw shot gathers (Fig. 3.2). Initial bandpass filtering was done using a code written by Mike Warner which uses a cosine-tapered time-reversed extension appended to the front of each trace so that each ensemble could be filtered in Landmark's seismic processing software ProMAX . This must be done in order to avoid edge effects at the start of each trace caused by filtering. After padding the data by 4 seconds the filters shown in Table 3.2 were applied.

Table 3.2: Filters and their values applied to the dataset in order to remove swell noise

Filter type	Corner frequencies
Low-cut filter	2-3-500-500Hz
High-cut filter	0-0-10-12Hz
Band-pass filter	2-3-10-12Hz

All were 0.1% noise, minimum-phase, Ormsby filters. Several band-pass filters were tested to remove the maximum amount of swell noise, whilst maintaining the maximum amount of low frequency data. The most effective band-pass filters are shown above in Table 3.2, and the lowest useable frequency was determined to be 3 Hz. The 4s of padding were then removed from the data. An example of a shot gather after bandpass filtering is shown in Fig. 3.4. The signal-to-noise ratio is greatly increased, however the gather is still quite noisy.

F-K filtering was then applied to remove unwanted tail-buoy noise at the end of each shot-gather. This is caused by the tail-buoy of the streamer bobbing in the water, producing a linear arrival in the opposite direction to the direct arrival as shown in Figs. 3.3(b) and 3.4(a). F-K filtering consists of a two-dimensional Fourier transform over time and space to produce a phase and amplitude spectrum of the data, shown in Fig. 3.3(c).

The F-K spectrum of the data is shown in Fig. 3.3(c) which shows the phase spectrum, with the corresponding amplitude spectrum displayed as colour intensity. Using this method I could pick out the tail-buoy noise, however, I noted that the tail-buoy noise lies very close to important reflection and refraction energy (Fig. 3.3(c)). In order to apply this only to the tail-end of the data, I created a tapered mask. This mask allowed me to remove the tail-buoy noise only from the end of the shot gather, without removing any important energy from the rest of the shot gather, as shown in Fig. 3.4.

Finally, I applied an F-X deconvolution to each shot gather to remove the majority of any remaining noise. F-X deconvolution is a process which predicts linear events based on a prediction. This prediction process depends on the presence of linear events in the frequency vs space domain. The F-X deconvolution

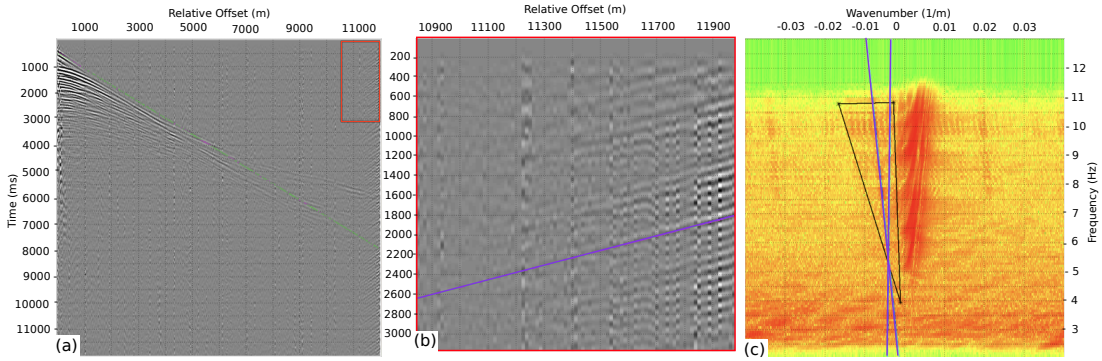


Figure 3.3: (a) shows an example shot gather from the 05CM-04 dataset after bandpass filtering. (b) is a zoom-in of the red box highlighted in A at the end of the streamer where the tail-buoy noise is seen. The purple line tracks one such reflection created by the tail-buoy, and displays it as the purple line in (c) on the F-K spectrum. All such reflections from the tail-buoy lie in a similar position across all shot gathers in the dataset. The black triangle is the selection of data in the F-K spectrum which will be cut out from the data, however, much of the usable low-frequency data also lies within the triangle.

first partitions the data into windows within which true events appear linear and coherent. Within each window, the data are then transformed to the frequency domain via a Fourier transform. For every frequency, a prediction filter is calculated and applied both forward and backward in space. An inverse Fourier transform is then applied to the sum of the predictions, and the windows merged back into the output. As this method is only dependent on the frequency being analysed, and therefore independent of other frequencies, a large degree of freedom is possible in the predicted output (Canales, 1984; Ferrara et al., 1985; Gulunay, 1986; Treitel, 1974). Fig. 3.5 shows the results of two shot gathers before (Fig. 3.5 (a) and (b)) and after (Fig. 3.5(c) and (d)) the application of the FX deconvolution.

The data are now sufficiently pre-processed to begin the FWI process. Fig. 3.6 shows an example shot gather at different stages in the pre-processing to show the improvement in the data quality.

3.4.2 Step 2. A source wavelet was extracted from the field data.

3.4.2.1 Directly extracting the source wavelet from the data

An initial attempt to extract the source wavelet was undertaken by extracting the first trace of six shot gathers in the deep ocean part of the model (sea depth ∼4km), between the trench and the Gisborne Knolls (Fig 4.1). This allowed for the largest possible separation between the direct wave and the seafloor reflection. These six traces were then stacked to obtain an average direct arrival into the nearest receiver with maximum signal-to-noise ratio. The trace was muted after 1500ms to remove any reflections. The resulting initial source wavelet is shown in Fig. 3.7A. This wavelet was then used to produce a synthetic dataset through the starting model. Fig. 3.7B shows a side-by-side comparison of 9 traces from a single shot gather with the synthetic data produced using the source wavelet estimate shown in Fig 3.7A, interleaved with the same 9 traces from the field data, up to offsets of 272.5m from the start of the

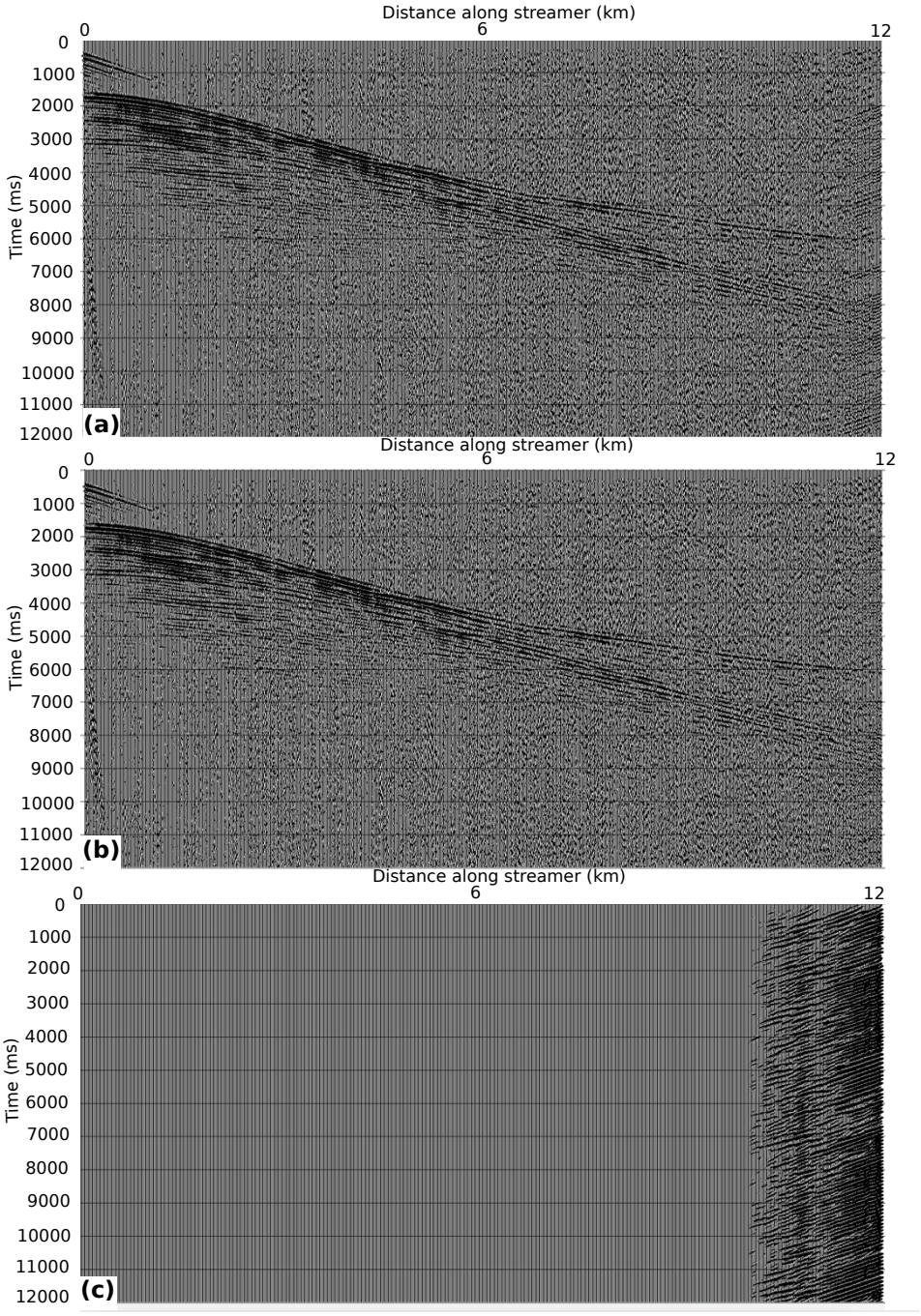


Figure 3.4: (a) shows an example shot gather after bandpass filtering, containing tail-buoy noise at the end of the streamer (11-12m along streamer).(b) shows the same shot gather after removing the tail-buoy noise. (c) shows this difference between (a) and (b), which is the tail-buoy noise which has been successfully removed using the mask, keeping all usable low-frequency data in the rest of the shot gather.

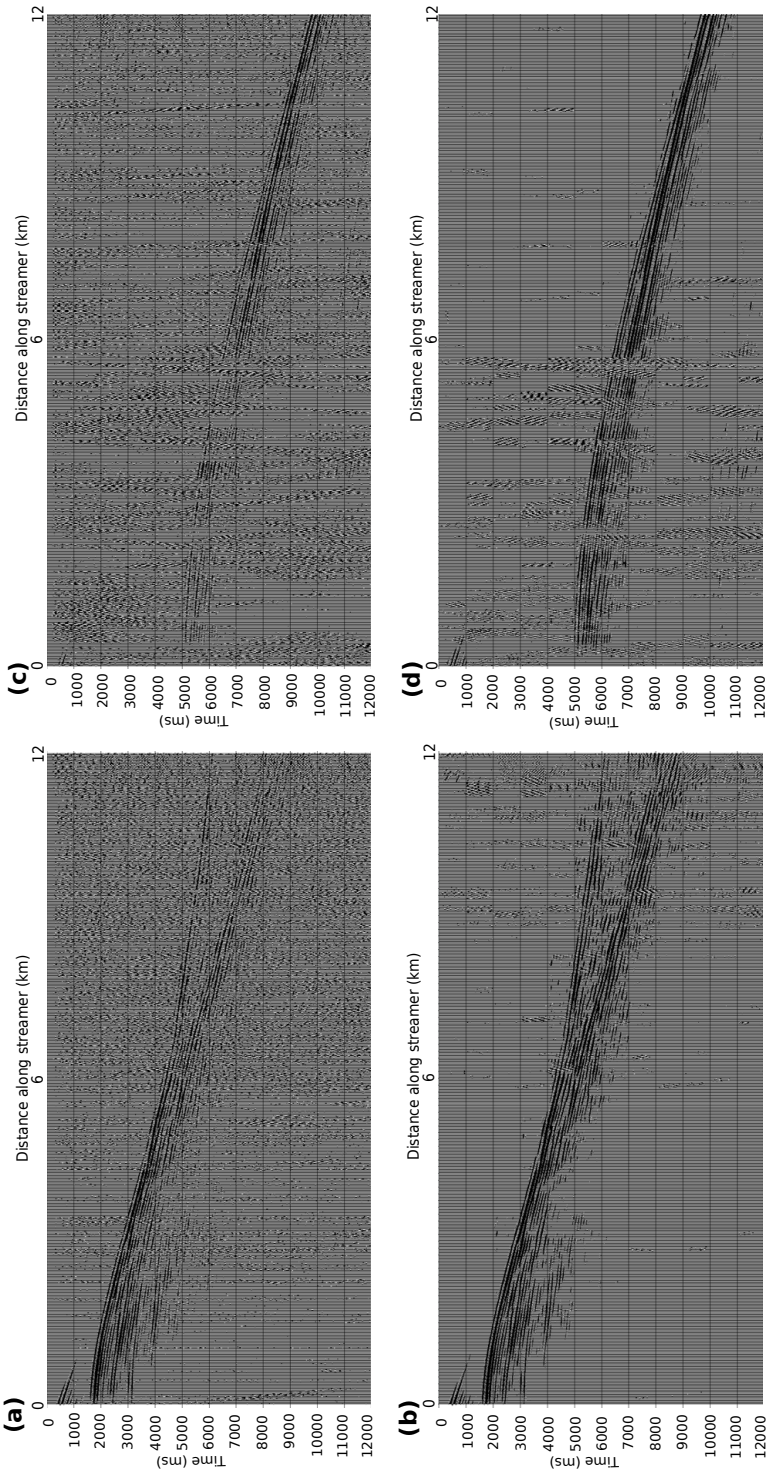


Figure 3.5: (a) and (b) shows two example shot gathers within the dataset, at different ocean depths (a) in the shallow ocean nearer onshore, and (b) in the deeper basin further offshore). (c) and (d) show the same two shot gathers after the application of the F-X deconvolution. We can see that a lot of the background noise has been removed and the signal to noise ratio greatly improved, however some noise still remains.

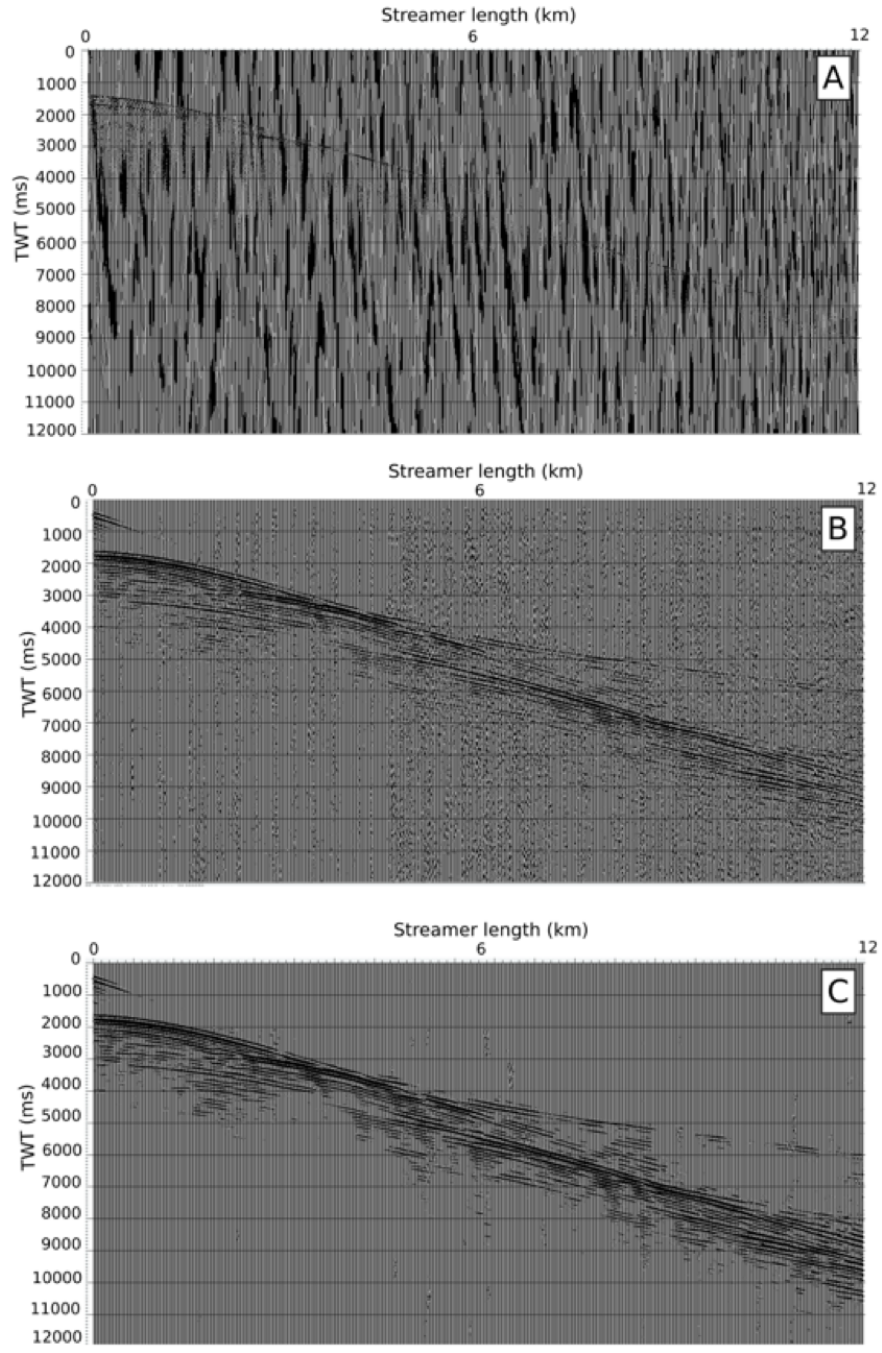


Figure 3.6: An example of a single shot gather through the pre-processing steps. (a) is the raw shot gather contaminated by swell noise. (b) is the shot gather after F-K filtering and (c) is the shot gather after F-K filtering and F-X deconvolution. The signal-to-noise ratio is greatly improved and the data is ready for inversion

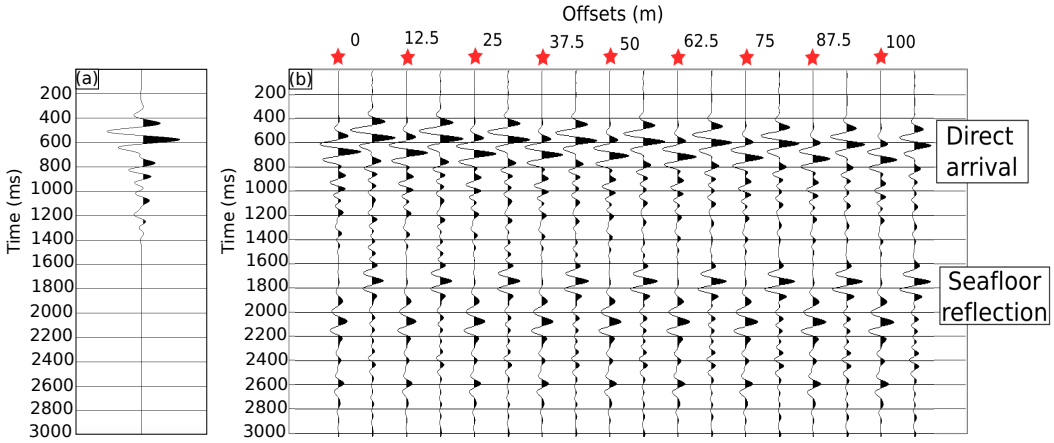


Figure 3.7: (a) shows the initial source wavelet that was extracted by stacking 6 near offset traces in parts of the model with deeper seafloor depths, muted from 1500 ms. This source wavelet was used to create forward modelled synthetic data, indicated by a red star, which I could directly compare, trace-by-trace, to the real data. Note that the shape and arrival time of the real and predicted data are different for both the direct arrival and seafloor reflection.

streamer. The image shows a mismatch between real and synthetic data for all traces, and that the shapes of the direct arrival and seafloor reflection are quite different. This indicates that the true source wavelet has not been extracted, and a more accurate method for devising a source wavelet from the real data needs to be implemented.

3.4.2.2 Predicting the source wavelet using Weiner filtering

A predicted dataset, $\mathbf{p_1}$, is obtained by propagating an initial source wavelet, $\mathbf{w_1}$, through the starting model. We wish to find a filter, $\mathbf{f}$:

$$\mathbf{p_1} * \mathbf{f} \approx \mathbf{d} \tag{3.1}$$

where $\mathbf{d}$ is the field data.

Here, the initial estimate of the source wavelet, $\mathbf{w_1}$, is a spike that has been filtered using the same filters that were applied to the field data, outlined above (Table 4.1). This source wavelet is then propagated though the water column to generate a direct water wave arrival on the streamer (Fig 3.8A). The filter, $\mathbf{f}$, is then determined by solving the equation:

$$\mathbf{p_1} * \mathbf{f} \approx \mathbf{d} \Rightarrow \mathbf{f} = \mathbf{p_1^{-1}} * \mathbf{d}. \tag{3.2}$$

For which $\mathbf{d}$ is the observed data at the same location as the predicted data (Fig 3.8B).

We then compute:

$$\mathbf{w_1} * \mathbf{f} = \mathbf{w_2}, \tag{3.3}$$

where $\mathbf{w_2}$ is the new source (Fig 3.8C). I then use $\mathbf{w_2}$ to generate the new predicted data, $\mathbf{p_2}$ such that:

$$\mathbf{p_2} \approx \mathbf{d} \tag{3.4}$$

By comparing the predicted data, $\mathbf{p_2}$, with the observed, $\mathbf{d}$, we can assess the accuracy of the new wavelet $\mathbf{w_2}$. Fig 3.8(d) shows a side-by-side comparison of 9 traces from a single shot gather with the synthetic data produced using $\mathbf{w_2}$ interleaved with the same 9 traces from the field data, up to offsets of 272.5 m from the start of the streamer. We can see that the travel-times of the main peaks and troughs in the arriving waveforms match well for both the direct water wave arrival between 200 and 1000 ms and the seafloor reflection, between 1600 and 2200 ms time. The principal difference between traces is the presence of noise within the observed data. 2D-to-3D changes in phase and amplitude spectra are properly accounted for by obtaining the source wavelet using this matching filter methos, as it matches the 3D real data to the 2D synthetic data.

3.4.3 Step 3. Selecting a starting velocity model

An initial velocity model was provided by Barker et al. (2018), which was created for a prestack depth migration (PSDM) of the seismic data using Paradigms Geodepth software. Prestack time migration (PSTM) velocities and a geological model were used to construct an interval velocity model as a function of depth, which was then iteratively refined through residual velocity analysis and inspection of the PSDM stack and gathers (Barker et al., 2018).

While this is an effective way to produce a velocity model for reflection imaging (Yilmaz, 2001), the method is dependent on Normal Move Out (NMO), which is relatively insensitive to velocity, as a range of subsurface velocity structures can be used to stack the same reflections successfully. NMO velocity estimation is influenced by several factors including reflector depth, spread length, bandwidth of the data, dip of the reflectors, signal-to-noise ratio and number of traces, hence NMO velocities are not always accurate sub-surface velocities. Using NMO velocity to locate the sea bed, for example, may be inaccurate due to the assumption that the ocean is a single virtual layer across the model.

3.4.4 Step 4. Modifying the starting velocity model

As outlined in Chapter 2, an accurate starting model is one of the most important ingredients for successful FWI. The two main factors which can produce cycle-skipping due to inaccurate starting models are an incorrect water column, and an incorrect sea bed. This is especially true for models with deep and variable ocean depths, such as line 05CM-04. Cycle-skipping in these areas arises from

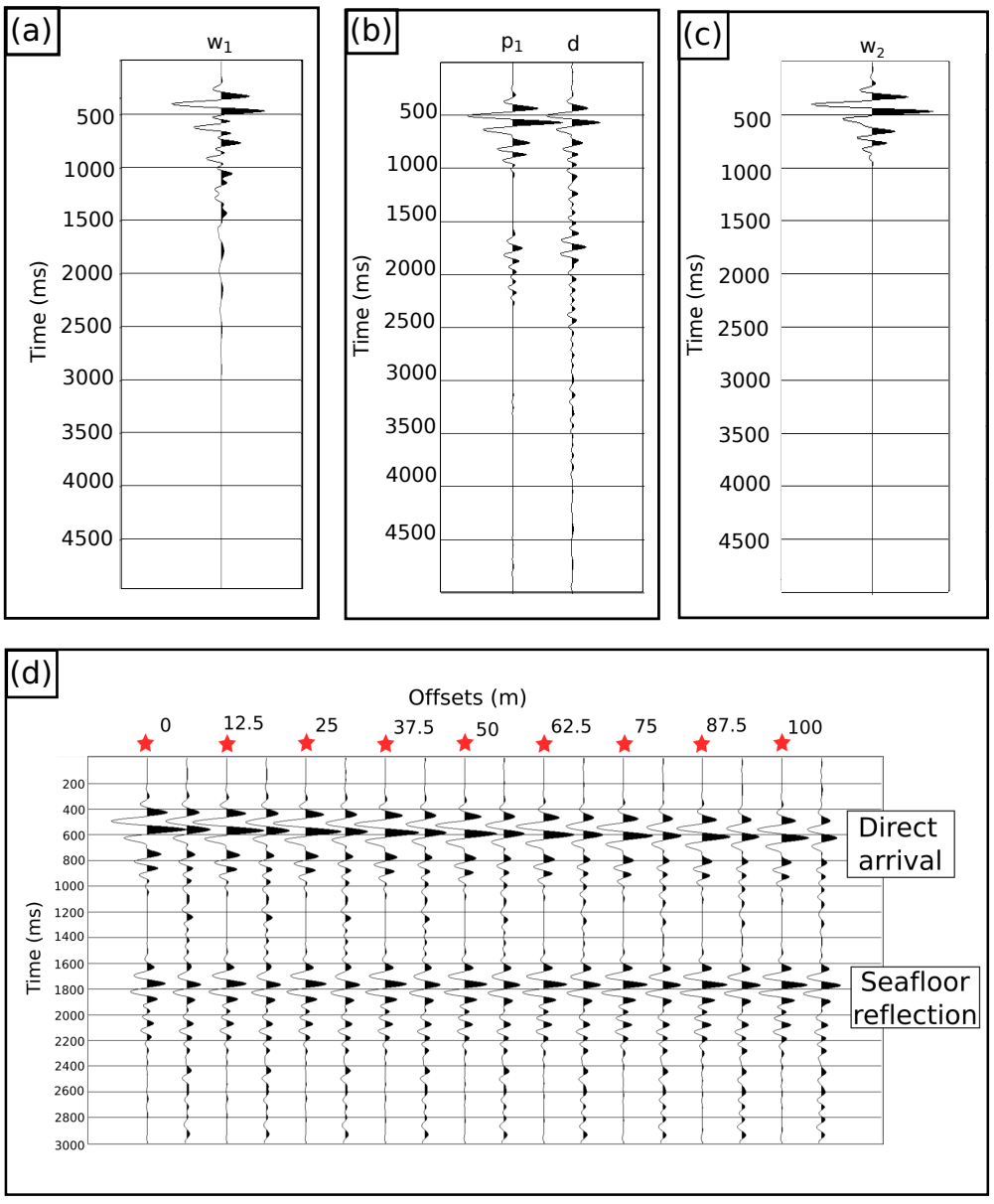


Figure 3.8: (a) The original source wavelet $\mathbf{w_1}$, a bandpass filtered spike. (b) The predicted data $\mathbf{p_1}$ on the left, and the same trace from the field data $\mathbf{d}$ on the right. (c) The final source wavelet $\mathbf{w_2}$ after application of the matching filter $\mathbf{f}$ to $\mathbf{w_1}$. (d) Side-by-side comparison of the predicted, $\mathbf{p_2}$ (indicated by a red star), and observed data, $\mathbf{d}$, for a single shot gather of the 2D seismic data used in this study. We note that the real and synthetic data match well, with matching shapes and arrival times

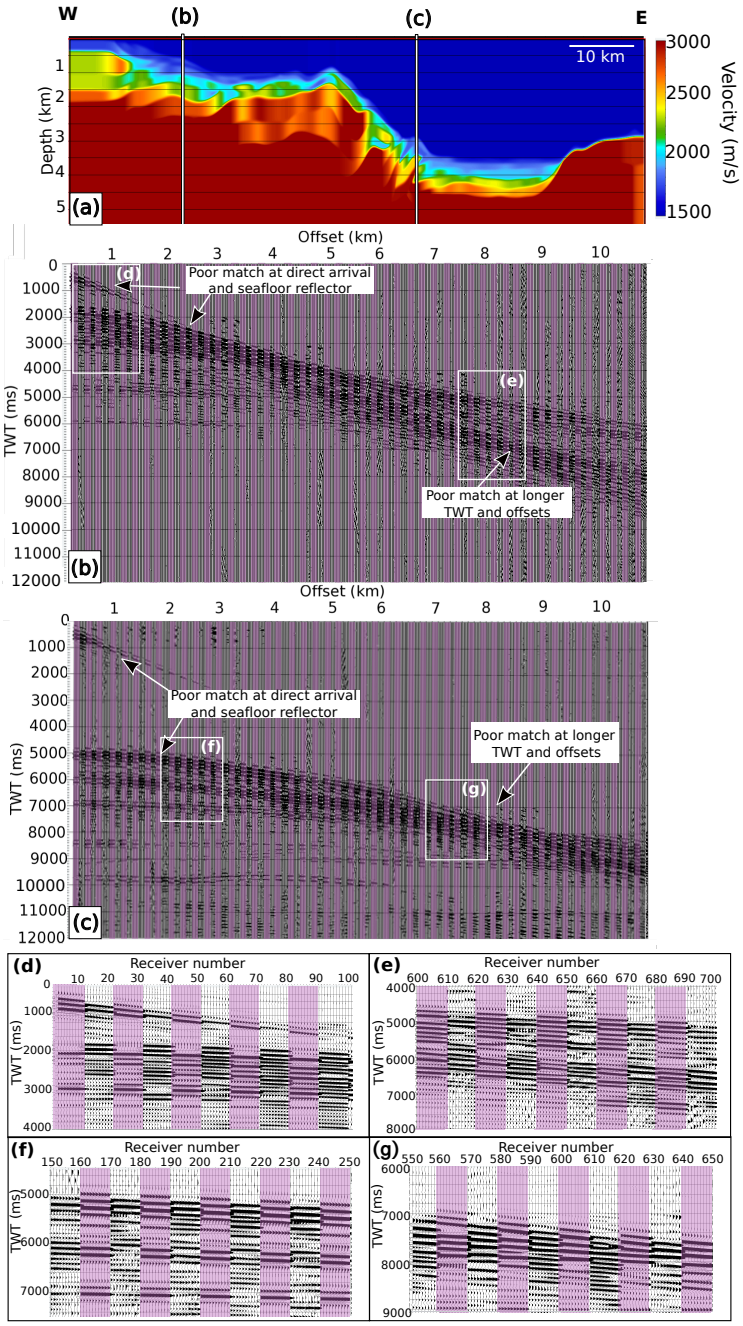


Figure 3.9: (a) Velocity model produced using PSDM by Barker et al. (2018). (b) and (c) show two shots gathers, with synthetic data generated using the PSDM model (highlighted in pink) interleaved with the observed data. The figure shows a poor match for both the direct water wave arrivals and seafloor reflections. (d), (e), (f) and (g) show zoomed in plots of data from within the boxes shown in (b) and (c). From these more detailed views, we can see that the arrivals are not well matched and are cycle skipped.

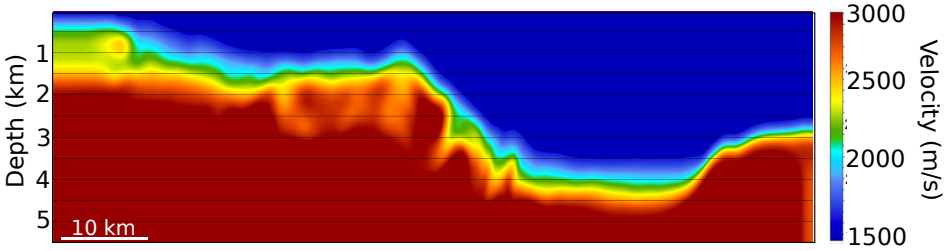


Figure 3.10: The PSDM velocity model produced by Barker et al. (2018) where rock velocities below the seabed were smoothed to remove all abrupt changes below the sea-floor except the seabed itself.

mismatched predicted and true data from the direct arrivals and seafloor reflection - waves travelling only in the water column, as well as because of the large impedance contrast between the ocean and the subsurface. Directly comparing predicted seismic data acquired through the starting model with the real field data allow an initial evaluation of the starting model. Propagating the source wavelet through the starting model should generate waveforms within half a cycle of the real data for the direct arrival into the streamer and seafloor reflection, if the model for the ocean velocity and seafloor depth is reasonably accurate. Fig 3.9 shows the interleaved predicted and field data for the PSDM generated starting model, with 10 traces of synthetic data followed by 10 traces of real data. The synthetic data is shown with a pink overlay in 3.9. 3.9(b) and (c) show that the synthetic data does not match the true data very well, neither for the direct water wave nor the seafloor reflection at both near and far offsets. 3.9(d)-(f) shows zoom-ins of highlighted areas, where we see that the two datasets do not match within half a cycle, and so inversions will cause cycle-skipping and convergence to local minima with this starting model. Discrepancies between the direct water wave and seafloor reflections indicate that we have an incorrect estimate of ocean velocities and seafloor bathymetry. As such, several changes were applied to the starting model to ensure it was accurate enough to begin the FWI process. Using synthetic data comparisons, as in 3.9, I was able to make several adjustments to ensure the starting model was appropriate.

3.4.4.1 Smoothing

Rock velocities below the seabed were smoothed in slowness to remove all abrupt changes below the sea-floor except the seabed itself, as FWI is more efficient if only well-constrained boundaries are placed in the initial starting models (Morgan et al., 2016). Sharp boundaries that are not well constrained will have large velocity contrasts which will produce strong synthetic reflections. FWI will try to match these strong reflections to the real data which can lead to cycle skipping and incorrect models.

3.4.4.2 Choosing accurate ocean velocities

Ocean velocities are extremely important in the FWI starting model, as the inversion does not alter velocities in the ocean due to the application of a cut-off velocity. This cut-of velocity is used in Gardeners equation (Gardner et al., 1974), which relates P-wave velocity, V_P, to bulk density, ρ as:

$$\rho = \alpha V_P^{\beta}, \tag{3.5}$$

where α and β are empirically derived constants based on the geology. The cut-off velocity is the lowest rock velocity in the model, below which is water, which FULLWAVE assigns a constant density, and does not alter during inversions. This means ocean velocities should be as realistic as possible to avoid cycle-skipping at the seafloor. The initial model provided by Barker et al. (2018) had variable sea floor velocities based on the PSTM. These velocities are shown in Fig 3.15(a). Synthetic testing using these velocities, (as shown in Fig 3.9) however, showed a mismatch between the sea floor reflections. Ocean velocities were testing in a number of ways in an effort to reduce cycle-skipping in synthetic testing, these include:

3.4.4.2.1 Using NMO to estimate ocean velocities The first attempt at adjusting the ocean velocities was made using a Normal Move-Out (NMO) correction to flatten the seafloor reflection. NMO works by compensating for the effects of separation distance between the source and receiver for a reflector, by using the travel time equation as a function of offset:

$$t^2 = t_0^2 + \frac{x^2}{v^2}, \tag{3.6}$$

based on the Pythagorean theorem for a shot-receiver pair for a horizontal reflector (Fig 3.11).

By estimating an NMO velocity accurately, the travel times can be corrected to remove the effect of offset, flattening the reflection (Fig 3.12(b)). Underestimating the NMO velocity causes an overcorrection and the reflection will curve upwards (Fig 3.12(c)). Overestimating the NMO velocity causes the reflection to be undercorrected and the reflection will curve downwards (Fig 3.12(d)).

NMO analysis was carried out across the model to find the best ocean velocities to flatten the seafloor reflection at small offsets. Fig 3.13 shows an example of an NMO test, where four shot gathers at varying seafloor depths are NMO corrected using an ocean velocity of 1500m/s. This velocity undercorrected shallower ocean velocities, over-corrected deeper oceans, and flattened seafloor reflections in the deepest part of the model (Fig 3.13). Many different ocean velocities were tested across the model, until a velocity model for the ocean that flattens CMP gathers across line 05CM-04 was selected, as shown in Fig 3.15(b).

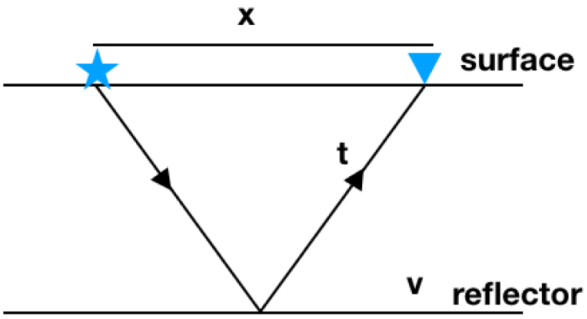


Figure 3.11: A source-receiver pair showing the distance the wave travels to and from the reflector (t x v) compared to the horizontal distance between the source and receiver (x), used in the derivation of the travel-time equation (equation 33.6).

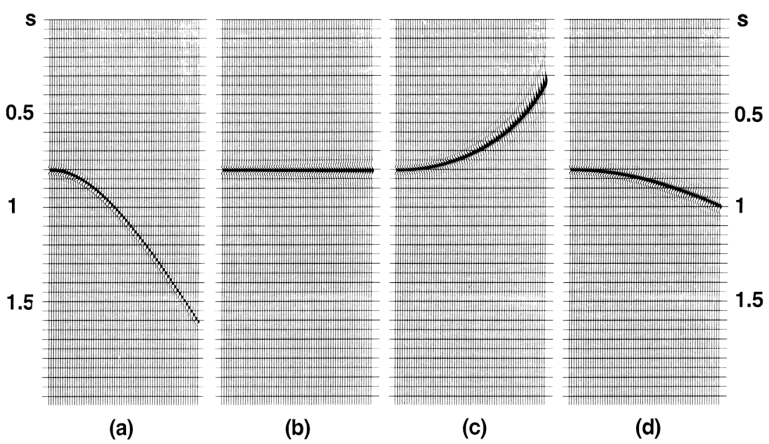


Figure 3.12: (a) a common mind-point (CMP) showing a single reflection. (b) The same reflection after the successful application of an NMO correction the gather is flattened. (c) The same gather shown in (a), by the NMO velocity used is too low, causing the gather to be overcorrected and curve upwards, and (d) The same gather shown in (a), but the NMO velocity used is too high, causing the gather to be undercorrected and curve downwards. From Yilmaz (1987).

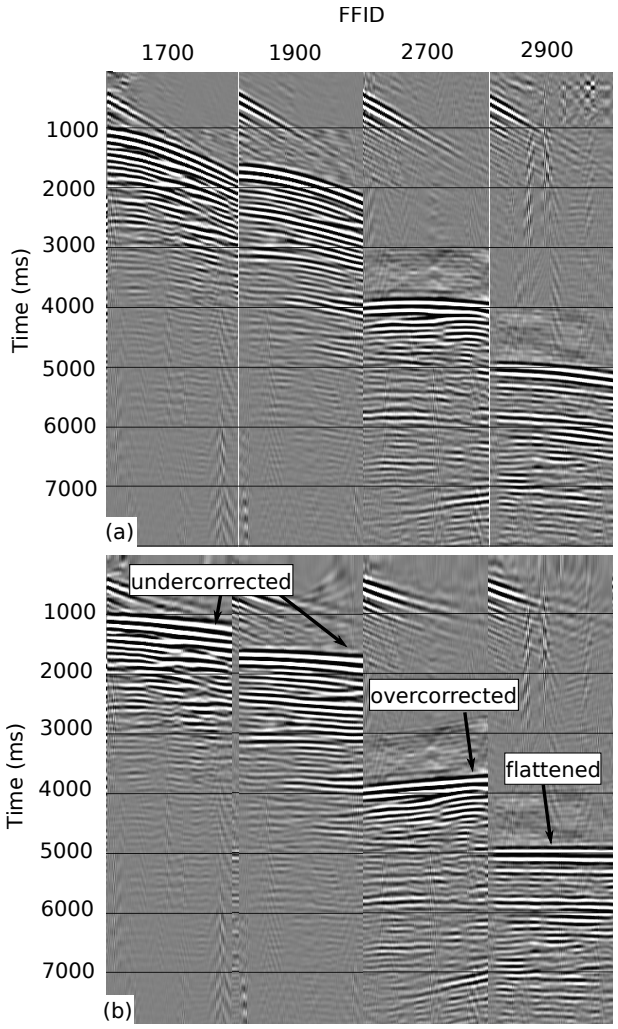


Figure 3.13: Four CMP gathers from the 05CM-04 dataset before (a) and after (b) the application of an NMO correction of 1500 m/s. The first two gathers from the shallower, landward part of the data are undercorrected, the deeper CMP gather is overcorrected, and the deepest seaward gather is flattened. This process was carried out over many CMP gathers with a variety of NMO velocities until a model was made which flattened CMP gathers across the model.

Even after extensive testing of the model, however, the results were unrealistic and still did not stop cycle-skipping in all parts of the model. For an isotropic medium and short-spreads the NMO velocity is equivalent to the stacking velocity (Robein, 2010). This means the velocity analysis assumes the ocean as one single virtual layer with constant velocity, which is, in reality not the case in oceans with largely varying depths such as along line 05CM-04. This method of determining the ocean velocity was therefore rejected.

3.4.4.2.2 A constant ocean velocity of 1500m/s I then tried to forward model with a constant ocean velocity of 1500m/s, as shown in Fig 3.15C. This is a standard value for P-wave velocities through salt water, and the numbers calculated in NMO testing (see above) were close to this value. Using a constant value for the ocean velocity produced non-cycle-skipped sea floor reflections in some parts of the model, however, also caused extensive cycle skipping of the sea floor reflection across the model. This method was therefore also rejected.

3.4.4.2.3 Using simplified velocities from the World Ocean Database (WOD) Using the National Oceanic and Atmospheric Administration (NOAA) World Ocean Database (WOD) (Boyer et al., 2013) I was able to extract ocean velocities recorded by Expendable Bathythermographs (XBTs) in the region at the same time of year as the time the data was recorded (May). The deepest XBT data retrieved from the NOAA database measured salinity and temperature to an ocean depth of 2km.

Using the XBT data, P-wave velocity was extracted with the equation for speed of acoustic waves in water by Medwin (1975):

$$V = 1449.2 + 4.6T - 0.055T^2 + 0.00029T^3 + (1.34 - 0.01T)(S - 35) + 0.016z, \tag{3.7}$$

where V are the ocean velocities, T represents temperature, S represents salinity and z represents depth. As the XBT data only measured values down to 2km, and the starting velocity model reaches ocean depths of $\sim$4 km, the derived ocean velocity profile was extended based on the assumption that at these ocean depths, the ocean becomes isothermal, and the P-wave velocity then becomes solely dependent on pressure and salinity, which increase linearly with depth (Howe et al., 1987). By taking the linear velocity of the graph at the deepest measured values, the profile was extended down to 4km (Fig 3.14). The velocity profile is shown in Fig 3.14, with the recorded data displayed as a solid line, and the predicted data as a dashed line. Note the high velocities in the upper 100m of the ocean. This is due to high temperatures in this upper ocean layer, and is an important addition to the model as the source and receivers are in this layer, and the direct wave will travel solely in this layer.

I then took the average velocity of three layers in the ocean where the velocity trends can be considered relatively constant. I divided the model into three layers between 0-1 km, 1-2 km and 2-4 km and extracted average velocity. I then created a layered ocean model as shown in Fig 3.15D. Although

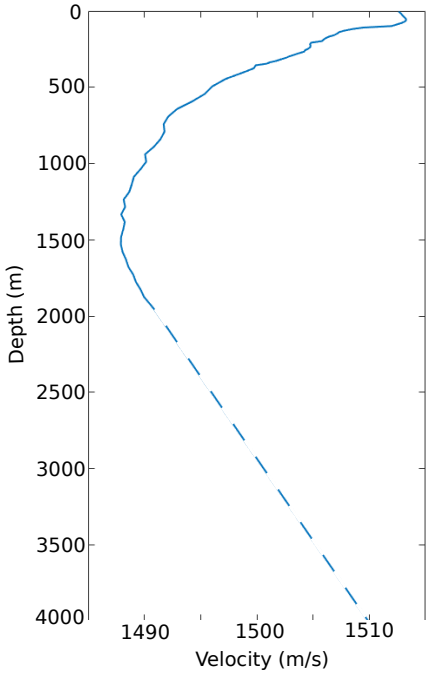


Figure 3.14: Ocean velocity vs depth based on XBT data from NOAA from the Hikurangi margin at the same time of year as the 05CM-04 survey. The solid line is the velocities calculated by equation 3.7 using data from the XBTs, and the dashed line is the projection of the velocity deeper than the XBT measurements based on a linear trend (Howe et al., 1987).

synthetic testing using this model for ocean velocities improved the reflection match over the NMO and constant velocity methods, there was still a mismatch between the synthetic seafloor reflections and the real data in some parts of the model. This method was therefore used but modified for further accuracy.

3.4.4.2.4 Using complete velocities from the World Ocean Database (WOD) The final method involved the use of the entire profile calculated from the XBT data, which is shown in Fig 3.14 to produce the ocean velocity model shown in Fig 3.15E. The gradual transition of ocean velocities involved in this model dramatically improved the fit between real and synthetic data for both the direct arrival and near-offset seafloor reflections. The fit of the mid-offset and far-offset arrivals is still potentially being cycle-skipped, but the direct wave and near-offset seafloor reflections are the key matches for providing an accurate starting model, as the other arrivals can be added into the inversion bit by bit.

3.4.4.3 Adjusting the sea floor

Now the ocean velocities are as accurate as possible to reduce cycle-skipping, the model can be improved further by adjusting the location of the sea-floor. This will further reduce cycle-skipping at greater shot-receiver offsets, and ultimately allow the inversion to more accurately predict sub-surface velocities by reducing the chances of converging to a local minima. The seafloor location is particularly important as it is the first and possibly largest impedance contrast in the model. An inaccurate sea floor location can produce errors in the model that will alter velocities below the sea floor, and is the main source of

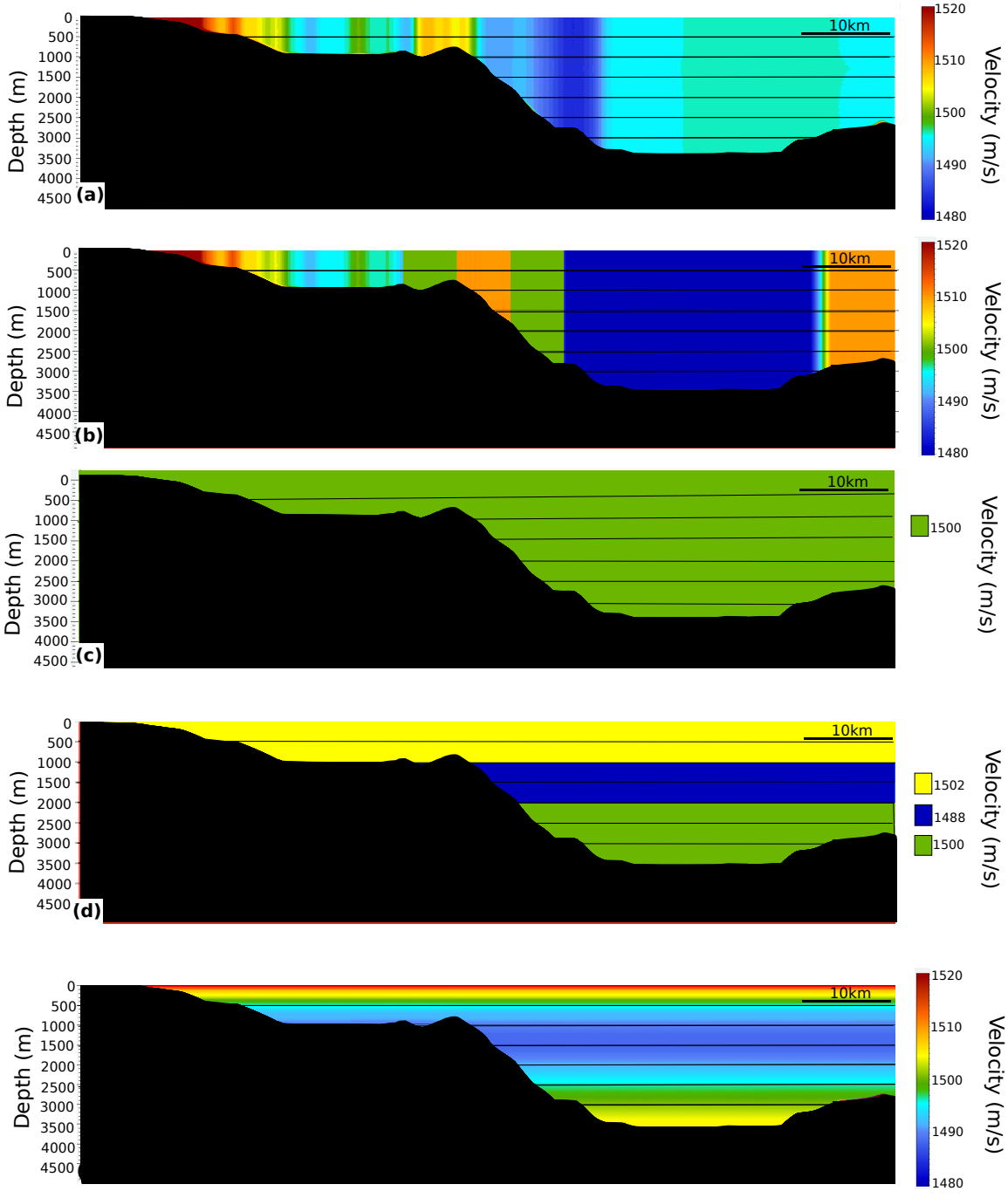


Figure 3.15: Different ocean velocities tested for the start model (a) shows the original ocean velocities found by Barker et al. (2018) using PSDM techniques. (b) Shows the velocities determined using NMO testing. (c) shows a constant ocean velocity of 1500 m/s. (d) shows a 3-layered ocean model based on XBT data from NOAA and (e) shows the final ocean velocity used which is based on the full data from XBTs.

cycle-skipping. The sea floor in the initial model was located using PSDM techniques (Figs. 3.9A, 3.10, 3.16A)(Barker et al., 2018). I investigate several different seafloor locations in the starting model.

3.4.4.3.1 Using minimum ocean velocities to pick the sea bed The first adjustment to the seafloor location was calculated using a threshold amplitude function in Landmark's SeisSpace software. This function was used to find the location where the model velocity increased above a certain value (in this case 1510m/s) in the initial PSDM model (Figs. 3.9(a), 3.10, 3.15(a)). This allowed me to extract a seafloor based on the highest ocean velocity. This new seafloor is shown in Fig 3.16(b), however, the ocean velocities in the PSDM model go up to 1520m/s, as shown in Fig 3.15(a), which is the same as the lower rock velocities in the model, which drop to 1518m/s in the basin on the incoming plate. This proved problematic for extracting the seafloor. Several tests were done using different threshold amplitudes between 1500-1520m/s, however this caused inaccuracies when testing the seafloor with synthetic forward-modelled data (in tests similar to that displayed in Figure 3.9). I therefore rejected this method.

3.4.4.3.2 Picking the sea bed based on a receiver gather Secondly, I attempted to re-pick the seafloor using a receiver gather from the nearest receiver to the source, over all shots along line 05CM-04, the result of which is shown in Fig 3.16(c). This new seafloor was applied to the starting velocity model and further synthetic testing was computed. It appeared that the match between real and synthetic data for the seafloor reflection had improved in some areas, but greatly declined in others. A series of tests were carried out with the picked seafloor being shifted by one model grid cell both above and below the picked seafloor, up to 5 cells either side of the initial picked seafloor. No one model gave a good match to the seafloor reflection across a selection of shots across the model. This method was therefore also rejected.

3.4.4.3.3 Using swath bathymetry data The final assessment was to obtain a fine-gridded swath bathymetry dataset courtesy of Stuart Henrys (GNS Science, New Zealand). This dataset is based on 25m-gridded data from 2011 (voyage TAN1114). These data were previously corrected using XBTs for the Sound Velocity Profile (SVP), and the results collected by the EM302 instrument onboard the research vessel are cleaned of bad beams, binned and gridded at GNS, New Zealand. The final grid spacing was 25m and all data processing was carried out on board (Stuart Henrys, pers comm). The extracted bathymetry profile is shown in Fig 3.16(d). Application of the the seafloor depths derived from bathymetry greatly improved the match between real and synthetic data in most of the model, however there are still some parts which appear to be cycle-skipped This is likely due to the fact that bathymetry measurements are made with acoustic instruments which make an assumption of the water velocity, which is usually a constant value and may be significantly inaccurate, especially in variable sea depths. While this is not an issue for tomography imaging, it is an issue in FWI. I therefore used most of the sea bed from the bathymetry measurements, but made some final adjustments to avoid cycle-skipping

across the whole model.

3.4.4.3.4 Final sea bed location adaptation Although the application of the seabed from swath bathymetry data produced a good match for most of the model, seafloor picking based on the receiver gather showed a better match at the east and west extremes of the model and on the slope in the central part of the model, landward of the trench (Fig 3.16). The final seafloor used in the starting model was therefore a combination of the bathymetry data across the majority of the seafloor, with the picked seafloor near the onshore part of the model (∼0-10 km horizontal distance), on the slope (∼45-55 m horizontal distance) and far offshore (∼81-89 m horizontal distance). This hybrid model produced the best matching synthetic gathers (Fig 3.16(e)). This final seafloor, as well as the ocean profile derived from XBT data, show a good match to the seafloor reflection across the model (Fig 3.17), and is suitable as the starting model for FWI.

3.4.5 Step 5. The adequacy of the source wavelet and starting velocity model

The quality of the source wavelet and starting model was investigated by directly comparing predicted seismic data acquired through the model with the real field data. The starting model will generate matching waveforms for the direct arrival into the streamer and seafloor reflection if the model for the ocean velocity and seafloor depth is reasonably accurate (see above). I also examined later-arrivals and longer-offset refractions to check whether they are cycle-skipped, and used this information to determine which offsets and times of the data should be input into the initial inversions (see step 6). By slowly adding in longer offsets, the likelihood of cycle-skipping is reduced because improvements to the velocity model move the synthetic arrival times towards the observed. Fig 3.17 shows the interleaved predicted and field data for the final starting model (shown in Fig 3.17(a)), with 10 traces of synthetic data followed by 10 traces of real data. The synthetic data is shown with a pink overlay in Fig 3.17.

Fig 3.17 shows a good match between real and synthetic waveforms for both the direct arrival and the seafloor reflection up to about 5km offset, a great improvement on the initial PSDM model shown in Fig 3.9. The waveforms also align well for the first seabed multiple (at ∼300ms for shot gather (b) and ∼10000ms for (c)). The match is shown in greater detail in boxes (d) - (g), where I have zoomed in on the shot gathers shown by the boxes in (b) and (c). (d) and (f) both show a continuous match across of the real and synthetic data for direct arrival and seafloor reflection. Boxes (e) and (g), however, highlight the mismatch between the real and synthetic data at longer offsets, as the reflections in the real data and the synthetic data do not align. This match is typical for shot gathers across the margin. This indicates that the sea-floor and water velocities are reasonably accurate, and suitable for use in FWI. The match at greater times and offsets is less good, as expected, but some seismic phases are seen to match within half a cycle (Fig 3.17(d),(f)). This indicates that I have selected a good enough starting velocity model to begin FWI, and that I can use these comparisons to remove any clearly cycle-skipped data from the inversions. For example, some of the reflections at long offsets appear to be over half

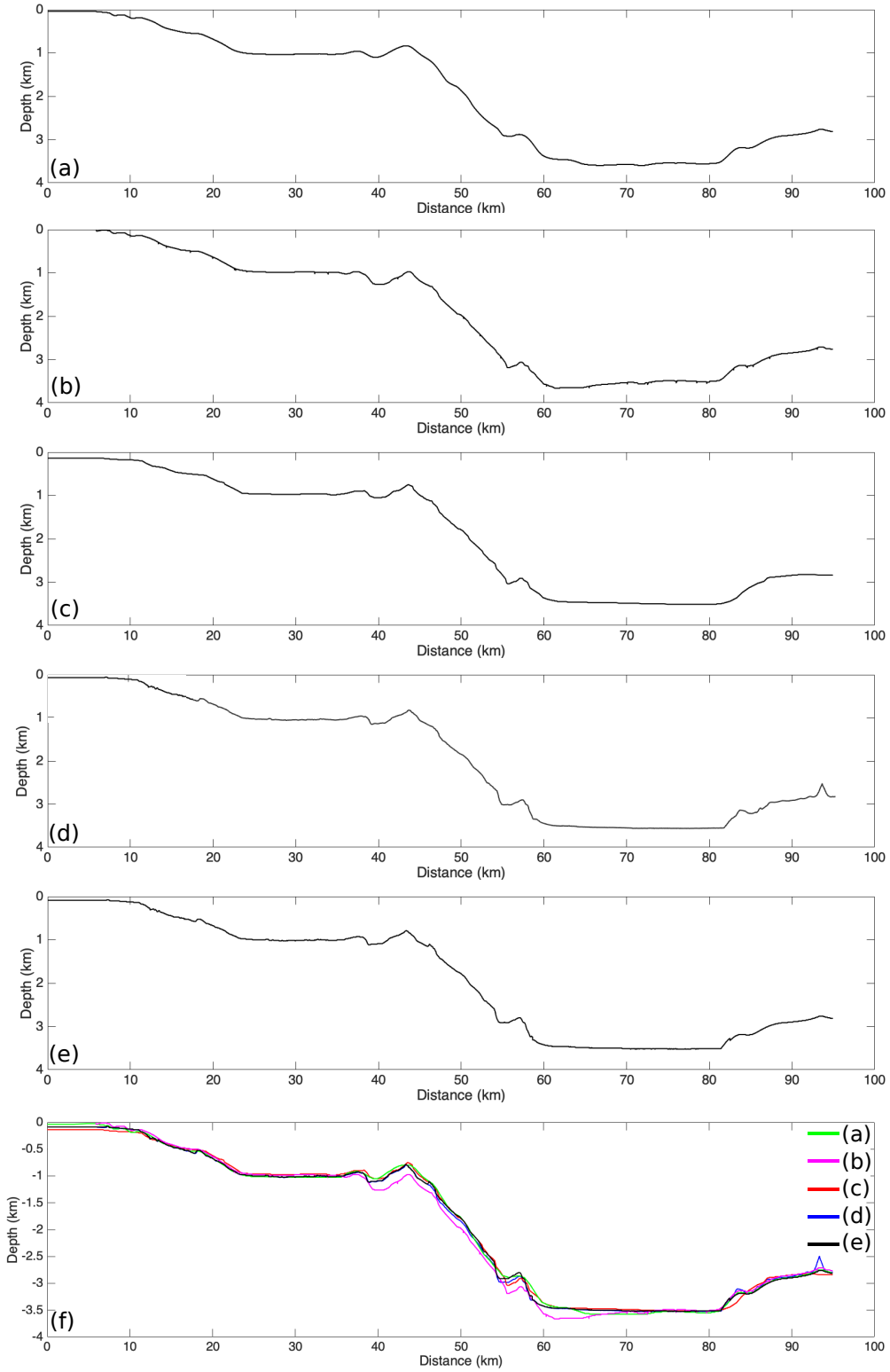


Figure 3.16: Different sea floor bathymetries tested in the start model. (a) is the original seafloor bathymetry used by Barker et al. (2018) based on PSDM. (b) Is the seafloor bathymetry found by using the minimum ocean velocity from the model shown in Fig 3.9(a). (c) shows the seafloor bathymetry picked from the nearest offset receiver gather over all shots. (d) is the bathymetry from the fine-gridded dataset provided by Stuart Henrys (GNS) and (e) is the final seafloor bathymetry I used which is the bathymetry data (d), edited near the onshore part of the model (∼0-10km horizontal distance), on the slope (∼45-55m horizontal distance) and far offshore (∼81-89m horizontal distance) for best matching synthetic gathers. (f) shows all the seafloor tests overlaid on one figure to better discern differences in the sea floor depths.

a cycle out of phase with the real data (Fig 3.17(e),(g)). In my adopted inversion scheme, outlined in section 3.4.6, cycle-skipped data are excluded from the initial inversions, and more data are added as the match improves to be less than a half-cycle out of phase.

3.4.6 Step 6. Inversion strategies were tested and a final inversion scheme selected

A good inversion strategy is important to ensure the majority of the input data are not cycle-skipped and the models are slowly improved, with the misfit function converging to a global, rather than a local minimum. The low-kernel stability criteria (equations 2.27 and 2.28) are taken into account when choosing the inversion parameters. Ideally, I want to use a grid size of 12.5m, the same as the receiver spacing (Table 4.1). Frequencies, time sampling and grid size are dependent on each other as the code requires the wavefield to cross <0.5 grid-points per timestep for the low-kernel, as described in Chapter 2. Based on equation 2.27, for inversion frequencies up to 8Hz and minumum velocities of 1520m/s, the maximum grid size is 38m. For best inversion results we wish to use a grid size equivalent to the receiver spacing of 12.5m, and this lies well within the stability criteria. Based on equation 2.28, this produces a maximum timestep of 1ms for a V_{max} of 6000m/s. These are the values that were decided on for the inversions (Table 4.1). I also ensured the inversion did not attempt to alter velocities in the ocean, or move the sea floor location, due to the extensive testing undertaken to ensure these were correct. As describes in Chapter 2, successful FWI requires wide azimuths, long-offsets and low frequencies. As the streamer used for data collection along line 05CM-04 is single-azimuth, limited in offset to 12km, and useable frequencies only go as low as 3Hz (Table 3.2), I had to carefully adapt the way the data was inverted to avoid cycle-skipping and convergence to local minima as best as possible. This included:

3.4.6.0.5 Muting the data A two-second window was applied to the data using mutes to remove the direct water wave, noise above the first arrivals from the sea-floor and later arriving multiples and possible S-waves. Some multiples are still present in this window, but are included as testing has shown that including multiples and ghosts in the FWI inversion produces reliable and stable results (Warner et al., 2013). Elastic effects by S-waves may introduce cycle-skipping into the model as they are not accounted for by the code.

3.4.6.0.6 Inverting in increasing frequency blocks The data were inverted in 8 frequency blocks, for which the input data were band-passed using minimum-phase Ormsby filters with 0.1% noise and 1Hz roll-off to remove frequencies higher than a maximum frequency, set to values from 3 to 8Hz, with 20 iterations for each frequency block (table 4.1). This allows the model to first add longer-wavelength structure to the subsurface, and slowly reduce the wavelength as frequency increases, greatly reducing the chances of cycle-skipping (chapter 2, Fig 2.2). This also improves the chances of converging to a global minimum as lower frequencies contain fewer local minima, and by slowly adding higher frequencies, we

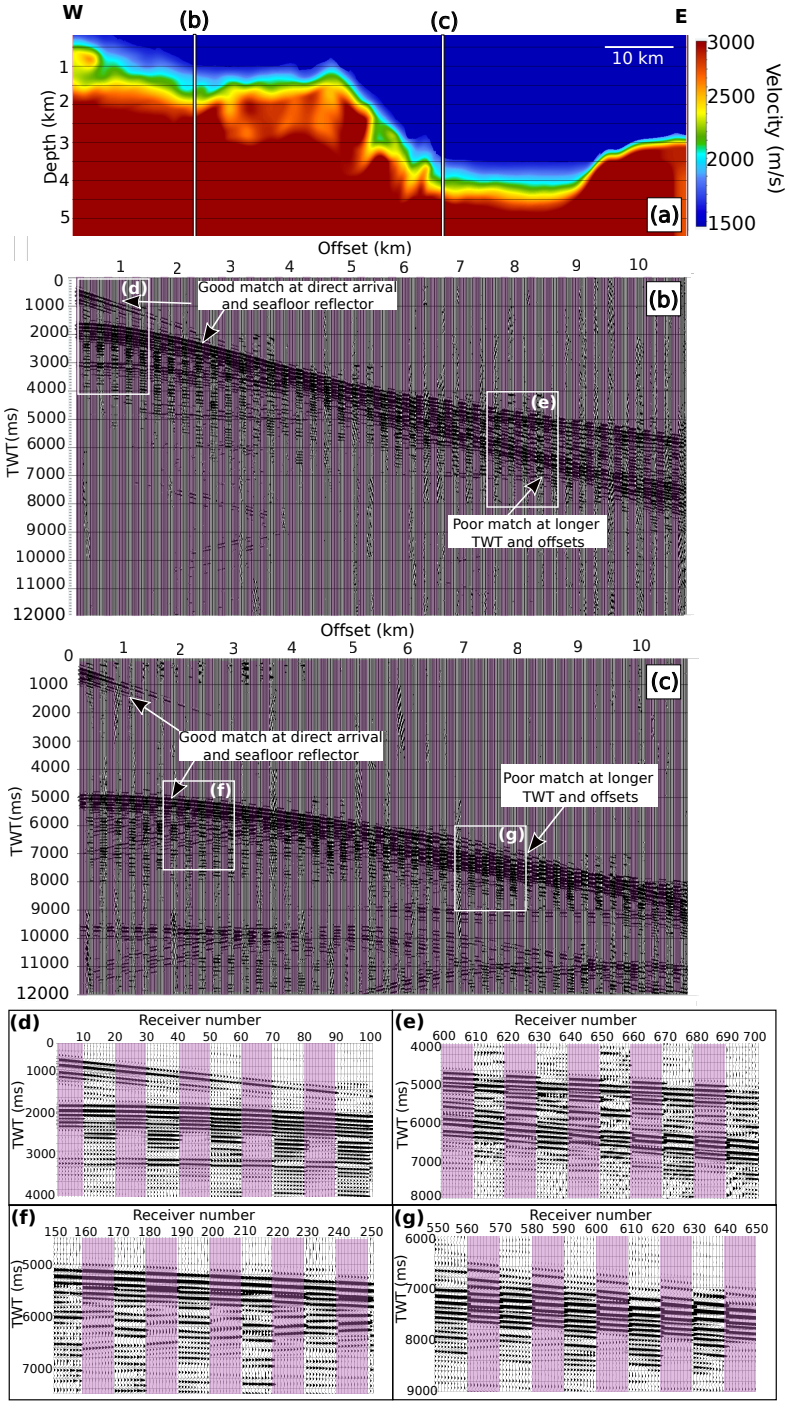


Figure 3.17: (a)) Plot of the final modified starting model for full-waveform inversion (FWI). (b) and (c) show two shot gathers, with synthetic data generated using the starting model (highlighted in pink) interleaved with the observed data. The figure shows a good match for both the direct water wave arrivals and seafloor reflections, and a reasonable match for some later arrivals and longer-offset refractions. (d), (e), (f) and (g) show zoomed in plots of data from within the boxes shown in (b) and (c). From these more detailed views, we can see that some of the later arrivals and longer offset data are not well matched and may be cycle skipped.

ensure each starting model estimate lies closer to the global minimum (Fig 2.1). This will affect the total number of receivers and maximum number of streamer receivers per composite shot in Table 4.1.

3.4.6.0.7 Inverting in increasing offsets of the data As shorter-offset data are dominated by reflections, which contain more local minima than refracted arrivals, it was important to account for this in the limited offset streamer data used in the inversion. I attempted to reduce inaccuracies in the model by slowing introducing larger offsets of the input data. Starting with offsets up to 6 km (half the streamer length), the frequencies included in the inversion were increased incrementally as described above. Once FWI was complete, the resulting model was smoothed in slowness as in section 3.4.4.1, using a 2D convolutional filter measuring 60 traces horizontally and 60 time samples vertically, and the result was used as the new starting model for the next inversion, which included data offsets up to 7.2km. The result of this inversion was again smoothed and used as the new starting model for input data up to 10.87m offset. By slowly increasing offsets in this way, the new starting models were closer to the global minimum, as shallower structure, dominated by reflections were more accurate before incorporating deeper turning rays. The final 1.13m of the streamer were not included as synthetic testing showed this caused cycle-skipping within the model, likely due to cable feathering at long offsets which could not be mitigated by modelling in 2D.

3.4.6.0.8 Adjusting for computational power With 2375 shots at each receiver, this produced a total number of 200,000 individual receiver positions. Inverting for this many receivers is extremely computationally expensive. To reduce computation time, I employed FULLWAVE's reciprocity function which allows sources to be modelled as receivers and vice versa, and used each shot twice in each iteration block of 20 iterations per frequency. This allowed 481 streamer receivers per composite source, and 237 shots per iteration, using each shot twice in each iteration block.

3.4.6.0.9 Final inversion scheme The final inversion scheme is as follows:

Starting with a default number of iterations per frequency, based on previous applications of the code, the dataset is inverted and the misfit is checked to ensure the reduction of the misfit has become minimal. Additional tests are run if this is not the case. If step lengths become very small, the inversion has converged at that frequency, and typically we would then move to higher frequencies. The inversions are run on a cluster of multi-core CPU nodes and take between 3 and 4 days to complete using 25 nodes which each have 8 cores. The inversions were performed using these parameters and repeated three times, starting with offsets up to 6km (481 streamer receivers per composite shot), then increasing to offset of 7.2km (576 streamer receivers per composite shot), and finally up to 10.87km (870 streamer receivers per composite shot). After each inversion block, before adding in longer offsets, the model was smoothed in slowness via a 2D convolutional filter measuring 60 traces horizontally and 60 time samples vertically.

Table 3.3: Parameters used in FWI of the dataset.

Property	Value
Inversion type	Time-domain, Isotropic
Total number of sources	2173
Shot spacing (m)	37.5
Total number of receivers	1045213
Maximum number of streamer receivers per composite source	up to 870
Receiver spacing (m)	12.5
Offset between shot and first receiver (m)	160
Grid size (m)	12.5
Time sampling rate (ms)	1
Maximum frequency in each frequency block	3.0, 3.4, 3.9, 4.5, 5.2, 6.0, 7.0, 8.0
Iterations per frequency	20

While I have chosen a time-domain acoustic inversion, I are aware that attenuation can produce phase effects. These effects can be important in industrial settings where anisotropy is well constrained and exact depths are important, however, with the 05CM-04 dataset, properly accounting for the dispersive effects of attenuation over the limited bandwidth that we use for FWI will not produce any substantial changes to the model other than minor shifts in absolute depths. These shifts are likely to be similar or smaller in magnitude to those produced by anisotropy which is also not constrained here.

3.4.7 Step 7. The dataset was inverted using the selected inversion scheme, with regular quality assurance to check for cycle skipping

After computing velocity models using the inversion scheme outlined in step 6, the models were checked after each increase in offset using the technique outlined in section 3.4.6.0.7. This was to ensure that the time differences between arrivals in the field and synthetic data were decreasing, and the synthetic reflections and refractions were aligning with the observed data and not cycle skipped. The resulting velocity models, obtained after including 6km and then 7.2km source-receiver offsets, were then smoothed in slowness and used as the new starting model for the next set of inversions. A total of 160 inversions, 20 for each frequency block, were performed for all three offset ranges (Table 3). The performance of the inversions was monitored throughout by regularly comparing the predicted and observed data, to ensure the velocity model was being updated in the right direction. Once it was insured the inversions were performing as desired, the final P-wave FWI model was obtained after 160 iterations, and will be discussed in the following chapter.

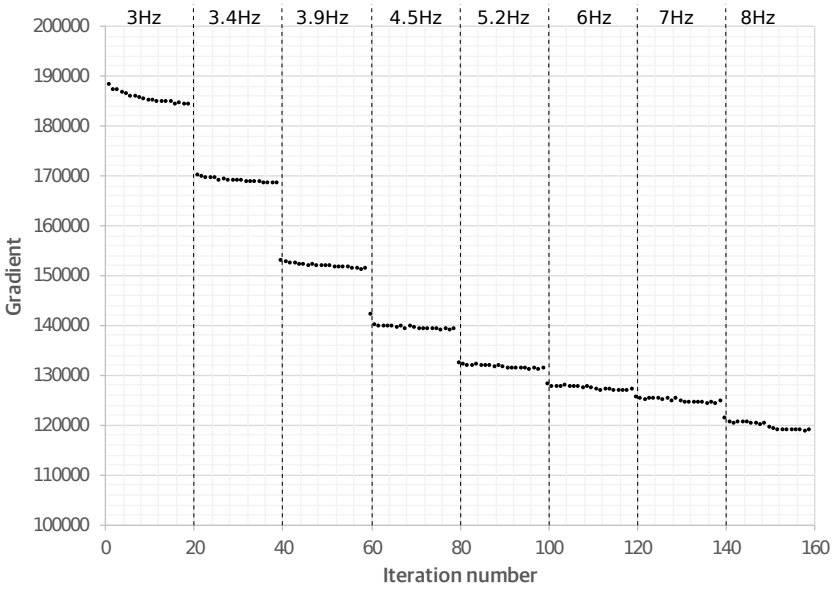


Figure 3.18: The gradient of the objective function at each iteration. A decrease in the gradient indicates the inversion is converging, however it is not an especially useful tool as we don't know whether it is converging to a local or global minima.

3.5 Quality Assurance of the model

3.5.1 Quality Assurance techniques

Quality assurance checks of the model are carried out during inversion to ensure the model is moving in the right direction. These tests can be carried out at any point during the inversion, and allow me to ensure that I am computing the best possible model. These quality assurance techniques include:

3.5.1.1 Monitoring the gradient of the objective function

As outlined in chapter 2, it is important that the gradient of the objective function is minimised. We can investigate how the gradient of the objective function changes at each iteration, an example of which is shown in Fig 3.18. This figure monitors the objective function over an inversion consisting of 160 iterations in 8 frequency blocks with maximum frequencies ranging from 3Hz to 8Hz, as in Table 4.1. The value of the gradient of the objective function will vary with overall reduction in error as well as with different normalisations applied to different subsets of the data. Within each frequency block, a general decrease in the gradient of the objective function can be seen, although occasional fluctuations do occur from one iteration to the next. As the maximum frequency of inversion is increased, a large decrease in gradient is seen, this is due to the greater detail that higher frequencies contain, and therefore a better representation between the real and predicted datasets. An overall decrease of $\sim$60% occurs over the entire inversion.

While monitoring the gradient of the objective function is useful, it is not especially effective, as if the model is cycle-skipped, and converging to a local rather than a global minimum (chapter 2), the gradient

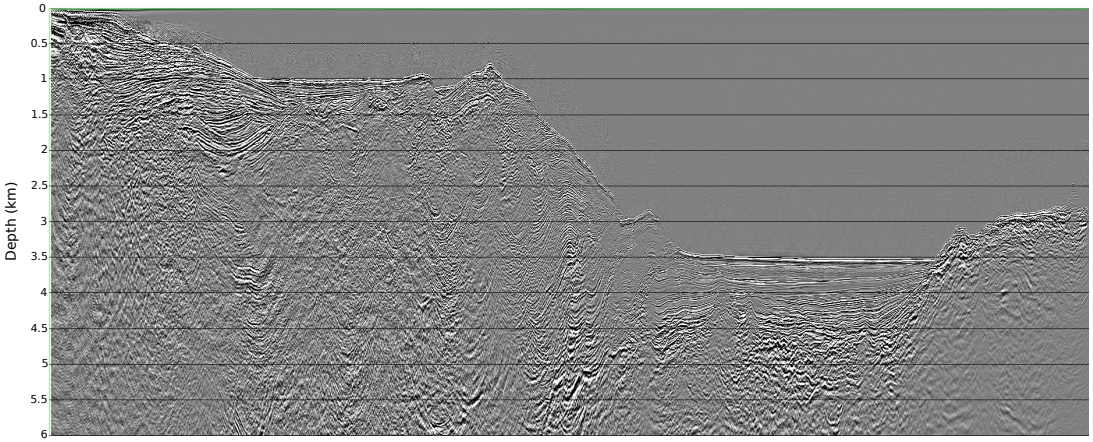


Figure 3.19: PSDM image of line 05CM-04 migrated using the tomography velocity model by Barker et al. (2018), displayed with root mean square (RMS) normalisation.

will still decrease. If the gradient remains large, however, we know the inversion is inaccurate. I therefore do not use this technique in later chapters, and instead use more relaible quality assurance methods.

3.5.1.2 Comparing the model with the PSDM seismic seflection Image

To investigate whether velocity features recovered by FWI correlate with geological features, I compare the model to the PSDM seismic image shown in Fig 3.19. By overlaying the two images, it is possible to see whether changes in velocity correlete with features present in the migrated reflection image, or whether the appear to be anomalous or incorrect. It is important to note that the PSDM reflection stack was processed using the unsmoothed starting velocity model in Fig 3.9a, and therefore features will not correlate exactly. As the FWI is isotropic (Table 4.1), any anisotropy in the subsurface will also not be accounted for, which means that we expect to see an offset in depth between individual reflections, which are more sensitive to changes in vertical velocity, and the velocities recovered by FWI, which are more sensitive to the horizontal velocity structure (Bentham et al., 2018; Christeson et al., 2018). This quality assurance technique is useful in determining whether strong velocity contrasts correlate to strong reflections in the PSDM image, which would indicate they are geologically accurate.

3.5.1.3 Comparrison between the real data and synthetic shot gathers

This quality assurance technique has already been demonstrated in this chapter in sections 3.4.3 and 3.4.5. By looking at the match between real and synthetic shotgathers during inversion we can determine whether the model is avoiding cycle-skipping and moving in the right direction. This technique is especially useful when comparing several possible velocity models to determine which is the most accurate. As the minimisation of the misfit would cause a match between real and synthetic shot gathers (chapter 2), seeing which of several models most closely matches the real data is an extremely useful tool. This method is used extensively throught the FWI process, as exhibited here, for determining sea-floor depths, ocean velocities, best inversion schemes and overall model accuracy.

3.5.1.4 Comparison with logging-while drilling (LWD) and wireline sonic data

LWD and wireline sonic P-wave velocity data were collected between November 2017 and January 2018, after completion of the FWI modelling presented here and in chapter 4. The LWD and wireline data sample the <1000mbsf every 0.5ft (0.124m) along seismic line 05CM-04 from three drill sites U1519, U1518 and U1520 (Fig 3.21). I can extract a velocity-depth profile from the models at the locations of these drill sites, and compare this to the in-situ LWD and wireline measurements. While this is an extremely useful technique as it allows the direct comparrison between modelled and real Vp values, the LWD tool is most sensitive to vertical changes in velocity while FWI, determined by refracted turning waves (chapter 2), is more sensitive to horizontal velocities. This means it is not a straightforward comparison between the LWD and modelled data. As the full-waveform inversion is isotropic (Table 4.1), any anisotropy in the subsurface geology will not be accounted for. This means that we expect to see differences in the size and depth of velocity anomalies within sonic velocity data and the FWI velocity model. As the model converges during inversion, any over- or under-estimations of velocities, which are due to anisotropy in the shallower parts of the model, will produce offsets between the FWI and well-log velocity-depth structure at deeper depths. The FWI velocity model has a lower resolution than the sonic data, which means we are not expecting the FWI model to reproduce the fine-scale detail within the sonic log. This tool is, however, useful is determining model accuracy by seeing how well the velocity structure is recovered compared to real downhole data.

3.6 Assessing further improvements to he model

While the inversion scheme selected in section 3.4.6 worked well on the 05CM-04 dataset, in order to ensure the final Vp model was indeed the best possible model I could produce using FWI, I tested several additional variations. These variations were tested with quality assurance techniques 3.5.1.2 and 3.5.1.3 extensively.

3.6.1 Inverting for all offsets up to 12km

A test was done to include the last 1.13 km of streamer data in the inversion, extending the maximum offset included to 12km, and the maximum streamer receivers per composite shot to 960. The addition of these extra offsets, however, caused a bigger mismatch between synthetically modelled and real wavelets. This is likely due to low signal to noise ratios for the very far-offset data (Fig 3.6) and/ or feathering of the streamer at longer offsets, rendering the data quality too poor to improve the inversion in 2D. This is an issue which motivates the acquisition of the large, NZ3D-FWI dataset detailed in chapter 5, which will be a 3D cube of data including 3D towed streamer, OBS instruments and land stations. This will improve overall data quality, as the experiment is designed specifically for FWI, and well as remove issues due to feathering by taking the model to 3D. Therefore, for this 2D dataset, we disregarded this option and kept the maximum offset to 10.87km.

3.6.2 Extending the mute from 2 seconds to 5 seconds.

Another test to improve the model was to extend the mute applied to the input data. I increased the time window of field data from 2s from the first seafloor reflection arrival to 5s. This still allowed for the removal of the direct water wave and noise ahead of the first arrivals, but allowed more data to be incorporated in the inversions, including multiples and possible S-waves. The starting model used in this scheme was the final model produced after applying the 2 second mute to the data, which was first smoothed before being used with the new extended mute. The smoothing was carried out in slowness via a 2D convolutional filter measuring 60 traces horizontally and 60 time sampled vertically. The rationale behind increasing the mute was that the updated starting velocity model would now be much more accurate than the original starting model, and hence including more data could persuade the model to converge further to the true answer. On completion of the inversion as outlined above (Table 4.1), increasing offsets in three stages as in the 2s muted data, the final result was again subject to synthetic testing. Comparing the resulting synthetic waveforms to the true data, it was noted that the mismatch had again increased. This is most likely due to contamination from multiples and S-waves. As I am inverting for P-wave velocities only using a time-domain isotropic code, S-wave arrivals may have caused the inversion to produce artefacts when trying to match waveforms. Therefore, the initial mute of 2s from the first seafloor reflection arrival was preferred.

3.6.3 Using different versions of the FULLWAVE code

Initially, I was using FULLWAVE code version 595 (2015), however, during the time taken for the extensive processing and testing outlined above, the code had advanced to version 686 (2017). I attempted to reproduce my results using the same parameters outlined in Table 4.1 with version 686, both with and without the application of spatial preconditioning. Spatial preconditioning applies a simple approximation to the diagonal of the inverse Hessian. This allows normalisation using a quantity dependent on the total incident wavefield energy, and is stabilised to avoid normalisation by unduly, potentially noise-dominated values. While the latest version (V686) often showed a slightly improved match to the near-offset data at large travel-times, it greatly underestimated velocities of the deeper parts of the model, causing the match between real and synthetic data at long offsets to be too late. This is likely due to the industrial datasets used for the optimisation in V686, which are not relatable to the Hikurangi dataset. Therefore I used version 595 to produce the final velocity model.

3.6.4 Increasing offset at each frequency band with different smoothing parameters.

Testing a slightly different inversion scheme was also carried out with various smoothing parameters. In this test, instead of inverting with increasing maximum frequency for each fixed offset, I inverted for each maximum frequency limit with increasing offset. For example, for a maximum frequency of 3Hz,

the inversion would go through 6 iteration blocks with maximum offsets of 3.75km, 5.75km, 7.75km, 9.75km and 10.87km. The process was repeated for maximum frequencies of 4Hz, 5Hz, 8Hz, 7Hz and 8Hz. This process was carried out using a range of smoothing factors in both the x- and z-direction, where the smoothing unit is the local seismic wavelength calculated using the local velocity and the frequency specified for the current iteration block, where SX1 is the smoothing factor in the x-direction and SX3 in the z-direction:

a SX1=0; SX3=0.

b SX1=1; SX3=0.25.

c SX1=2; SX3=0.5.

d SX1=4; SX3=1.

Note that this smoothing is different to the smoothing described in step 4. Step 4 describes an initial smoothing of the model before inversions. The smoothing described here occurs within the inversion after each iteration. Previous inversions tested in this chapter used FULLWAVE's default smoothing within iterations which is the minimal smoothing based on local seismic wavelengths in the model.

While at low frequencies this method appeared to be improving model fit, the models soon began producing large velocity anomalies and models which were not geologically plausible. Test (a) did not produce such anomalies but the inversion appeared to emphasize features in the previous inversions drastically. Comparing the synthetic and real shot gathers showed a worse fit to the real data, especially at longer offsets. A final test was carried out by drastically smoothing the final model from the frequency inversion and repeating the original inversion scheme as in Table 4.1, but again anomalies were introduced early on and so this was abandoned after inverting for half the streamer length. These inversion schemes were therefore rejected, and I finally concluded that the initial inversion scheme was the most accurate way to produce the final velocity model.

3.7 Raytracing was computed to determine maximum target depths.

Paraxial ray tracing was computed through a smoothed version of the final starting velocity model (Fig 3.17A). This was carried out to determine the depths of turning rays recorded by the 12km streamer, and therefore which parts of the final FWI model were constrained by real data. Results of the ray tracing show good coverage of the subsurface by seismic waves in the uppermost 1.5-2 km depth below the sea floor (Fig 3.20). This indicates that recoverable subsurface P-wave velocities are expected up to ∼2km bsf depth, but not from within the subducting slab and not from within the known source area of SSEs at depths of >4 kmbsf, although imaging is possible in regions of SSE propagation which reach as shallow as 2km, and possibly to the trench (Wallace et al., 2016). Wider offset data collection is required

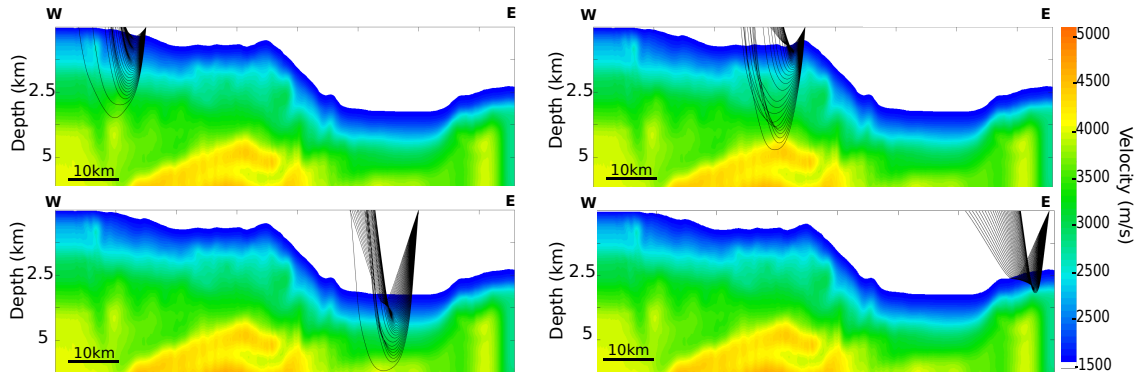


Figure 3.20: Paraxial ray tracing through the starting model at 4 locations along line 05CM-04. The black lines show the rays being recorded by the 12-km long streamer. There is good ray coverage in the uppermost 1.5-2 km of the sub-seafloor, with some rays penetrating down to 3.5 km depth.

to image to these deeper depths.

3.8 3D synthetic testing for key targets

In 2017/18 funding was granted for the acquisition of a large 3D seismic dataset in the Hikurangi region, in the vicinity of line 05CM-04. In chapter 5, the design and execution of this large 3D experiment is detailed. While the 2D streamer dataset was not acquired optimally for FWI, this new dataset would be wide-angle, large-azimuth, and acquired specifically for FWI (chapter 2). Similar pariaxial ray tracing was computed as in 4.5.2, and it was determined that incorporating OBS instruments as well as land instruments into the experimental design allowed for the illumination of much deeper targets, and imaging down to the plate interface, which was not possible with the 2D streamer dataset (Fig 3.20). In order to determine the best possible receiver layout for the experiment, 3D synthetic FWI testing was carried out.

A suite of tests for localised small-scale structure, achieved by adding checkerboard type structures in areas of particular interest was carried out on a synthetic 3D model of the region. This involved creating a synthetic 3D velocity model, inserting a checkerboard at key areas of interest, and attempting to recover the checks. The details of this synthetic testing for different land receiver layouts is explained in detail in part I of Chapter 5, and the execution of this experiment in New Zealand in Part II of Chapter 5.

3.9 Using physical properties to transform the final FWI model into models of a range of physical properties

As outlined in section 4.6.1.3, in 2017/2018, two International Ocean Discovery Program (IODP) Expeditions 372 and 375 collected various data along the 05CM-04 seismic profile (Fig 3.21). Expedition 372 collected Logging-while-drilling (LWD) physical property data which, when processed produced measurements every 0.1524m (0.5 ft) at three drill sites, and collected logs including: ultrasonic caliper, neutron-gamma bulk density, gamma ray (collected every 0.3m), NMR, neutron porosity, propagation resistivity, annular pressure/temperature and compressional and shear velocity (Pecher et al., 2019; Wallace et al., 2019). During IODP Expedition 375 core samples were collected at five drill sites along 05CM-04, however I will not be using one of the sites, U1526, in this thesis due to the shallow depths (∼85m) and the proximity of the drill site to the edge of the FWI model. Physical property measurements were also taken at discrete locations along the recovered core, and include porosity, moisture and density (MAD), natural gamma ray, gamma ray attenuation (GRA) bulk density, P-wave velocity, undrained shear strength, compressional strength, magnetic susceptibility, thermal conductivity and gamma ray attenuation. Details on drilling depths and core recovery are detailed in the Datasets section of chapter 6.

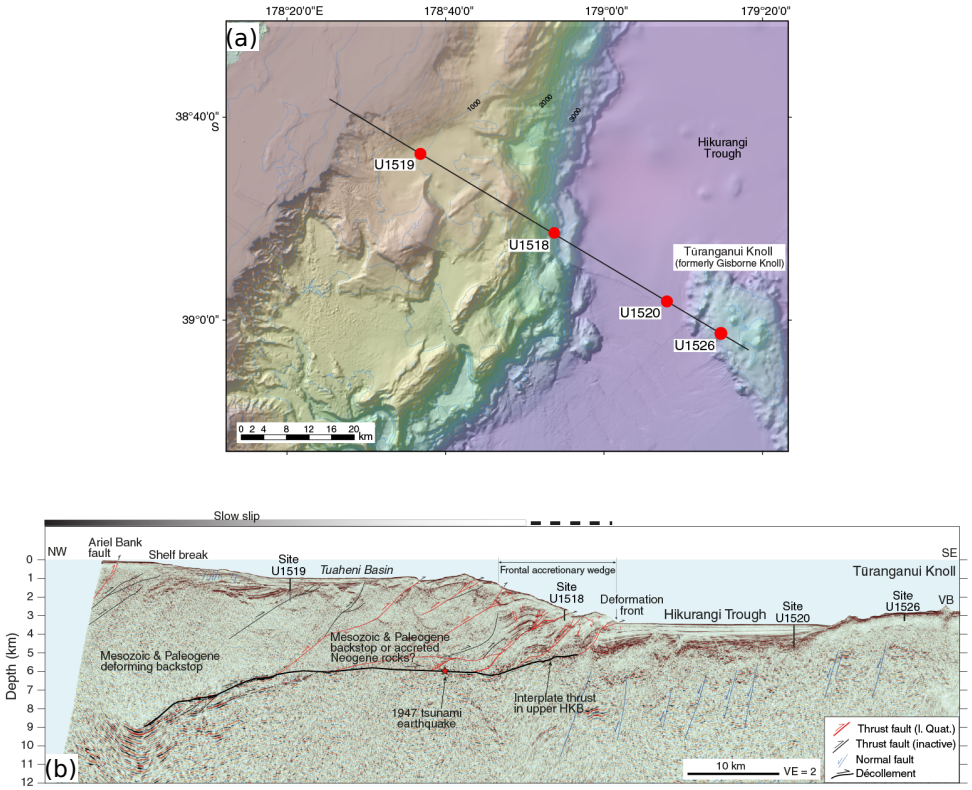


Figure 3.21: (a) shows the location of the IODP drill sites on a bathymetry map of the area. Black line represents line 05CM-04. (b) shows the locations and depths of the same drilling sites on a depth converted seismic image of line 05CM-04. Structurat interpretation is modified from Barker et al. (2018), star represents the projected location of the March 1947 tsunami earthquake. VB = volcanic cone and VE = vertical exaggeration. Figures from Wallace et al. (2019)

By using these direct measurements of physical properties, various relationships could be derived which could be used to transform the final Vp FWI model. Relationships include:

- Velocity vs depth of undeformed sediment on the incoming plate.
- Porosity-density relationships.
- Porosity-velocity relationships.
- Vp-Vs relationships.

These relationships can be used to transform the P-wave velocity model derived using FWI into models of:

- Velocity difference between deformed sediment in the wedge and undeformed sediment in the Hikurangi Trough.
- Porosity.
- S-wave velocity.
- Vp/Vs.
- Bulk modulus.
- Shear modulus.

These transformed models can give insight into the various physical properties at high resolution away from drill sites, and on the overriding plate.Details on how these relationships are derived and applied to the FWI model are described thoroughly in the methods section of chapter 6.

Chapter 4

Imaging the shallow subsurface structure of the Hikurangi subduction zone, New Zealand, using 2D Full-Waveform Inversion

Gray, M., Bell, R.E., Morgan, J.V., Henrys, S., Barker, D.H.N., and the IODP Expedition 372 and 375 science parties.

Journal of Geophysical Research: Solid Earth.

doi:10.1029/2019JB017793 Manuscript Received 3 April 2019, Revised Manuscript Received 18 July 2019, Manuscript Accepted 27 July 2019

4.1 Abstract

The northern Hikurangi plate boundary fault hosts a range of seismic behaviours, of which the physical mechanisms controlling seismicity are poorly understood, but often related to high pore fluid pressures and conditionally stable frictional conditions. Using 2D marine seismic streamer data, we employ full-waveform inversion (FWI) to obtain a high-resolution 2D P-wave velocity model across the Hikurangi margin down to depths of ∼2 km. The validity of the FWI velocity model is investigated through comparison with the pre-stack depth migrated seismic reflection image, sonic well data, and the match between observed and synthetic waveforms. Our model reveals the shallow structure of the overriding plate, including the fault plumbing system above the zone of SSEs to theoretical resolution of a half seismic wavelength. We find that the hanging walls of thrust faults often have substantially higher velocities than footwalls, consistent with higher compaction. In some cases, intra-wedge faults identified

from reflection data are associated with low-velocity anomalies, which may suggest they are high-porosity zones acting as conduits for fluid flow. The continuity of velocity structure away from IODP drill site U1520 suggests that lithological variations in the incoming sedimentary stratigraphy observed at this site continue to the deformation front and are likely important in controlling seismic behaviour. This investigation provides a high-resolution insight into the shallow parts of subduction zones, which shows promise for the extension of modelling to 3D using a recently-acquired, longer-offset, seismic dataset.

Key Points:

- Full-waveform inversion was used to produce a high-resolution P-wave velocity model of the upper ∼2km of the north Hikurangi subduction zone.
- Recovered velocities and gradients correlate well with drilled sonic logs, suggesting the details we see in our FWI velocity models are real.
- Velocity changes across faults may relate to compaction and in some cases low-velocities along faults may indicate conduits for fluid flow.

4.2 Introduction

The Hikurangi plate boundary fault offshore the east coast of the North Island, New Zealand, exhibits a range of seismic behaviour ranging from stick-slip to aseismic creep. Perhaps most notably, the north Hikurangi plate boundary fault experiences slow-slip events (SSEs) every 18-24 months, identified using continuous GPS (cGPS) data (Wallace and Beavan, 2010; Wallace et al., 2012, 2016). Recent results from absolute pressure gauges (APGs) offshore indicate that SSEs at north Hikurangi occur at depths as shallow as 2km below the seafloor, and may even propagate to the seafloor in some areas, making them some of the most well-characterized, shallow recorded SSEs worldwide (Wallace et al., 2016). North Hikurangi is therefore an ideal study area for investigating the mechanisms that generate and promote SSEs.

The fact that the Northern Hikurangi margin experiences such regular SSEs has led to speculation about the physical properties at the margin including fluid presence. Some laboratory experiments and numerical models suggest slow slip may be more likely to occur when pore pressures reach near-lithostatic levels (Audet et al., 2010; Liu and Rice, 2005, 2007; Shibazaki and Iio, 2003; Song et al., 2009). This view is supported by evidence in seismic data for the presence of fluids at several margins where slow-slip occurs, for example at Nankai (Bangs et al., 2009; Kamei et al., 2012; Tobin and Saffer, 2009), Costa Rica (Bangs et al., 2014; Saffer, 2003; Sahling et al., 2008) and Cascadia (Rogers and Dragert, 2003; Wech et al., 2009). We might therefore expect a complex fault plumbing system at the margin above regions where slow-slip is known to occur.

Reflection seismic data acquired across subduction zones provides information on impedance contrasts (the product of velocity and density) between subsurface layers. Fluid presence has previously been

interpreted within plate boundary zones or within splay faults on the basis of polarity reversals and brightness of reflections observed from seismic sections (Bangs et al., 1999; Bell et al., 2014; Rondenay et al., 2008), however, these observations are in-direct indicators of fluids. Alternatively, it has been suggested that variations in frictional behaviour are required to promote SSEs (Ikari and Saffer, 2011). A mixture of rheology, potentially caused by very heterogeneous lithology within the fault zone or within the incoming section could be one mechanism to produce such conditionally frictionally stable conditions (Fagereng and Sibson, 2010). Recovering physical properties at high resolution at the margin could provide insight into fault mechanisms, fluid presence and incoming lithology at the margin, which may all potentially affect seismicity. Drilling data are also required to develop relationships between rock properties and elastic properties at drill sites to further understand the relationships between physical properties and seismicity at the margin.

At northern Hikurangi, Bell et al. (2010) have suggested that high-amplitude reflections in the zone of maximum cumulative slow slip since 2002 could indicate fluid presence and potentially high fluid pressure. However, this interpretation is solely based on the high-amplitude of reflections at depth, which may also be caused by lithological variations. Regional earthquake tomography at Hikurangi, including Vp/Vs ratios (Eberhart-Phillips and Chadwick, 2002), provide low-resolution models of physical properties (grid spacing >10 km offshore). Barker et al. (2018) have developed a velocity model by conducting pre-stack depth migration (PSDM) across the margin and concluded that wavespeeds in the zone of high-amplitude reflections are 7% lower than the surrounding strata. This finding supports the interpretation of high fluid pressures within subducting sediments, which may facilitate SSEs at northern Hikurangi; however, the presence of a low-velocity lithology within the fault zone cannot be yet ruled out. Recently, two International Ocean Discovery Program IODP Expeditions 372 and 375 have collected logging while drilling (LWD) and wireline data, as well as core samples from four drill sites across the margin (Fig. 4.1) (Pecher et al., 2019; Wallace et al., 2019), which provide direct-constraints on physical properties. However, these data are limited in depth to 750 metres below seafloor (mbsf) for the LWD data, 946 mbsf for the wireline and 1054 mbsf for the core data, but they provide an insight into the velocity structure, porosity and fluid properties at isolated locations.

Full-Waveform Inversion (FWI) is an imaging technique which uses waveforms beyond first arrivals to create a detailed model of a selected physical property of the subsurface. Models produced by FWI are able to recover subsurface physical properties to approximately half the seismic wavelength (Virieux and Operto, 2009), and can thus be used to image fine-scale geological features with a higher-resolution than traditional tomographic models (for example, for rock with velocity ∼2200 m/s using our inversion strategy we would be able to resolve features measuring ∼140 m). FWI is often used to recover P-wave velocities, and has previously been successfully applied to seismic data acquired across the central Nankai subduction zone in Japan, revealing a continuous low-velocity zone that was interpreted as a potential fluid conduit associated with the megasplay fault system (Kamei et al., 2012).

Using 2D marine seismic data along line 05CM-04 (Fig. 4.1), recorded on a 12-km streamer, we employ

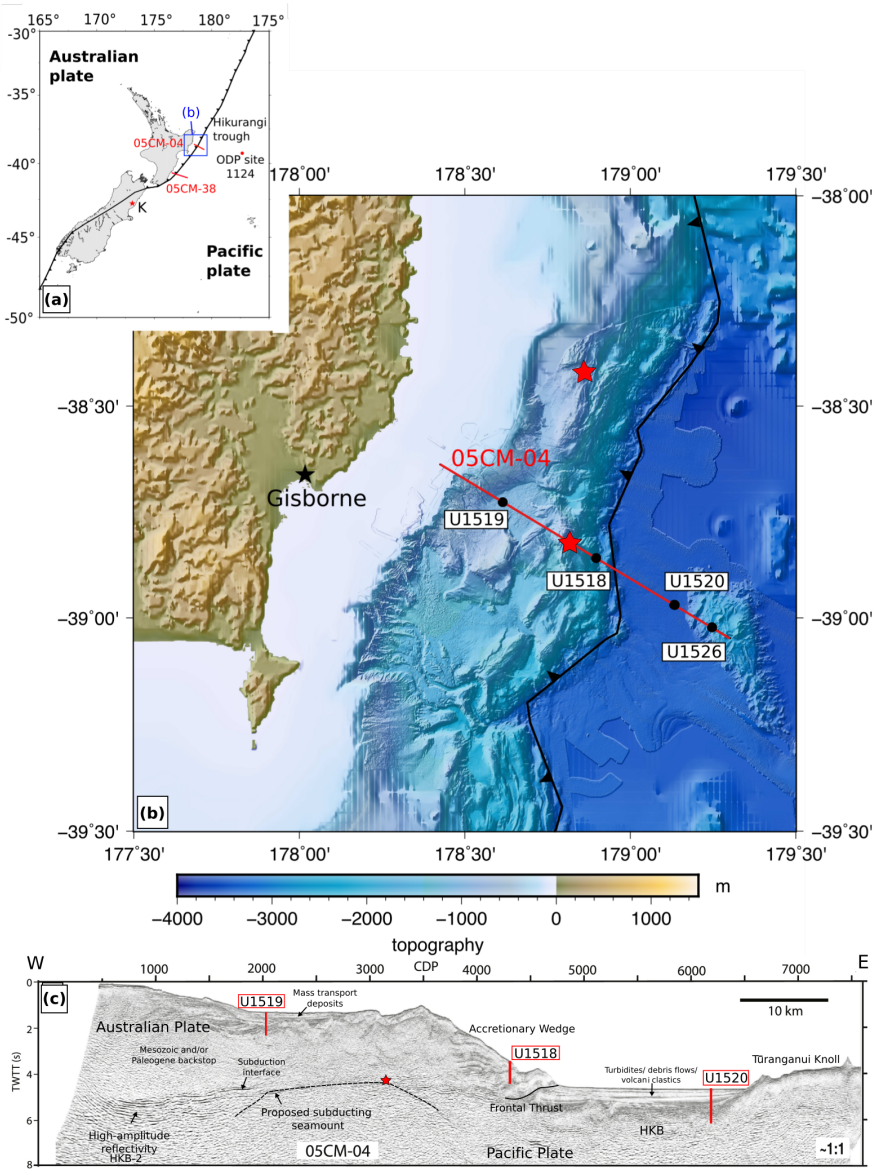


Figure 4.1: (a) Regional map of New Zealand showing plate boundaries. Red lines show the 2D multichannel seismic lines 05CM-04 (used in this study) and 05CM-38 (Barker et al., 2009). The blue box shows the location of (b), the larger map, in which the colour scale is offshore bathymetry across the Hikurangi margin, based on 25-m gridded swath data. The black dots represent the drill sites, where borehole velocity measurements were taken on IODP Expedition 372 at U1519, U1518 and U1520. The red stars show the location of the 1947 Offshore Poverty Bay (along line 05CM-04) and Tolaga Bay tsunami earthquakes (Bell et al., 2014).(c) Reflection seismic section of 2D line 05CM-04. The dashed line shows the location of the proposed subducting seamount from Bell et al., (2014) based on magnetic data, and the red star shows the location of the March 1947 tsunami earthquake event offshore Poverty Bay. The red lines represent three IODP drill sites. The different lithology types based on interpretations from the literature are shown as well as the location of the frontal thrust in the near surface, the variable reflectivity of the subduction interface, and the Tūranganui Knolls. After Bell et al. (2014)

FWI to obtain a high-resolution 2D P-wave velocity model of the subsurface across the north Hikurangi subduction zone. Paraxial ray-tracing shows that the refracted part of the input wavefield, which FWI principally utilizes, does not travel through the subducting slab (see section 4.5.2), so we cannot accurately resolve velocity structure across the plate boundary fault within the area of confirmed slow slip at a depth of 2000 mbsf (Fig. 4.1(c)) (Wallace et al., 2016) . Here, we use FWI to image the overriding plate above the plate boundary fault, including the fault plumbing system above the zone of SSEs, and provide constraints on the fault structure, and lithological nature of incoming rocks, which may influence seismic behaviour. This study also provides a framework for the future application of 3D FWI to recently-acquired, longer-offset, seismic data to recover high-resolution physical properties in zones of slow slip directly.

4.3 Geological Setting

The Hikurangi subduction margin is located along the east coast of the North Island, New Zealand where the Pacific Plate is subducting obliquely below the Australian Plate at a rate of between <30mm/yr and ∼60mm/yr, with a rate of ∼55mm/yr offshore the town of Gisborne (Barker et al., 2009; Walcott, 1987b; Wallace et al., 2004) (Fig 4.1). The margin exhibits a variety of seismic behaviour and seismic reflection and bathymetry data reveal that the northern Hikurangi margin is characterised by the subduction of seamounts and extensive splay-faulting. In this section the seismic behaviour of the margin and geology of the accretionary wedge and incoming sedimentary section are discussed.

4.3.1 Seismic character of the north Hikurangi margin and seamount subduction

The Hikurangi subduction plate boundary fault has experienced limited historically-recorded large-scale interplate seismicity over the last two hundred years. Some of the largest historically known Hikurangi plate boundary fault rupturing earthquakes occurred in March and May 1947 (Bell et al., 2014, 2010; Doser and Webb, 2003; Hamling et al., 2017). These earthquakes had Moment magnitudes of Mw 6.9-7.1, but local magnitudes of only ML 5.6 and 5.9, and caused abnormally large tsunami compared to other earthquakes at comparable depth and magnitude (run-up heights up to 10 m) (Bell et al., 2014; Downes, 2001); events such as these have previously been termed tsunami earthquakes and are inferred to have long rise times compared to other earthquakes (Kanamori, 1972). Tsunami earthquakes have been linked to regions of conditional frictional stability, possibly associated with high fluid pressures (Bell et al., 2010; Bilek and Lay, 2002; Scholz and Small, 1997; Seno, 2002).

Geodetic data reveal that the Hikurangi margin hosts a range of slow slip events (SSEs). SSEs are defined as episodic events causing ∼10s of centimetres of slip over timescales of days to months; too slow to generate seismic waves yet faster than the rate of plate boundary displacement (Bartlow et al., 2014; Wallace et al., 2014, 2012, 2016). Continuous GPS data have shown that the Hikurangi plate-boundary

fault experiences both deep and shallow SSEs, (Bell et al., 2010; Douglas et al., 2005; McCaffrey et al., 2008; Wallace and Beavan, 2006, 2010; Wallace et al., 2009, 2016). SSEs at the northern Hikurangi margin, offshore Gisborne, are generally shallow (<2-15 km below seafloor) and occur every 18 to 24 months (Wallace et al., 2016). The updip extent of these SSEs has been poorly constrained by the land-based cGPS observations, but the recent addition of data from offshore APGs has produced direct evidence for events extending to within 2 km of the sea floor, and possibly extending all the way to the trench (Wallace et al., 2016). These shallow SSEs accommodate slip equivalent to that in an earthquake with moment magnitude of ∼6.3-6.8 Mw and typically result in 1-3 cm of horizontal surface displacement over 1 to 2 weeks (Wallace et al., 2004, 2009; Wallace and Beavan, 2010; Wallace et al., 2012, 2016). The southern part of the Hikurangi margin experiences larger (∼Mw7.0), longer lasting (>200 days) and deeper (25-60 km depth) SSEs than in the north (Wallace et al., 2004, 2009; Wallace and Beavan, 2010; Wallace et al., 2012, 2016).

Seamount subduction occurs along the Hikurangi margin, with several large seamounts observed both at the sea floor of the incoming plate (eg. Tūranganui Knoll, Fig. 4.1) and subducted, as inferred from seismic reflection and magnetic data along the northern part of the margin (Fig. 4.1(c)), (Barker et al., 2009, 2018; Barnes et al., 2010, 2018; Bell et al., 2010, 2014; Collot et al., 2001; Pedley, 2010). The subduction of seamounts has been proposed to cause extensive faulting and deformation within the upper plate (Dominguez et al., 1998; Wang and Bilek, 2014). Ocean bottom seismometers (OBS) and absolute pressure gauges (APGs) also resolve episodic tremor occurring after SSEs, localized in the vicinity of two subducted seamounts within and up-dip from areas exhibiting SSEs (Todd et al., 2018). Three areas of high-amplitude reflectivity have been identified down-dip of subducted seamounts, and have been interpreted as being the result of entrainment of fluid-rich sediments (Bell et al., 2010). The subduction of seamounts surrounded by trench sediment would also produce large lithology variations within the plate boundary fault zone, which may lead to variable slip mode behaviour (Bell et al., 2010; Bilek et al., 2014; Saffer and Wallace, 2015; Wang and Bilek, 2014). As large amounts of unconsolidated, fluid-rich sediment are entrained by subducting seamounts, and subjected to extensive loading, increased overburden stress may lead to increased pore fluid pressures, if a low permeability seal exists above the plate boundary fault (Ellis et al., 2015). If, however, parts of the plate boundary fault zone are permeable, these fluids, together with fluids sourced from dehydration reactions at depth, will percolate into the overriding plate and potentially also escape along splay faults if they are higher-permeability conduits than the surrounding wedge (Antriasian et al., 2018; Barnes et al., 2010; Lauer and Saffer, 2012; Saffer, 2003; Saffer and Tobin, 2011; Tobin and Saffer, 2009).

4.3.2 Character of the Plate Interface and Accretionary Wedge

The plate interface itself is marked by both low- and high-amplitude reflections, and in places its position is inferred from frontal thrust fault intersections (Fig. 4.1(c)). Seismic reflection data reveal that several large splay faults exist within the accretionary wedge, which sole into the subduction plate boundary

fault (Barker et al., 2009; Barnes and de Lpinay, 1997; Barnes et al., 2010; Ghisetti et al., 2016; Lewis and Pettinga, 1993; Mountjoy and Barnes, 2011; PlazaFaverola et al., 2012, 2016). Splay faults across the Hikurangi margin are primarily north-west dipping and some have large measurable displacements within the frontal wedge (Barnes et al., 2010, 2018; Ghisetti et al., 2016). Fluid flow along splay faults may be expected due to widespread active fluid seepage observed at the seafloor on the crests of thrust-related bathymetric ridges offshore of Hawkes Bay and Wairarapa (Barnes et al., 2010, 2018; Fagereng et al., 2019b; Greinert et al., 2010; PlazaFaverola et al., 2016). PlazaFaverola et al. (2016) conducted a pre-stack depth migration (PSDM) along profile 05CM-38 (Fig., 4.1(a)), ∼220 km to the SW of line 05CM-04, and identified splay faults branching from the decollement associated with high-amplitude reflections, some with polarity reversals, indicating a decrease in acoustic impedance. Velocity analysis by PlazaFaverola et al. (2016) resolved the depth of the subduction interface between ∼7-14 km depth, and showed reduced P-wave velocities below several bright, dipping reflections, which they suggest could indicate the upward flow of fluids. PlazaFaverola et al. (2016) also note a correlation between the zone of maximum cumulative slow slip and the lowermost (∼14 km) level of splay faulting and posit that the presence of overpressured fluid-rich sediment could be related to mechanisms of slow slip. Faults observed in seismic data offshore Gisborne are mostly defined by stratigraphic cut-offs rather than fault plane reflections (e.g. Fig. 4.1(c); Barker et al. (2009, 2018); Bell et al. (2010); PlazaFaverola et al. (2016)), so we cannot use reflection polarity to interpret whether the faults are low acoustic impedance zones here or not. While several instances of fluid seeps have been identified in the region, typically in 700-1200 m water depth on the crests of thrust-faults in the mid-slope, it is yet undetermined whether the faults identified along like 05CM-04 are conduits or seals (Barnes et al., 2010). As the role of fluids at subduction zones may play a key role in determining the seismicity of the interface (Bangs et al., 1999, 2014; Saffer and Wallace, 2015; Tobin and Saffer, 2009), one of the key aims of this study is to determine whether faults offshore Gisborne may be high-porosity, high-permeability fluid conduits.

4.3.3 Incoming Sedimentary Section

The lithology of the material that forms the incoming subducting plate is important, as the plate boundary fault will form somewhere within it when it reaches the deformation front. Lithologies across the margin were previously not well known due to a lack of drilling data, and interpretation of the stratigraphy up until now has been based on comparisons between reflection seismic data and ODP borehole data (Leg 181, wells 1123 and 1124) from east of the trench (Davy et al., 2008). New IODP drilling data (Expeditions 372 and 375) collected in 2017/2018 will provide a much improved understanding of stratigraphy (Pecher et al., 2019; Wallace et al., 2019).

Reports from IODP Expedition 372 and 375 site U1520 have determined six lithostratigraphic units in the incoming section, consisting of turbidites, mass-transport deposits, and hemipelagic muds down to 509.82 mbsf, pelagic carbonate facies from 509.82 848.45 mbsf, volcaniclastics from 848.45 1016.24 mbsf and a blend of volcaniclastics, mudstone, limestone and siltstone down to 1045.75 mbsf (Wallace et al.,

2019). Based on the seismic reflection character, the seaward part of the accretionary wedge is likely to be largely composed of accreted turbidites and pelagic sediments (e.g. Barnes et al. (2017); Fagereng et al. (2019b); Ghisetti et al. (2016). The subducting plate (Hikurangi Plateau) is a ∼10km thick, buoyant Large Igneous Province (LIP) that includes large seamounts and other volcanic features (Carter et al., 2002; Davy and Wood, 1994; Davy et al., 2008; Hoernle et al., 2010). The upper seismic sequence (HKB, Fig. 4.1c) has been interpreted as reflective volcaniclastics and other Cretaceous sedimentary rocks (Wallace et al., 2019). Based on seismic and magnetic data (Barker et al., 2018; Davy et al., 2008), the underlying plateau basement is thought to comprise a higher velocity igneous layer.

4.4 Datasets

Fig. 4.1 shows the location of the 2D marine seismic profile used in this study, acquired in May 2005 as part of the 05CM survey (Barker et al., 2009; Multiwave, 2005). Line 05CM-04 is 90-km long and was collected by Multiwave Geophysical aboard the MV Pacific Titan, using a 12-km-long streamer with 960 channels spaced 12.5 m apart. Data were recorded to 12s TWT and with a shot spacing of 37.5m. The reflection seismic section is shown in Fig. 4.1(c) (Bell et al., 2014), pre-stack depth migration (PDSM) velocity image of profile 05CM-04 is shown in Fig. 4.4(a) (Barker et al., 2018), and two example shot gathers from this dataset are shown in Fig. 4.4 (b) and (c).

In 2017-2018 IODP drilled four sites along line 05CM-04 (Fig. 4.1) during Expeditions 372 and 375 (Pecher et al., 2019; Wallace et al., 2019). These expeditions collected LWD, wireline (U1520 only) and core data within the accretionary prism and trench (Fig. 4.1(c)). In this study sonic logs recorded in these expeditions will be compared with our FWI velocity models. LWD sonic data was recorded to a depth of 590.4 mbsf in U1519, 564.9 mbsf in U1518, and 714.6 mbsf in U1520. In U1520 open hole wireline sonic logs were also recorded down to 947 mbsf.

4.5 Method and data analysis

We use FWI as it has the potential to produce high-resolution models of any physical property that influences the seismic wavefield (Pratt, 1999; Sirgue et al., 2010; Tarantola, 1984; Virieux and Operto, 2009; Warner et al., 2013). In practice, in most commercial applications, a robust model of P-wave velocity is recovered using three-dimensional acoustic, anisotropic FWI codes (Sirgue and Pratt, 2004; Warner et al., 2013). Although, accurate modelling of the seismic wavefield requires a three-dimensional elastic code that can account for changes in S-wave velocity, anisotropy, density and attenuation, this is normally prohibitively computationally expensive. In addition, the amplitudes of individual arrivals are sensitive to several physical properties, so multi-parameter inversions tend to be less robust due to cross-talk between individual parameters (Sirgue and Pratt, 2004; Virieux and Operto, 2009). In the inversions shown here, we have normalized amplitudes between different time slices using stabilized amplitude matching that varies smoothly and slowly in both space and time independently for both

observed and predicted data, and we have balanced trace amplitudes between predicted and observed data using a scheme that is sensitive to the similarity between the two datasets, and that is also stabilized and varies smoothly in space (Warner et al., 2013). This largely, but not completely, mitigates for amplitude changes that are related to attenuation, density, elasticity and short-wavelength changes in anisotropy, while largely, but not completely, retaining those amplitude affects that are related directly to the P-wave velocity model. Apart from applications focused on imaging the reservoir and drilling hazards in petroleum exploration, FWI has also been used to resolve the P-wave velocity structure of crustal-scale targets in a range of tectonic settings, including subduction zones (Calvert et al., 2011; Christeson et al., 2012; Kamei et al., 2012; Morgan et al., 2011).

Here we use a 2D version of the 3D Imperial College time-domain code (Warner et al., 2013)). The code uses both velocity and density contrasts to produce reflections, and the two models are coupled together using Gardners law to estimate density from Vp. We utilise the acoustic approximation of the wavefield, since there are no a priori constraints on anisotropy, S-wave velocity, attenuation or density. Given this approximation, we can expect there to be some inaccuracies in the recovered P-wave model; for example, if anisotropy is not accounted for, FWI velocity models are stretched and the depths inaccurate. This was observed in the recent drilling of the Chicxulub impact crater, where FWI-determined (sub-horizontal) velocities obtained prior to drilling (Morgan et al., 2011) led to an overestimate in the vertical velocity within the sedimentary overburden and corresponding depth to the crater (Christeson et al., 2018).

In FWI a source wavelet is propagated through a starting P-wave velocity model, $\mathbf{m}$, to obtain a predicted seismic dataset, $\mathbf{p}$:

$$\mathbf{G}(\mathbf{m}) = \mathbf{p} \tag{4.1}$$

Where $\mathbf{G}$ describes a function, which calculates the seismic data given the model. A residual dataset is calculated by taking the difference between $\mathbf{p}$ and the acquired field dataset $\mathbf{d}$, and this residual dataset is then back-propagated through the model. A cross-correlation between the forward and back-propagated wavefields is computed in time at every point in the model, $\mathbf{m}$, to produce a gradient for each source. Stacking these gradients together produces a global gradient, which is used to update the model, m. These steps are repeated and the starting velocity model is iteratively updated via a sequence of linearised local inversions to solve the equation:

$$\mathbf{G}^{-1}(\mathbf{d}) = \mathbf{m}' \tag{4.2}$$

Where $\mathbf{m}'$ is the final model of the subsurface at the point when the misfit, or the sum of the squares of the residual dataset, is minimised, and model updates become small (Asnaashari et al., 2013; Tarantola, 1984; Warner et al., 2013).

The FWI workflow adopted here follows Warner et al. (2013) and involves the following steps, which will be discussed in more detail below:

i. The dataset was preprocessed in preparation for FWI;

ii. A source wavelet was generated;

iii. A starting velocity model was selected;

iv. The adequacy of the source wavelet and starting velocity model were quality checked by comparing the observed and predicted data;

v. Inversion strategies were tested and an inversion scheme selected;

vi. The dataset was inverted using the selected inversion scheme, with regular quality assurance to check for cycle skipping.

Steps v and vi are particularly important in order to avoid cycle skipping in the inversion (Asnaashari et al., 2013; Pratt, 1999; Tarantola, 1984; Warner et al., 2013). Cycle skipping occurs when arrivals within the synthetic and real datasets differ by more than half a cycle, causing the velocity model to converge to a local rather than global minimum (Sirgue et al., 2010; Tarantola, 1984; Virieux and Operto, 2009). Ideally, to mitigate this problem FWI should start at low frequencies, since the travel times are easier to match within half a cycle for larger periods. The inclusion of lower-frequency data in the inversions leads to improvement in the long-wavelength velocity structure, and the maximum frequency of the input data can then be gradually increased to introduce the finer-scale structure. As frequencies are increased, however, so too do computational costs due to the necessity of finer grids and smaller time-steps, so frequencies need to be selected carefully based on the minimum and maximum subsurface velocity structure (Delescluse et al., 2011; Pratt, 1999; Tarantola, 1984; Virieux and Operto, 2009; Warner et al., 2013).

4.5.1 Implementing the workflow

i. The dataset was preprocessed in preparation for FWI.

As noted above, FWI is more likely to be successful when the input data include low- frequency signal. The 2D seismic line used in this study, however, was contaminated with swell noise, as shown in the raw shot gather (Fig. 4.2(a)). As a result of this noise, the lowest usable frequency was determined to be ∼3Hz. A small amount of pre-processing was undertaken to prepare the data for input to FWI. This consisted of F-K filtering to remove tailbuoy noise, and bandpass filtering to limit data to frequencies between 3 and 8 Hz (Fig. 4.2(b)). An additional F-X deconvolution was applied to further reduce swell noise, and this produced a much cleaner dataset (Fig. 4.2(c)). This was applied to all data (see further examples of filtered data in Fig. 4.4(b) and (c)).

ii. Generate a source wavelet

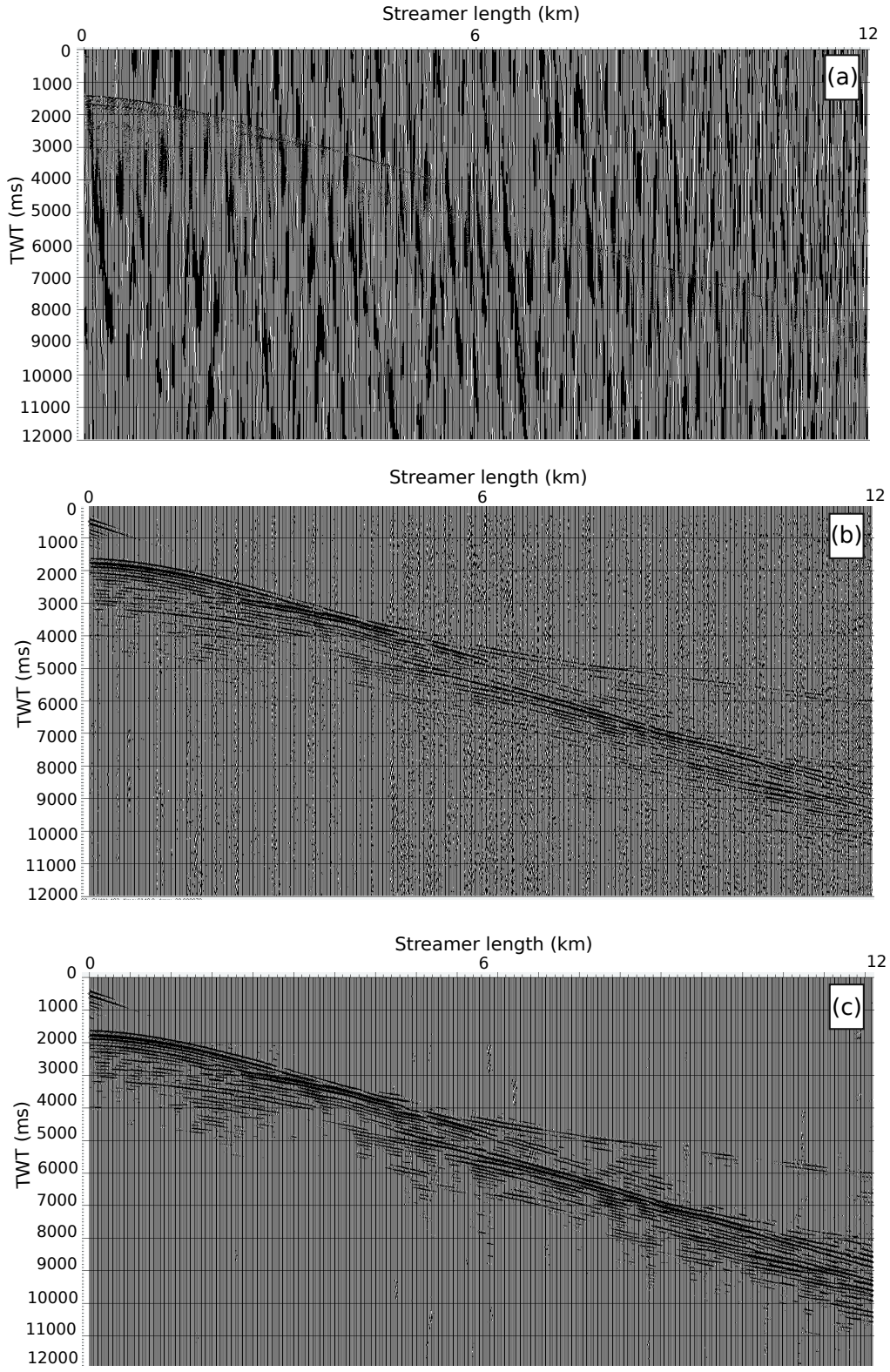


Figure 4.2: (a) Raw shot gather; the data are dominated by swell noise. (b) The same shot gather after bandpass and F-K filters have been applied to remove swell noise. The shot gather is much cleaner, however there is still a large amount of random noise across the gather. (c) The same shot gather after the application of F-X deconvolution to the gather shown in (b). While the data still contain some noisy traces, the majority of swell noise has been removed.

A predicted dataset, $\mathbf{p}_1$, is obtained by propagating an initial source wavelet, $\mathbf{w}_1$, through the starting model. We wish to find a filter, $\mathbf{f}$:

$$\mathbf{p}_1 * \mathbf{f} \approx \mathbf{d} \tag{4.3}$$

where, $\mathbf{d}$, is the field data.

Here, the initial estimate of the source wavelet, $\mathbf{w}_1$, is a spike that has been filtered using the same filters that were applied to the field data (Fig. 4.2(a)). This source wavelet is then propagated though the water column to generate a direct water wave arrival on the streamer (Fig. 4.3(b), left hand trace). The filter, $\mathbf{f}$, is then determined by solving the equation:

$$\mathbf{p}_1 * \mathbf{f} \approx \mathbf{d} \Rightarrow \mathbf{f} = \mathbf{p}_1^{-1} * \mathbf{d} \tag{4.4}$$

For which $\mathbf{d}$ is the observed data at the same location as the predicted (Fig. 4.3(b)).
We then compute:

$$\mathbf{w}_1 * \mathbf{f} = \mathbf{w}_2 \tag{4.5}$$

Where $\mathbf{w}_2$ is the new source (Fig. 4.3(c)), and then $\mathbf{w}_2$ is used to generate the new predicted data, $\mathbf{p}_2$ such that:

$$\mathbf{p}_2 \approx \mathbf{d} \tag{4.6}$$

By comparing the predicted data, $\mathbf{p}_2$, with the observed, $\mathbf{d}$, we can assess the accuracy of the new wavelet $\mathbf{w}_2$. Fig. 4.3(d) shows a side-by-side comparison of 9 traces from a single shot gather with the synthetic data produced using w2 interleaved with the same 9 traces from the field data, up to offsets of 272.5m from the start of the streamer. We can see that the travel-times of the main peaks and troughs in the arriving waveforms match well for both the direct water wave arrival between 200 and 1000 ms and the seafloor reflection, between 1600 and 2200 ms time. The principal difference between traces is the presence of noise within the observed data.

iii. Selecting a starting velocity model

An initial velocity model was provided by Barker et al. (2018) (Fig. 4.4(a)), which was created for a prestack depth migration (PSDM) of the seismic data using Paradigms Geodepth. Prestack time migration (PSTM) velocities and a geological model were used to construct an interval velocity model as a function of depth, which was then iteratively refined through residual velocity analysis

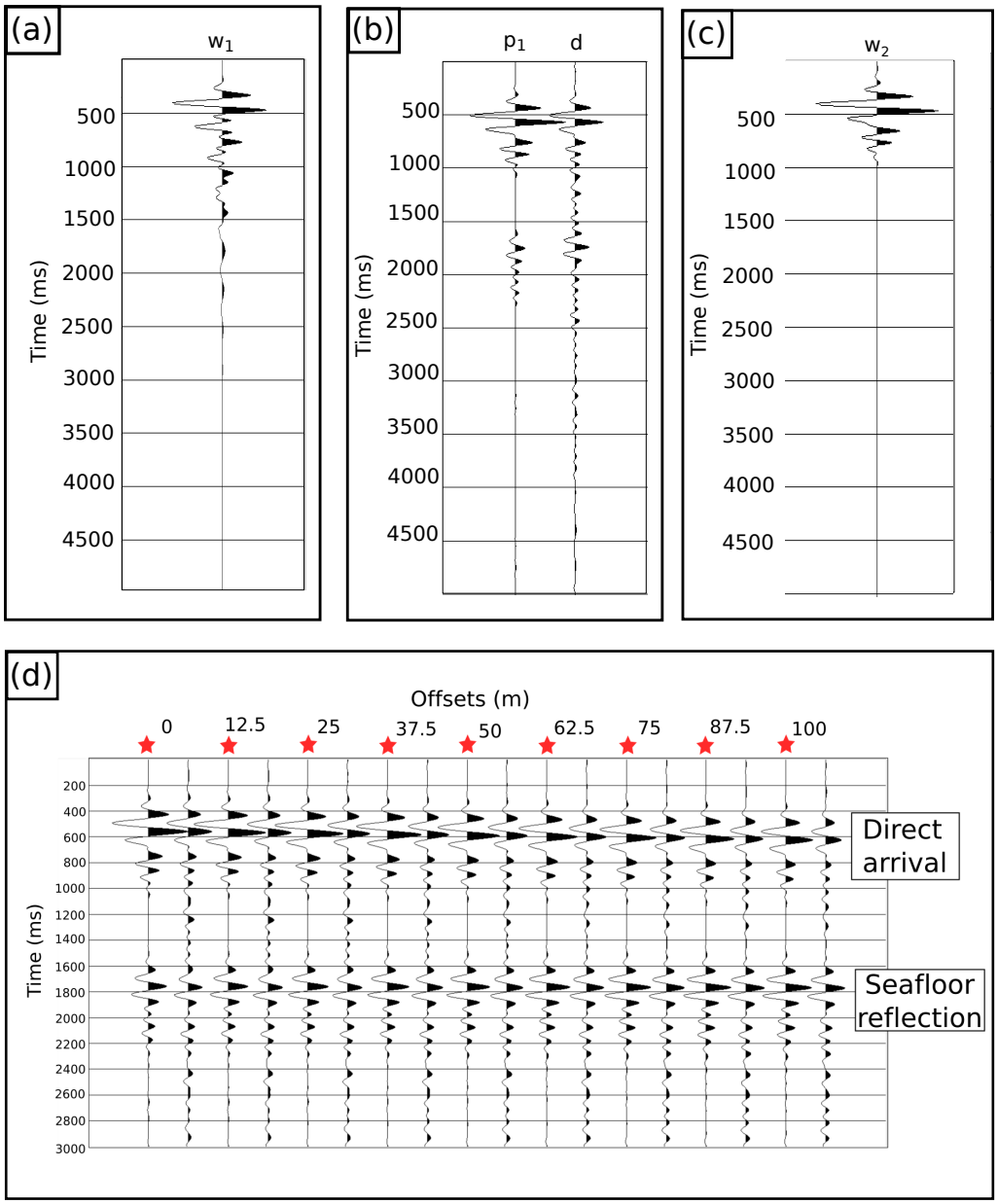


Figure 4.3: (a) The original source wavelet $\mathbf{w}_1$, a bandpass filtered spike (b) The predicted data $\mathbf{p}_1$ on the left, and the same trace from the field data $\mathbf{d}$ on the right. (c) The final source wavelet $\mathbf{w}_2$ after application of the matching filter $\mathbf{f}$ to $\mathbf{w}_1$. (d) Side-by-side comparison of the predicted, $\mathbf{p}_2$ (indicated by a red star), and observed data, $\mathbf{d}$, for a single shot gather of the 2D seismic data used in this study.

and inspection of the PSDM stack and gathers. While this is an effective way to produce a velocity model for reflection imaging (Yilmaz, 2001), the method is dependent on Normal MoveOut (NMO), which is relatively insensitive to velocity, as a range of subsurface velocity structures can be used to stack the same reflections successfully. Prior to use as a starting model for FWI, several changes were made to the PSDM velocity model presented in Barker et al. (2018). First, water velocities that were collected using expendable bathythermographs (XBTs) in the area from the National Oceanic and Atmospheric Administration (NOAA) were used to construct the velocity in the water column. Then the sea-floor was modified to match the bathymetric data collected in the area (Fig. 4.1). Selecting the water velocities and seafloor depths are important factors in completing successful inversions using FWI, so much care was taken in selecting these. Extensive testing of different seafloor depths and ocean velocities using techniques such as NMO analysis and short-offset receiver gathers, and careful determination of how these affected synthetic gathers lead to the final selection of appropriate values for both the seafloor and ocean velocities. Finally, rock velocities below the seabed were smoothed to remove all abrupt changes below the sea-floor except the seabed itself, as FWI is more efficient if only well-constrained boundaries are placed in initial starting models (Morgan et al., 2016).. The modified starting velocity model that is used for FWI in this study is shown in Fig. 4.5(a).

iv. The adequacy of the source wavelet and starting velocity model

The quality of the source wavelet and starting model was investigated by directly comparing predicted seismic data acquired through the model with the field data. The starting model will generate matching waveforms for the direct arrival into the streamer and seafloor reflection if the model for the ocean velocity and seafloor depth is reasonably accurate. We also examined later-arrivals and longer-offset refractions to check whether they are cycle-skipped, and we use this information to determine which data should be input into the initial inversions. Fig. 4.4(b) and 4.4(c) show the field data for two shot gathers, whose locations are indicated on the model in Fig. 4.4(a). Fig. 4.5(b)-(g) shows the interleaved predicted and field data, with 10 traces of synthetic data followed by 10 traces of real data. The synthetic data is shown with a pink overlay.

From Fig. 4.5 we can see that there is a good match between real and synthetic waveforms for both the direct arrival and the seafloor reflection out to about 5-km offset. We can also see the waveforms align well for the first seabed multiple (at ∼300 ms for shot gather B and ∼10000 ms for C). The match is shown in greater detail in boxes D and F. Boxes D and F both show a continuous reflection across both the real and synthetic data for the direct arrival and seafloor reflection. Boxes E and G, however, highlight the mismatch between the real and synthetic data at longer offsets, as the reflections in the field data and the synthetic data do not align. This match is typical for shot gathers across the margin. This indicates that the sea-floor and water velocities are reasonably accurate, and suitable for use in FWI. The match at greater times and offsets is poorer, as expected, but some seismic phases are seen to match within half a cycle (Fig. 4.5(d),(f)). This indicates that we have selected an appropriate starting velocity model, and that

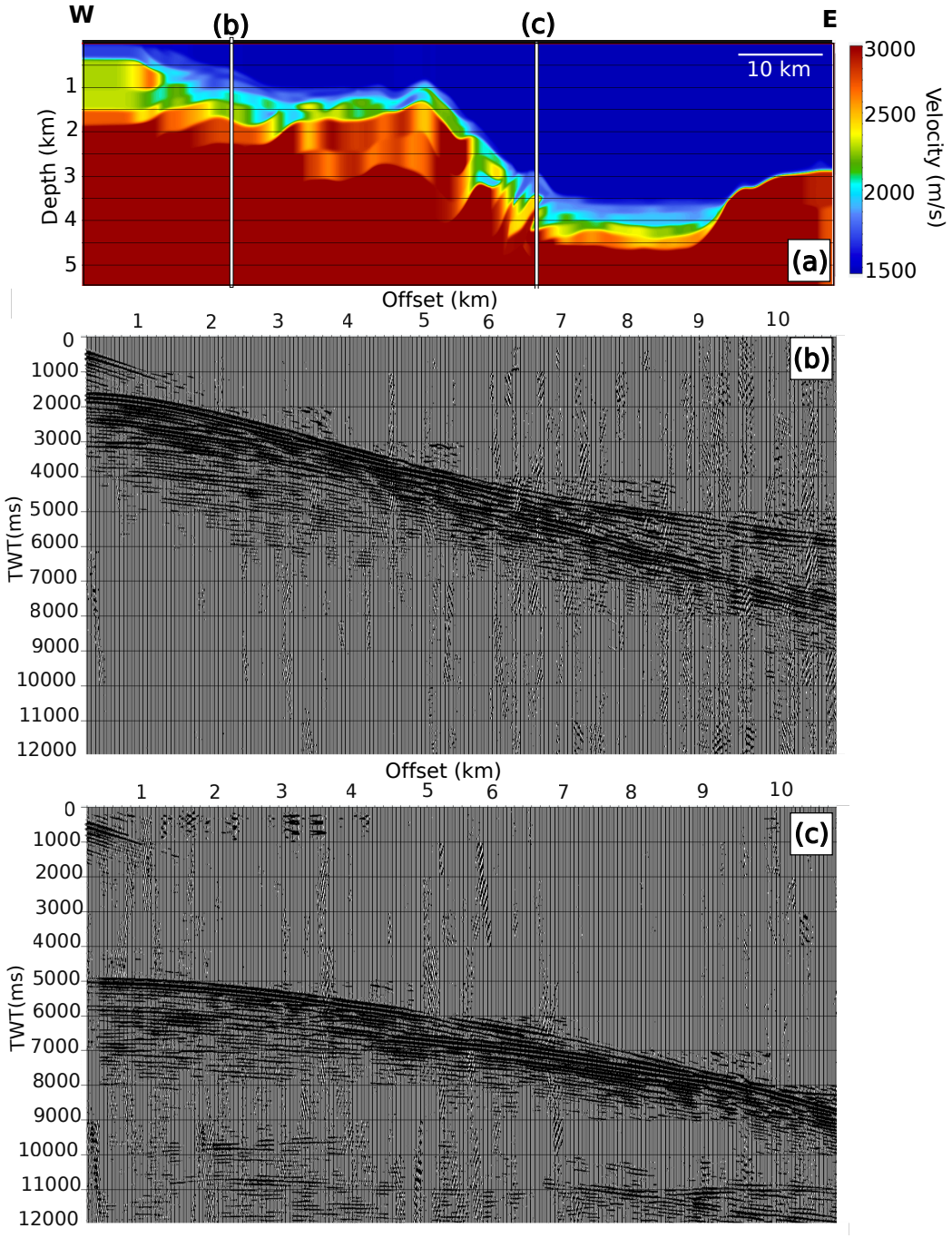


Figure 4.4: (a) PSDM velocity model by Barker et al., (2018). Panels (b) and (c) show filtered shot gathers at the two points labelled on the model.

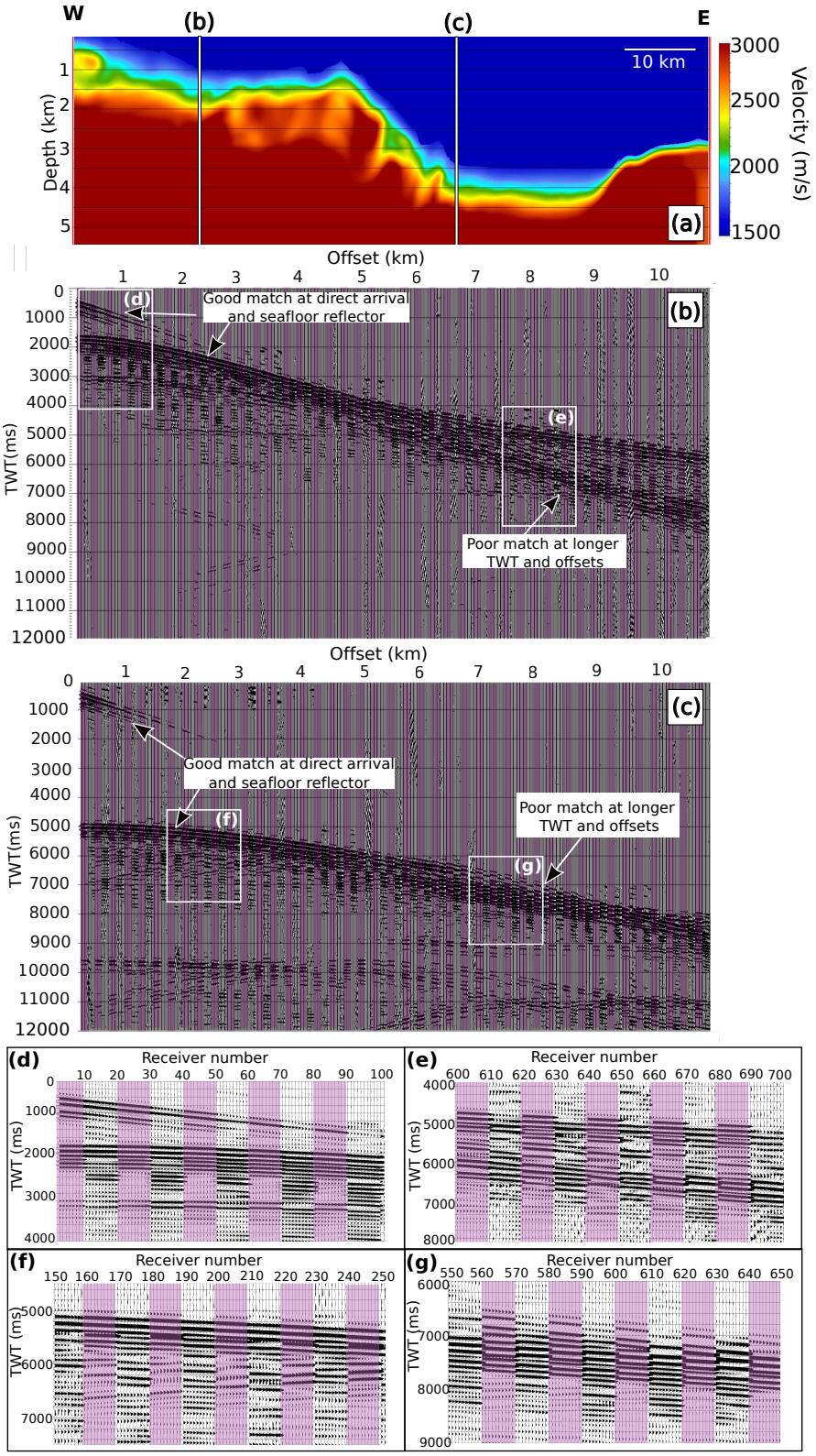


Figure 4.5: (a) Plot of the smoothed PSDM model from Barker et al. (2019) used here as the starting model for full-waveform inversion (FWI). (b) and (c) show the same two shots gathers as in Fig. 4.4, with synthetic data generated using the starting model (highlighted in pink) interleaved with the observed data. The figure shows a good match for both the direct water wave arrivals and seafloor reflections, and a reasonable match for some later arrivals and longer-offset refractions. (d), (e), (f) and (g) show zoomed in plots of data from within the boxes shown in (b) and (c). From these more detailed views, we can see that some of the later arrivals and longer offset data are not well matched and may be cycle skipped.

we can use these comparisons to remove any clearly cycle-skipped data from the inversions. For example, some of the reflections at long offsets appear to be over half a cycle out of phase with the real data (Fig. 4.5(e),(g)). In our adopted inversion scheme cycle-skipped data are excluded from the initial inversions, and more data are added as the match improves to be less than a half-cycle out of phase.

v. Inversion strategies were tested and an inversion scheme selected

A good inversion strategy is important to ensure the majority of the input data are not cycle skipped and the models are slowly improved, with the misfit function converging to a global, rather than a local minimum. Several different inversion tests were undertaken, including using different time windows, frequency windows, and offsets. One of the main issues with FWI is that its specific application is highly dependent on the dataset, and so no individual inversion strategy works for all datasets. Exhaustive testing of this dataset revealed the most effective inversion scheme as outlined below. The chosen inversion scheme is as follows:

Table 4.1: Parameters used in FWI of the dataset.

Property	Value
Inversion type	Time-domain, Isotropic
Total number of sources	2173
Shot spacing (m)	37.5
Maximum number of streamer receivers per composite source	481
Receiver spacing (m)	12.5
Offset between shot and first receiver (m)	160
Grid size (m)	12.5
Time sampling rate (ms)	1
Maximum frequency in each frequency block	3.0, 3.4, 3.9, 4.5, 5.2, 6.0, 7.0, 8.0
Iterations per frequency	20

A two-second window was applied to the data using mutes to remove the direct water wave, noise above the first arrivals from the sea-floor and later arriving multiples and possible S- waves. Multiples are still present in this window, but are included as testing has shown that including multiples and ghosts in the FWI inversion produces reliable and stable results (Warner et al., 2013). The data were inverted in 8 frequency blocks, for which the input data are band-passed using minimum-phase Ormsby filters with 0.1% noise and 1Hz roll-off to remove frequencies higher than a maximum frequency, set to values from 3 to 8 Hz, with 20 iterations for each frequency block (Table 4.1). Frequencies, time sampling and grid size are dependent on each other as the code requires the wavefield to cross <0.5 grid-points per timestep. Velocities within the water column, and the location of the seabed, were kept fixed during the inversion. At these inversion frequencies (up to 8Hz) we can theoretically resolve spatial features ranging from ∼100 m in size at the lowest velocities in the model of ∼1520 m/s to ∼200 m at greater depth where velocities increase to ∼3200

m/s. Each shot was used twice in each iteration block of 20 iterations per frequency, with each iteration using every tenth shot.

Starting with a default number of iterations per frequency, based on previous applications of the code, the dataset is inverted and the misfit is checked to ensure the reduction of the misfit has become minimal. Additional tests are run if this is not the case. If step lengths become very small, the inversion has converged at that frequency, and typically we would then move to higher frequencies. The inversions are run on a cluster of multi-core CPU nodes and take between 3 and 4 days to complete using 25 nodes which each have 8 cores. The inversions were performed using these parameters and repeated three times, starting with offsets up to 6 km (481 streamer receivers per composite shot), then increasing to offset of 7.2 km (576 streamer receivers per composite shot), and finally up to 10.87 km (870 streamer receivers per composite shot). After each inversion block, before adding in longer offsets, the model was smoothed in slowness via a 2D convolutional filter measuring 60 traces horizontally and 60 time samples vertically.

While we have chosen a time-domain acoustic inversion, we are aware that attenuation can produce phase effects. These effects can be important in industrial settings where anisotropy is well constrained and exact depths are important, however, with the 05CM-04 dataset, properly accounting for the dispersive effects of attenuation over the limited bandwidth that we use for FWI will not produce any substantial changes to the model other than minor shifts in absolute depths. These shifts are likely to be similar or smaller in magnitude to those produced by anisotropy which we also have not constrained here.

vi. The dataset was inverted using the selected inversion scheme, with regular quality assurance to check for cycle-skipping

After computing velocity models using the inversion scheme outlined in step vi, the models were checked after each increase in offset using the technique outlined in step iv. This was to ensure that the time differences between arrivals in the field and synthetic data were decreasing, and the synthetic reflections and refractions were aligning with the observed data and not cycle skipped. The performance of the inversions was monitored throughout by regularly comparing the predicted and observed data, to ensure the velocity model was being updated in the right direction. Once it was ensured that the inversions were performing as desired, the final P-wave FWI model was obtained after 160 iterations, and will be discussed in section 4.6.

4.5.2 Raytracing was computed to determine maximum target depths.

As FWI primarily uses transmitted energy in the form of post-critical, horizontally propagating refracted waves and diving waves which allow for better illumination of subsurface velocities (Warner et al., 2010), paraxial ray tracing was computed through a smoothed version of the starting velocity model (Barker et al., 2018; Stockwell and Cohen, 2002). This was carried out to determine the depths of turning rays

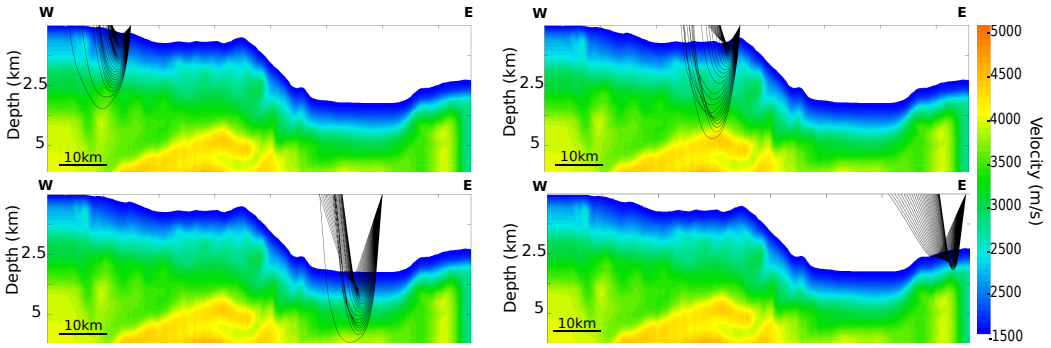


Figure 4.6: Paraxial ray tracing through the starting model at 4 locations along the line. The black lines show the rays being recorded by the 12-km long streamer. There is good ray coverage in the uppermost 1.5-2km of the sub-seafloor, with some rays penetrating down to ∼3.5km depth.

recorded by the 12 km streamer. Results of the ray tracing show good coverage of the subsurface by seismic waves in the uppermost 1.5-2 km of the sub-seafloor, with some rays penetrating down to ∼3.5 km depth (Fig. 4.6). This indicates that we can expect to recover subsurface P-wave velocities up to ∼2000 mbsf, but not from within the subducting slab and not from within the known source area of SSEs at depths of >4000 mbsf. We also do not expect to image the igneous basement of the Hikurangi Plateau (Fig. 4.1). Wider offset data collection is required to image to these deeper depths.

4.6 Results

The final P-wave velocity model recovered with the FWI workflow discussed above is shown in Fig. 4.7(a). Compared to the PSDM velocity model by Barker et al. (2018), which has a layered, blocky appearance (Fig. 4.4(a)), FWI has introduced fine-scale structure within the upper sub-seabed section which appears to be geologically plausible. Close to the edge of the profile up to ∼ 5 km from the model boundaries, and in the deeper parts (>2000 mbsf) of the model, there are curved (ray-path-like) velocity anomalies. These are typical artefacts in areas of poor wavefield coverage and can also be produced by cycle skipping. Hence, below, we focus our discussion on the parts of the velocity model that are likely to be well-constrained, indicated by the white dashed line in Fig. 4.7.

4.6.1 Quality Assurance

4.6.1.1 Comparison with the PSDM Seismic Reflection Image

To investigate whether the recovered velocity anomalies correlate with geological features observed in the PSDM seismic reflection image, we compare them in Fig. 4.7(b). We note that the PSDM reflection

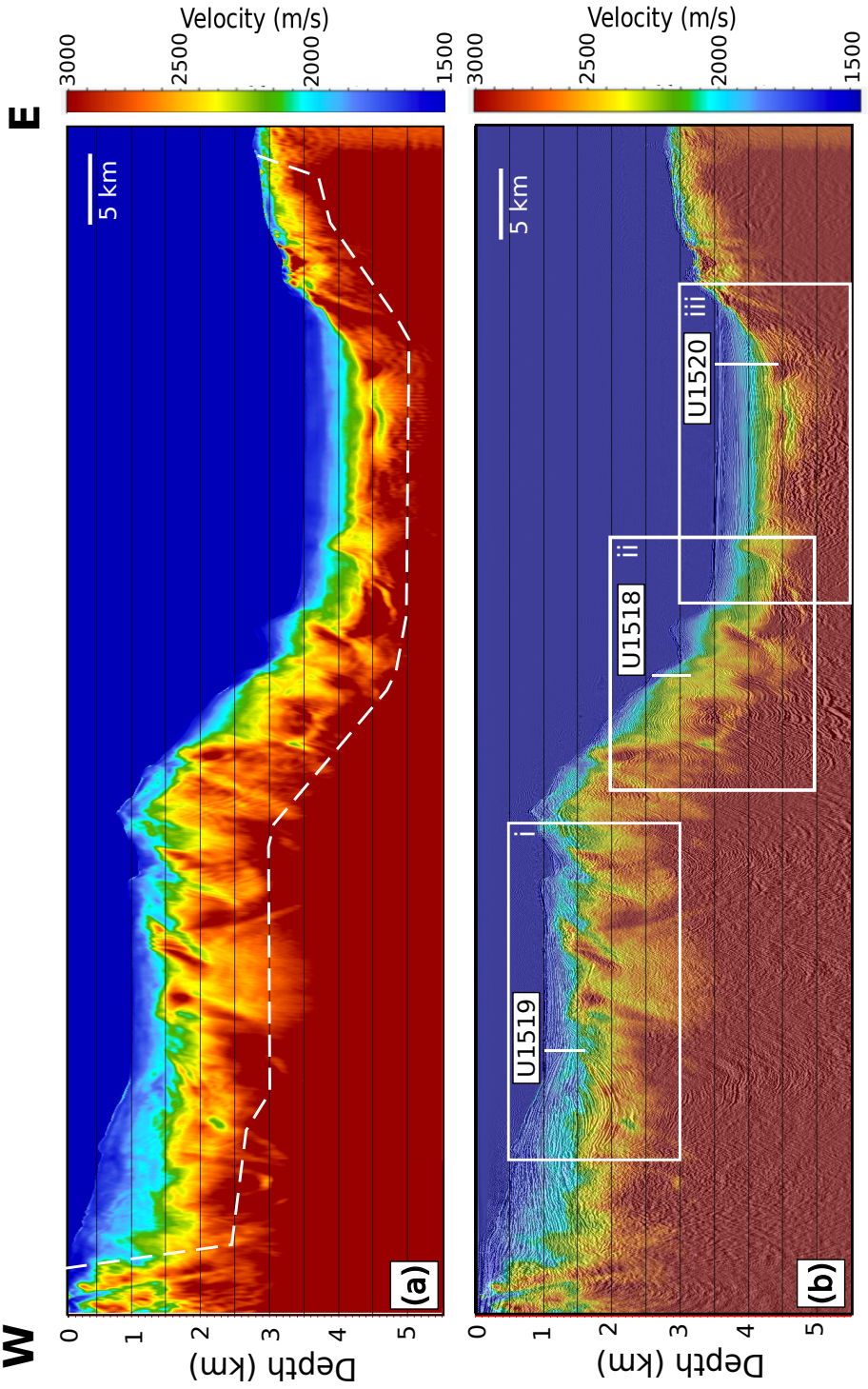


Figure 4.7: (a) Final P-wave velocity model recovered after 160 iterations of FWI. The white dashed line indicates the extent of the model that we consider to be reasonably well constrained: the area below this line is likely to suffer from poor wavefield coverage (b) Final P-wave FWI velocity model overlain on the PSDM seismic image from Barker et al. (2018). Three areas of interest, i, ii and ii have been highlighted for discussion in the text. Thin white vertical lines show the location of three drill holes (U1519, U1518 and U1520) where LWD and wireline (U1520 only) data were collected during IODP Expeditions 372 and 375 (Pecher et al., 2018; Wallace et al., 2019)

stack was processed with a different velocity model (the unsmoothed starting velocity model in Fig. 4.4(a))), so we do not expect perfect alignment between reflections and changes in the FWI velocity model. The velocity model will be smoother than the reflection section because the former contains wavelengths corresponding only to frequencies up to 8 Hz while the latter is at full bandwidth. In addition, the reflection section represents the vertical differential of the perfect velocity model, and differentiation enhances the shorter wavelengths so that reflections sections are always rougher/sharper than their corresponding velocity models even when their nominal bandwidths are the same. Finally, as the FWI is isotropic (Table 4.1), any anisotropy in the subsurface will not be accounted for, which means that we also expect to see an offset in depth between individual reflections, which are more sensitive to changes in vertical velocity, and the velocity anomalies recovered by FWI, which are more sensitive to the horizontal velocity structure (Bentham et al., 2018; Christeson et al., 2018). All of these points mean that we expect the dips and depths of reflectors in the PSDM, to be slightly offset and more smoothed in the FWI velocity model. Fig. 4.7(b) shows that features in the velocity model often do correlate quite closely with features that can be interpreted from the reflection image. For example, many abrupt velocity changes align with high-amplitude reflections in the seismic section. To investigate the relationship between the two models further, we have selected three areas of particular interest labelled i, ii and iii in Fig. 4.7(b), which will be discussed in section 4.6.2.

4.6.1.2 Comparison of Real Data with Synthetic Shot Gathers

As outlined in section 4.5.1, the final step (step vii) in the development of a FWI velocity model is to determine the fit of the model by comparing synthetic waveforms produced by propagating the source wavelet (Fig. 4.3(c)), through the final P-wave velocity model (Fig. 4.7(a)), with the real field data (e.g. Fig. 4.2(c), 4(b), (c)). In Fig. 4.5 we saw that the match between synthetic data and field data was good for the direct arrival and seafloor reflection. In Fig. 4.8 we see comparisons between the synthetic data generated using the final model at the same points (b) and (c) shown in Figs. 4.4 and 4.5, with 10 traces of the real seismic data interleaved with 10 traces of synthetic data through the final model, highlighted in pink. We see in both shot locations, the two datasets match well at longer streamer offsets and later travel times compared to the starting model, no longer just for the seafloor reflection. The synthetic and observed traces for many sub-critical reflections and refractions are now aligned, notably, in boxes (d), (e), (f) and (g), which show zoom-ins of the shot gathers shown in (b) and (c). By comparing Figs. 4.5(e) and (g) with Figs. 4.8(e) and (g), a significant improvement to the match of the reflections across the two datasets can be seen. Comparisons show that most of the data are no longer shifted by over half a cycle, instead we can follow the data across continuous reflections, and this is true for shot gathers across the entire model. The comparison of Figs. 4.8 and 4.5 reveals that the final FWI model provides a better fit to the real seismic data than the smoothed starting model. The overall improvement in fit between the observed and synthetic waveforms suggests that the recovered FWI velocity structure is real.

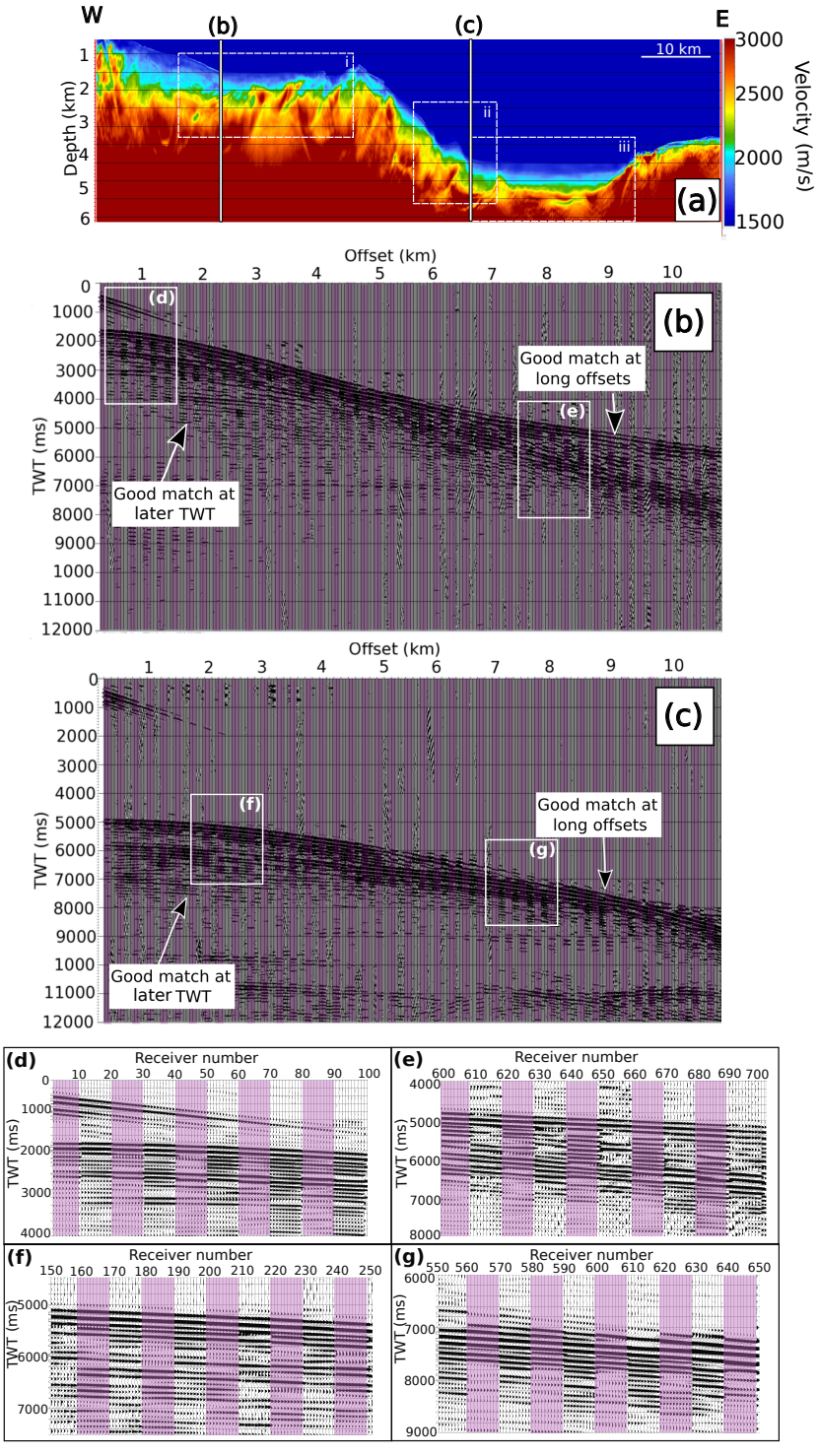


Figure 4.8: (a) The final P-wave velocity model produced by FWI. (b) and (c) show the same two shots gathers as Figure 4.5, with the observed and synthetic data interleaved. In this figure the synthetic data (highlighted in pink) are generated using the final FWI velocity model shown in (a). (d), (e), (f) and (g) show zoomed in plots of data from within the boxes shown in (b) and (c), at the same streamer positions as in Figure 4.5. These plots show that there is an improvement in the match between the synthetic and observed data, in comparison to the synthetics shown in Figure 4.5.

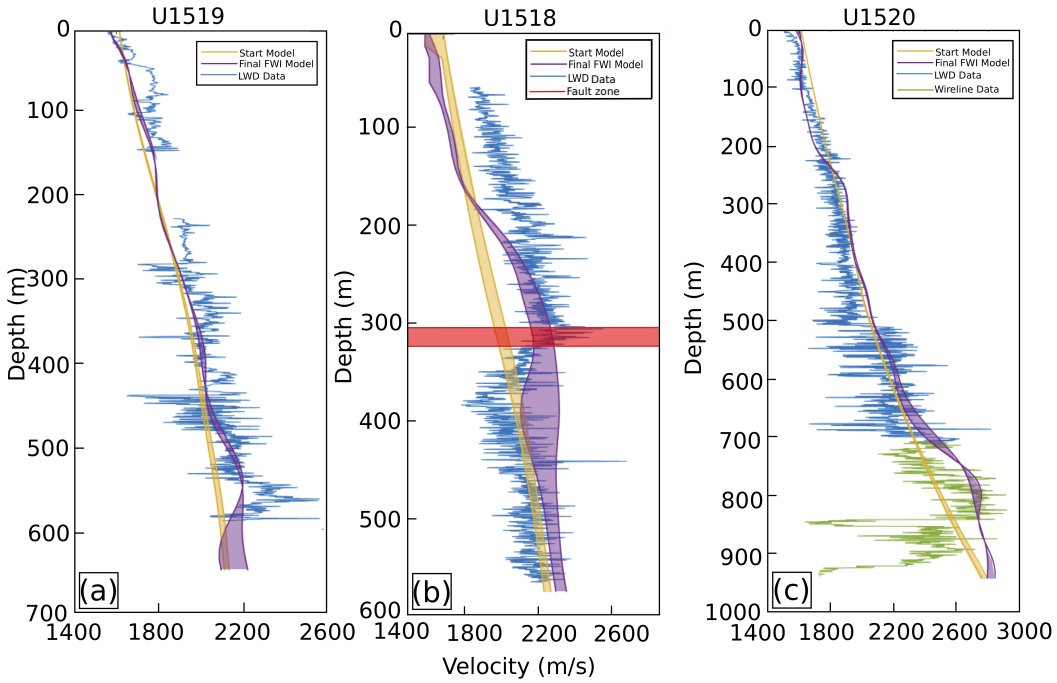


Figure 4.9: P-wave velocity at the IODP Expedition 372 drill sites: (a) 1519; (b)1518; and (c) 1520. Blue lines show LWD data, green line shows wireline data collected at 1520 on Expedition 375. Yellow and purple lines are the velocities through the starting and FWI velocity models, within a region that extends 100 m either side of the drill site. Red rectangle in B shows the location of the fault identified in Pecher et al. (2019).

4.6.1.3 Comparison with LWD and wireline Sonic Logs

LWD and wireline sonic P-wave velocity data are available along seismic line 05CM-04 from three drill sites U1519, U1518 and U1520 (Fig. 4.1). The LWD and wireline tools sample the <1000 mbsf every 0.5ft (0.124m), and the results were compared to the P-wave velocities predicted by the starting model (Fig. 4.5(a)) and the final FWI model (Fig. 4.7(a)).

In general, at all three locations, the final FWI model shows an improvement over the smoothed starting velocity model, with the velocities predicted by FWI showing a closer match to the average velocities and incorporation some velocity variations recorded in the LWD and wireline data (Fig. 4.9). An exception is in the shallow part of site U1518 where the final model is not as close to the well data as the starting model until ∼180 mbsf. We take an envelope of velocities from the models, spanning 100 m either side of each drill site. At site U1519, the predicted velocities from the final FWI model match well on average throughout the logged section, however slightly underestimates the velocities between ∼50-300 mbsf (Fig. 4.9(a)). The final FWI model also detects a velocity inversion shown by the logs at a depth of ∼580 mbsf, which is not shown in the starting model, but does not detect the small velocity inversion between ∼330-340mbsf nor at ∼500-510mbsf. At site U1518, the final FWI model underestimates velocities down to ∼320 mbsf, and then overestimates velocities below this (Fig. 4.9(b)). Compared to the starting model, however, the final FWI model captures the velocity inversion at ∼300 mbsf and follows the general trend of the velocities from the log much better than the starting model. At site U1520 the final FWI model slightly underestimates velocities between 100-220 mbsf, and slightly overestimates velocities

from ∼220-500 mbsf, however matches the velocity trend well (Fig 4.9(c)). The predicted velocities from the final FWI model show a good match from ∼500-850 mbsf. The velocity inversions detected by the Vp log at ∼850 mbsf and ∼900 mbsf are present in the final FWI model, but are not as pronounced.

The LWD tool is most sensitive to vertical changes in velocity while FWI, determined by refracted turning waves, is more sensitive to horizontal velocities (Fig. 4.6). This means it is not a straightforward comparison between the LWD data and the velocity data produced by FWI. As the full-waveform inversion is isotropic (Table 4.1), any anisotropy in the subsurface geology will not be accounted for. This means that we expect to see differences in the size and depth of velocity anomalies within sonic velocity data and the FWI velocity model. As the model converges during inversion, any over- or under-estimations of velocities, which are due to anisotropy in the shallower parts of the model, will produce offsets between the FWI and well-log velocity-depth structure at deeper depths. The FWI velocity model has a lower resolution than the sonic data, which means we are not expecting the FWI model to reproduce the fine-scale detail within the sonic log. The sonic data is also collected with much higher frequencies (1-20kHz) that those used in the inversion (3-8Hz), which will cause different behaviours between the two techniques, especially in highly porous zones. The final velocities produced by FWI do, however, better match the sonic velocities compared to the starting velocity model. As the drilling occurred post-FWI modelling, we were unable to incorporate the well data into the creation of a starting model. However, it is important to note that comparison between the FWI model created with no available drilling data, and the data collected during Expeditions 372 and 375, have shown that FWI is a useful imaging tool for the subsurface structure even in the absence of drilling data.

4.6.1.4 Quality Assurance: Summary

Although the quality assurance tests presented in sections 4.6.1.1 to 4.6.1.3 suggest our FWI model is an improvement on the starting model, we recognise that our testing is not exhaustive, and the fit between the observed and synthetic data remains imperfect (Fig. 4.8). The most significant contributor to any inaccuracies in our final Vp model will likely arise from modelling a 3D world with a 2D dataset, something we cannot avoid with single streamer data. As there is a newly acquired, 3D, high-resolution streamer, OBS, and land dataset, we have the potential to significantly improve the Vp model in 3D in the future. In addition, since we use several approximations when propagating the seismic wavefield (see section 4.5), we should expect there to be some inaccuracies and artefacts in the recovered FWI velocity model. Velocity anomalies below the resolution of the inversion (a maximum inversion of 8Hz would give a resolution of ∼140 m in material with P-wave velocities of ∼2200 m/s) will also not be displayed in the final model, but exist in the true geology within smaller features such as faults, as evidenced by core data (Pecher et al., 2019; Wallace et al., 2019). However, the FWI model does produce a geologically-realistic model that better fits drilling data than the starting model. Therefore, we now discuss the recovered velocity anomalies in the context of the geology of the margin.

4.6.2 Observations from the FWI velocity model

4.6.2.1 The Overriding Plate

We first look at Area i (Fig. 4.7(b)), which is within the overriding plate above the plate boundary fault that experiences SSEs. In the west of the section we see several strong reflections, most notably a synformal structure at ∼1700 mbsf consisting of several bright, continuous reflections, labelled 1 in Fig. 4.10. When we overlay the FWI velocity model over the seismic reflection section, we see that higher velocities of ∼2500 m/s track these reflections for ∼5 km across their entire length (Fig. 4.10). Also, of note are three faults in the reflection seismic section, labelled 2, 3 and 4 in Fig. 4.10. On the overlay plot these faults are coincident with abrupt changes in velocity within the FWI model, which were not apparent in the smoothed starting velocity model. Faults 3 and 4 (Figs. 4.7, 4.10) correspond to zones of reduced velocity, with values of ∼2000-2200 m/s down to depths of ∼2000 and 2250 mbsf, respectively. These low-velocity zones have a width of ∼500 +/- 100 m and are surrounded by rocks with velocities of ∼2500-2800 m/s. For fault 2, there is a velocity contrast between the footwall and the hanging wall of up to ∼700 m/s between 500 1500 mbsf, with velocities of ∼2500 m/s in the hanging wall, and higher velocities (2900 m/s) in the footwall.

There are some small, unusually low-velocity anomalies within the FWI model, for example below the synform labelled a in Fig. 4.10 and b and c between the U1519 and fault 2. While these at first appeared anomalous, they correlate extremely well with shallow gas anomalies associated with the bottom simulating reflections (BSRs) as interpreted by Navalpakam et al. (2012) (Fig. 4.10) along 05CM-04 using a combination of rock physics modelling and seismic analysis. Wang et al. (2017) also interpreted reduced seismic velocity zones as free gas zones beneath BSRs, elsewhere along the margin and similar to the feature labelled a in Fig 4.10. We therefore consider these small-scale features as real and not artefacts of the inversion.

4.6.2.2 The Toe of the wedge

The wedge toe is associated with an imbricate stack of faults and associated folds. The seismic reflection profile in Fig. 4.11 shows three reverse splay faults labelled 5, 6 and 7. To the east of fault 7, we see flat lying reflections of sediments and sedimentary rocks beneath the Hikurangi Trough, which is shown in more detail in Fig. 4.12. Fault 7 is the first mapped fault, and is presumably the youngest in the accretionary wedge. Fault 7 is associated with a low-velocity zone in the final FWI model (Fig. 4.11), which shows a sharp drop in the modelled velocity from ∼3000 m/s in the hanging wall to ∼2300 m/s within the footwall at depths of 900 to 1200 mbsf. It appears that a low velocity channel exists in the region where fault 7 can be mapped in the reflection data. This channel has a velocity of 2300 m/s and it separates hanging wall and footwall rocks with velocities of around 2800 m/s. In the FWI model this low-velocity zone extends down to ∼1.5 km bsf (∼4.5 km absolute depth in Fig. 4.11), but cannot be resolved any deeper. Fault interpretation is based on Barker et al. (2018) and updated using the

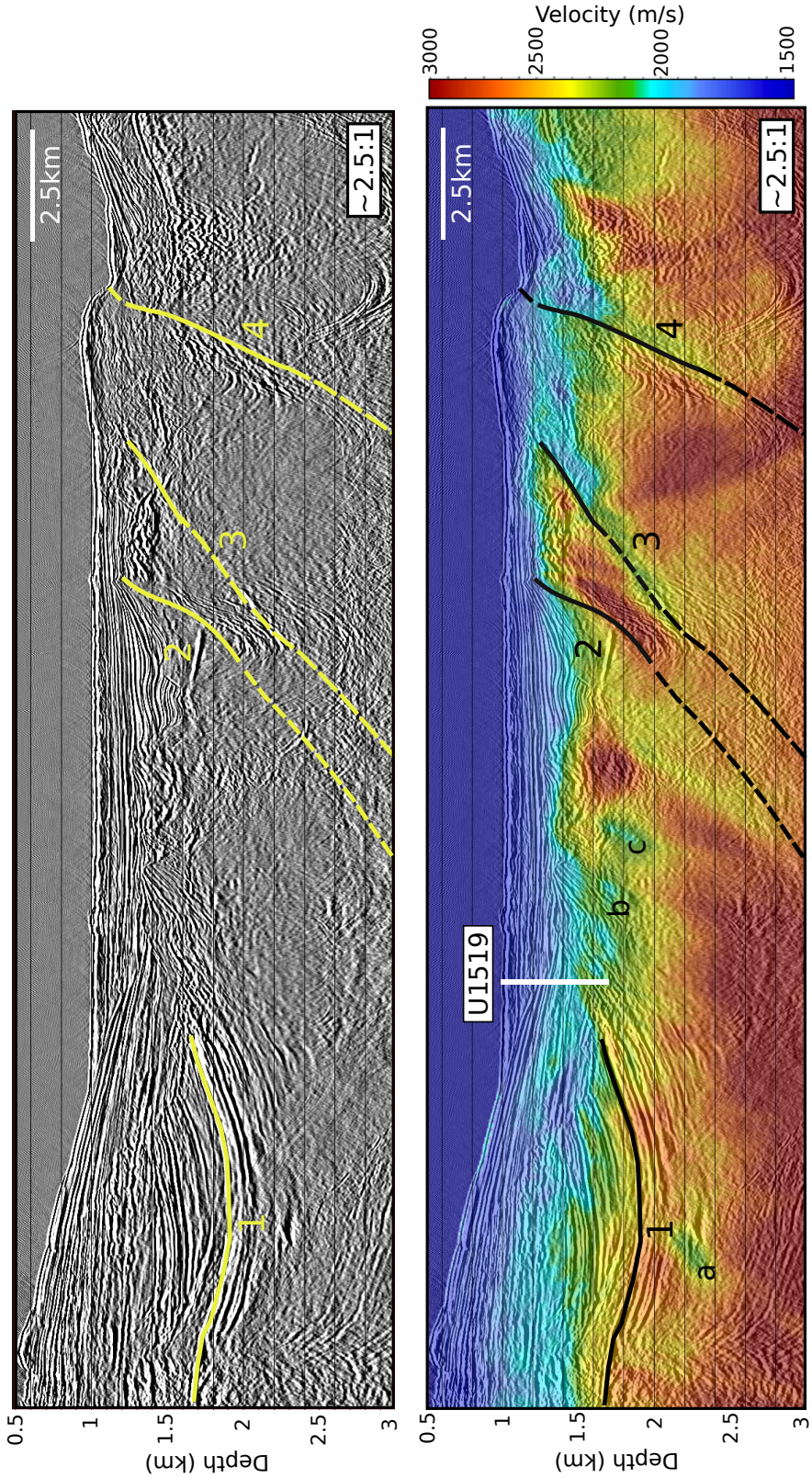


Figure 4.10: Detailed view of the PSDM seismic image from (Barker et al., 2018) and the overlay of the velocity model onto the PSDM seismic image shown in Figure 4.7, showing the location of site U1519. This is the overriding plate and a synform has been highlighted, labelled 1, as well as three faults labelled 2, 3 and 4, as well as smaller anomalies labelled a, b and c, which corresponds to shallow gas anomalies associated with the BSR (Navalpakam et al., 2012)

.

reflection data and final FWI velocity model.

In the general region of the toe of the wedge (Fig. 4.11), velocity increases gradually from ∼1600 to 2300 m/s between 0 and 1000 mbsf, and the velocity structure follows the general trend of the reflections. Below 1000mbsf, both the seismic reflection and velocity model gain complexity. Faults 5 and 6 differ from faults 2, 3, 4 and 7 in that they appear not to be associated with a discrete low-velocity channel around the fault zone, but rather a moderate velocity contrast between the footwall and hanging wall. Site U1518 drilled through fault 5 (Fagereng et al., 2019b)(Fig. 4.11) and LWD sonic velocities decrease below the fault zone (see Fig. 4.9(c)) from ∼2550 m/s to ∼1900 m/s. This reduction in velocity was not observed within the starting velocity model, shown in yellow in Fig. 4.9(b), but is partially recovered by FWI.

There are some potential artefacts in the final FWI model, for example the low-velocity-anomalies with values between 2200 and 2400 m/s labelled d to the left of fault 5 and e to the right of fault 7. We suspect these are artefacts as they do not directly match reflections in the depth migrated section. As these features are quite small (<100m) we do not see a mismatch between the real and synthetic shot gather that we can directly correlate with these features (Fig. 4.8(c)). However, unlike unconstrained anomalies, we do not see any raypath-like shape to these anomalies, so they may be real features. Without direct drilling data at these anomalies, we cannot say for certain whether they are real features or not.

4.6.2.3 The Incoming Section

An enlargement of the image across the incoming plate, labelled iii in Fig.4.7(b), is shown in Fig. 4.12. In the reflection profile the trench wedge has a horizontally-layered stratigraphy which onlaps two dome-like features (labelled 8 in Fig.4.12), which were not present in the starting model (Fig. 4.5(a)). The final FWI velocity model introduces more stepped changes in velocity compared to the starting model, as well as more abrupt changes around features such as feature 8, which exhibits a rapid increase in velocities (∼2500 m/s) compared to the surrounding velocity structure. A low-velocity feature also becomes apparent at ∼4.5-km depth in the centre of Fig. 4.12, labelled 9, with a velocity of ∼2200m/s within surrounding velocities of ∼2600m/s. This low-velocity feature appears to correspond to a strong reflection, to the right of which we see a small high-velocity anomaly with amplitudes of ∼3300 m/s within the surrounding volume. Synthetic shot gathers in the region match well with real field data, however, indicating that this feature could be real. The east of Fig. 4.12 shows a sharp change in velocity, labelled 10, and when overlain with the seismic section we can clearly see the slower sedimentary material of the trough, shown in blues and greens, onlapping onto the faster material of the Tūranganui Knoll seamount shown in oranges and reds. The velocity inversion at 850 mbsf in the wireline log (Fig. 4.9(c)) coincides with this feature, but is not seen as strongly in the final FWI model.

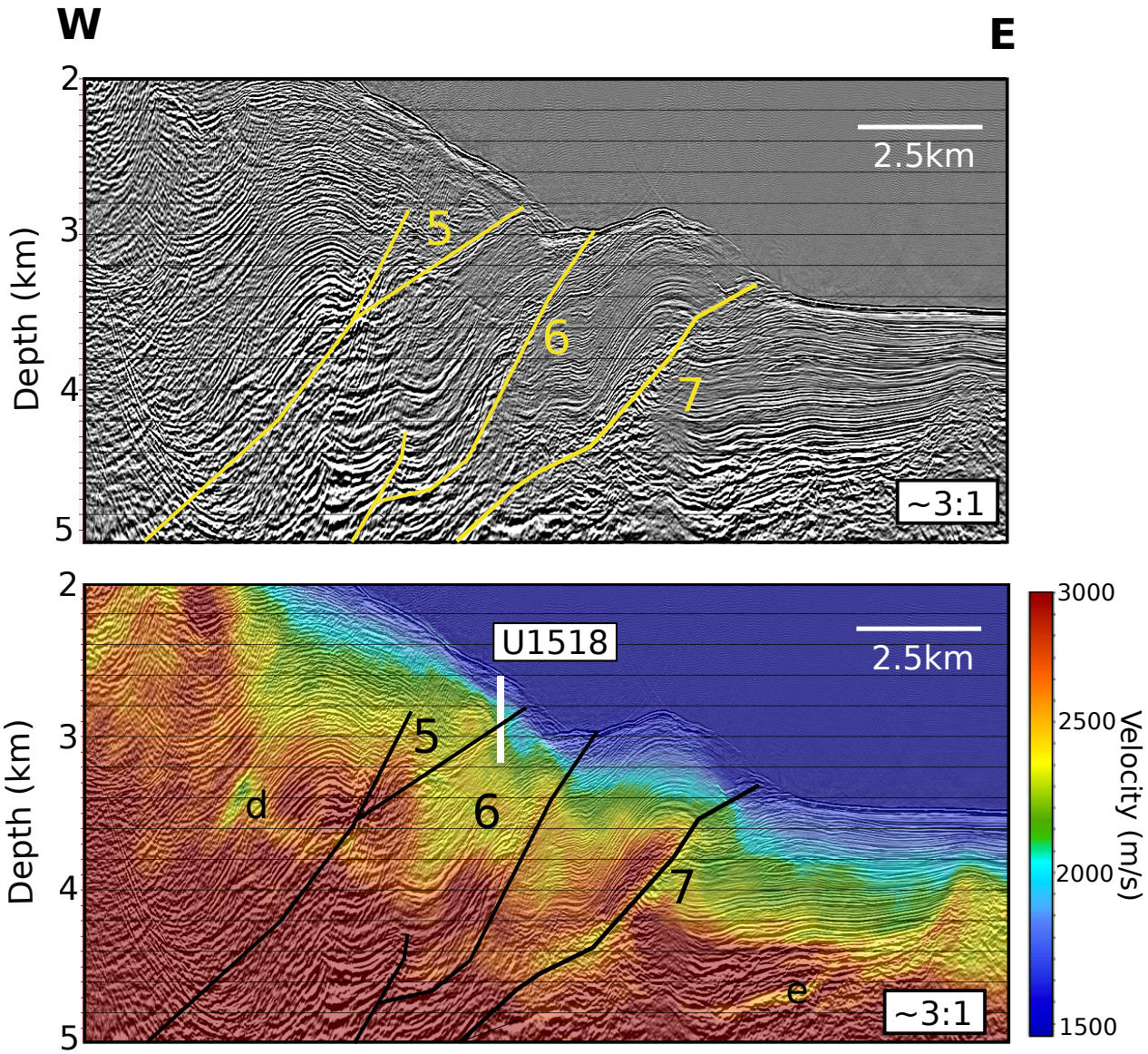


Figure 4.11: Detailed view of the PSDM seismic image from Barker et al. (2018) and the overlay of the velocity model onto PSDM seismic image shown in Figure 4.7ii and the location of site U1518. This is the toe of the dcollement where and 3 faults have been highlighted labelled 5, 6 and 7 (Barker et al., 2018) as well as potential inversion artefacts labelled d and e. A package of material of approximately the same velocity has been traced across fault 6, highlighted by the dashed white lines.

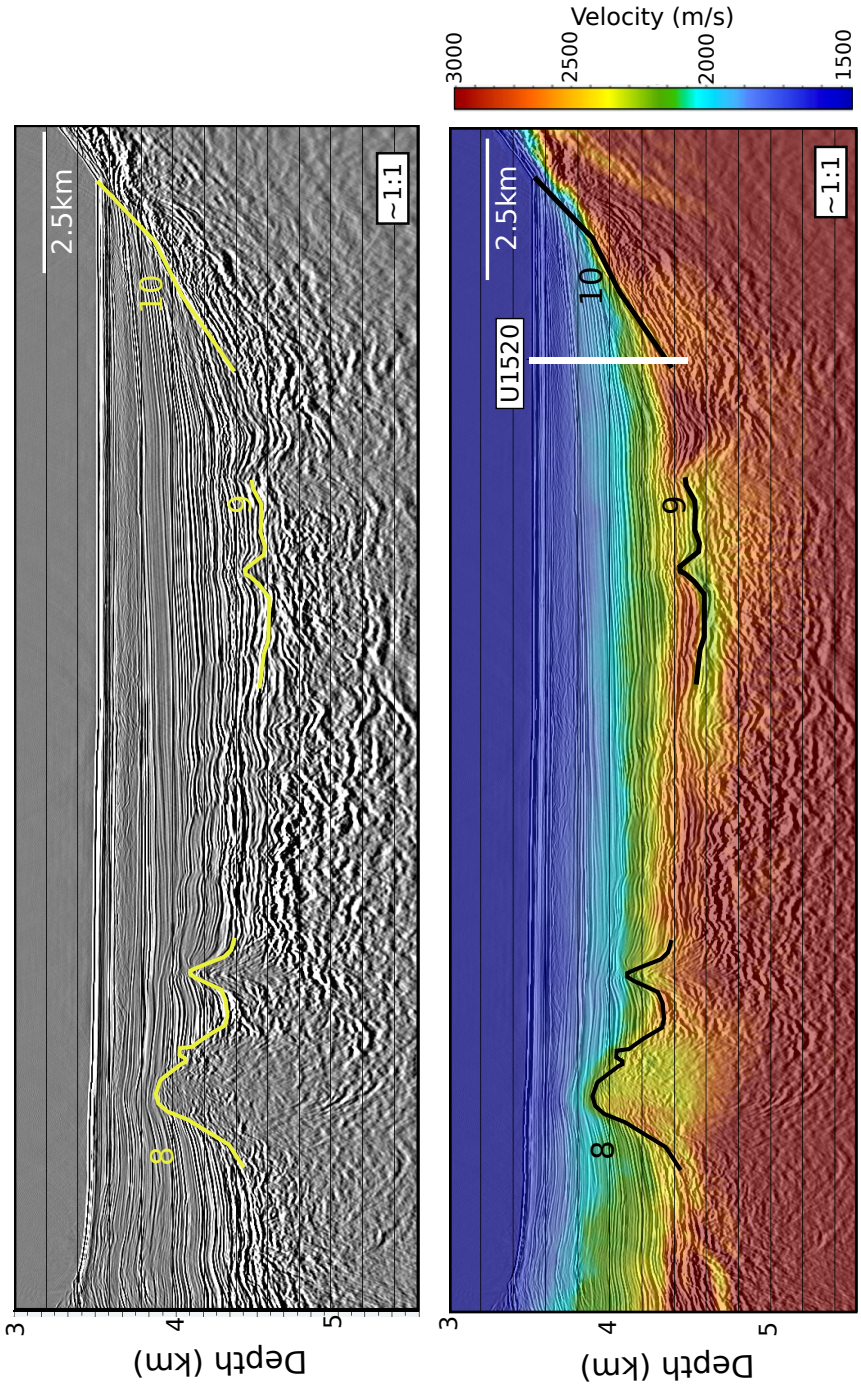


Figure 4.12: Detailed view of PSDM seismic image from Barker et al. (2018) and the overlay of the velocity model onto the PSDM seismic image shown in Figure 4.7iii. This is the Hikurangi Trough on the incoming plate, where well U1520 is located. The final model shows two dome-like features of higher velocity, labelled 8, a low velocity feature labelled 9 and an area of onlapping labelled 10. The velocity inversion west of U1520 highlighted as 9 does correspond to a strong reflector in the PSDM seismic image, however, as the well did not penetrate this zone, we cannot say for sure whether this feature is real or an artefact of the inversion. Nevertheless, synthetic shot gathers in the region match well with real field data, indicating that this feature could be real.

4.7 Discussion

4.7.1 Lithology of the Incoming Section

The final P-wave FWI velocity model reveals the fine-scale velocity structure across the trench wedge (Figs. 4.7 and 4.12). Velocities range from ∼1700 m/s near the seafloor and gradually increase to ∼3000 m/s at depths of ∼2000 mbsf. Preliminary reports from IODP Expedition 372 and 375 have determined six lithostratigraphic units in this area, consisting of turbidites, mass-transport deposits, and hemipelagic muds down to 509.82 mbsf, pelagic carbonate facies from 509.82 848.45 mbsf, volcaniclastics from 848.45 1016.24 mbsf and a blend of volcaniclastics, mudstone, limestone and siltstone down to 1045.75 mbsf (Wallace et al., 2019). The final FWI model is consistent with these findings as around site U1520 there are distinct changes in velocities at similar depths (Fig. 4.12). We suggest that we can track these lithologies extracted from core data across the trough, away from the well towards the deformation front. The low velocity zone labelled 9 in Fig. 4.12 approximately corresponds with the feature labelled e in Fig. 4.11, as well as the velocity inversion from the wireline data at ∼850 mbsf (Fig. 4.9(c)). This may suggest spatial variability within the top of the HKB unit across the basin floor. These lithologies could be part of the sedimentary package that surrounds the subducting seamounts. The ∼600 m thick features at the base of the trench wedge at about 4000 mbsf (labelled 8 in Fig. 4.12,) have previously been interpreted as volcanic domes which are part of a larger seamount complex which includes the Tūranganui Knolls (Fig. 4.1) (Barker et al., 2018). These domes have too low a velocity (∼2500 m/s) to be pure basalt, thus it is more likely that they are formed from volcaniclastic material or highly altered, fractured basalt. This interpretation is consistent with measured velocities of volcaniclastic sediments within the drill hole, which had significant scatter and ranged in value from 1800 5000 m/s (Wallace et al., 2019).

4.7.2 Low-Velocity Zones, Faults, and Fluid Flow

Velocity contrasts between the footwall and hanging wall of some faults in the model (e.g faults 2 and the upper part of fault 7 between 900 1200 mbsf) likely indicate underconsolidated, lower-velocity sediments in the footwall compared to the hanging wall which is now over-consolidated at its current depth, causing velocities to be higher. The availability of drilling data and our high-resolution FWI velocity model will allow models of porosity, effective stress and pore-fluid pressure to be developed in the future to test this hypothesis.

In addition, some splay faults visible in the reflection data correlate with low-velocity zones (reductions of ∼500 m/s) in the P-wave velocity model (Fig. 4.10 faults 2,3 and 4). This phenomenon is not unique to Hikurangi; such a relationship has also been noted from waveform tomography across the Nankai subduction zone in Japan where the megasplay fault system interpreted from the reflection image correlates with a sharp P-wave velocity reduction of ∼500-1000 m/s (Kamei et al., 2012). Lower

velocities in the shear zone of the megasplay fault system at Nankai have been identified as potential fluid conduits (Kamei et al., 2012), and this interpretation is supported by the observation of fluid seeps identified by submersibles above faults which have reversed-polarity (Park et al., 2002). The low velocity zones resolved along some faults at Hikurangi may indicate that these are zones of high porosity, which may be maintained by fluid through-put from depth. The interpretation of fluid flow, potentially along faults, is supported by elevated heat flow (Antriasian et al., 2018) and the observation of a number of fluid flow features in the vicinity of seismic line 05CM-04 near the frontal thrust, including pockmarks, flares and mounds. Porosity values across fault 5 increase by ∼5% within the fault, and ∼15% below the fault (Pecher et al., 2019; Wallace et al., 2019). Across faults with larger velocity reductions (e.g. faults 3,4, 5 and 7), however, we predict larger porosity increases due to the lower P-wave velocities recovered by FWI, leading to the possible presence of fluid and relatively unconsolidated footwall sequences.

The third splay fault in the system (fault 5 in Fig. 4.11) was drilled by Expedition 372 and 375 (Fagereng et al., 2019b; Pecher et al., 2019; Wallace et al., 2019). This fault is associated with a velocity decrease of ∼100 m/s in the FWI model, and the LWD data shows the fault (Fig. 4.9(b) red region) occurring above a velocity inversion between ∼300 - 400 mbsf (Fig. 4.9(b)). IODP drilling has revealed a zone of intense deformation, between 304.5 322.4 mbsf (Fagereng et al., 2019b) (Fig. 4.9(b)). If there is only a velocity reduction associated with the fault over a ∼20 m thick region, it will be below the resolution of the FWI model (∼140 m in material with P-wave velocities of ∼2200 m/s at up to 8Hz). This velocity reduction below the fault zone in the top of the footwall is small compared to the ∼700 m/s velocity decrease observed along other faults in the FWI model (e.g. fault 7 in Fig. 4.11), but is consistent with shipboard measurements of decreased porosity below the fault (Pecher et al., 2019; Wallace et al., 2019). This drilled fault may therefore not be acting as a conduit for fluid flow in the same way as other faults, which are associated with discrete, low-velocity anomalies that follow faults mapped in the seismic reflection data (faults 2,3,4 and 7). Fault age may also play a part in why a low-velocity zone is observed below fault 7, but not below faults 5 and 6 (Fig. 11). As fault 7 is likely to be the youngest in the sequence, subducting sediments may be less consolidated here, and/or be in the process of dewatering along the fault as the overburden increases, resulting in the presence of a low-velocity zone.

4.7.3 Relation to SSEs

SSEs have been associated with low-velocity zones along the megathrust (<35km depth) in several margins including Cascadia (Audet et al., 2009), Nankai (Kamei et al., 2012; Kodaira et al., 2004), and Costa Rica (Saffer et al., 2000; Tobin et al., 2001). Unfortunately, the limited shot-receiver offset of the dataset means we could not image down to the slow slip zone in this study due to the limited data recorded by the wavefield penetrating these depths (Fig. 4.6). While we cannot constrain the model down to the SSE zone (Fig. 4.1), we do image the plumbing system above the plate interface which is known to accommodate SSEs, and IODP Expedition 372 have successfully installed an observatory within fault 5 which will monitor physical properties across the fault during SSEs to determine whether

these events propagate along splay faults in the shallower parts of the margin. Future results from this observatory may reveal that we have in fact imaged slowly slipping faults, however this cannot be confirmed presently. The HRZ-2 SSE source region at a depth of 4km, shown by high-amplitude reflectivity in Fig. 4.1(c) is a target of newly-acquired, long-azimuth OBS data collected as part of the NZ3D experiment in January-February 2018.

Another factor suggested to control SSEs is a heterogeneous stress field caused by varying frictional properties at the interface (Peng and Gomberg, 2010). This is often associated with rough subducting seafloor and heterogeneous lithologies within the fault zone (Saffer and Wallace, 2015; Todd, 2017). As outlined in section 4.6.2.3, variation in the P-wave velocity within the incoming section which may be indicative of variations in lithology, as well as the presence of volcanic cones

While the 2D FWI modelling we have presented in this paper gives insight into some of these mechanisms, the upcoming results of the NZ3D seismic experiment, the IODP drilling Expeditions 372 and 375, and the permanent observatories installed at the interface will help to improve understanding of the processes at work at the Hikurangi margin. The performance of FWI improves significantly in 3D, and full-waveform inversions of the newly acquired 3D seismic dataset will allow us to obtain a more accurate velocity model and image deeper targets. Future work will include the downward continuation of first arrivals, the incorporation of anisotropy and attenuation in our 3D FWI inversions, and the creation of a new PSDM image using the 3D FWI velocity model.

4.8 Conclusion

We have demonstrated that FWI is a useful tool in exploring the physical properties of subduction margins at a high-resolution, and the imaging technology can be used effectively even in areas of very deep water and structural complexity. The model has improved on previous velocity models made using PSDM to produce a detailed, geologically realistic model across the shallow subsurface of the margin, that reveals details of the incoming lithology and fault plumbing system above a zone of shallow slow slip.

The high-resolution velocity model allows lithologies in the incoming section to be interpreted from drill site U1520 towards the deformation front. This reveals the inputs into the subduction zone as a combination of pelagics and volcaniclastics as well as volcaniclastic domes. The FWI velocity model also contains several-low velocity zones that are coincident with faults and their footwall sequences. Velocity changes across the faults from higher velocity hanging walls to lower velocity footwalls (faults 2, 6 and upper parts of fault 7) indicates that the footwall of some faults is underconsolidated, while the hanging wall over-consolidated for its current depth. Low-velocity channels along faults (faults 3, 4 and 7) likely indicate high porosity, which may be maintained through the transport of fluids from the subduction interface along these faults. This study has provided a framework for the future application of 3D FWI to recently-acquired, longer-offset, seismic data to recover high-resolution physical properties in zones of

slow slip directly.

4.9 Acknowledgements

The authors declare that they have no conflict of interest.

Data supporting the conclusions made in this contribution can be obtained through the references provided.

This research was supported by NERC grant NE/M021203/1 and NE/S00291X/1. M. Grays PhD is funded by Imperial College Department of Earth Science and Engineering, and the FULLWAVE research group.

The authors would like to thank the Imperial College London FULLWAVE group providing the full-waveform inversion code used in this contribution, as well as GNS Science, New Zealand for providing the data used in the inversions. We would additionally like to thank the International Ocean Discovery Program Expeditions 372 and 375 for providing the well data used in this contribution (now available through IODP at
http://iodp.tamu.edu/scienceops/expeditions/hikurangi_gas_hydrate_slides.html and
http://iodp.tamu.edu/scienceops/expeditions/hikurangi_subduction_margin.html). In particular, we would like to thank Mike Warner and Tenice Nangoo for technical discussion and Nathan Bangs for comments on the interpretation of the model. We would also like to thank Sally Watson and Philip Barnes for discussion regarding fluid seeps in the region.

Chapter 5

Aims, design and configuration of NZ3D-FWI: a large 3D seismic experiment at the Hikurangi margin

5.1 Abstract

Chapter 4 shows that using FWI on seismic data across the Hikurangi margin is able to produce high-resolution models of P-wave velocity detailing fault blocks, input into the subduction zone, and details of frontal thrust faults. The use of streamer data, however, limits the constraint of the inversion to ∼2km bsf. The collection of a large 3D dataset using land and marine receivers (both OBS and streamer hydrophones) will allow for deeper illumination of target areas as well as laterally varying features offshore Gisborne. This experiment was approved by NSF/NERC to be carried out between December 2017 and February 2018. This chapter details the use of different land receiver layout geometries and how these layouts can potentially affect imaging of key targets.

In the first part of the chapter, I use 3D synthetic FWI testing, employing checkerboards in target areas, to investigate how the 3D experiment can maximise imaging of areas of interest based on land receiver placement. Three geometries are tested for both deep and shallow checkers. The results show that the checkerboard is recovered when imaging key targets of the large 3D experiment. The geometry chosen consists of a 2 x 2km background grid of receivers with a central receiver in the middle of each gridded square, and a smaller, denser 500m x 500m grid of receivers concentrated in one area, representing the location of mud volcanoes identified during initial fieldwork.

The second part of this chapter describes how these tests were used to design the field experiment. I describe the types of sources which were used, as well as the different types of receivers, mainly focussing

on the land geophones. Finally, some examples of real data recorded during the experiment are shown.

5.2 Introduction

In order to constrain hydrology, lithology and structure at the Hikurangi margin, and how these factors influence seismicity in the region, a large 3D seismic survey, NZ3D-FWI, was proposed in 2014. This experiment was funded by a variety of agencies, from the UK, USA, Japan and New Zealand, and was conducted in 2017-2018. The experiment included the acquisition of a 3D multi-channel seismic volume, with airgun shots being recorded on 100 JAMSTEC Ocean Bottom Seismometers (OBSs), 50 NERC SeisUK broadband seismometers, 120 short-period Cube seismometers from GIPP Potsdam, and 25 short-period GSX seismometers from the Earthquake Research Institute (ERI), Tokyo. This experiment incorporated both active-source and passive seismic measurements in order to image a volume including the overriding and subducting plates as well as the plate boundary fault, where shallow slow-slip events are known to occur (Wallace et al., 2012, 2016). The primary aim of the tomographic part of the experiment was to use both onshore and offshore instruments to collect data optimally designed for high-resolution, 3D FWI. As outlined in chapter 2, successful FWI requires long offsets, wide azimuths and low frequencies (Morgan et al., 2013), so design of the NZ3D-FWI experimental geometry should take these factors into account.

In chapter 4 I showed how FWI was used to produce a high-resolution velocity model of the upper $\sim$ 2km of the subsurface along a 2D seismic profile. The 2D modelling produced reliable results, proven through a series of quality assurance tests (Gray et al., 2019), however the dataset used in the modelling was not acquired optimally for FWI (chapter 2). This meant that depths were constrained based on the maximum streamer length (12km) and imaging of the plate boundary at key target depths along the décollement was not possible. What the 2D modelling did show was the fact that FWI is a useful tool in recovering physical properties at Hikurangi even with sub-optimal data. This is promising for a more detailed investigation into deeper and laterally varying targets at the margin using data that is optimised for FWI. With approved funding for collection of a 3D dataset specifically for use in FWI modelling, as well as two drilling expeditions (IODP Expeditions 372 and 375) set to record in-situ measurements of physical properties, the physical controls on seismicity at Hikiurangi controlling why the plate boundary slips slowly in SSEs and tsunami earthquakes can be better understood.

In this chapter I aim to provide insight of what the NZ3D-FWI geometry should be, specifically for the land geophones. I achieve this through using FWI on a 3D synthetic model and testing the recovery of checkerboards at key targets in the model (Part I). By testing different land receiver geometries and seeing how these different geometries affect the recovery of the checkerboard, I can suggest a layout for the real experiment which will allow for the recording of data most optimal for future 3D FWI modelling. In Part II, I describe the experiment and show the true final positions of the instruments based on the modelling in Part I, as well as show real data recorded on some instruments after the experiment was completed.

5.2.1 Additional notable features at Hikurangi associated with the subduction zone

The seismicity, seamount presence and lithology across the Hikurangi margin are detailed in chapter 4 which are important features related to subduction at the margin. In this chapter, several other feautures are important to note in relation to the NZ3D-FWI experiment. These include a distinct change in geodetic coupling between the downgoing Pacific plate, and the overriding Australian plate (Wallace et al., 2004) (Fig 5.1). Interplate coupling is the ability of a fault between two plates to lock and accumulate stress (Yoshioka, 1991). There is a deep, interseismically coupled zone beneath the southern North Island, which shallows quickly to the North-East, near Cape Turnagain. Beneath the North island there is an abrupt transition zone, where the two plates become uncoupled, and the interface changes from coupled to creeping behaviour (Wallace et al., 2004). Along-strike, there is an abrupt change in the downdip limit of interseismic coupling. The change cannot be explained by changes in temperature along the interface, as has been done at other subduction zones (Hyndman et al., 1995; McCaffrey and Goldfinger, 1995; Oleskevich et al., 1999). The depths at which the change in coupling occurs at predicted temperatures as low as 100°C whereas the base of the frictionally unstable portion of the fault is suggested to occur at temperatures of 350°C, and the beginning of the free slipping behaviour is suggested to occur at 450°(Liu and Rice, 2007; McCaffrey and Goldfinger, 1995; Oleskevich et al., 1999). The cause of the change in coupling at Hikurangi is argued to be a combination of interface temperatures, fluid pressure, structure of the upper and lower plates, and tectonic stress state of the upper plate (Fagereng and Sibson, 2010; Wallace et al., 2004, 2009), but it should be noted that the changes in plate coupling both laterally and down-dip occur in the same regions as SSE origination at the margin (Fig 5.1). The location of the down-dip change in plate coupling was not imaged in the 2D FWI model presented in chapter 4 due to the limited penetration depth (∼2kmbsf). With the NZ3D-FWI project, we expect to image deeper using experiment design optimal for FWI and hopefully recover properties in this zone.

During a pre-experiment scouting trip to review seismometer site locations, several mud volcanoes were identified within the proposed land-instrument grid. Mud volcanism is known to occur on the east coast of the North Island including Hawkes Bay and the Raukumara Peninsula (Pettinga, 2003; Ridd, 1970). Mud volcanoes and seeps have been identified and monitored by GNS Science in the Waimata Valley region within the field area (Mazengarb and Speden, 2000). These mud volcanoes are associated with gas and fluid seeps, and diapiric mud extrusion along fault zones, which have also been identified in seismic profiles offshore (Katz, 1981). The largest documented eruption occurred in Waimarama 1994 in which an estimated 8-10000 m^3 of mud was erupted in a matter of hours (Pettinga, 2003). Another key target of the 3D seismic imaging is therefore the mud volcano system at play onshore North Island. As this particular target is located onshore,, investigation of this hazard is useful to local residents.

The 2D fine-scale P-wave velocity structure in the uppermost ∼2 kilometers of crust across the Hikurangi subduction margin recovered in chapter 4 is insightful into the character of the upper overriding plate and incoming sedimentary section, but is too shallow to image the part of the plate interface where SSEs

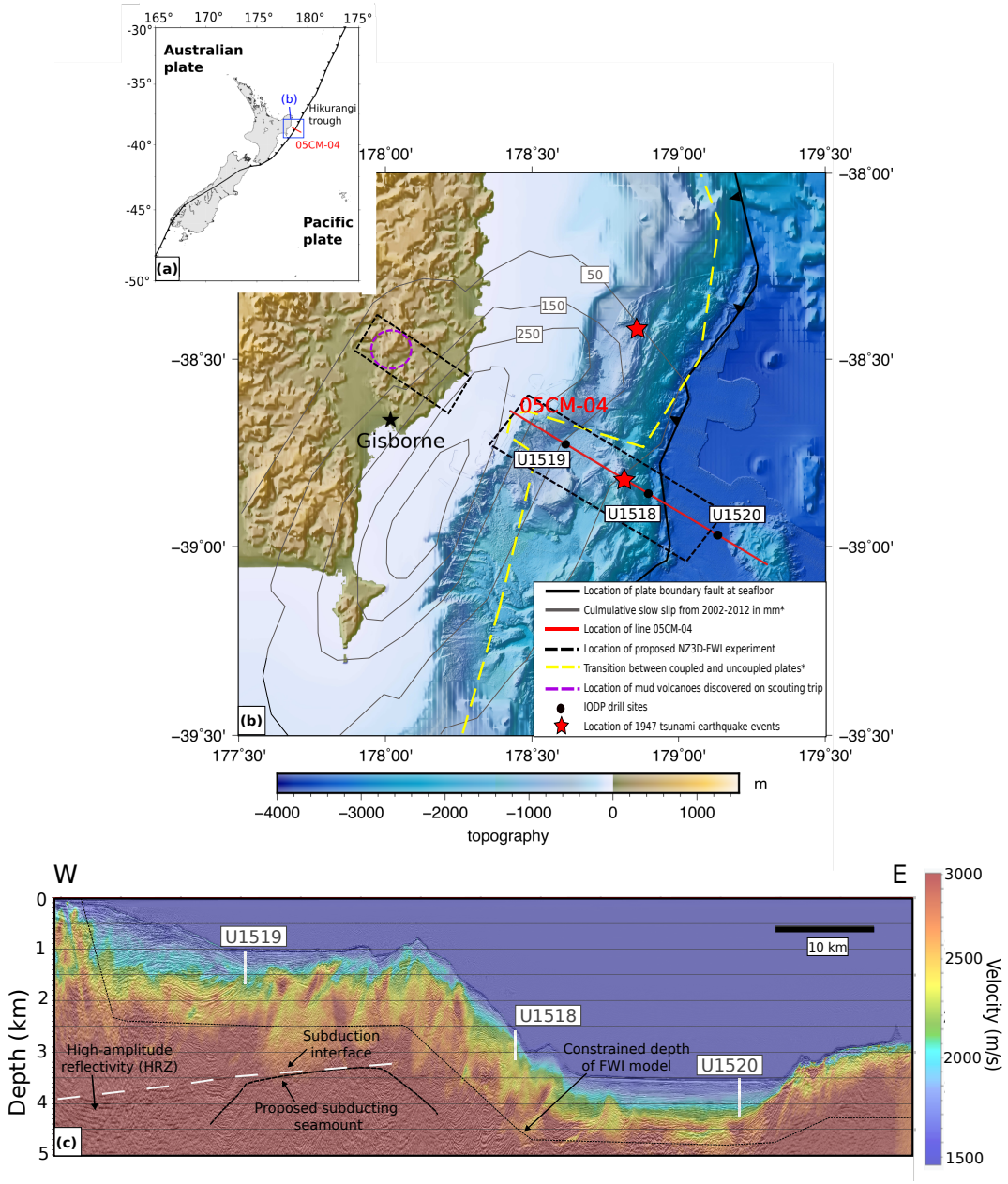


Figure 5.1: (a) Regional map of New Zealand showing plate boundaries between the Australian and Pacific plates. The red line shows the 2D multichannel seismic line 05CM-04 used in chapters 3 and 4. The blue box shows the location of (b), the larger map, in which the colour scale is bathymetry across the Hikurangi margin, based on 25-m gridded swath data. Grey contours show culmulative slow slip from 2002 - 2012 in mm and yellow dashed line shows the location of the boundary between coupled (east of the line) and uncoupled (west of the line) plate boundary behaviour, both from Wallace et al. (2012). The black dots represent the IODP drill sites, where LWD core and wireline (1520 only) measurements were taken on Expeditions 372 and 375. The red stars show the location of the 1947 Offshore Poverty Bay (along line 05CM-04) and Tolaga Bay tsunami earthquakes (Bell et al., 2014). The black dashed boxes show the proposed location for the NZ3D-FWI experiment, and the purple dashed circle shows the region in which evidence for mud volcanism was noted on a scouting trip of the area. (c) Reflection seismic section of 2D line 05CM-04. overlain onto the final FWI P-wave velocity model from chapter 4, showing the depth to which P-wave velocities are constrained by turning rays. The black dashed line shows the location of the proposed subducting seamount from Bell et al., (2014) based on magnetic data, and the red star shows the location of the March 1947 tsunami earthquake event offshore Poverty Bay. The white dashed line shows the approximate location of the plate interface where SSEs are known to occur (Wallace et al., 2016), and the HRZ is shown, where strong reflectivity is seen in reflection seismic images.

are known to occur (∼15 - 2km depth) (Bell et al., 2010; Wallace et al., 2016) or the potentially-related subducted seamount which, from seismic and magnetic data, is considered to be ∼6.5km below the sea floor (Barker et al., 2009, 2018; Bell et al., 2014). It is also too shallow to image the down-dip change in interplate seismicity at depths of 3-12 kmbsf (Fig 5.1). To be able to distinguish between the various hypotheses for the cause of SSEs, we need to be able to obtain fine-scale images of physical properties down to the subducting plate as well as lateral variations in physical properties at the margin. It is therefore essential to improve on models such as that presented in chapter 4 at Hikurangi, to acquire a new, large 3D, wide-azimuth dataset which would have the ability to image deeper targets across the margin.

5.2.2 Motivation for the NZ3D-FWI Experiment

The proposed NZ3D-FWI experiment location (Fig 5.1) spanned the SSE zone, proposed subducting seamount, the location of the March 1947 tsunami earthquake, down-dip change of interplate coupling, and the overriding and incoming plates. Line 05CM-04 (the focus of 2D FWI in chapter 4) lies within the area covered by the new, 3D survey (Fig 5.1). The 3D survey was designed with four main objectives:

i. To develop high resolution images of the plate interface in order to determine the geometry and reflection characteristics down to depths of > 10km.

ii. To image the structure and stratigraphy within the upper plate in order to gain more insight into constraints on hydrogeology and faults in the incoming and overriding plate, plate interface, and subducting sediments.

iii. To image structures related to seamount subduction to better understand sediment subduction, sediment underplating, and patterns of deformation and inferred stress at subduction zones due to seamount subduction.

iv. To obtain a large dataset containing high-precision seismic attributes, most notably P-wave velocity, with the intention of using this together with Full-Waveform Inversion (FWI) to produce high resolution velocity models within the area. This will allow inferences of physical properties across the margin. The 3D volume will provide information on structure and stratigraphy, which may help us to understand the deformation and development history of the margin. This data can be using in conjunction with rock properties obtained from drilling data in order to extrapolate interpretations of rock properties away from the wells.

5.2.3 Hypotheses for the generation of SSEs

The suite of new data and subsequent FWI analysis at Hikurangi will be used to test three specific hypotheses relating tectonic and hydrogeologic processes and seismic behaviour at the margin:

5.2.3.1 Elevated fluid pressures exist in zones of slow slip leading to transitional frictional stability.

In this hypothesis, numerical models and laboratory experiments suggest that SSEs may be spontaneously generated under condiions of very low effective stress, facilitated by high pore fluid pressure (e.g. Liu and Rice (2005, 2007); Peng and Gomberg (2010)). The evidence for this hypothesis includes low Vp and high Vp/Vs ratios, indicative of fluids (Audet et al., 2009; Bangs et al., 2004; Kamei et al., 2012; Matsubara et al., 2009; Peng and Gomberg, 2010; Song et al., 2009; Tobin and Saffer, 2009), elevated *in-situ* effective stress along the subducting plate interface (Bell et al., 2010; Kitajima and Saffer, 2012; Kodaira et al., 2004), and elevated porosities (Bangs et al., 1990; Saffer, 2003; Screaton et al., 2002; Zhao et al., 1998). The resolution of these current models, however, is relatively low (500m - 10km resolution within various models at various depths) (Audet and Schwartz, 2013; Bangs et al., 1990; Bell et al., 2010), and it is therefore difficult to determine whether these anomalies in physical properties are related to changes in lithology or fluid-filled porosity without the addition of drilling data. *In-situ* measurements from IODP drilling can provide key insights into the physical properties at Hikurangi including porosities and fluid presence. A large 3D seismic dataset would allow the identifications of low velocity zones which could be associated with increased porosity, fluids filling this increased pore space, as well as allowing interpretations of recovered physical properties relating to higher porosities and Vp/Vs to propagate away from IODP wells. We might also expect to recover a narrow ultra-low-velocity zone along the plate interface caused by a thin zone of over-pressured fluids (Audet et al., 2009; Hansen et al., 2012; Shelly et al., 2006; Song et al., 2009).

5.2.3.2 Rheological heterogeneity exists in zones of slow-slip.

This hypothesis states that variable frictional properties in the fault zone produce variable frictional behaviour at plate margins are necessary to promote SSEs. This causes some areas along the interface to be stable or unstable, as well as velocity strengthening or velocity weakening. This is suggested to be due to the subduction of a range of lithologies, creating a heterogeneous zone which will in turn produce a heterogeneous stress field. The resulting subduction interface becomes a mosaic of lithologies which includes carbonates, basalt, clays and quartz (Fagereng and Sibson, 2010; Saffer and Wallace, 2015; Wang and Bilek, 2014). The heterogeneous structure is suggested by seismic reflection images which show interleaving zones of high and low amplitude reflectivity (Bell et al., 2010; Saffer and Wallace, 2015). By maintaining a heterogeneous stress field, SSEs are believed to originate as the plate cannot rupture over large areas to produce a stick-slip event (Ikari et al., 2013; Marone, 1998). Seamounts may also create a heterogeneous stress field, fracturing the upper plate as they are subducted (Wang and Bilek, 2011). This fracturing can disrupt the spatial continuity of the plate interface, creating a mixture of velocity strengthening and velocity weakening zones (Ando et al., 2012; Lavier et al., 2013; Saffer and Wallace, 2015; Skarbek et al., 2012). Core, wireline and LWD data from Expeditions 372 and 375 have allowed us to identify several different lithologies on the incoming plate ranging from turbidites, mass transport

deposits, hemipelagic muds, pelagic carbonates and volcaniclastics (Pecher et al., 2019; Wallace et al., 2019), and the 2D FWI model has allowed the tracing of these units across the input section towards the frontal thrust (see chapter 4). Presence of such heterogeneous rheology cmay be identifiable in the NZ3D-FWI reflection and velocity data, caused by either a mixture of lithologies, changing physical properties within the same lithological unit, or a mixture of the two. With information about Vp and Vp/Vs properties from cores tested for different pore pressures and fluid saturations, 3D velocity imaging can be more accurately interpreted for lithological variations across the incoming plate which represents the inputs into the subduction zone. Fracturing along the upper plate due to the subducting seamount could also be identified with deeper seismic imaging, as chapter 4 shows how faults and fractures can be identified from high-resolution FWI velocity models.

5.2.3.3 SSEs occur within thickened shear zones, compared to narrow faults that host large earthquakes.

In this hypothesis SSE and aseismic creep occur along a thick (100's m - km), mixed, heterogeneous zone of fractured and sheared rocks. In this zone, the slow observed displacement is due to steady deformation distributed within the fine-grained matrix (Fagereng and Sibson, 2010; Wang and Bilek, 2011). This hypothesis is consistent with observations linking shear localisation with slip-weakening behaviour (Audet et al., 2009; Shelly et al., 2006; Song et al., 2009), as well as ocean drilling observations (Ikari and Saffer, 2011; Moore et al., 2001; Rowe et al., 2013) . Results of previous drills have suggested rapid large slip events are associated with highly localised faults(Chester et al., 2013; Sakaguchi et al., 2011) . Chapter 4 has shown how faults can be identified from FWI velocity models, and with a larger dataset, imaging how these faults vary laterally and at greater depths will be possible. Imaging deeper into the margin may also reveal a patchy velocity structure, similar to that described in hypothesis 5.2.3.2, in a thick zone along the interface. Combining resulting velocity models with IODP data, particularly properties from well U1518 which crosses a frontal thrust fault, will provide insight into how physical properties are changing within and across fault zones, and can be used alongside velocity models to investigate fault zone thickness.

Part I : NZ3D-FWI

Here I present an overview of synthetic testing of a 3D model of the proposed NZ3D-FWI experiment in order to determine optimum location of land instruments for data acquisition. The background model used was a 3D extrapolation based on models presented in chapter 4. I carry out a suite of checkerboard tests, using different onshore seismometer geometries. For the initial tests, the checkerboard was placed along the décollement and then, in later tests, also directly below the land instruments where the source of mud volcanoes are expected to be located. Using these checkerboards to represent key experimental targets, three land receiver layouts are tested to determine how recovery of these targets change when spacing of the receivers in changed.

5.3 Method

This section outlines how I designed a 3D model for synthetic FWI testing. Here I will explain how I created a 3D model based on the 2D models used in chapter 4, and how I implemented a checkerboard which was used to assess the performance of 3D FWI target depths. I explain why I chose to run checkerboard testing, and how I chose the parameters and location of the checkerboard. I also examine the inversion scheme which had to be used in order to process such a large synthetic dataset.

Checkerboard tests have long been used to assess the reliability of inversions (Bijwaard et al., 1998; Eberhart-Phillips and Reyners, 1997; Graeber and Asch, 1999; Kamei et al., 2012; Morgan et al., 2013; Spakman et al., 1989). Due to the ill-posed nature of inverse problems (Pratt, 1999; Virieux and Operto, 2009; Warner et al., 2013), it is important to test the robustness of an adopted inversion. This type of testing involves adding alternating positive and negative anomalies to an initial model. Checkerboard testing is beneficial for resolution analysis as the pattern is straightforward and memorable, therefore by displaying the recovered checkerboard, it is easy to see where resolution is good or poor (Lei and Zhao, 2005). While checkerboard testing is used across many geophysical techniques, I will be using the method for velocity modelling. The workflow involved in checkerboard testing for velocity modelling is as follows:

A A checkerboard is created and added to a velocity model. This then becomes the 'True Model'.

B A synthetic seismic dataset is created by propagating an arbitrary source wavelet through the True Model.

C The synthetic seismic data are inverted, using the velocity model with no checkerboard, known as the 'Start Model'.

D The Start Model is subtracted from the final inversion result to show the recovered checkerboard.

If we are able to resolve the checkers, then we can be confident that we can resolve features of a similar size as the checks when inverting the real data.

Using checkerboard testing to investigate the resolution of data inversion schemes has a long history at subduction zones (Bijwaard et al., 1998; Eberhart-Phillips and Reyners, 1997; Graeber and Asch, 1999; Kamei et al., 2012; Morgan et al., 2013; Spakman et al., 1989). These studies used P-wave velocity models derived from thermal models (Spakman et al., 1989), local earthquakes (Eberhart-Phillips and Reyners, 1997; Graeber and Asch, 1999) and active source seismic data (Bijwaard et al., 1998; Kamei et al., 2012; Morgan et al., 2013) in order to assess the resolution of modelling at subduction zones, particularly along the subducting slab. The most common type of checkerboard testing in these subduction zone models is a tightly spaced checkerboard, with alternating positive and negative anomalies.

5.3.1 Creation of a 3D Hikurangi volume and application of checkerboard testing.

The methods used to test potential experiment layouts for the NZ3D-FWI experiment were as follows:

i. Create a start model.

ii. Determine the wavefield coverage and maximum depth of penetration using ray-tracing.

iii. Add a checkerboard to generate a true model.

iv. Propagate the source wavefield through the true model.

v. Generate a synthetic field dataset for different receiver geometries.

vi. Choose an inversion scheme and run FWI.

vii. Subtract the resulting velocity model from the start model to determine how well the checkerboard is resolved.

5.3.1.1 Creating a start model

The initial velocity model was created based on the PSDM model by Barker et al. (2018) (see chapter 4), which ends before reaching the New Zealand coast. To extend the velocity model onshore, the velocity-depth profile at the western edge of the PSDM model was extrapolated westwards. The model was then flattened along a picked décollement, below which oceanic crustal velocities of 5-7km/s were added, based on the velocity structure of oceanic crust close to the East Pacific Rise (EPR) (Toomey et al., 1990). The model was then unflattened, smoothed, and extended downwards to a depth of 20km. This 2D velocity model was then repeated 150 times, one grid cell apart, to create a 3D cube. The picked décollement was gradually shallowed laterally along the décollement by ∼1000 m near the centre of the 3D cube to add structure and simulate the seamount identified by Bell et al. (2014). The final dimensions of the

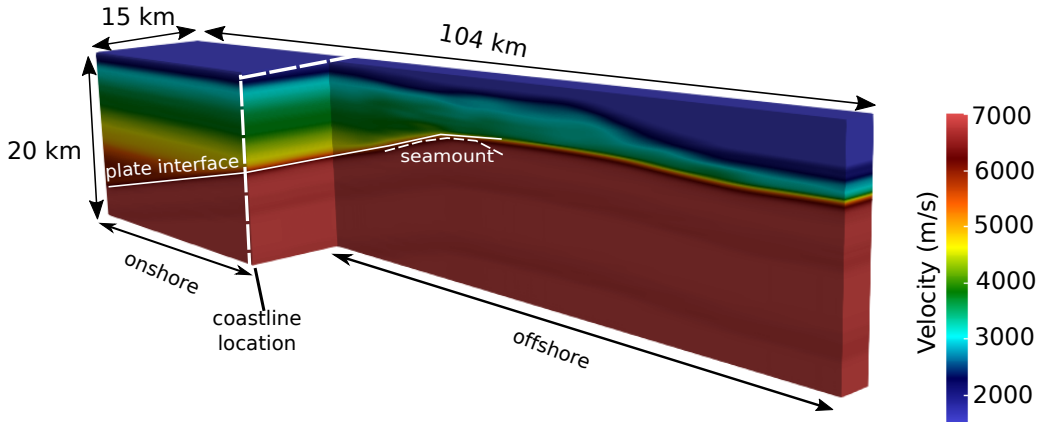


Figure 5.2: Cut-away image of the Start model showing the different sub-surface seismic velocities, plate interface and proposed subducting seamount.

model were 1040 x 150 x 200 grid cells with a grid spacing of 100m giving a total model area of 104km x 15km x 20km as shown in Fig 5.2.

The start model is an oversimplification of the true geology at the Hikurangi margin. The model is heavily smoothed, and does not contain lateral velocity variations which we expect in nature, apart from the shallowing of the décollement to represent a seamount. The model also does not include any of the fine detail of complex fault plumbing system above the décollement observed from the 2D FWI investigation in chapter 4. A simple model is considered appropriate because the main purpose of the tests is to examine the resolution across specific target zones, which are in general deeper than the constrained region of the 2D model (∼2kmbsf). Hence, as long as the long-wavelength velocity structure is broadly correct, the path of the transmitted wavefield will be representative of the real experiment. We also wish to examine a best-case scenario with regards to the ability of FWI to resolve features along the plate interface. The onshore section is also over-simplified, it contains no topography, despite the area around Gisborne and the Waimata valley having topographic elevation changes of 0 - 400 m, and the coastline is modelled as a straight boundary. The FWI code used for these simulations did not have the capability to invert geophone data or include land topography at the time of this study, hence, the land seismometers were treated as hydrophones at sea level.

5.3.1.2 Determine the wavefield coverage and maximum depth of penetration using ray-tracing.

Paraxial ray-tracing was performed through the model to investigate ray coverage at the deeper plate boundary targets. By having OBS instruments as well as land stations, we have a long-offset, wide-azimuth experiment, and expect to be able to image to significant depth using FWI (Morgan et al., 2013)(also see chapter 2). I computed rays through the model from three source locations offshore, through a 2D slice at the centre of the 3D model (Fig 5.2). This was computed using the seismic unix

function RAYT2D which creates traveltime tables calculated by 2D paraxial ray tracing, in which shadow zones are particularly compensated for by solving the eikonal equation (Stockwell and Cohen, 2002). I then took the output from RAYT2D and used MATLAB to create the plot shown in Fig 5.3. In this plot, all reflected rays and rays which did not reach receivers have been removed, to display just the transmitted rays, as these are the arrivals that are most important in FWI (see chapter 2). It should be noted that, as ray tracing is calculated in 2D, Fig 5.3 does not include turning rays which will arrive from shots at lateral offsets in the model (wide-azimuths). This is because RAYT2D only works in 2D. While this is a good estimate for the depths we can expect to measure turning rays, the density of turning rays is underestimated due to the lack of a third dimension in model space, therefore we expect more ray coverage than shown in Fig 5.3, but similar depth of imaging, which we are mainly using ray-tracing to determine.

Ray tracing shows that we expect to record turning rays down to ∼19km, which will allow the recovery of velocity:

i. Down to the depth of the plate boundary fault and plate interface >10km.

ii. Within the upper plate both onshore (for imaging of the mud volcano system) and offshore (for imaging of the overriding plate and incoming subducting plate).

iii. In the region of the proposed subducting seamount including the epicentres of the March and May 1947 tsunami earthquakes (Fig 5.1).

iv. Within the confirmed SSE zone ∼15km - <2km below seafloor, shown in the reflection seismic section as the HRZ (Fig 5.1(c)).

v. The plate interface between 3 and 12km depth where the downdip transition between coupled and uncoupled plates occurs (Fig

This suggested that imaging the experimental targets is possible with the proposed offshore-onshore experimental geometry when including shots sufficiently close to the shore.

5.3.1.3 Adding the checkerboard to generate a true model.

The checkerboard comprised of small checks measuring 300 x 300 x 300m and large checks measuring 600 x 600 x 600m down to 8km, as shown in Figs 5.4 and 5.5. As the theoretical resolution of FWI is approximately half the seismic wavelength (Pratt, 1999), for inversion up to 5.8 Hz, in the shallow décollement where background velocities are ∼3500m/s, theoretical resolution is ∼300m and in the deeper décollement where background velocities are ∼5500m/s, the theoretical resolution is ∼475m. From a depth of 8km to the bottom of the model, the size of the checkerboard was increased to small checks of 500 x 500 x 500m and larger 1 x 1 x 1km checks (Figs 5.4 and 5.5), to reflect the decrease in resolution caused by increasing velocity and reduced wavefield coverage (Fig

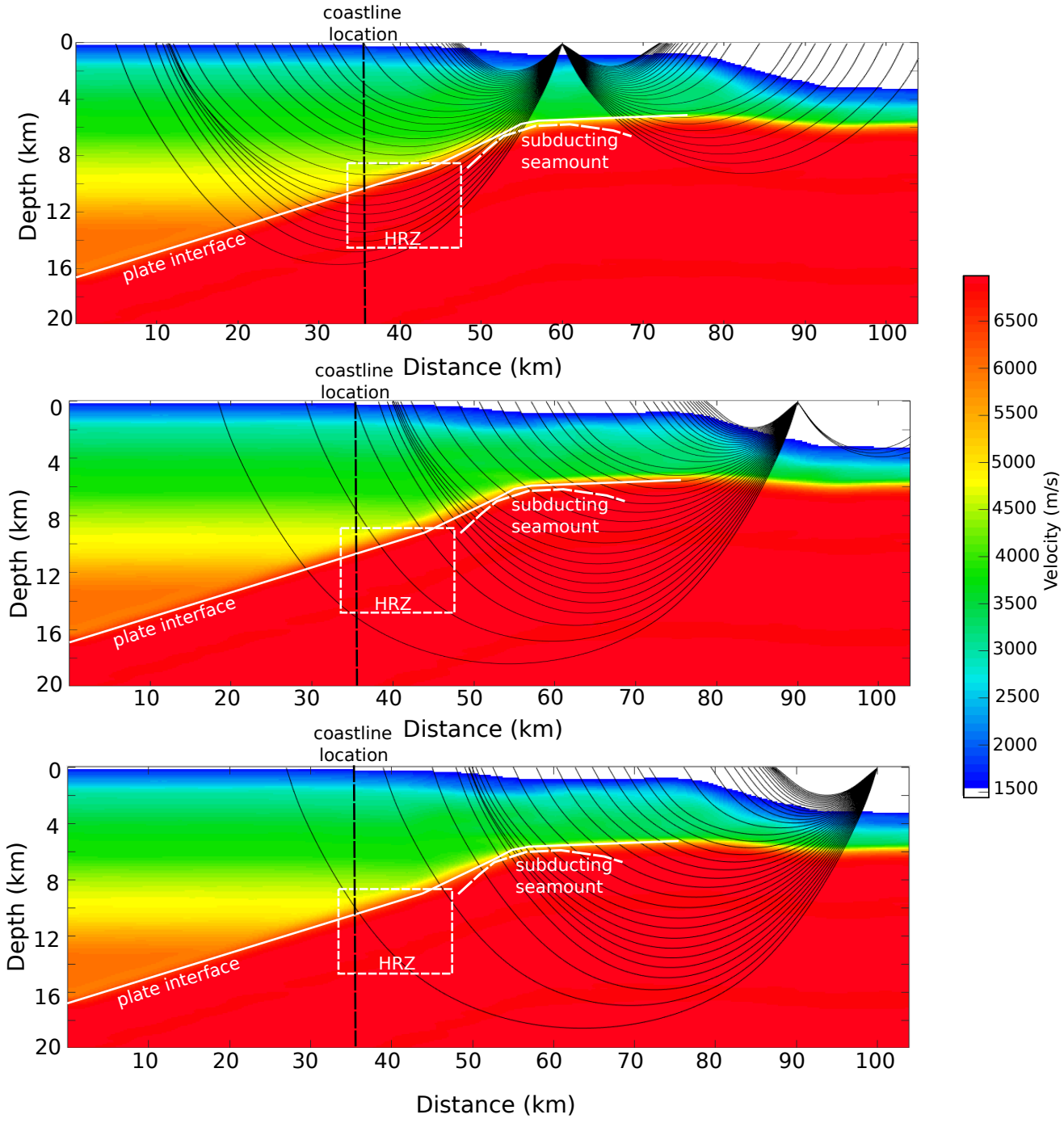


Figure 5.3: Paraxial ray-trace tests through a 2D slice through the centre start model (Fig 5.2) at 3 different shot locations. Some of the key targets of the 3D-FWI experiment are shown including the plate interface, HRZ and subducting seamount. Receivers will record data from depths of ∼19km.

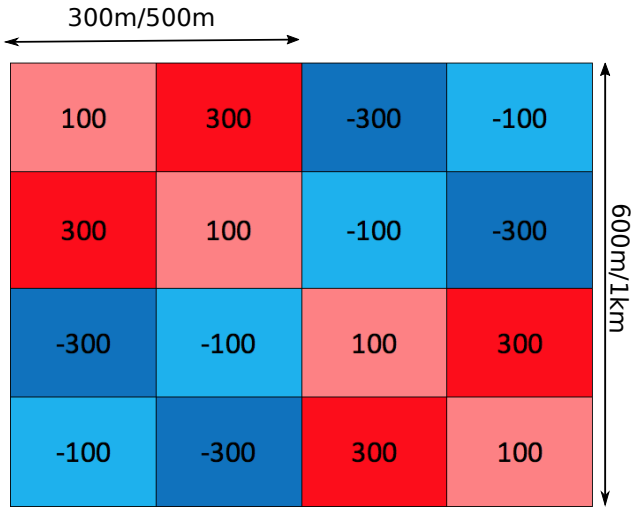


Figure 5.4: Schematic of the checkerboard used in the synthetic testing. The numbers represent the velocity difference between the checkerboard and the background velocity model in Fig 5.2.

5.3). Velocities were chosen to give a change in velocity between 1.6 and 5% to the background velocity. Percentages are kept around these values to avoid cycle skipping in the FWI code caused by large anomalies which may cause the code to converge to a local, rather than global minimum, as detailed in chapter 2. Over 300m in the 2D modelling presented in chapter 4, velocity variations in the range of 0.5% have been recovered in the near surface. The difference between low velocity zones in footwalls and along faults and high velocities in hanging walls in the 2D FWI (chapter 4) ranged from 10-25%. Anomalies of this size would cause cycle-skipping in synthetic checkerboard testing due to the sharp boundaries introduced by the checkerboard, however, it is promising that the scale of velocity variations we have been recovering are large enough for the modelling to detect.

The checks were arranged to follow the décollement, lying just above the plate interface, as shown in Fig 5.5. The checks were then added to the start model to produce the True Model as shown below in Fig 5.6. This is the model which was used to create the synthetic seismic data for the checkerboard testing.

5.3.1.4 Propagating the source wavefield through the true model.

The synthetically created forward modelled data will act as the field data for the checkerboard tests. This dataset was created by propagation of a source wavelet through the true model shown in Fig 5.6. The source wavelet used was a Ricker wavelet of amplitude 1 shifted to start at 350ms, as shown in Fig 5.7. As I am only comparing results for synthetic testing, and creating the field data myself, there is no need to extract a source wavelet from the field data as described in chapters 3 and 4. Here the same source wavelet is used for generating and inverting the seismic data.

The source array was comprised of 9000 shots, evenly spaced 300 x 300m apart to cover the marine section of the model, starting 5km from the coastline, as shown in Fig 5.8. Each white point

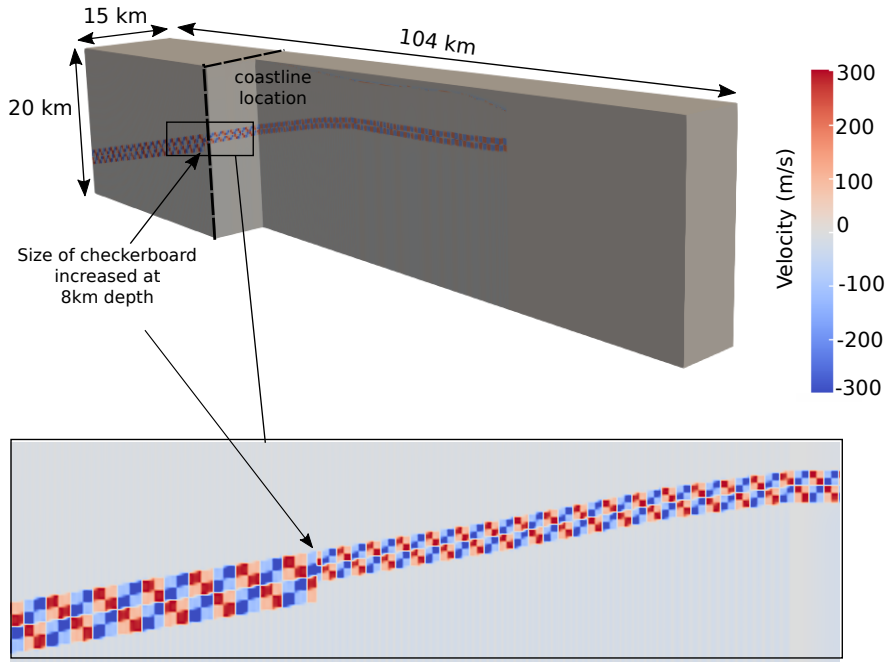


Figure 5.5: Cut-away diagram of the 3D checkerboard which will be added to the Start Model (Fig 5.2). The checkerboard lied along the top of the picked décollement.

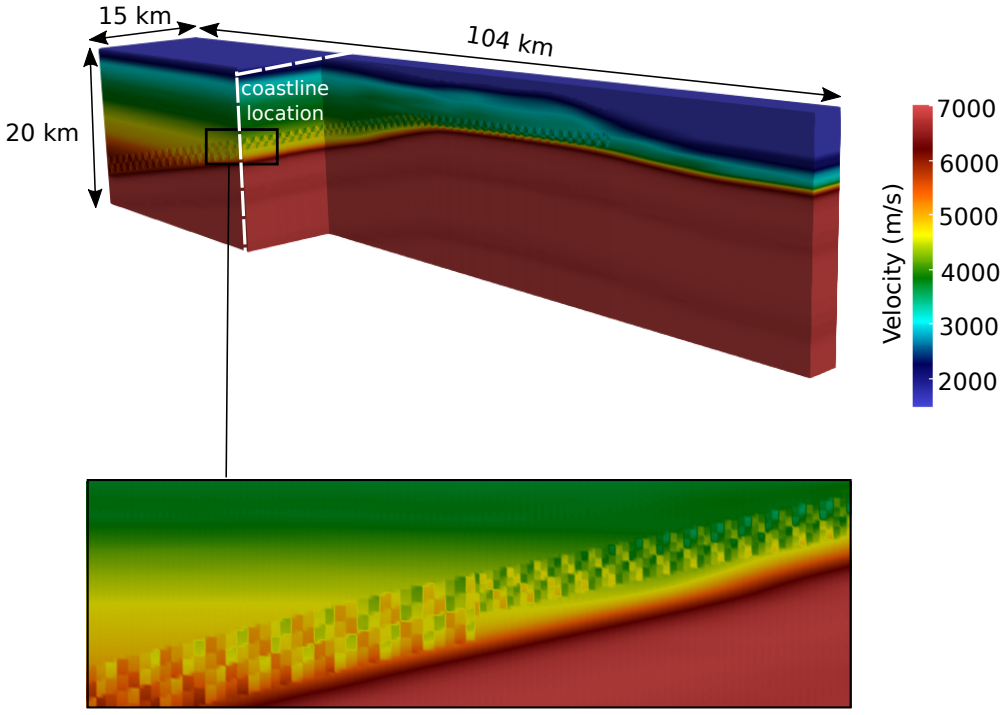


Figure 5.6: Cutaway image of the 3D true model the start model (Fig 5.2) with the checkerboard (Fig 5.5) added to it.

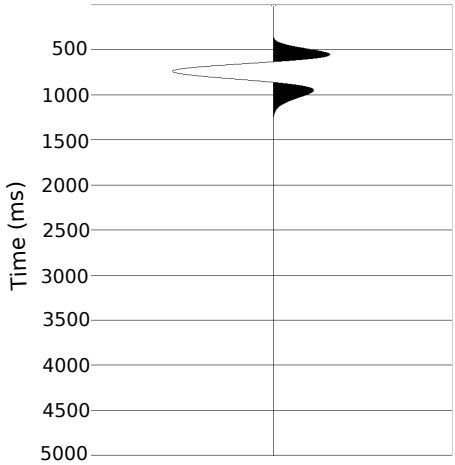


Figure 5.7: The source wavelet used to create the synthetic forward modelled seismic data to be used in the inversion. It is a Ricker wavelet of amplitude 1 shifted to start at 350ms.

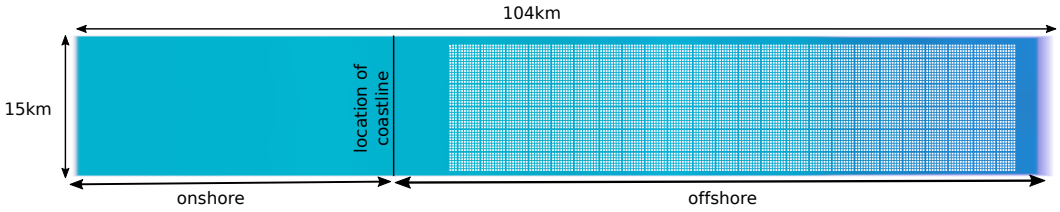


Figure 5.8: Bird's eye view of the 9000 offshore shots used in the synthetic FWI testing.

represents a marine source where the wavelet shown in Fig 5.7 is injected into the model, and recorded on the different receiver arrays.

5.3.1.5 Generating a synthetic field dataset for different receiver geometries

The layout of the OBS instruments had been previously decided as an offshore grid with 2km spacing between instruments within the region of the source shot points shown in Fig 5.8. I will test different layouts of the 180 land instruments which will be used for the real data acquisition. All layouts will use all 180 funded land receivers.

(a) Regular Grid layout

The first configuration is called the 'Regular Grid'. In this set-up, the 180 land receivers are placed in a regularly spaced grid, with a receiver every 1km, as shown in Fig 5.9. This covers the entire onshore portion of the study area as densely and evenly as possible. The land portion of the experiment is constrained to a maximum distance of 32km from the coast to keep the model appropriately small enough to reduce computational cost. Receivers are also ∼7km from the coastline to avoid noise caused by crashing waves at the coast.

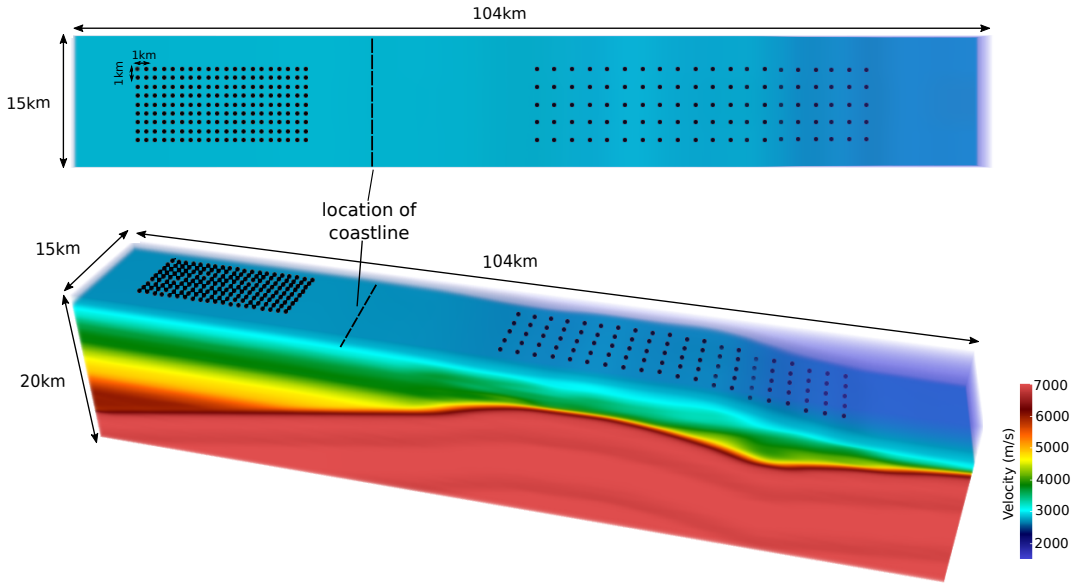


Figure 5.9: The arrangement of OBS and land receivers for the Regular Grid geometry shown in both birds eye view and across the entire 3D model.

(b) Dense Grid layout

The second layout is called the 'Dense Grid' and is shown in Fig 5.10. The layout comprises of a background coverage grid of receivers every 2km, with a dense concentration of 119 receivers in the centre with 500 x 500m spacing. The Dense Grid covers the entire study area at a similar spacing to the offshore instruments, but contains a much more concentrated area of receivers in the centre, which would represent the area where a mud volcano system could be present onshore, such as the one seen during the initial field scouting trip 5.1. This layout should test whether concentrating land receivers would be able to recover structure within the mud volcano system, without affecting the imaging resolution along the décollement.

5.3.1.6 Choosing an inversion scheme and running FWI.

5.3.1.6.1 Computing power The 3D model inversion requires a large amount of computational power. The low-order kernel has been used for inversions in chapter 4. The low-order kernel is 4th order in space and 2nd order in time. Based on the stability criteria (equations 2.27 and 2.28 in chapter 2), the time-sampling interval, δt, must be selected such that <50% of a grid-cell is crossed in one time-step. This means a relatively fine mesh has to be used which causes inversions to become computationally expensive.

The high-order kernel, on the other hand, is 10th order in space and either 2nd or 4th order in time. This improves the stability criteria, outlined in equations 2.29 and 2.30, and requires 3.6 grid points per wavelength to avoid numerical dispersion. Inversions on the high-order kernel are stable when

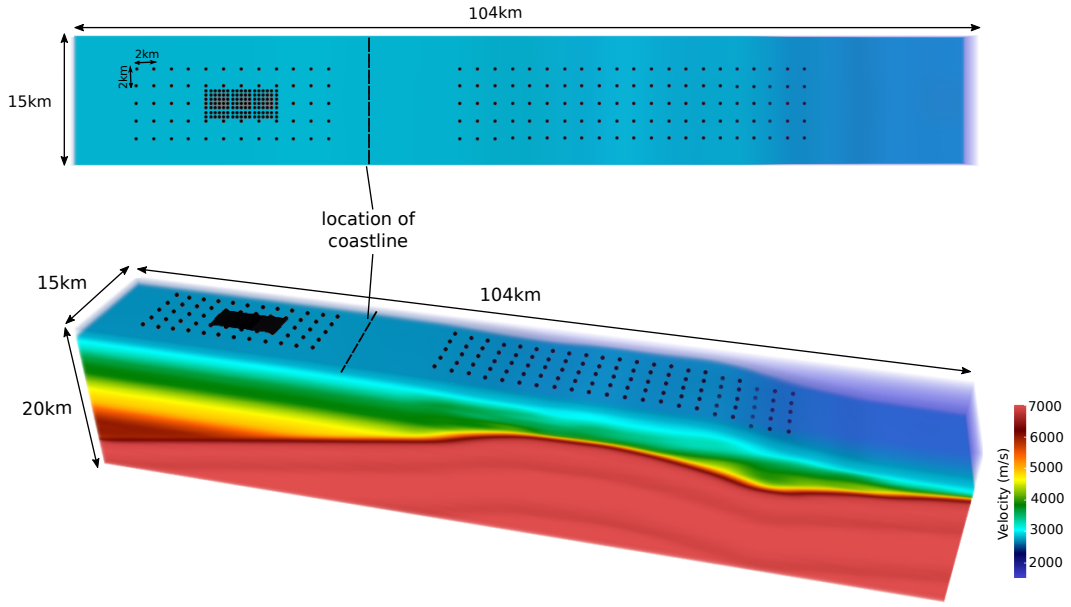


Figure 5.10: The arrangement of OBS and land receivers for the Dense Grid geometry shown in both birds eye view and across the entire 3D model.

the time-step, δt, is chosen such that <38% of each grid-cell is crossed per time step. This allows for a coarser grid and longer time-step for the same maximum frequency. The 4th order stencil in time operates as the double application of the 2nd order stencil. The 4th order stencil improves accuracy still, requiring 2.61 grid points per wavelength and remains stable when the wave field crosses <66% of each grid-cell per time step. When using the high-kernel, the 4th order stencil is automatically selected for better accuracy. During inversion, FULLWAVE uses the minimum velocity in the model and the frequency of the current iteration block to determine whether to use the 2nd or 4th order stencil. If the stability criteria are met for both stencils, the 2nd order stencil is automatically selected, if the criteria are only met for the 4th order stencil, then that stencil is used, otherwise, if neither criteria are met, the code will terminate (Silverton, 2015).

Using the high order kernel allows for a coarser grid-spacing of 100m and time sampling rate of 9ms with a maximum reliable pressure wave propagation frequency of 7.7 Hz and a maximum trace length of 15.012s. Moving to the high kernel dramatically reduces the computational effort needed during inversion, however the problem is still computationally expensive, taking ∼24 hours running on 53 nodes on a HPC system located in Brazil, with each iteration taking ∼30 minutes.

5.3.1.6.2 Inversion parameters As the tests use synthetic data, and the start and true models differ only by the addition of the checkerboard, there is no need for extensive testing of the start model as outlined in chapter 3, as it is known to be accurate.

The starting frequency is selected to ensure the majority of the data are not cycle-skipped, and the

misfit function is converging to a global, rather than a local minimum throughout the inversion, as outlined in chapter 2. The programs reciprocity functionality was also utilised, which allowed for the receivers to act as sources and vice versa, which drastically reduced computational costs. The parameters chosen for the checkerboard testing were as follows:

Table 5.1: Details of parameters used in the FWI modelling for the 3D checkerboard testing.

Property	Value
Total number of shots	9000
Total number of receivers	280
Minimum cut-off velocity (m/s)	1440
Maximum cut-off velocity (m/s)	8000
Grid size (m)	100
Time sampling rate (ms)	9
Maximum frequency in each iteration block (Hz)	2, 2.5, 3, 4, 5, 5.8
Iterations per frequency block	6-8
Number of shots used per iteration	38

The data were inverted over 6 frequency blocks, for which the input data are band-passed to remove frequencies higher than the maximum frequencies detailed in table 5.1 from 2 to 5.8 Hz. At a maximum frequency of 2 Hz, 6 iterations were performed, and for all other blocks, 8 iterations were performed. 38 composite shots were used per iteration, skipping 5 shots between each shot used. As outlined in chapter 2, low frequencies are beneficial for FWI imaging, and OBS instruments can contain usable data down to 2Hz (Morgan et al., 2013). I did fewer iterations at the lowest frequency band of up to 2Hz based on standard iteration suggestion outputs by the FWI code set-up.

5.3.1.7 Subtracting the resulting velocity model from the start model to determine how well the checkerboard is resolved.

Once the inversion is complete, the model produced by FWI, called the 'Final Model' can be subtracted from the start model. The result of subtracting the two models should recover the original checkerboard, or as close to the checkerboard as we are able to resolve using the chosen inversion scheme (Table 5.1). How well or poorly the initial checkerboard (Fig 5.5) is recovered will determine how well each receiver layout works, and help to determine how the land receivers will be distributed in the real NZ3D-FWI data acquisition.

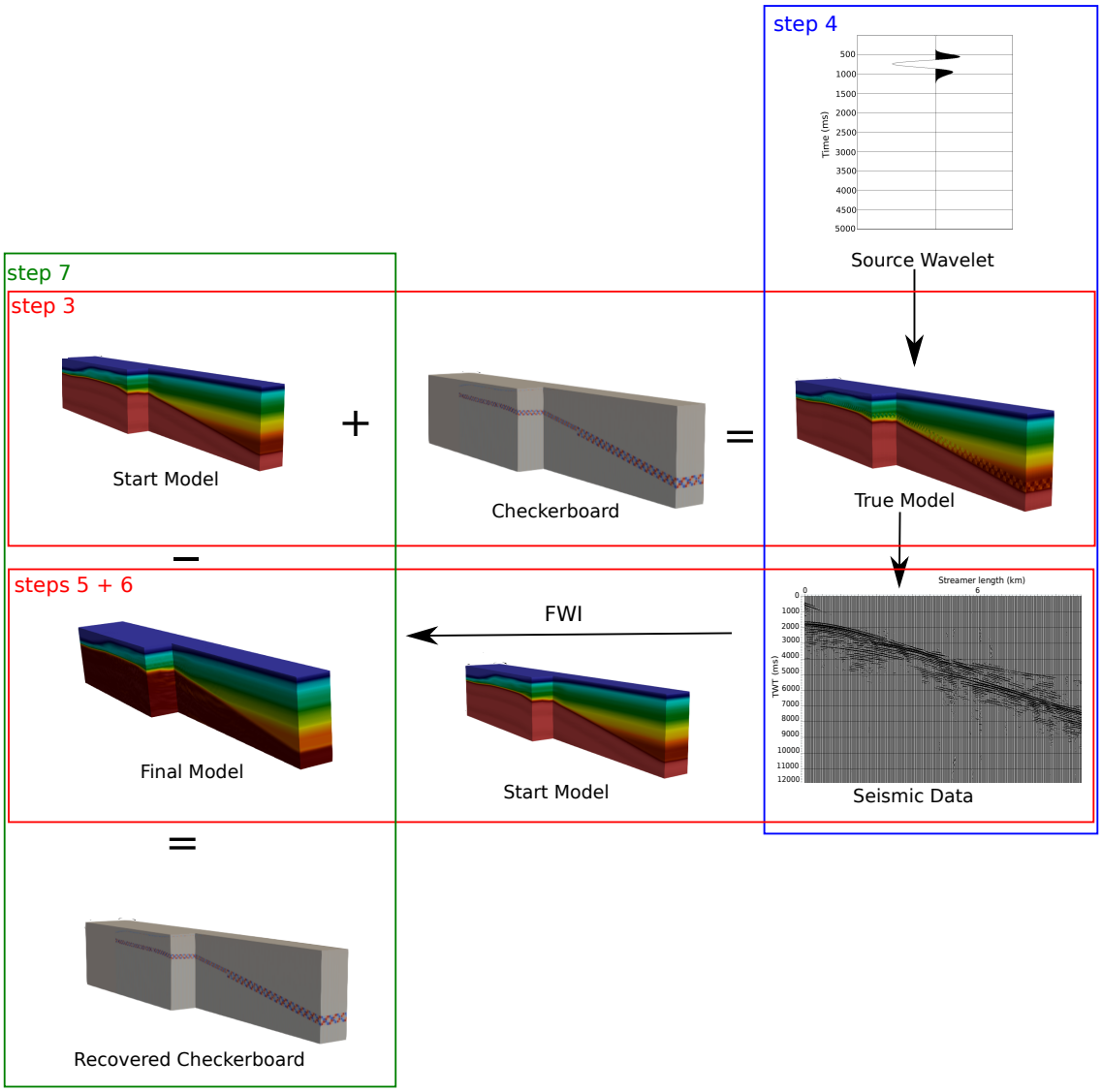


Figure 5.11: Schematic overview of the methods outlined in this section and how the results are calculated.

5.4 Results

5.4.1 General checkerboard recovery.

The results should ideally be close to the original checkerboard, as in Fig 5.5. We view the checkerboard on a surface extracted along the décollement as shown in Fig 5.12(a). The surface on which I display the results contains some areas where the full checkerboard is not displayed due to the presence of the seamount and topography along the décollement (Fig 5.12(b)). This is due to the inability to select the picked décollement in Paraview, the program used to create comprehensible images of the results used in this chapter, but rather a single, flat plane.

Fig 5.12(c) shows the recovery of the décollement checkerboard using the regular grid layout of land receivers (Fig 5.9). We see a good recovery of the smaller 300 x 300 x 300m checkerboards in the upper part of the décollement, however the full magnitude of the checks is not recovered. The results resolve between 50-80% of the original amplitude difference of the input checkerboard. In the central part, however, the checkerboards become quite smeared, and in the deep region where I use the larger checkerboard, coherent checks are not recovered, but rather a smeared striping effect. In the deepest parts of the model I do not recover the checkerboard at all.

Fig 5.12(d) shows the recovery of the décollement checkerboard using the dense grid layout of land receivers (Fig 5.10). There is a good recovery of the smaller 300 x 300 x 300m checkerboards in the upper part of the décollement, and again we do not recover the full magnitude of the checkers, but resolve between 50-75% of the original amplitude difference. The checks remain resolved until the transition between the small and larger checks, where we get a small portion of unresolved checks, and in the deeper part of the model which uses larger checks, we do not see coherent checks but rather a smeared striping effect. In the deepest parts of the model we again do not recover the checkerboard at all.

A positive feature of both models arises from the recovery of checkerboards outside the area of active sources highlighted by the white dashed boxes in Fig 15.12. This is extremely promising for the incorporation of land receivers into the NZ3D-FWI experiment geometry where there is no active source shooting, as some structure is still recoverable to large depths.

5.4.2 Target areas along the décollement

Three main areas I investigated were the proposed subducting seamount, the HRZ, and the region of plate coupling transition (Fig 5.13), as these are key targets of the 3D experiment, as detailed in section 5.2.3. At the proposed subducting seamount both the regular grid (Fig 5.14(b)) and dense grid (Fig 5.14(c)) recover the small 300 x 300 x 300m checks reasonably well, displaying distinctive alternating velocity increases and decreases. While we recover the approximate shape

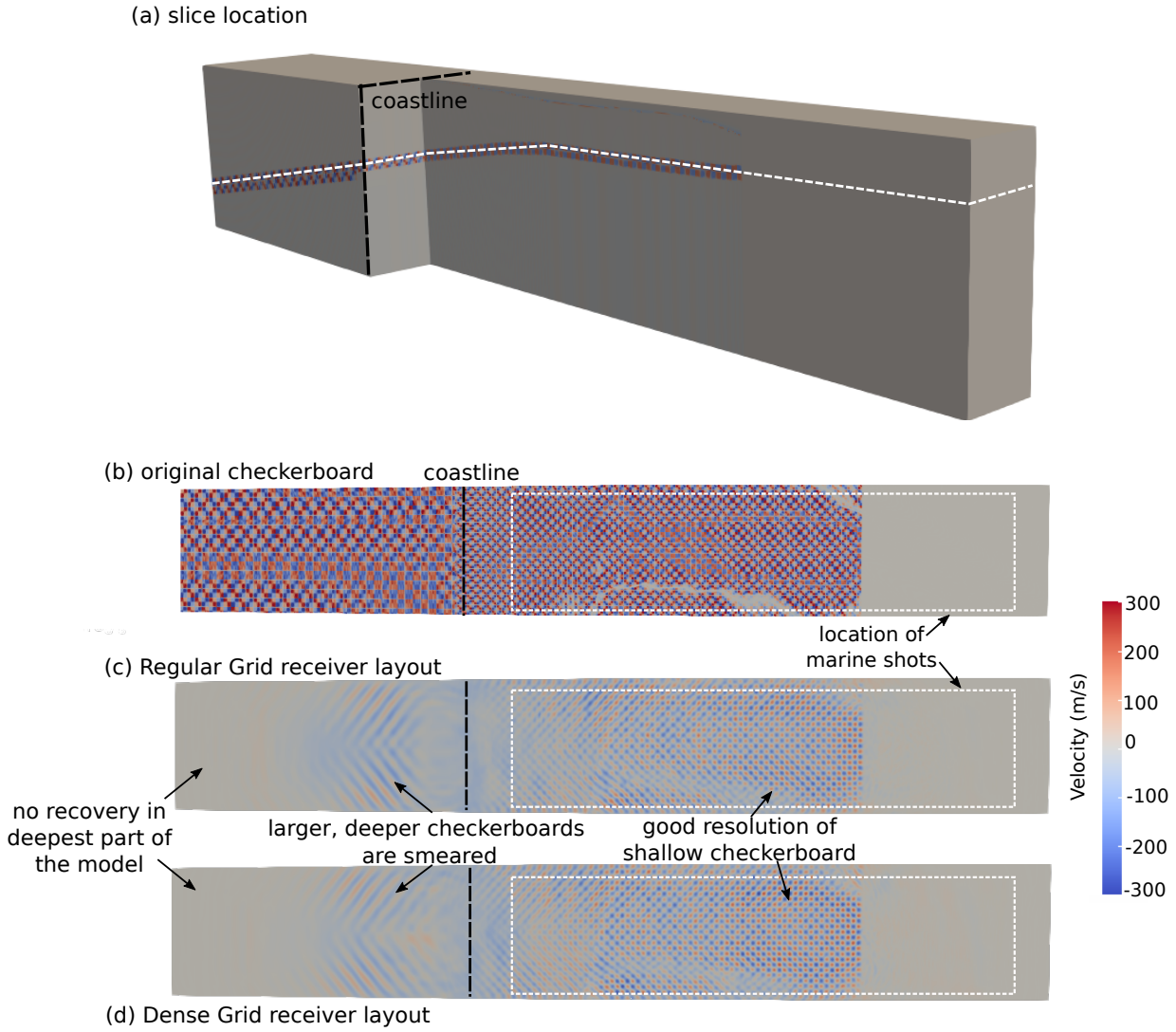


Figure 5.12: (a) The location of the slice taken through the model. (b) The original checkerboard. With perfect model resolution this is what we should resolve after FWI. Note that as the slice had to be picked along flat planes, topography of the checkerboard due to the addition of the seamount along the décollement causes some parts of the model to contain missing checks. (c) Results of the checkerboard test for the regular grid land receiver layout and (d) Results of the checkerboard test for the dense grid receiver land receiver layout.

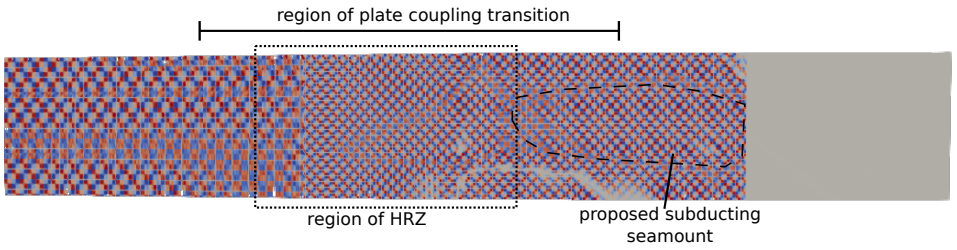


Figure 5.13: The slice extracted from the checkerboard shown in Fig 5.12, and (b), highlighting deeper target areas the subducting seamount, the HRZ and the region of the plate coupling transition outlined in Fig 5.1.

of the checkerboard, the distinction within checks of +/-100m/s and +/-300m/s are not recovered.

The dense grid array seems to recover the checkerboard slightly better in this region, showing a more defined checkerboard shape, and slightly less smearing, with higher amplitude recovery of ∼60% up to 80% both within the area containing the seamount and within the surrounding subducting plate. The regular grid recovers slightly less well defined checks with more smearing and slightly smaller recovered amplitudes of around ∼50% up to 70% averages over each check (Fig 5.14).

Within the HRZ and confirmed SSE zone ∼15km - < 2km below seafloor, a checkerboard pattern can still be seen for both land receiver layouts. The shallower part of the plate interface, further offshore, is relatively well resolved in terms of both checker shape and amplitude with ∼60% amplitude recovery and distinctive alternating positive and negative anomalies. While both layouts contain some smearing of the checkerboard at the edges of the model, as we move towards the coastline, the results from the two different layouts are slightly different. The regular grid (Fig 5.15(b)) resolves the checkerboard pattern in the centre of the model well, but poorly recovers amplitudes, in the range of ∼10-20%. The dense grid, however, has better amplitude recovery of ∼15-30%, but does not resolve individual checks, with the positive and negative checks merging together to form a striped pattern.

The region of transition between coupled and uncoupled plate interface lies between the subducting seamount and the HRZ (Fig 5.13) and therefore based on Figs 5.14 and 5.15, we can resolve the shallow transition well in both layouts (Fig 5.14), with resolution decreasing with depth (Fig 5.15).

5.4.3 Shallow targets

5.4.3.1 Additional checkerboard and receiver geometry.

As both land receiver layouts showed good recovery of the deeper targets - the plate interface, HRZ, and the proposed subducted seamount - we inserted an additional checkerboard into the model in order to see which layout might best resolve the shallow mud volcano targets in the onshore section of the model. This shallow mud volcano system was represented as a checkerboard comprising of small checks of +/- 20m/s and +/- 40m/s, equating to a 1-2% velocity anomaly from the background velocity of 2000m/s (Fig 5.16). This experiment was carried out using checks of 800 x 800 x 400m.

The smaller, 400 m checks were chosen as this is the expected recoverable size of anomalies with a background velocity of 2000m/s and inversion frequency up to 5.8Hz, however, we may not be able to resolve anomalies in this region of the model using only active source data from the marine shots, as the wavefield will be sub-vertical and have travelled a long distance from the source before reaching the receivers here (Fig 5.3).

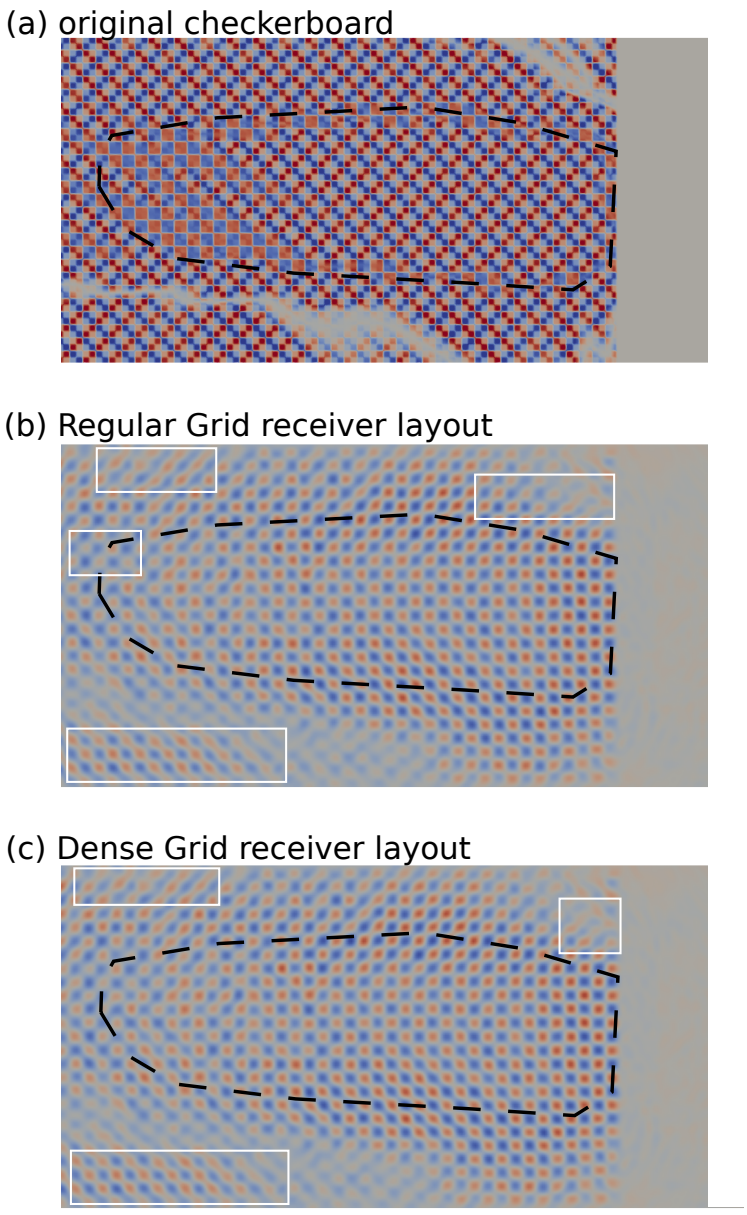


Figure 5.14: (a) Zoom-in of the true checkerboard along the picked slice (Fig 5.13(a)) at the key target of the subducting seamount shown by the black dashed outline. The results of the checkerboard test for the regular grid land receiver layout (b) and dense grid land receiver layout (c) at the seamount. White boxes highlight areas where the checkerboard structure is not fully resolved and a smearing effect between checks is seen.

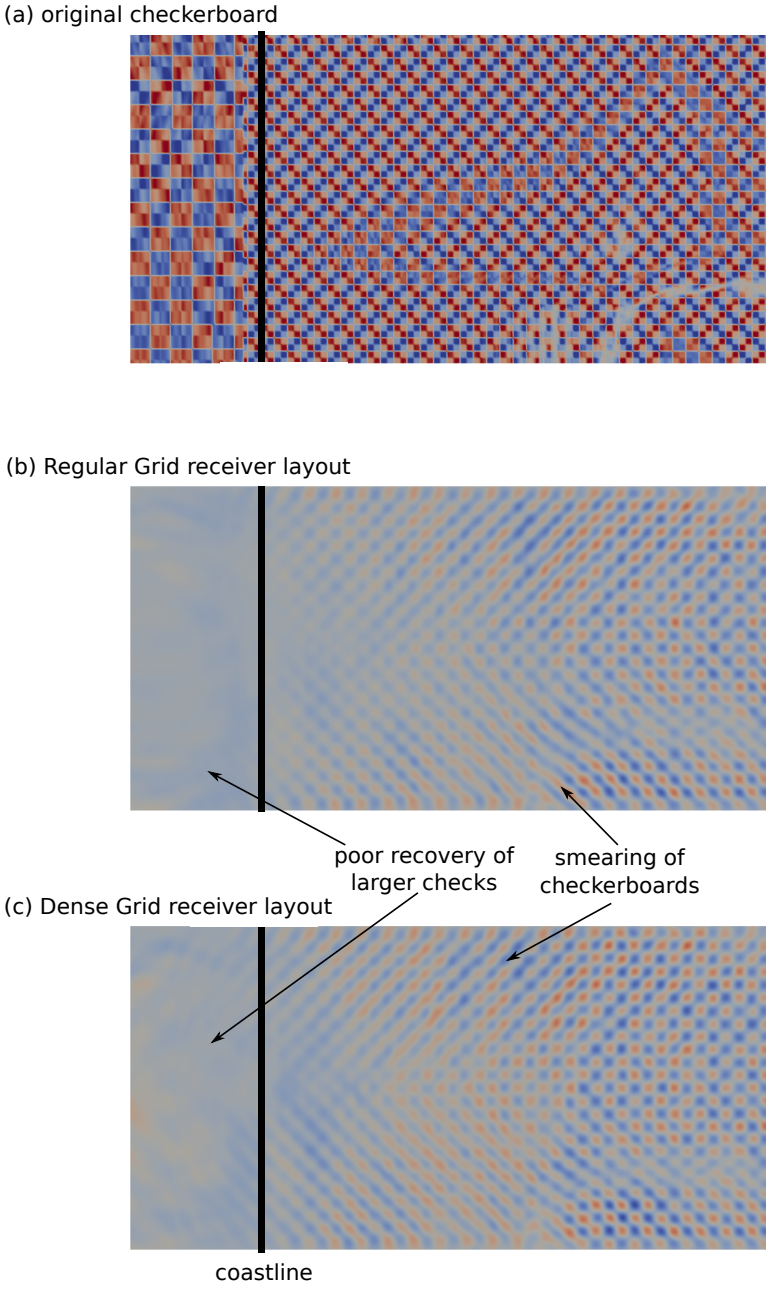


Figure 5.15: (a)Zoom-in of the true checkerboard along the picked slice (Fig 5.13(a)) at the key target of the HRZ. The results of the checkerboard test for the regular grid land receiver layout (b) and dense grid land receiver layout (c) at the HRZ. While checks are relatively well resolved in the offshore part of the model, there is poor recovery of the larger checks in the onshore part of the model.

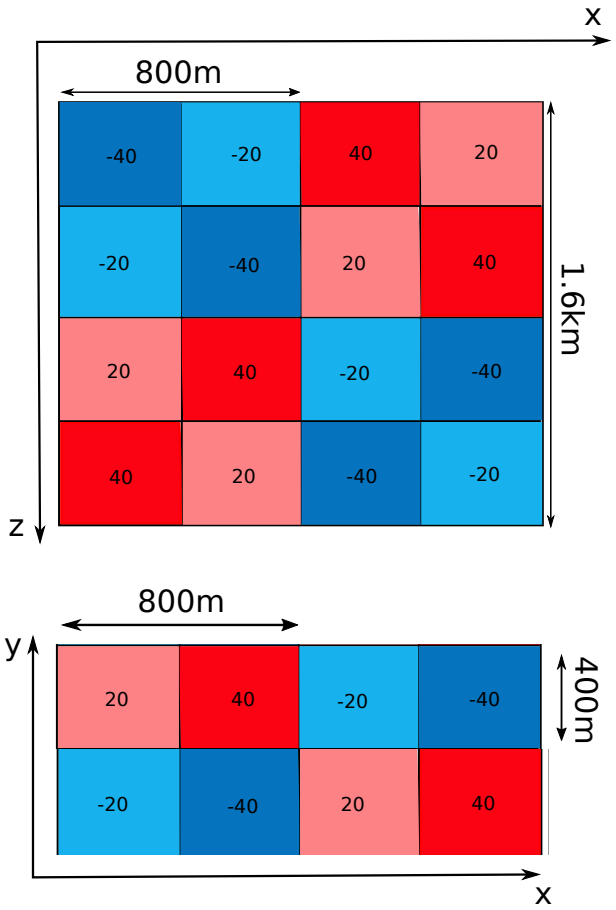


Figure 5.16: Schematic of the checkerboard used in the synthetic testing of the shallow target in the area of the mud volcano system. The numbers represent the velocity difference between the checkerboard and the background velocity model in Fig 5.2.

Without shots onshore, the limited azimuthal coverage may adversely affect recovery of the velocity structure across the mud volcanoes. Having land receivers around the mud volcano system will allow the instruments to pick up any activity directly caused by the mud volcano system, and passive seismic data can also be used to image this target.

The true model still includes the checkerboard along the décollement, as shown in Fig 5.17, to determine whether anomalous features such as the mud volcanoes on land will affect the use of FWI for imaging the deeper targets in this area. I specifically want to determine whether heterogeneities in the true model will affect the imaging along the plate interface.

I also included an additional instrument layout, called 'Combination Grid'. This layout takes aspects of the two previous receiver layouts, with instruments evenly spaced over the onshore part of the model in a 2 x 2km grid with a central receiver in the middle of each gridded square. A smaller, denser concentration of 85 land receivers was then inserted in the centre of the layout with regular spacing of 500 x 500m, outlined in Fig 5.18.

5.4.3.2 Recovery of shallow targets

Three slices through the checkerboard were compared, the first runs vertically through the checkerboard while the second and third run horizontally, near the top and bottom of the checkerboard (Fig 5.19).

Fig 5.20 shows a comparison between each of the receiver layouts for slice 1 through the small checkerboard in the region of the mud volcano (Fig 5.19). Fig 5.20(a) shows the actual checkerboard placed in the model while (b), (c) and (d) show results for the dense grid, regular grid and combination grid respectively. From the images we can see no real resolution of the checkerboard for either receiver layout. There is some potential faint recovery of the checkerboards in the uppermost parts of the regular and dense grid layouts, nearest to the offshore shot locations, highlighted by the white checkered boxes in Fig 5.20, however the amplitude recovery is extremely low and hence checks are difficult to determine. While in all three layouts we can perhaps see some alternating blue and red features, there is no real resolution of the distinct checkers within the model, and the results recover ∼10-25% of the initial amplitudes of the checkerboards, but across the whole slice rather than in the expected locations of the checkerboard. Several features are introduced which appear to be vertically-travelling rays through the vertical slice. From Fig 5.3 we see that all waves travelling through this part of the model, in the upper crust onshore, come from rays travelling sub-vertically. As features sub-perpendicular to the wavefield can be recovered, while parallel features cannot, this is likely the cause of these anomalies.

Fig 5.21 shows the results through depth slice 2, taken horizontally through the checkerboard, nearest to the surface (Fig 5.19). Results through this slice are slightly better, with some of the checkerboard being resolved, due to these check being sub-perpendicular to the wavefield. For the

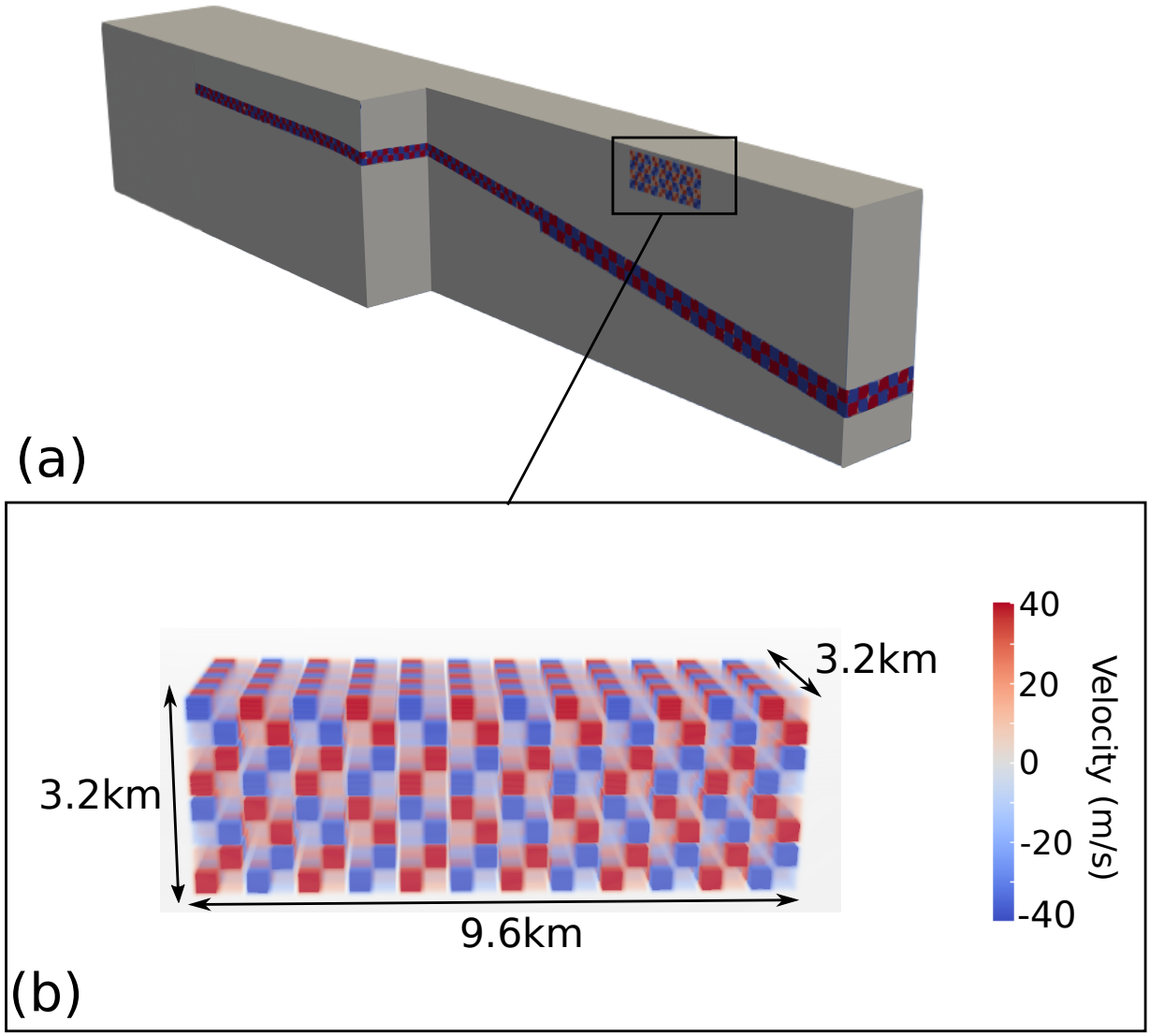


Figure 5.17: (a) The location of the checkerboard which represents the mud volcano as well as the checkerboard along the décollement. Note the model has been rotated horizontally 180 degrees to show the shallow checkerboard in the onshore part of the model. (b) Zoom-in of the checkerboard, detailing the dimensions.

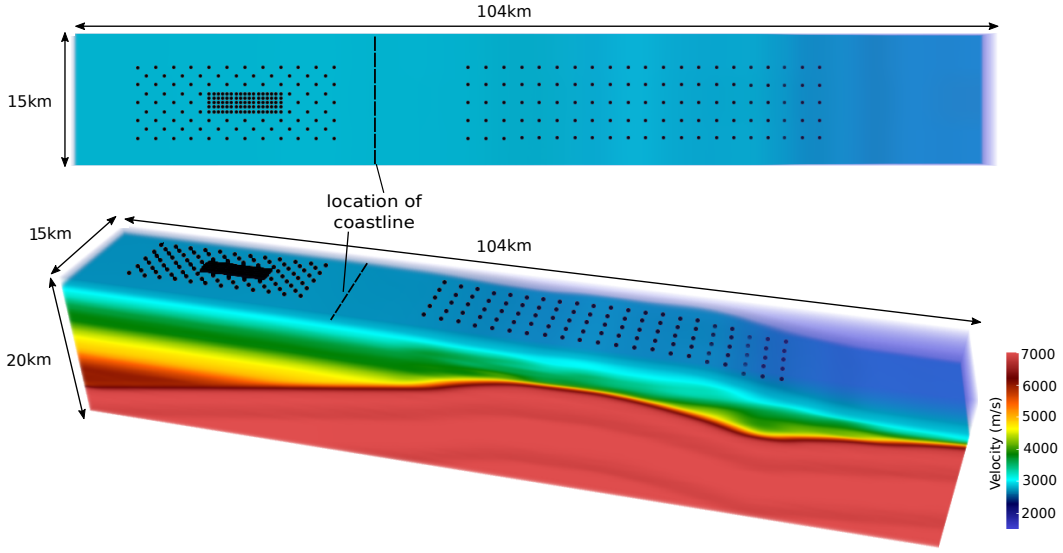


Figure 5.18: The arrangement of OBS and land receivers for the Combination Grid geometry shown in both birds eye view and across the entire 3D model.

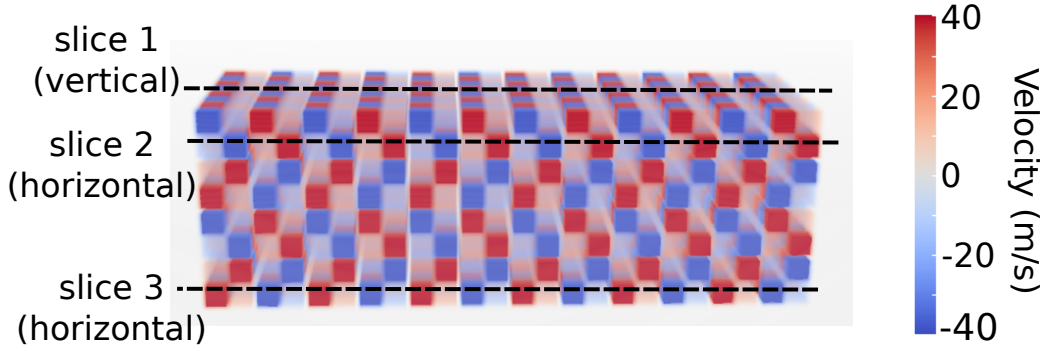


Figure 5.19: The shallow checkerboard shown in Fig 5.18, highlighting the three slices where results are compared for the three land receiver layouts. Note slice 1 is taken vertically through the block while slices 2 and 3 are taken horizontally.

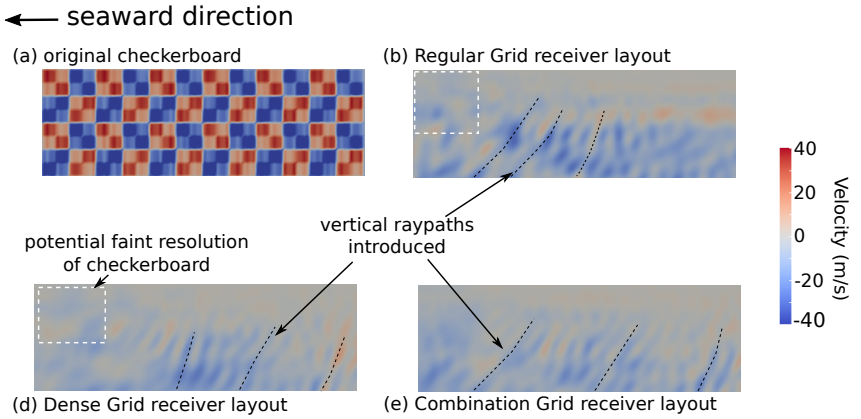


Figure 5.20: (a) Vertical slice 1 (Fig 5.19) through the actual checkerboard placed in the model. Results for the regular grid land receiver layout (b), dense grid land receiver layout (c) and combination grid land receiver layout (d) All three layouts poorly resolve the shallow checkerboard, with vertical anomalies shown, likely representing ray-paths in the inversion.

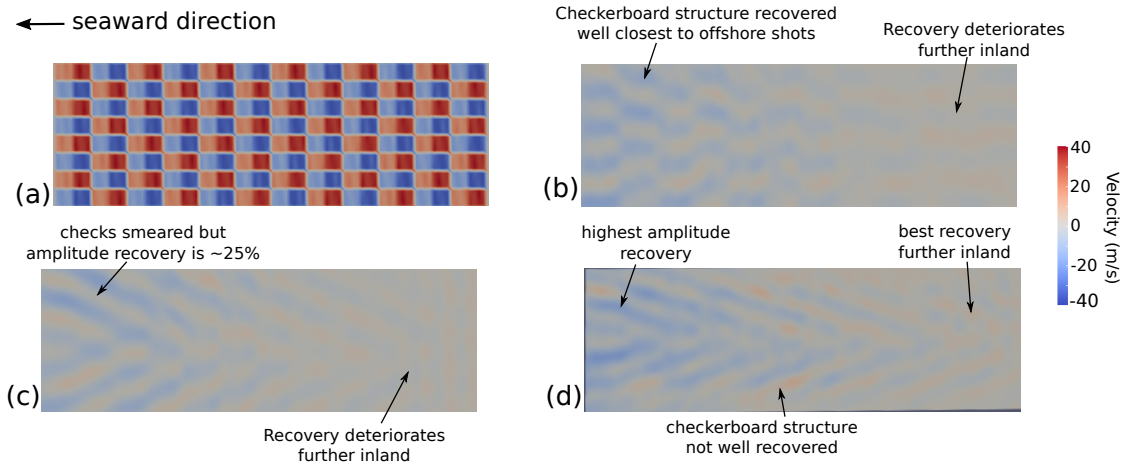


Figure 5.21: (a) Horizontal slice 2 (Fig 5.19) through the actual checkerboard placed in the model. Results for the regular grid land receiver layout (b), dense grid land receiver layout (c) and combination grid land receiver layout (d). Some resolution of structure and amplitude can be seen.

regular grid receiver layout, the checkerboard structure is recovered in the slice, especially in the part of the checkerboard nearer to the offshore part of the model where the sources are coming from. Amplitude recovery for these checks are ∼10-20% of the original checkerboard amplitudes. The dense grid and combination grid layouts also recover some checkerboard structure with amplitudes of ∼10-30% of the original checkerboard, however the checks are smeared into one another to produce the striped effect seen in Fig 5.21 (c),(d). In all three layouts the recovery deteriorates as the slice moves further inland away from the shots, until very little to none of the original checkerboard is recovered. The combination grid layout recovers some semblance of the checkerboard pattern the best further inland, but amplitudes are ∼10% of the original checkerboard. Improved resolution of checks in this slice is likely due to the proximity of the anomalies to the receivers.

The final slice, slice 3 (Fig 5.22), is taken horizontally through the checkerboard area in the deeper part of the test location (Fig 5.19). Here we see that all three layouts produce poor checkerboard

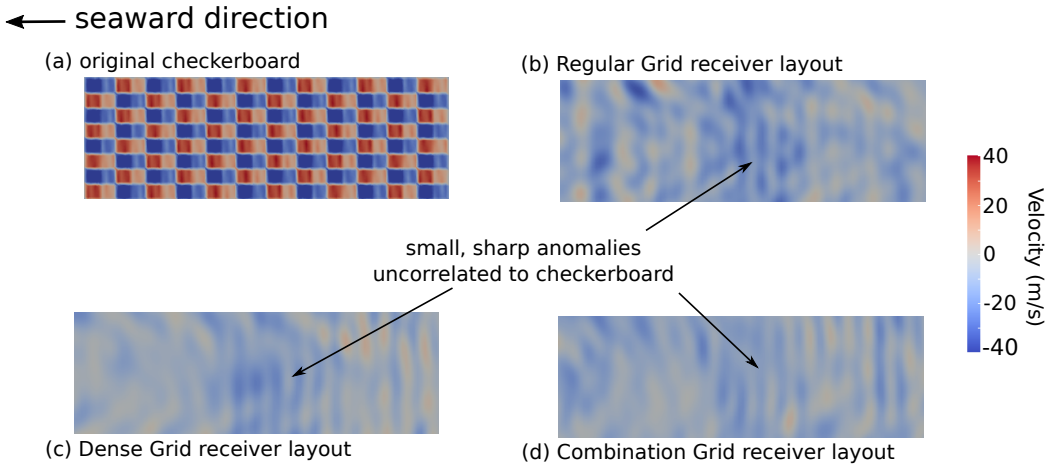


Figure 5.22: (a) Horizontal slice 3 (Fig 5.19) through the actual checkerboard placed in the model. Results for the regular grid land receiver layout (b), dense grid land receiver layout (c) and combination grid land receiver layout (d) All three layouts poorly resolve the shallow checkerboard, displaying several small, sharp anomalies.

recovery. Each layout produces small, sharp anomalies which do not correlate well to the initial checkerboard. This is likely related to the sub-vertical ray-paths shown in Fig 5.20. As the inversion employs reciprocity as well as skipping shots at each iteration (Table 5.1) these rays will not be inverted all at once, making the resolution of features in this slice increasingly difficult to recover.

Overall it should be noted that the checkerboard used to test resolution of the mud volcano system is an extremely complicated and difficult test for resolution in the area furthest from the offshore shots. The sharp velocity boundaries between checkerboards will cause reflections which will interfere with each other and a complicated waveform, as well as reduce the amplitude of the transmitted arrivals. As FWI uses the Born approximation to compute the gradient (see chapter 2), resolution of these extremely complex arrivals may be possible with many more iterations than used in the synthetic testing, but time constraints and computational cost did not allow for this in these synthetic tests. The inversion scheme used in these synthetic tests (Table 5.1) used all offsets and times of the real field data travelling through the true model containing the checkerboard. As the shallow, complex checkerboard is likely to produce many small reflections and spurious arrivals, windowing the data and/or adding offsets slowly to the inversion, as done with the real data in chapters 3 and 4 may also help to resolve the shallow checkerboard better, however, again due to time constraints and computational costs, this was not investigated. The checkerboard is also an unrealistic representation of the mud volcano system, which will likely contain larger, smoother velocity anomalies. Therefore, the fact that we are still able to resolve some features in the upper part of the checkerboard (Fig 5.21) is promising in the use of FWI to image some features in this region.

5.4.3.3 Recovery of deeper targets with heterogeneities in the shallow model.

A secondary reason for adding the smaller, shallow checkerboard was to test the recovery of the deeper targets when heterogeneities exist in the shallow subsurface. As there is no model for the true smaller-scale structure expected to be caused by the volcanic system, this may produce errors in the deeper target checkerboard tests, which will appear as a superposition of velocity errors through shallower heterogeneities (Morgan et al., 2013).

Results (Fig 5.23) show that the checkerboard along the décollement is again resolved relatively well for the three layouts, with little discernible difference between results for the initial tests (regular grid and dense grid - Fig 5.12) and the test including the shallow heterogeneities. The results for the third, additional layout, the combination grid (Fig 5.18), are of a similar resolution to the other land receiver geometry layouts. The smaller 300 x 300 x 300m checkerboard is resolved both in the shallower offshore part of the décollement, as well as along the steeply sloping part of the plate interface up to the coastline (Fig 5.23(e)). The larger 500 x 500 x 500m checks, however, are still less well resolved, and are smeared into each other, producing a striped effect. In the deepest part of the model, the large checkerboard is no longer recovered.

Looking more closely at the targets along the décollement, it is clear that the introduction of the shallow heterogeneities has not deteriorated the results for the regular and dense grid layouts (Fig 5.25). Some smearing of the checkerboards has still occurred around the edges of the model and the proposed subducting seamount, but the checkerboard structure remains well resolved across the target.

The combination grid array seems to recover the checkerboard slightly better than the other layouts in this region, showing defined checkerboard shape, with higher amplitude recovery of ∼60% and up to 80% both within the area containing the seamount and within the surrounding subducting plate.

Resolution of the HRZ is again very similar to initial tests for the three receiver layouts, with well resolved, smaller checks furthest away from the coastline. Moving further towards the coastline and into the onshore section, resolution deceases. No layout resolves the larger 500 x 500 x 500m checks, but instead each produces striped positive and negative anomalies where the checks have smeared together. The regular grid layout (Fig 5.9) resolves structure slightly better in the central part of the model, while the dense grid layout (Fig 5.10) better recovers the amplitude but less structure. The combination grid layout (Fig 5.18) appears to lie somewhere in between these two results, with the recovered structure more defined than the dense grid layout but less defined than the regular grid layout, and the amplitudes higher than the dense grid layout buy lower than the regular grid layout.

Again we can use these same inferences for recovery of the plate coupling transition zone (Fig

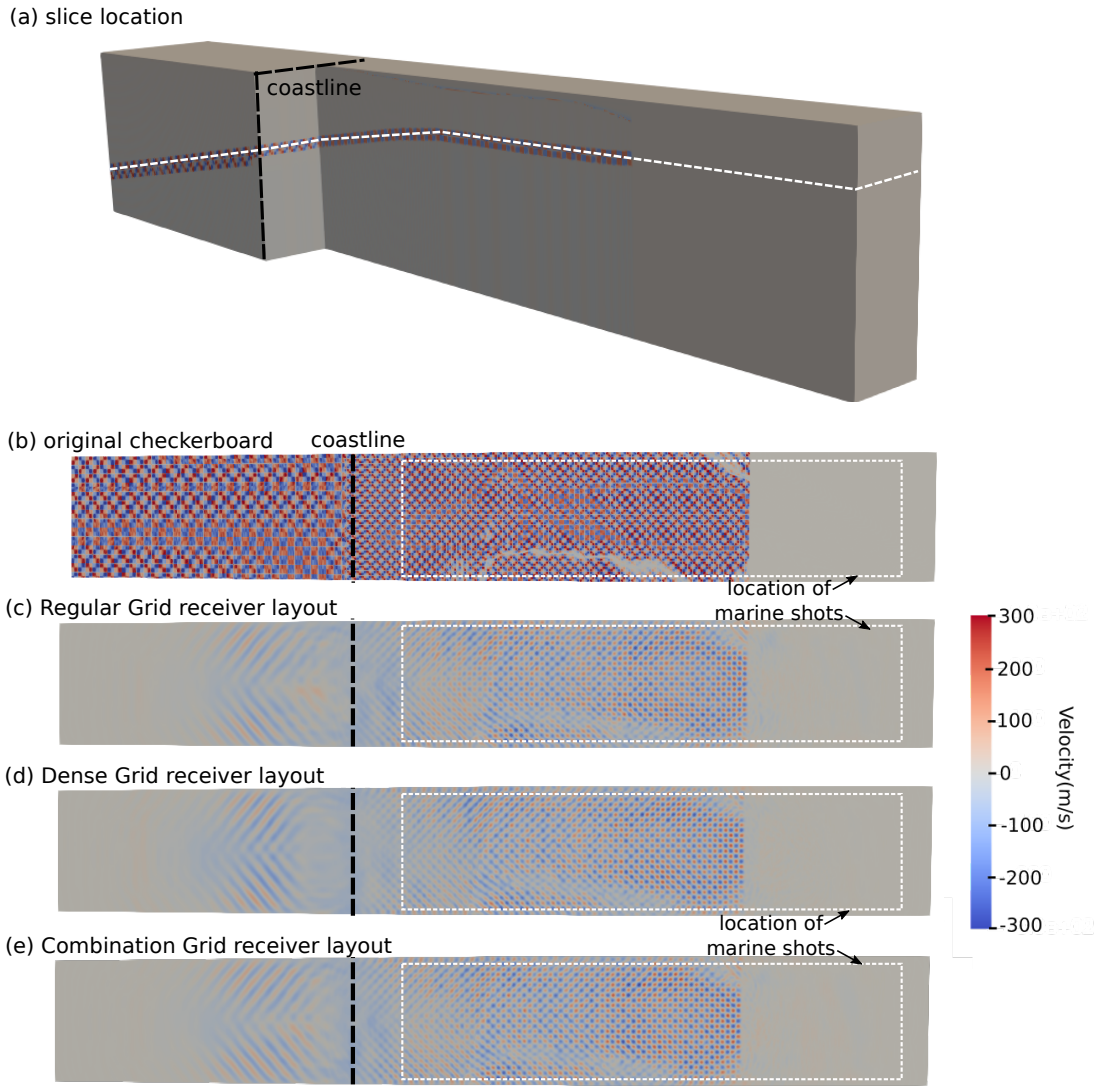
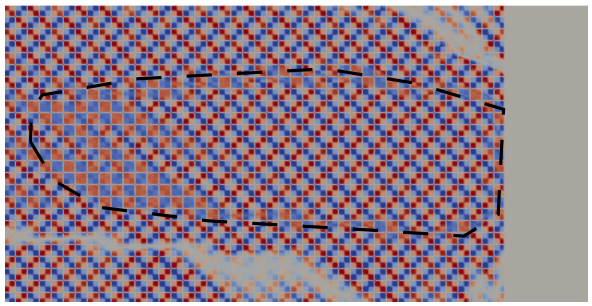
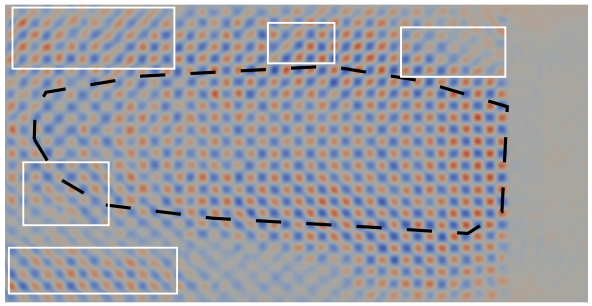


Figure 5.23: (a) The location of the slice taken through the model. (b) The original checkerboard. With perfect model resolution this is what we should resolve after FWI. Note that as the slice had to be picked along flat planes, topography of the checkerboard due to the addition of the seamount along the décollement causes some parts of the model to contain missing checks. Results of the checkerboard test for the regular grid land receiver layout (c), dense grid receiver land receiver layout (d) and combination grid land receiver layout (E). White dashed boxes show the location of the marine shots.

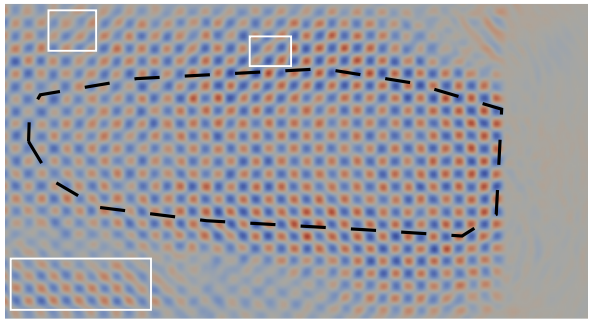
(a) original checkerboard



(b) Regular Grid receiver layout



(c) Dense Grid receiver layout



(d) Combination Grid receiver layout

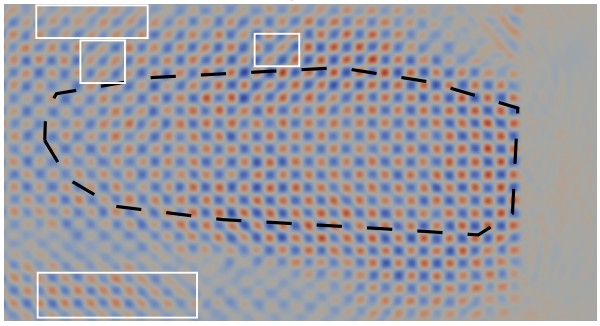


Figure 5.24: (a) Zoom-in of the true checkerboard along the picked slice (Fig 5.23(a)) at the key target of the subducting seamount shown by the black dashed outline. The results of the checkerboard test for the regular grid land receiver layout (b), dense grid land receiver layout (c), and combination grid receiver layout (d) at the seamount. White boxes highlight areas where the checkerboard structure is not fully resolved and a smearing effect between checks is seen.

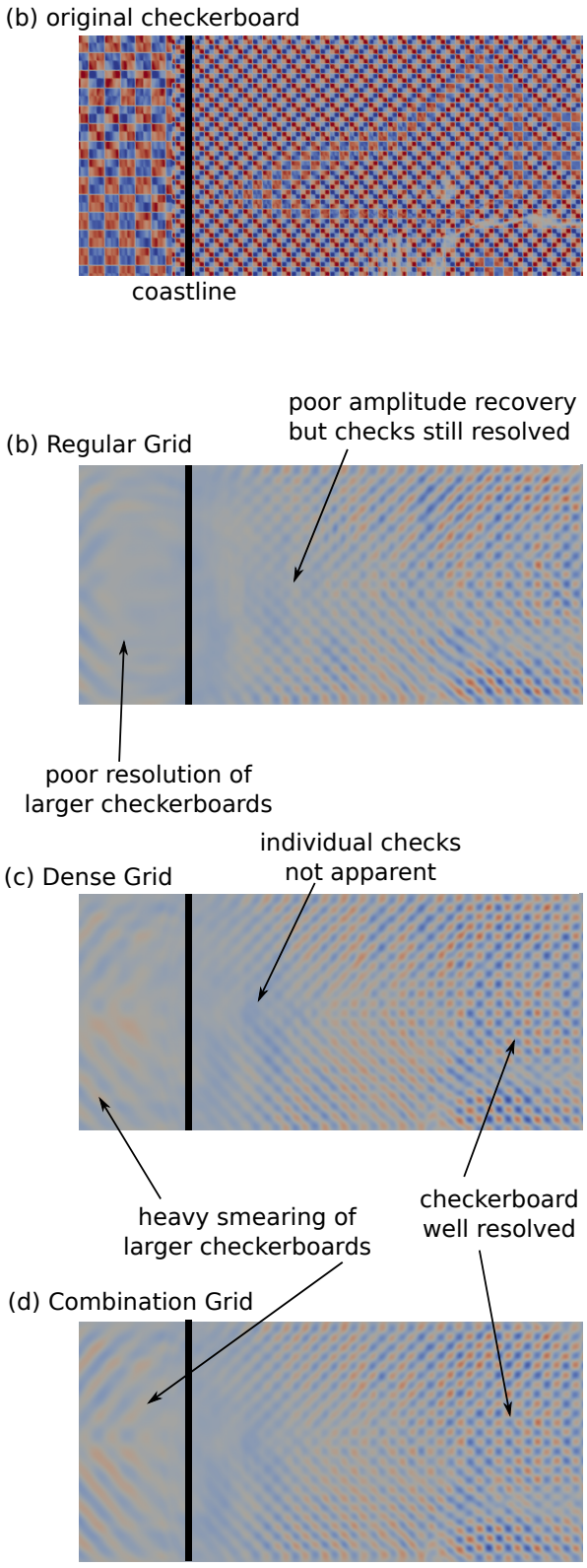


Figure 5.25: (a) Zoom-in of the true checkerboard along the picked slice (Fig 5.23(a)) at the key target of the HRZ. The results of the checkerboard test for the regular grid land receiver layout (b), dense grid land receiver layout (c), and combination grid land receiver layout (d) at the HRZ. While checks are relatively well resolved in the offshore part of the model, there is poor recovery of the larger checks in the onshore part of the model.

5.1(a)), as this region lies between the subducted seamount and the HRZ (Fig 5.13).

5.5 Discussion

The checkerboard tests reveal that we can expect to recover features with a size of ∼ 300 x 300 x 300m at the target depths along the décollement. This includes the proposed subducted seamount, the HRZ and the region where there is a down-dip change in plate coupling. This finding is encouraging and suggests the NZ3D-FWI experiment will allow imaging of the deeper targets outlined with the given amount of receivers. As the theoretical resolution of FWI is approximately half the seismic wavelength (Pratt, 1999), for inversion up to 5.8 Hz, in the shallow décollement where background velocities are ∼3500 m/s theoretical resolution is ∼300 m and in the deeper décollement where checkerboard size increases and background velocities are ∼5500m/s the theoretical resolution is ∼475m. In chapter 4, the final FWI model was computed up to 8Hz. If we inverted up to 8Hz for the 3D model, theoretical resolution in the shallow décollement would increase to ∼220m and in the deeper dcollement to ∼340m.

The resolution revealed through checkerboard testing achieves close to this theoretical resolution in the shallow décollement up to 5.4 Hz, however in the deeper décollement >8kmbsf, the FWI was unable to resolve the larger checkerboard features of 500 m. This indicates that we can harness close to the full potential of FWI to image targets in the shallow décollement, such as the subducting seamount and HRZ, but the deeper décollement will be less well resolved given the number of available instruments. This is to be expected as at these depths of ∼15km there are less turning rays travelling through the model, and therefore less illumination of these deeper targets (Fig 5.3). The shallower décollement, however, is well illuminated, with the majority of turning rays between sources and receivers passing through this part of the model with various offsets and azimuths, both useful ingredients for successful FWI as outlined in chapter 2 (Fig 5.3) (Morgan et al., 2013). Although untested with the checkerboard models shown in this chapter, these results are promising for the targets of the upper plates and incoming section, which lie at shallower depths that the décollement, as these region contain many turning rays (Fig 5.3), and with lowered velocities of ∼2000m/s we can theoretically expect resolution of ∼170m for inversions up to 5.4Hz. As close to theoretical resolution was achieved at the décollement, this may also be achievable at shallower depths where there are more turning rays (Fig 5.3), and high resolution analysis of upper plate structure was achieved in chapter 4 with limited streamer offsets, which are much improved by using OBS instruments in the NZ3D-FWI experiment.

The checkerboard tests also reveal that for imaging of the deeper targets, the onshore receiver layouts produce small differences in the resolution of the checkerboard along the décollement. This indicates that in these areas, primary imaging will arise from the OBS instruments located offshore. As the OBS instruments are located within the region of the offshore shots, the instruments will record the maximum range of offsets and azimuths for the most illumination of the shallow

décollement targets. The addition of the land instruments allows imaging outside of this region of offshore shots, evidenced by checkerboard recovery beyond the shot locations. Including these land instruments is important for extending imaging both deeper, and further inland than using just marine receivers alone.

The smaller checkerboard representing the mud volcano system, on the other hand, is poorly resolved for each model layout. These results are to be somewhat expected due to the lack of turning rays within the land portion of the model (Fig 5.3). Along the upper décollement, the OBS receivers and shots allow for sub-horizontal, multi-azimuthal coverage (Fig 5.3), with data from horizontal rays being collected at each receiver. In the land portion, however, there are no shots, only receivers and so it is difficult to resolve anomalies here. Within the land portion, we therefore have a lower ray density with a majority of vertical rays (Fig 5.3). The checkerboard used to test resolution in the region of the mud volcano is also quite intricate, and so expecting to resolve these small scale, highly variable features was perhaps quite optimistic. In the case of the true geology of the mud volcano system we can expect smoother edges to the anomalies and will likely be able to resolve some features in this region using FWI. It is also worth noting that sources besides marine shots may be recorded on the land receivers such as local earthquakes and activity from within the volcanic system itself which can be used to better image the system by receivers in this area, therefore having more receivers in this region is likely to be beneficial for imaging the mud volcano.

Despite the addition of these extremely complex heterogeneities introduced by the smaller checkerboard representing the mud volcano, the larger checkerboard along the plate interface is still well resolved, shown for each receiver layout in Fig 5.23. The results of the analysis show the combination grid appears to take the benefits of the two other layouts by maximising the trade of between amplitude resolution and structure.

While the results of the checkerboard testing are promising, one should not forget the simplistic models used in producing these tests. The simple velocity model containing no lateral variations aside from the introduction of the seamount are not realistic in the true study area, and the layered velocity structure is also unrealistic, as examined in chapter 4. The checkerboards contain unnaturally sharp boundaries, the coastline is modelled as a straight boundary, and the land portion of the model contains no topography despite complex, steep changes in topography at the real study area. Therefore, while synthetic testing shows good resolution can be achieved using FWI, by using the real experimental data, containing complex laterally and vertically changing velocities, and complex land topography, we may not achieve this level of resolution.

5.6 Choosing a layout

The results produced two main finding for choosing a land receiver layout:

(a) Inclusion of a dense receiver array did not make much difference in the resolution of imaging key targets along the plate interface.

Imaging of the key targets including the proposed subducting seamount, the region of the HRZ, and the region where the down-dip plate coupling changes is not degraded when modelling a land receiver grid spaced 2 x 2km compared to a denser 1 x 1km spaced array. While the inclusion of a land array is extremely beneficial in imaging deeper targets outside of the offshore grid of OBS instruments, away from all marine shots, increasing the spacing between these receivers has little effect on the quality of imaging along the plate interface.

(b) The inclusion of the dense array onshore may result in investigation of the mechanisms at play within the mud volcano system.

As extra instruments are not needed for the improvement of active source modelling with FWI, it would be beneficial to place these instruments in an area with interesting passive targets. Based on landowners accounts of mud volcanoes erupting and fences moving over time, and the seismically active nature of New Zealand, it would make most sense to have more receivers near to the mud volcanoes. Possibilities of recording activity from the mud volcano system including passive seismic by local earthquakes and any seismic activity caused by the volcano itself could potentially allow further insight into the relationship between the mud volcanoes and the subduction zone. As well as the further insight into what drives the mud volcanic system, and additional activity recorded by receivers in this region can illuminate any potential hazards for the land-owners and nearby residents and/or infrastructure.

Based on these findings, the combination grid array (Fig 5.18) was chosen as the optimal layout for data acquisition. This allowed for the best overall land coverage while still including a denser array of receivers around the mud volcanoes.

The following section shows the field acquisition report for the NZ3D-FWI experiment where the selected layout of land instruments was used in data acquisition, detailing the types of receivers used, and example data from the instruments recording marine seismic shots.

Part II : Execution of NZ3D-FWI Experiment

The NZ3D-FWI experiment was a large 3D seismic survey across the Hikurangi megathrust in the vicinity of offshore Gisborne. The experiment consisted of a 3D streamer dataset, as well as a 3D dataset made up of OBS and land geophone instruments. The 3D streamer dataset will be processed to produce a 3D volume of reflection seismic data (Solomon et al., 2018), and the land and OBS data can be used to compute a large, 3D FWI model, the design of which is explained in Part I. The instruments will record data produced by a marine acoustic source, and the land and OBS instruments, in addition, will record passive data measurements produced by local, regional and global seismic activity. The layout of the land geophones was based on the analysis shown in part 1 of this chapter. The experiment coincided with two IODP Expeditions (372 and 375), some data of which was shown in chapter 4, and will be presented more in the following chapter (chapter 6). This section will deal exclusively with the experiment layout of receivers, as they relate to the experimental design and synthetic experiments described in Part I of this chapter.

I was fortunate enough to be part of the land deployment crew, installing the three types of geophone (6TD, GSX and Cube geophones) between December 2017 and January 2018. After the deployment of all these land instruments, I joined the science party onboard the R/V Marcus G. Langseth from January 6 to February 9, 2018. Onboard I was involved in the deployment and recovery of the four streamers, quality control of incoming seismic data, creating acquisition logs, monitoring weather conditions, and initial interpretations of some of the incoming seismic lines in the 3D streamer dataset.

This part of the chapter has been incorporated into an official project field report: *New Zealand 3D Full Waveform Inversion (NZ3D-FWI) 2017-2018 Field Acquisition Report*(R. Bell, **M. Gray**, J. Morgan, M. Warner, A. Fagereng, L. McNeill, K., Jacobs, S. Henrys, B. Fry, S. Watkins, H. Lacey, J. Black, V. Lane, D. Daly, D. Lindsay, N. Bangs, R. Arai, S. Kodaira and the NZ3D-FWI team) which has been published through GNS Science. This chapter primarily details my contribution to the report, some figures and figure-parts which I produced for the report are shown, but the report is cited as the source of these figures.

5.7 Deployments

The NZ3D-FWI project consisted of three main dataset acquisitions:

(a) A 3D cube ($\sim$ 60 x15km surface area) of multi-channel hydrophone streamer data (MGL1810) collected by the R/V Marcus G. Langseth using four 6km streamers.

(b) A wide-azimuth OBS dataset collected at 100 OBS instruments in the same area as the 3D

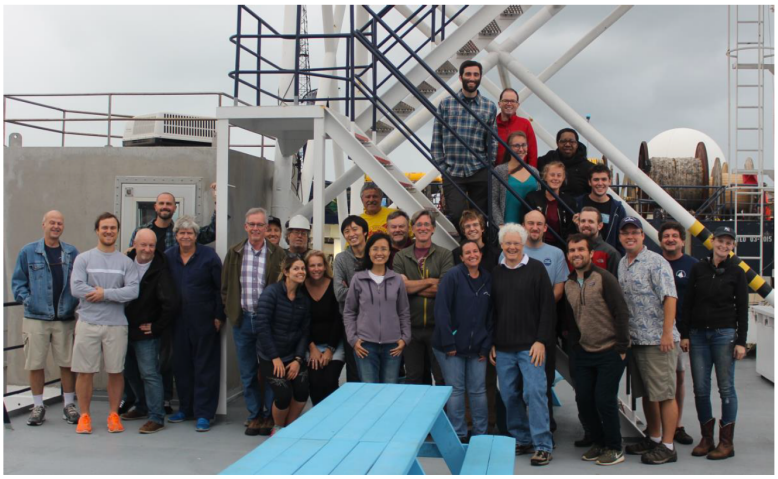


Figure 5.26: Crew and science party onboard the R/V Marcus G. Langseth for the NZ3D-FWI experiment.

streamer dataset.

(c) The NZ3D-FWI dataset recorded on 193 land geophones deployed in the Gisborne region over a ∼30 x 15km surface area.

All three datasets were recorded using active source signals produced by airgun sources towed by the R/V Marcus G. Langseth between 7th January and 9th February 2018, with additional data from passive measurements recorded by OBS and land instruments. This additional passive data was recorded by the OBS array and part of the land array.

The land data were recorded by stations deployed in two different arrays with different objectives. This was based on the synthetic testing carried out in part 1 of this chapter, and the chosen, 'Combination Grid' layout (Fig 5.18). Below, I outline these two different deployments, the datasets collected, and their main objectives. The deployments include a broad array named the 'Gisborne array' aimed at imaging the Hikurangi subduction zone and collecting data suitable for 3D FWI. A dense array named the 'Waiamata Valley array' is also aimed at imaging the Waimata Valley mud-volcano system in high-resolution. During the active source shooting, an additional experiment called SHIRE, funded by NSF and New Zealand had 88 instruments deployed onshore. In total, 144 short-period, and 49 long-period instruments were deployed specifically for this experiment, meaning the NZ3D-FWI and SHIRE experiments combined led to a total of 281 instruments recording shots from the R/V Marcus G. Langseth.

5.7.1 Gisborne Array

50 Guralp CMG-6TD broadband seismometers from NERC Geophysical Equipment Facility SeisUK were shipped to New Zealand for deployment, and 49 of these instruments were in working order to be deployed. They were deployed in a roughly regular array over a region of approximately 15 x 20km (Fig 5.27). The primary focus of this array is to record offshore seismic shots produced

by the R/V Langseth during the 3D seismic reflection data collection. Instruments were deployed from December 2017 until October 2018, and recorded local, regional and global earthquakes, in addition to the active source signals. The location of 6TD sites were positioned on a roughly regular 2km spacing, however, site locations were controlled by vehicle access. In some parts of the study area vehicle access precluded the deployment of broadband instruments, and in these areas more portable short-period GSX instruments were used to fill gaps in the array. In total, 49 6TD seismometers were used in the Gisborne array, together with 25 GSX and 19 Cube seismometers. The 6TD are 0.03-100 Hz and the short periods are 4.5 Hz. The 6TDs were set to a sample rate of 200 samples per second for the active shooting period, and the sample rate was changed to 100 samples per second for the passive component of the experiment from March - October 2018.

5.7.2 Waiamata Valley Array

103 DATA-CUBE3 seismometers from Geophysical Instrument Pool Potsdam (GIPP), were deployed in the Waiamata Valley area roughly every ∼500m (Fig 5.28). This is a region of active mud volcanism, experiencing significant eruptions in 1908 and 1930 (Ridd, 1970). The objective of these instruments is to provide extra high-resolution imaging of the upper plate, and in addition image the plumbing system of volcanoes, as described in Part I of this chapter.

5.8 Instrumentation

The NZ3D-FWI experiment involved a range of different instruments including broadband and short-period seismometers. This section will briefly outline the various characteristics of each instrument and review the energy sources.

5.8.1 Energy Sources

5.8.1.1 Active source - Airgun array

From January 7 to February 9, 2018, I was onboard the seismic vessel R/V Marcus G. Langseth, which collected 3D seismic reflection data offshore Gisborne in a NSF, NERC and GNS Science funded experiment.

The 3D seismic source was a 3300 in^3 array made up of two gun strings, each made up of 9 airguns (Fig 5.29), separated by 75m and shooting in flip-flop every 25m. Shots were recorded by the NZ3D-FWI onshore array, JAMSTEC OBS and four 6km seismic streamers, with 200m streamer spacing towed behind the ship (Fig 5.29(b)). 149904 individual shots were fired during the experiment, this included 48 primary shot lines, 2 reshoot lines, 10 infill lines and additional shots around turns (Fig 5.30). To maximise the number of shots for wide-angle imaging by land and OBS instruments,

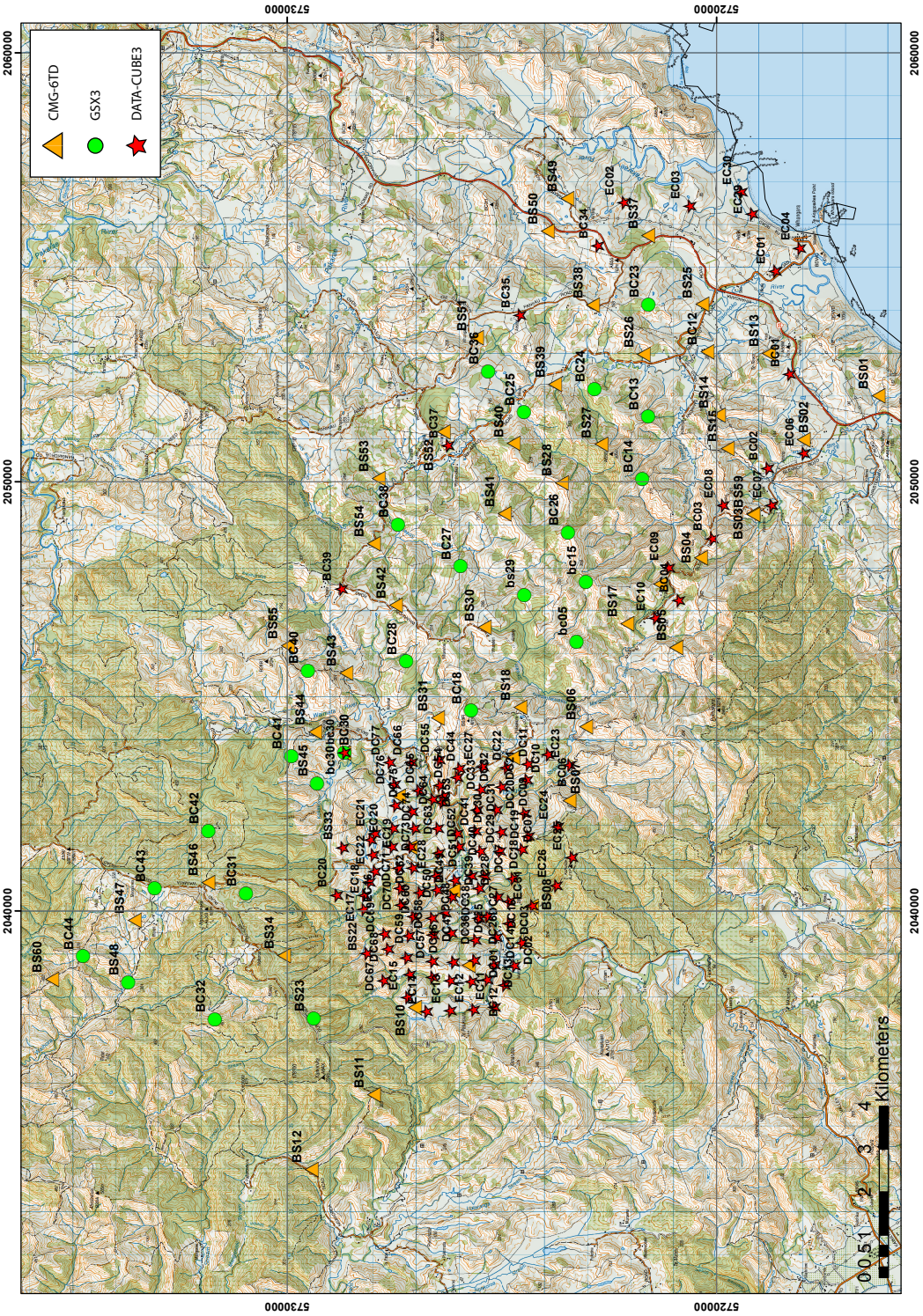


Figure 5.27: Map of the Gisborne region showing land receiver deployment locations. The deployments consists of two main arrays, the Gisborne array composed of instruments spaced every ∼2km mostly made of CMT-6TD and GSX3 instruments, and the Waimata Valley array, more densely spaced every ∼500m and mostly composed of DATA-CUBE3 instruments. All instruments were deployed from December 2017- February 2018. Coordinate system is New Zealand Regional Grid. Image courtesy Bell et al., (submitted).

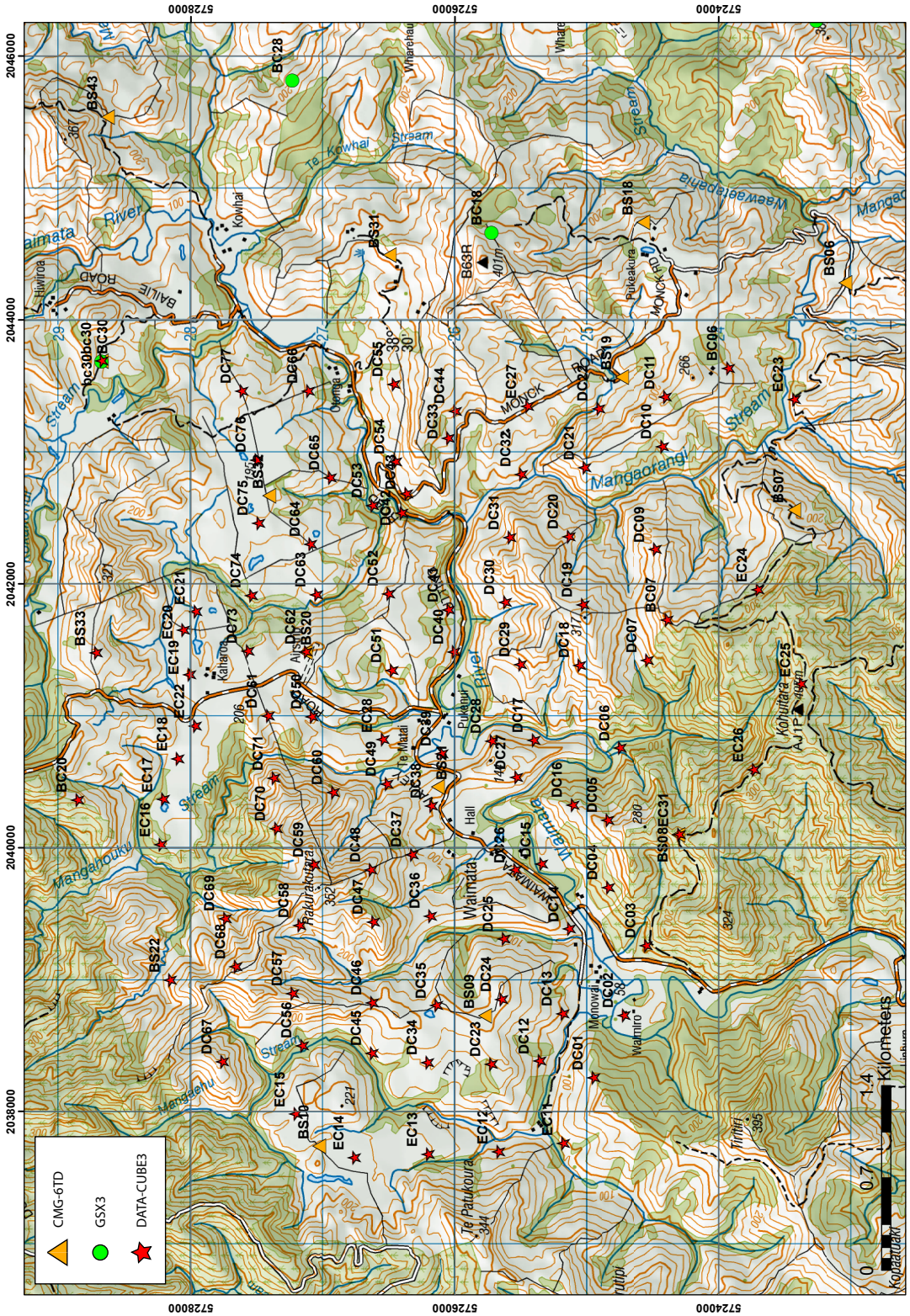


Figure 5.28: NZ3D land station locations in Waimata Valley array with instruments spaced every $\sim$ 500m. Instruments were deployed and recording between December 2017 February 2018. Coordinate system is New Zealand Regional Grid. Image courtesy Bell et al., (submitted).

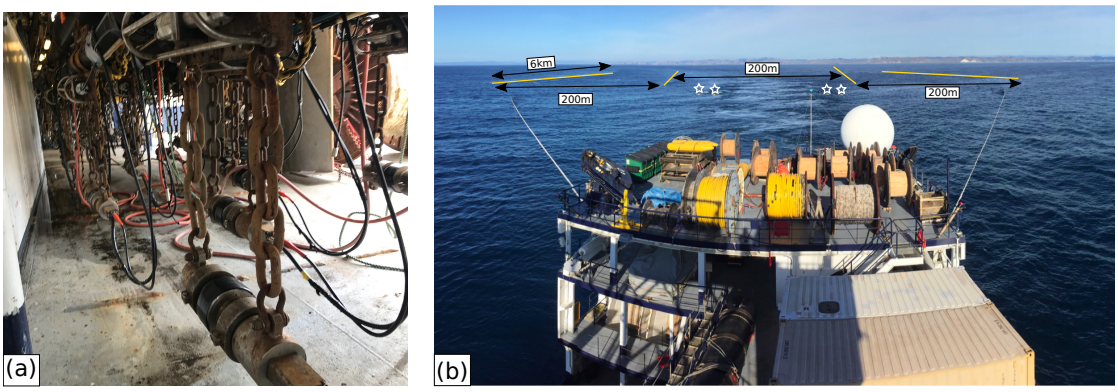


Figure 5.29: (a) Airgun Source onboard the R/V Marcus G. Langseth (b) The R/V Marcus G. Langseth showing towed streamers in yellow and towed airgun sources in white stars.

the Langseth continued to shoot seismic signals around turns, at an irregular shot interval in time to avoid coherent noise from previous shots.

The quality of the data was generally good, although slight disturbances from bad weather (e.g. Cyclone Fehi) and hitting fishing gear caused the initial schedule to be slightly disrupted. Some of the data was badly contaminated by swell noise due to bad weather, particularly data collected between January 31st - February 4th, however good weather conditions and lack of protected species shut-downs in the early stages of the experiment meant little infill and reshoot lines were necessary.

5.8.1.2 3.2.1.2. Passive sources local, regional, and global earthquakes

New Zealand experiences a large amount of seismic activity, with regional 750 earthquakes > Mw 3 occurring between 19th December 2017 and 10th October 2018 (Fig 5.31(a)). This includes 6 earthquakes with Mw > 5. In this time period, the GeoNet monitoring array detected 14556 earthquakes with Mw> 1(Fig 5.31(b)), and 90 teleseismic earthquakes with Mw > 6 occurred globally (Fig 5.31(c)) (GeoNet). These events will be recorded by the broadband 6TD land instruments.

Between the shorter time period of 30th December 2017 and 12th February 2018 one local earthquake with Mw > 3.5 was recorded, alongside 162 events of Mw > 1 recorded by the GeoNet monitoring array within the study area (Fig 5.32(a)) (GeoNet). These will be recorded by 119 DATA˙CUBE3, 25 GSX and 49 CMG-6TD land instruments deployed at this time. Due to the dense spacing of the experiment array, we additionally expect to detect events in the region with lower magnitudes.

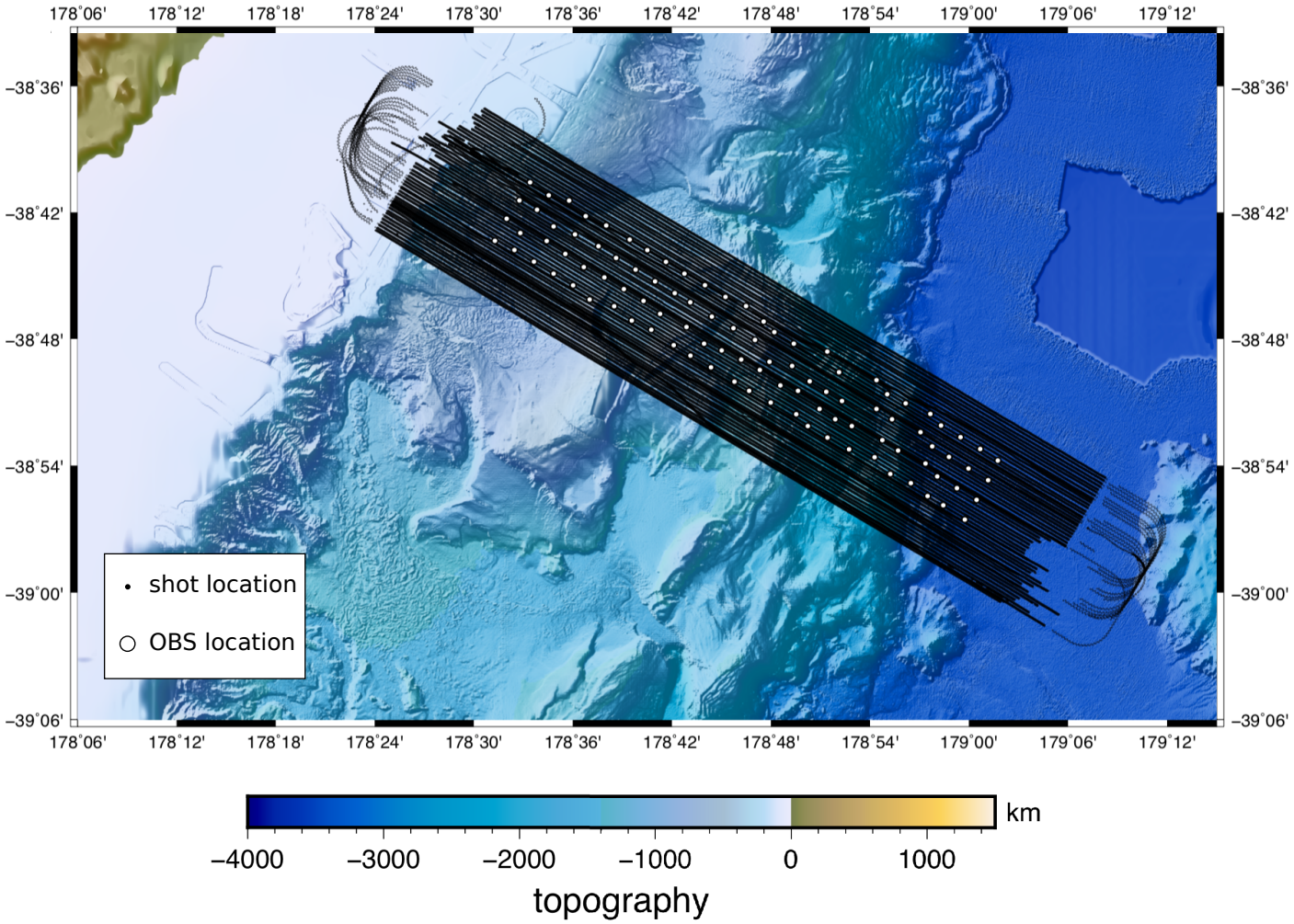


Figure 5.30: Map showing the location of each shot point. The streamer data only recorded shots within the main rectangle. The land and OBS instruments (shown as white circles) additionally recorded shots around the corners.

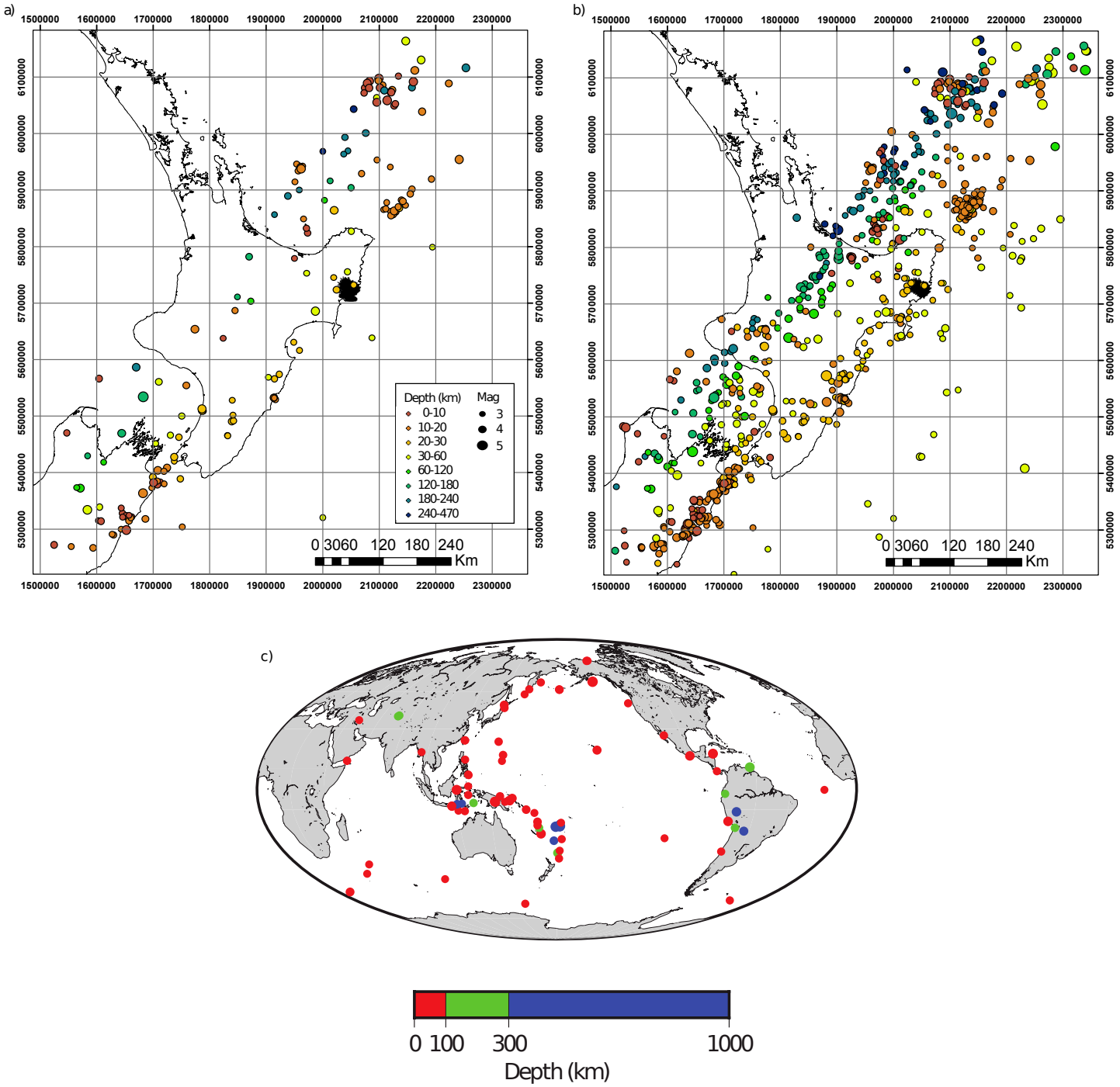


Figure 5.31: (a) Regional earthquakes with magnitudes larger than Mw 3 which occurred during the NZ3D-FWI Waimata Array deployment (19/12/17 12/2/18) and (b) during the Gisborne Array deployment (19/12/17 10/10/18) Image courtesy Bell et al., (submitted). (c) Global earthquakes with magnitudes larger than 6 occurring between 19/12/17 - 10/10/18 during instrument deployment.

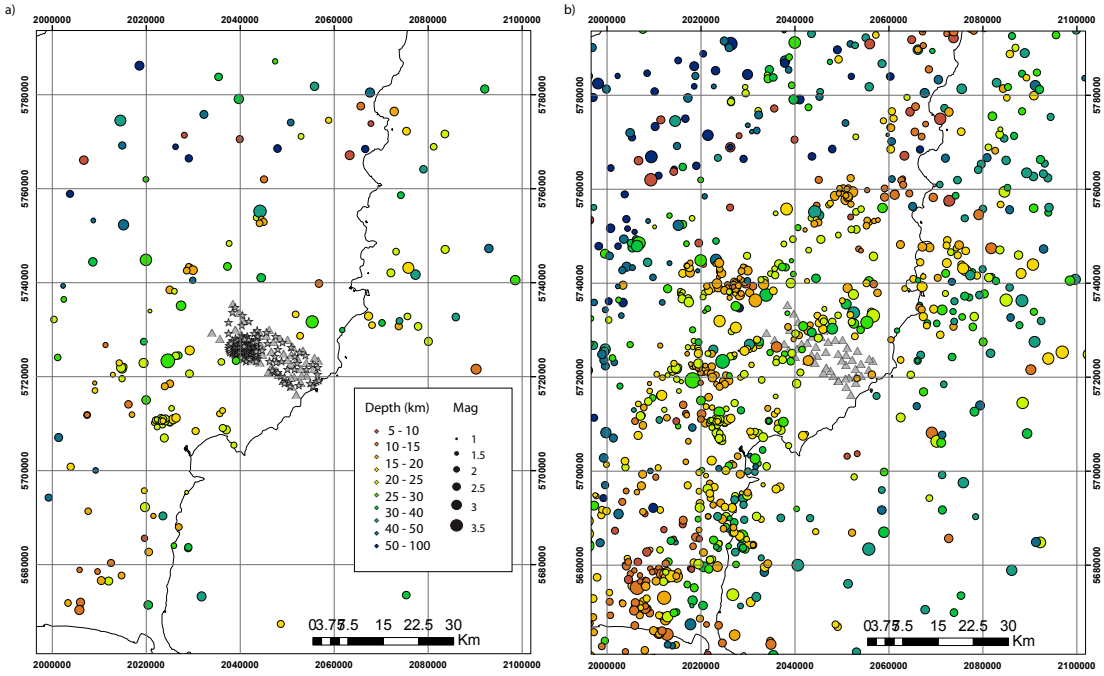


Figure 5.32: (a) local earthquakes which occurred during the NZ3D-FWI Waimata Array deployment (19/12/17 12/2/18) and (b) during the Gisborne Array deployment (19/12/17 10/10/18) Image courtesy Bell et al., (submitted)

5.8.2 Onshore instruments and site design

5.8.2.1 6TD broadband instrument

The Guralp CMG-6TD is a broadband seismometer with integrated digitiser (Fig 5.33(a)) is a small (240 - 155mm), easy to deploy, light-weight (2.7kg) instrument with integrated data storage. the instrument has a frequency response of 30s (0.03 Hz) to 100 Hz. For NZ3D-FWI the site design was as shown in Fig 5.33(b). A ∼60cm deep hole was dug and sand poured in to provide a stable base for the instrument. The 6TD was put in a waterproof bag and levelled using the bubble level on top of the instrument. All instruments were aligned with true North. The 6TD was buried with a mixture of soil from the hole and sand. The instrument was carefully buried, checking that the masses were below acceptable levels during burial. The waterproof bag was taped up and the cables run along a dug-out channel to a plastic battery box. The instruments were powered by a single 20W solar panel with a back-up 12V car battery. The battery and regulator were stored in a water proof box. A tarpaulin was laid in front of the solar panel, using garden staples, to limit vegetation growth in front of the solar panel.

Almost all of the instrument sites were in areas of active farming, including cattle, sheep and pigs. Fences were erected to protect the sites using metal posts and wire fencing (Fig 5.33(b)). For sites in forests two car batteries were used instead of a solar panel. GPS were positioned above the solar panel. Data are recovered from the instruments in the field using an external hard drive while the instrument is still buried. Site installation took a team of 3 around 2-3 hours. All 6TD sites could



Figure 5.33: (a)CMG-6TD instruments in the Gisborne field centre where a huddle test was carried out - this ensures all instruments are working and able to get a GPS lock (b) the CMG-6TD instrument. (c) and (d) show examples of CMG-6TD sites during the Gisborne Array deployment (19/12/17 10/10/18) including GPS, solar panel and fences. The instrument in (b) is buried beneath the tarpaulin. Image courtesy Bell et al., (submitted).

be accessed to within 100m with a vehicle.

5.8.2.2 CUBE3

120 DATA-CUBE3 recorders were shipped to New Zealand from the GIPP seismic pool in Potsdam. Only one of these instruments was unresponsive and could not be deployed. The DATA-CUBE3 recorders were attached to 3D Geophone PE-6/B. These contain one vertical and two horizontal geophones. The geophones respond to ground velocities from 4.5 Hz to $>$ 150 Hz. The geophones weigh 1kg each and the DATA-CUBE3 recorders just over 1kg.

The site design involved digging a ∼30cm deep hole for the geophone, and stabbing the three metal spikes in the ground. The geophone is levelled using the bubble-level on the instrument.

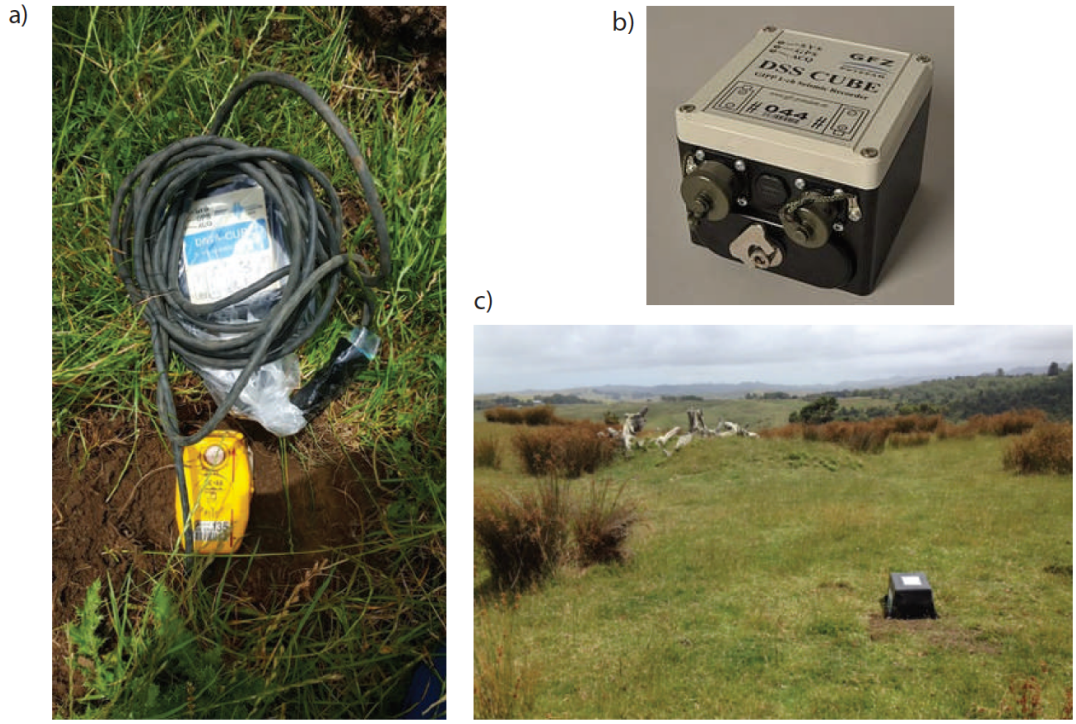


Figure 5.34: (a)the CUBE3 geophone in the ground ∼ 30cm below the surface, and the recorder in a plastic bag. (b) The CUBE3 recorder (image from www.gfz-potsdam.de). (c) An example of a CUBE3 site during the deployment (19/12/17 10/10/18). The plastic box is placed over the instruments to protect them from cattle. Image courtesy Bell et al., (submitted)).

The geophone is connected to the DATA-CUBE3 which was wrapped in a plastic bag and left at the surface (Fig 5.34). To protect the DATA-CUBE3 from animals, but still ensure the GPS could get lock, the instruments were covered with plastic boxes, with holes drilled at the corners for long-garden staples to attach them into the ground. This simple experiment design and light-weight nature of the equipment meant that these instruments could be located in remote areas and many instruments deployed quickly. The instruments are powered by 2 DC batteries which were replaced by servicing teams every ∼11 days.

5.8.2.3 GSX

25 GSX3 seismic recorders from the Earthquake Research Institute, Japan, were also used in the experiment. These 3 component recorders are attached to a 4.5 Hz, 3 component geophone. These instruments are also light-weight, with the geophones weighing 1.8kg and the GSX 0.9kg. The instrument is powered by two battery packs, which each weigh 2.75kg. These batteries allowed operation for 40 days so the GSXs were deployed shortly before the shooting started to ensure that the batteries would not need charging during the active source experiment.

Given the light-weight nature of the instruments, and the fact that batteries did not need replacing, these instrument were ideal for installation in the most inaccessible parts of the study area. This was ideal for plugging gaps in the Gisborne array in areas where limited vehicle access prohibited

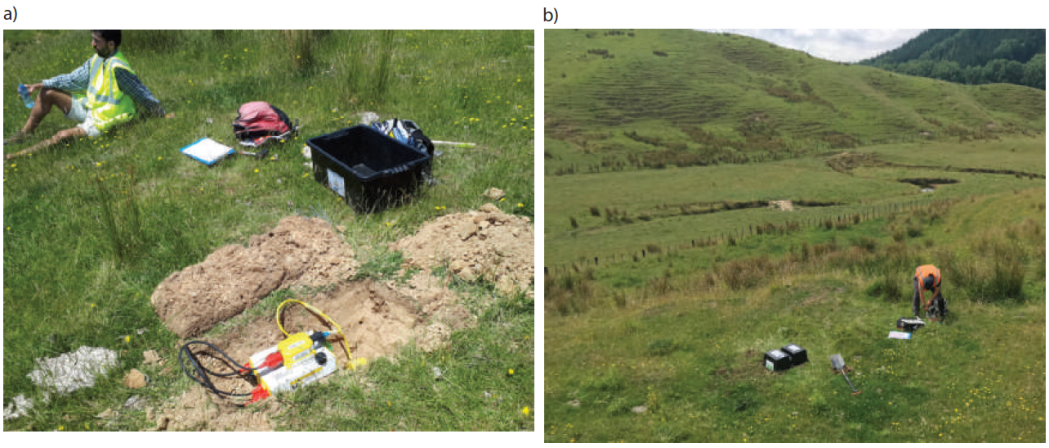


Figure 5.35: (a)The GSX geophone in the ground ∼30cm below the surface alongside two batteries and yellow GSX recorder. (b) An example of a GSX site during the deployment (19/12/17 10/10/18). Two plastic boxes are placed over the instruments to protect them from cattle. Image courtesy Bell et al., (submitted).

the installation of broadband 6TD instruments. The installation of these instruments involved digging a ∼30cm deep hole for the geophone. The recorder and batteries were kept at the Earths surface. A large plastic box was put over the top to protect them from cattle.

5.8.3 Offshore Instruments

The main focus of this chapter is on the land instruments, however a brief overview of the offshore instruments is included here. These datasets will be described in detail in marine data acquisition reports.

5.8.3.1 Ocean Bottom Seismometers (OBS)

JAMSTEC provided 100 OBS (Fig 5.36) instruments which were deployed in a ∼6.5 x 58km grid with 2km spacing as shown in Fig 5.30. The gridpoints are randomly shifted from a uniformed grid by up to a few 10s of meters to avoid one dominant wavelength being sampled as in a uniform grid. Slightly offsetting this regular grid by a few 10s of meters broadens the spectrum of the data and avoids compressive sensing, which is important when dealing with sparse data. Each OBS contains a hydrophone and a three-component geophone, there are therefore four sensors in different orientations: vertical (channel 1), east-west (channel 2) south-north (channel 3) and hydrophone signal (+ve pressure is recorded as ve). Data are recorded at 100 samples per second in 16 bit resolution.

5.8.3.2 Hydrophone streamer

The R/V Marcus G. Langseth towed four 6km streamers (Fig 5.29 and 5.37) with 200m streamer spacing. Each streamer contained 480 Sentinel Solid Acquisition Section (SSAS) 3 Hz hydrophones

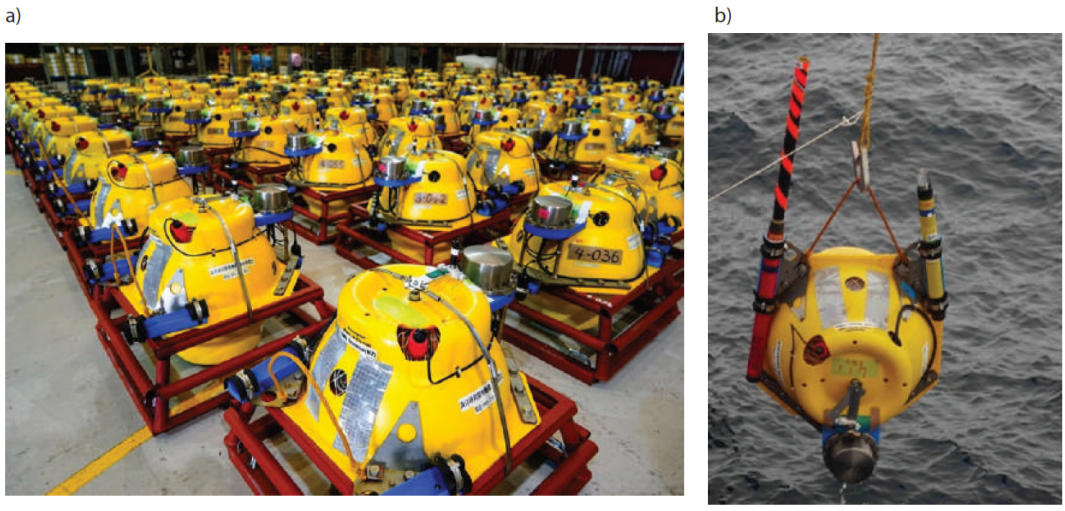


Figure 5.36: (a)The OBS instruments on deck and (b) and being lowered overboard. Image courtesy GNS Science

at 12.5km spacing. 9.5 seconds of data were recorded for each airgun shot, and streamer depth and feathering were controlled by ION Digicourse 5011 Compassbirds (birds) (Fig 37). Each streamer contained 22 birds at 250m spacing. A total of 60 passes (48 primary, two reshoot and 10 infill lines) were recorded over the survey grid with 300m line spacing over the entire 14 x 60km grid (Fig 5.30). It was part of my duties as a member of the science party onboard the R/V Marcus G. Langseth to help with streamer deployments, attaching birds, and quality controlling data recorded by the streamers.

5.9 Data

The NZ3D-FWI experiment successfully recorded 4 key datasets:

(a) Broadband 6TD seismometer data with sample rate 200 sps from December 2017 - February 2018.

(b) Broadband 6TD seismometer data with sample rate 100 sps from February - October 2018.

(c) Short-period DATA-CUBE3 data with sample rate 200 sps from December 2017 - February 2018.

(d) Short-period GSX3 data with sample rate 200 sps from December 2017 - February 2018.

All active and passive sources described above were recorded and data quality was generally good, with coherent arrivals seen at all stations currently processed.

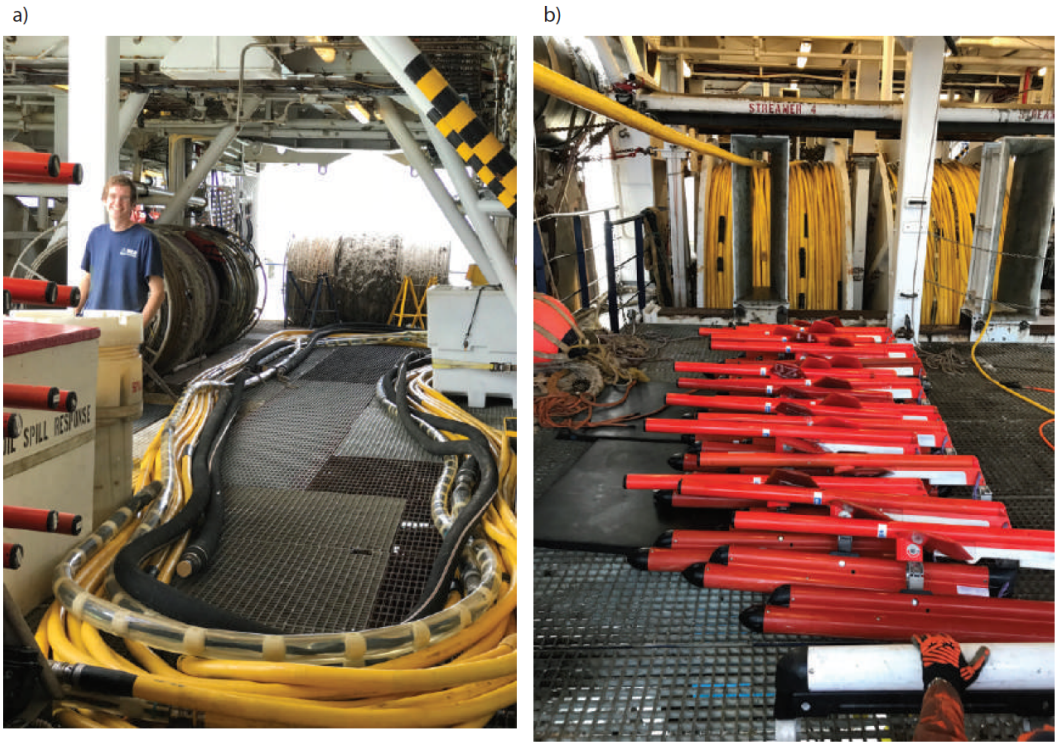


Figure 5.37: (a) One of the 4km streamers on deck and (b) Compassbirds on deck

5.9.1 Examples of active source data

Figures 5.38 and 5.39 show 25 seconds of data recorded on four CUBE3 instruments from the data acquisition. Figure 5.38 shows shot gathers from station BC03 and EC23, and figure 5.39 from stations BS28 and BS60 (Fig 5.27) for two shotlines from the R/V Marcus G. Langseth, lines 1236 and 1244 (Fig 5.30). These data were processed using GIPP tools and Seismic Unix, with no automatic gain control (AGC) applied. Coherent signal can be seen up to offsets of 90 -110km.

5.9.2 Examples of passive source data

A magnitude 3.5 earthquake occurred on 13th January, 2018, 15km west of the array at a depth of 28.4km as detected by the GeoNet monitoring array. This event was detected by the land instruments, with clear P- and S-wave arrivals up to a maximum offset of 32km from the event.

Fig 5.40 shows the data recorded by all instruments vs offset. Initial processing shows that picking P-wave arrival times at the instruments allows investigation of arrival time anomalies across all stations. This could be useful for investigation of anomalous travel-times by waves passing through the mud volcano source region when investigating earthquakes from different orientations to the array.

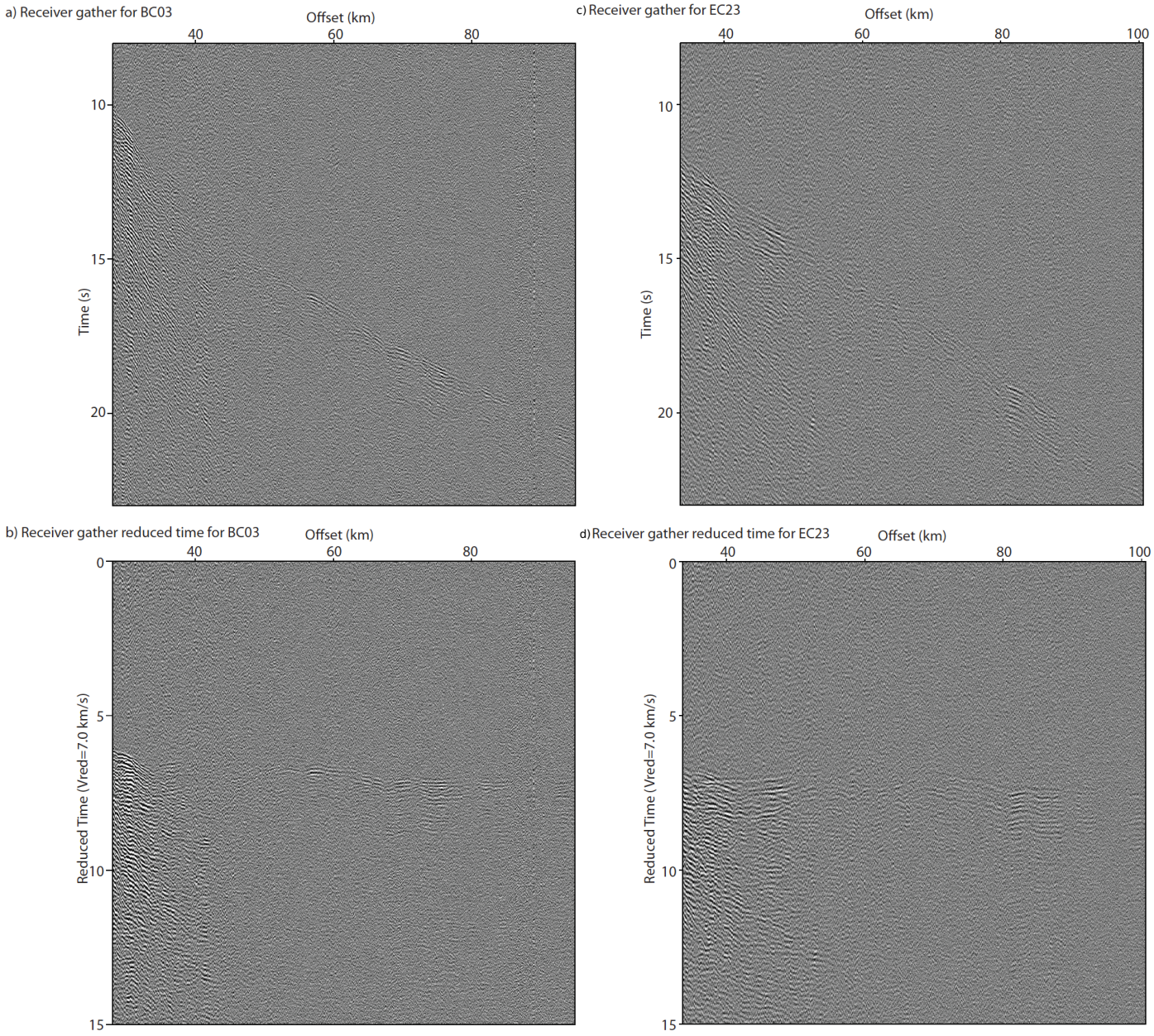


Figure 5.38: Receiver gathers for shot lines 1236 and 1244 for vertical components of CUBE3 stations BC03 and EC23. (a) and (c) show the receiver gathers from BC03 and EC23 respectively, while (b) and (d) show gathers in reduced time using a velocity of 7km/s. Data have been bandpassed filtered between 8 and 100 Hz. Image courtesy Bell et al., (submitted)

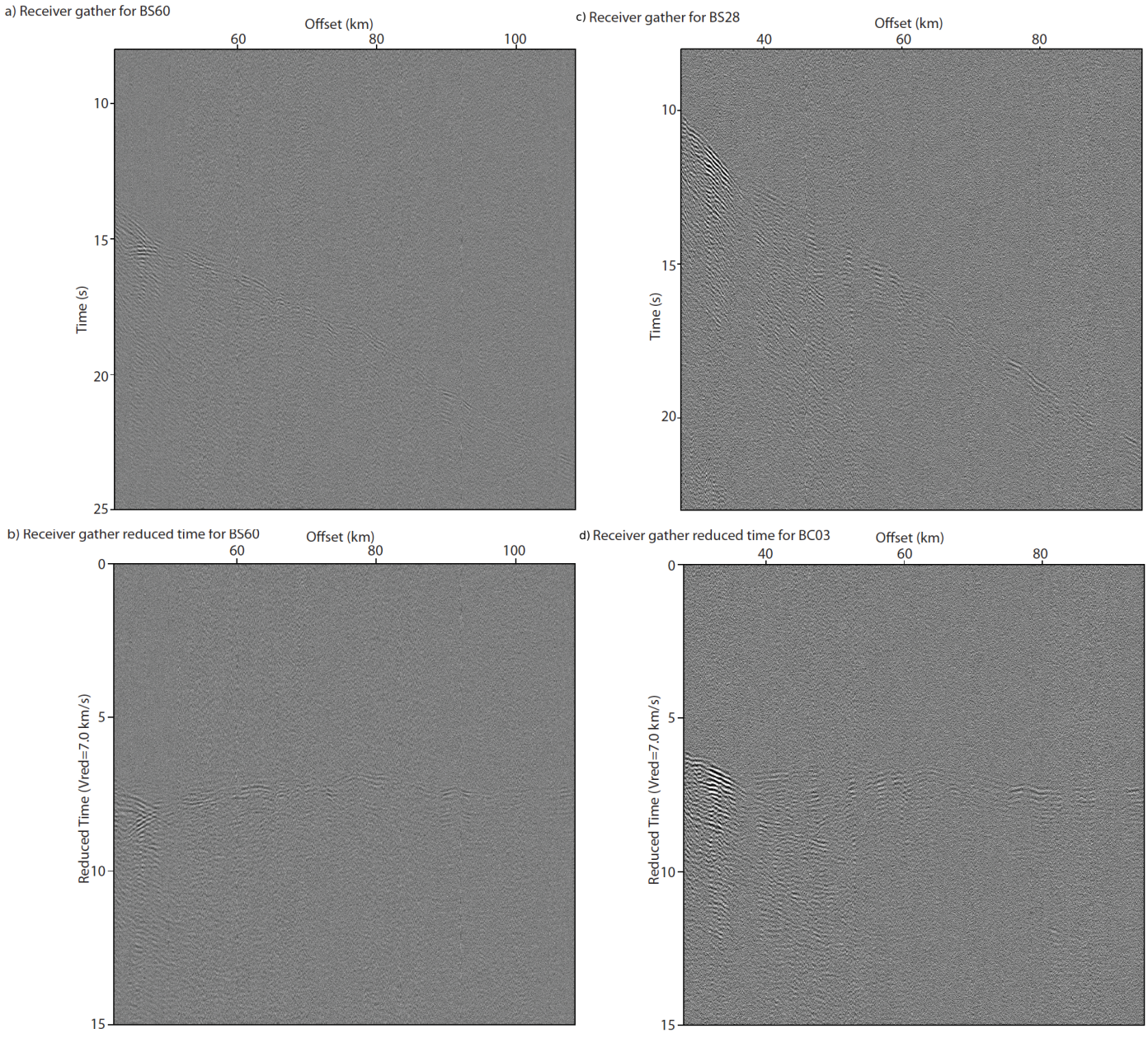


Figure 5.39: Receiver gathers for shot lines 1236 and 1244 for vertical components of CUBE3 stations BS28 and BS60. (a) and (c) show the receiver gathers fro BS28 and BS60 respectively, while (b) and (d) show gathers in reduced time using a velocity of 7km/s. Data have been bandpassed filtered between 8 and 100 Hz. Image courtesy Bell et al., (submitted)

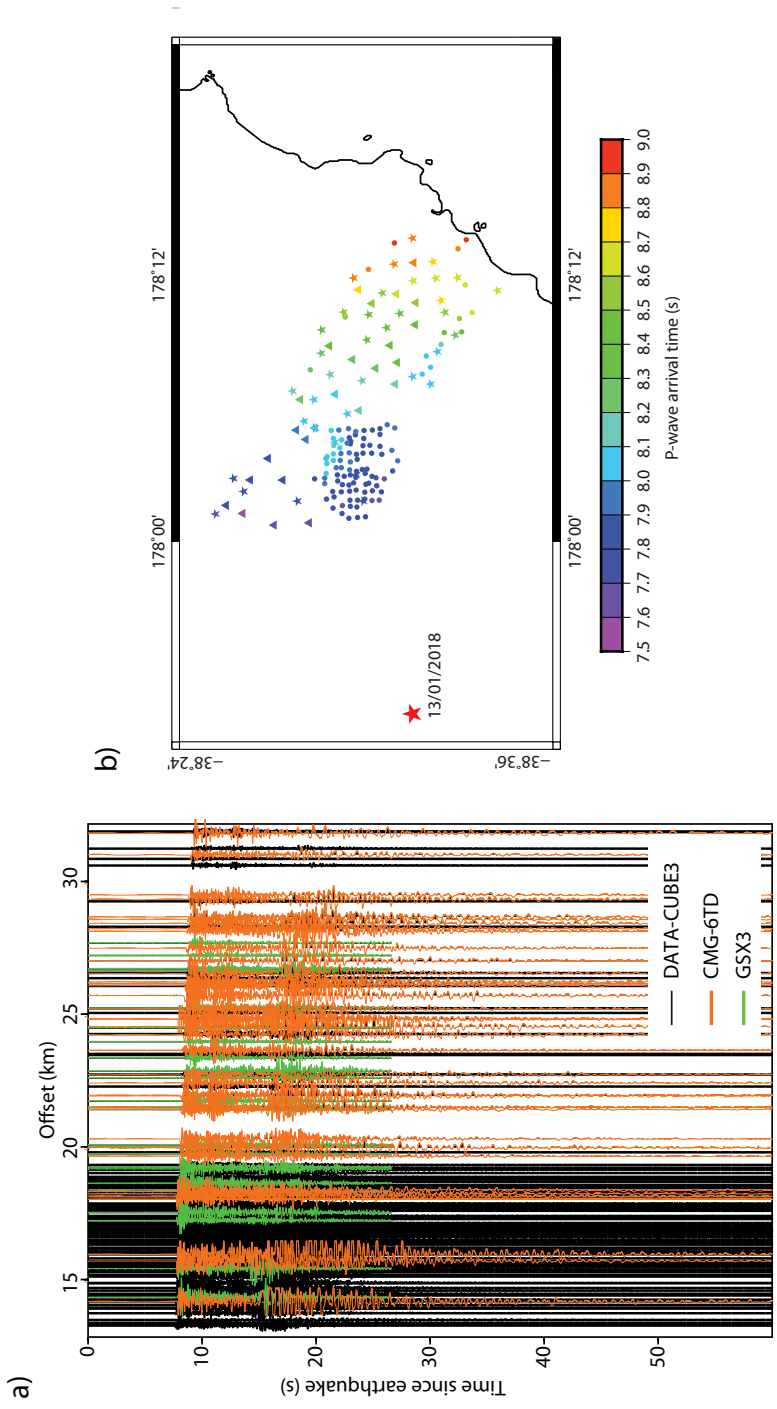


Figure 5.40: (a)The 13th January, 2019 magnitude 3.5 Gisborne earthquake as recorded on all land instruments. (b) P-wave arrival times at all instruments in the array

5.10 Conclusion

By assessing several experimental layout designs using checkerboard testing and synthetic modelling, a land receiver layout was determined for the NZ3D-FWI experiment. This layout allowed for imaging of several key targets including the plate boundary fault, plate interface >10kmbsf, proposed subducted seamount including epicentres of the March and May 1947 tsunami earthquakes, the SSE origination zone (shown as the HRZ in 2D reflection seismic sections), region of plate coupling transition, upper plate offshore including inputs into the subduction zone, and finally, onshore mud volcanism. The layout chosen was the 'Combination Grid' layout which consisted of evenly spaced geophones over the onshore part of the model in a 2 x 2km grid with a central receiver in the middle of each gridded square, and a smaller, denser concentration of land receivers inserted in the centre of the layout with regular spacing of 500 x 500m, outlined in Fig 5.18.

This layout was then adapted to the study area, to include the Gisborne array (Fig 5.27) and Waimata Valley array (Fig 5.28). These geophones, as well as OBS instruments and hydrophone streamers recorded 149904 individual shots from airgun sources on the R/V Marcus G. Langseth between January 6 and February 9, 2018. Deployment and acquisition went smoothly, and all three types of land instrument recorded data which can be used in 3D FWI.

Collecting this large dataset over the Hikurangi margin is an exciting first step in using 3D FWI to produce high resolution, well constrained P-wave velocity models at the key targets, which, in combination with in-situ measurements of physical properties from drilling, can help to further investigate the hypotheses of what drives SSEs at Hikurangi.

Chapter 6

Using logging-while drilling, wireline and core data to investigate physical properties at the Hikurangi margin based on the FWI model

6.1 Abstract

A suite of physical property data were obtained from logging-while drilling (LWD), wireline logs and core samples during International Ocean Discovery Program (IODP) Expeditions 372 and 375 at the Hikurangi subduction margin offshore Gisborne, North Island, New Zealand. In this chapter, these physical property data are used to transform the high-resolution P-wave full-waveform inversion (FWI) velocity model presented in chapter 4 into models of porosity, velocity difference between undeformed and deformed sediments across the margin, Vs, Vp/Vs, bulk modulus and shear modulus. These models help to resolve the physical properties across individual fault blocks, at a much higher resolution than previous studies have been able to achieve. Differences in velocity between undeformed basin sediments and sediments closer to the trench suggest that the incoming section begins to undergo deformation due to subduction at a distance of ∼5.3-8km from the trench. Models of porosity indicate that shallow clastic sediments that have been over-thrust in fault hanging walls are over-compacted with ∼55% of pore fluids removed by 5km landward from the trench, and ∼62% by 25km into the wedge. Deeper (>∼1.25kmbsf) clastic sediments across

the model, particularly in the footwalls of faults, are under-compacted for their depth and have porosities of around 40%, which is ∼10% lower than the surrounding rock. Pelagics which have been incorporated into the wedge are under-compacted, likely due to low permeability, which may indicate they are relatively undrained during accretion, while shallow (<∼1.25kmbsf) clastics being accreted and in the hanging walls of faults appear over-compacted which suggests that they are more drained than the pelagics. This is emphasised by porosity measurements across the Pāpaku fault which indicate ∼33% of fluid is expelled across the fault in the clastic layer compared to ∼20% in the pelagic layer. Finally, the elastic modulii indicate that previous models for tsunami modelling at Hikurangi use a rigidity which is too high (7GPa)(Bell et al., 2014), while instead values of ∼1-3GPa in the upper ∼2kmbsf seem to be more appropriate. This has implications for improving tsunami hazard modelling in the region by using more lower, laterally varying elastic modulus values which change with depth.

6.2 Introduction

Modelling of physical properties including porosity and elastic moduli at subduction zones can provide insights into deformation, seismicity and hydrology at these highly destructive plate boundaries. Physical property data can be obtained from LWD, wireline logs and core samples, and these properties can be used to infer mechanisms at work at subduction zones worldwide. For example, porosity data can be used to infer the amount of expelled fluid at subduction margins (e.g. (Saffer and Bekins, 1998; Saffer, 2003; Saito and Goldberg, 2001; Screaton et al., 2002; Von Huene et al., 1998; Zhao et al., 1998)), Vs and Vp/Vs data to examine the role of fluids at margins (e.g. Audet et al. (2009); Eberhart-Phillips and Reyners (1999); Kodaira et al. (2004); Reyners et al. (2006)), elastic modulii to estimate the response of the earth to earthquakes and is a direct input into tsumani models (e.g. Geist and Bilek (2001); Johnson and Satake (1997); Mendoza and Hartzell (1999); Satake (1993)), and seismic velocities to investigate sediment compaction (e.g. Bangs et al. (1990)).

Many studies of physical properties at subduction zones are limited in their extent or resolution. For example, studies based on drilling data are limited to the immediate surrounds of the borehole (e.g. Hoffman (2004); Jeppson et al. (2018); Tobin et al. (1994, 1995)) while studies based on tomography or passive data measurements are often low resolution (1-10km) (e.g. Audet et al. (2009); Bangs et al. (1990); Eberhart-Phillips and Reyners (1999)) and therefore cannot resolve small-scale property differences across smaller scale features such as individual fault blocks. In chapter 4, I introduced a high-resolution P-wave velocity model along line 05CM-04 across the Hikurangi subduction margin, offshore Gisborne, North Island, New Zealand (Fig 6.1). This model showed that, by employing full-waveform inversion, a large improvement in P-wave velocity resolution can be obtained compared to traditional travel-time techniques, resolving features on the fault-block scale. This improved resolution allows further insight into the lithologies and hydrology along the

margin. However, this model was constrained in depth to ∼2kmbsf and limited only to P-wave velocity.

During recent drilling at the Hikurangi margin on IODP Expeditions 372 and 375, logging-while-drilling (LWD), wireline log and core sample data were acquired at three drill sites along seismic line 05CM-04, which provide direct, in-situ measurements of a range of physical properties beyond P-wave velocity including porosity, density and S-wave velocity. A suite of empirical relationships between various physical properties have been previously proposed in a number of different studies (e.g. Anderson (1989); Bangs et al. (1990); Castagna et al. (1985); Erickson and Jarrard (1998); Greenberg and Castagna (1992); Hamilton (1978); Hyndman et al. (1993); Wyllie et al. (1958)), and here I apply these relationships to obtain estimates of physical properties along the Hikurangi margin by transforming my high-resolution P-wave velocity model. This not only produces physical property models of Vs, porosity, Vp/Vs and elastic modulii away from individual drilling sites, but also reveals, for the first time, how these physical properties vary on the fault-block scale across the deformation front and within accretionary wedges.

With detailed models of a range of physical properties along line 05CM-04, we can investigate: (1) how far from the deformation front the incoming section begins to undergo subduction-related deformation: (2) the porosity distribution and use it to distinguish between over- or under-compacted sediments as they are accreted into the footwalls and hanging walls of faults; (3) how much fluid is expelled by sediments as they are accreted; (4) Vp/Vs ratios along faults across the margin; and (5) changes in elastic modulii and their implication for tsunami hazard modelling. All these factors have important hydrological implications at Hikurangi and, thus, how the composition of the incoming section may influence the stress state of the plate boundary. The incoming section at Hikurangi is composed of a mixture of clastic, pelagic facies and volcaniclastics, so results can be compared to subduction zones with pelagic and hemipelagic inputs, such as Nankai, Costa Rica and Barbados as well as clastic inputs such as Makran and western Canada, where similar but lower resolution studies have been conducted (Bangs et al., 1990; Fruehn et al., 1997; Moore et al., 2001; Saffer and Bekins, 1998; Saffer et al., 2000; Saffer, 2002, 2003; Screaton et al., 2002; Von Huene et al., 1998).

6.3 Datasets

6.3.1 Seismic data

In chapter 4, I detailed how full-waveform inversion (FWI) was used to create a P-wave velocity model with improved resolution compared to traditional travel-time techniques (for example, for rock with velocity ∼2200m/s using the inversion strategy outlines in chapter 4, features >∼140m in size are able to be recovered). This model was obtained by inverting 2D seismic streamer data, which was collected in May 2005 as part of the 05CM-04 survey. Chapter 4 details how this

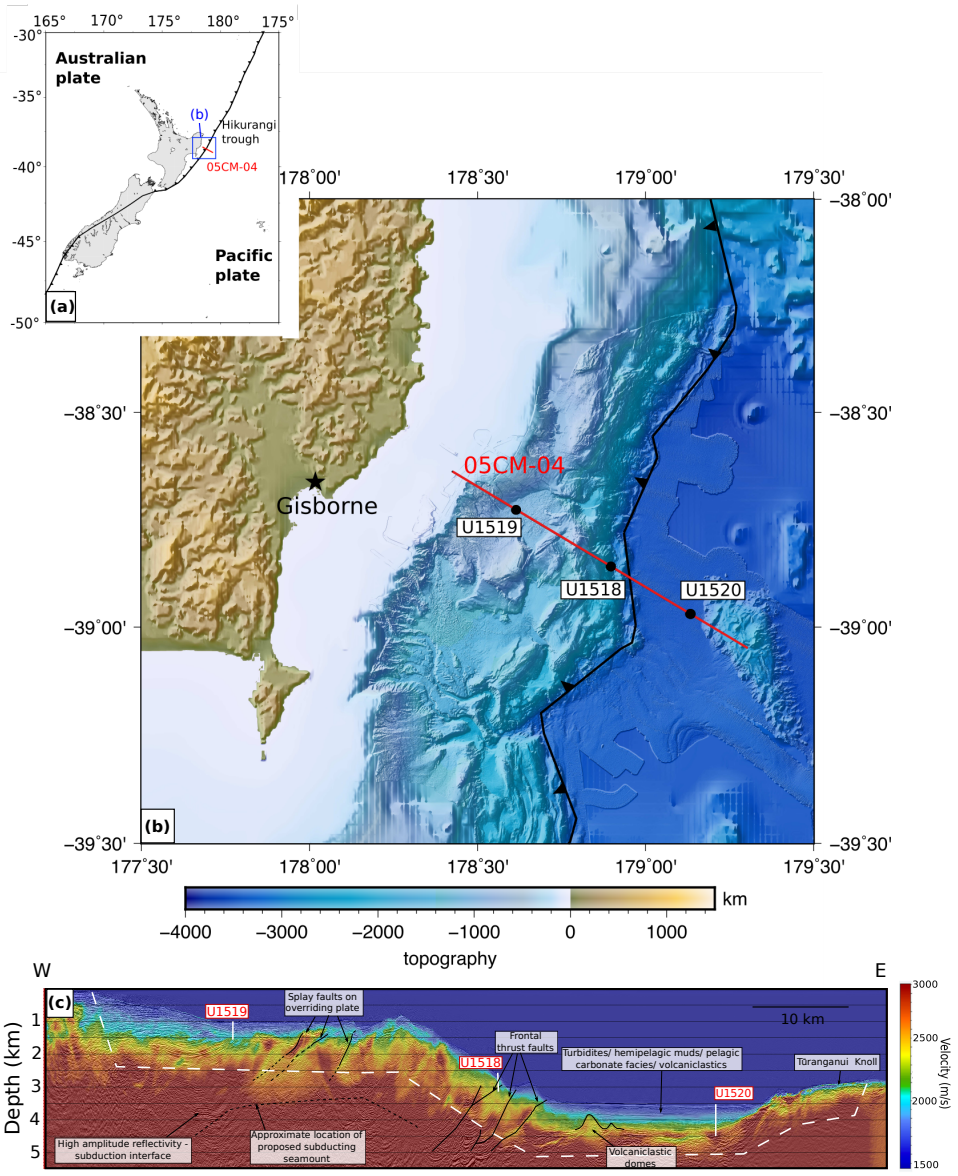


Figure 6.1: (a) Regional map of New Zealand showing plate boundaries between the Australian and Pacific plates. The red line shows the 2D multichannel seismic line 05CM-04 used in this study (see chapter 4). The blue box shows the location of (b), the larger map, in which the colour scale is offshore bathymetry across the Hikurangi margin, based on 25-m gridded swath data. The black dots represent the drill sites, where LWD core and wireline (1520 only) measurements were taken on IODP Expeditions 372 and 375. The red stars show the location of the 1947 Offshore Poverty Bay (along line 05CM-04) and Tolaga Bay tsunami earthquakes (Bell et al., 2014). (c) Reflection seismic section of 2D line 05CM-04. The dashed line shows the location of the proposed subducting seamount from Bell et al. (2014) based on magnetic data, and the red star shows the location of the March 1947 tsunami earthquake event offshore Poverty Bay. The red lines represent three IODP drill sites. The different lithology types based on interpretations from the literature are shown as well as the location of the frontal thrust in the near surface, the variable reflectivity of the subduction interface, and the Tūranganui Knolls (after Gray et al. (2019)).

velocity model was quality checked using a combination of comparisons between synthetic and real waveforms, the velocity model and a pre-stack depth migration (PSDM) seismic image, and extracted velocity profiles from the model and wireline data. The model is constrained to ∼2kmbsf based on approximate penetration depths of turning rays recorded on the 12km streamer.

6.3.2 Logging data

In 2017/2018, two IODP Expeditions - 372 and 375 - collected various data along the 05CM-04 seismic profile (Fig 6.1). Expedition 372 collected logging-while-drilling (LWD) data, processed to produce measurements every 0.1524m (0.5ft) at three drill sites, and collected logs including: ultrasonic calliper, neutron-gamma bulk density, gamma ray (collected every 0.3m), nuclear magnetic resonance (NMR), neutron porosity, propagation resistivity, annular pressure/temperature and compressional and shear velocity (Pecher et al., 2019; Wallace et al., 2019)(Fig 6.2, 6.3 and 6.4. Site U1519 is located the furthest landward, on the overriding plate, approximately 35km from the shore on the upper continental slope (Fig 6.1); LWD data were collected here down to 650 mbsf (Fig 6.2). The site is at the landward edge of a midslope sedimentary basin, and was drilled to sample the upper sedimentary sequence above the overriding plate (Pecher et al., 2019; Wallace et al., 2019). Site U1518 is located on the lower continental slope, ∼62km from the shore, on the frontal accretionary wedge, ∼6.5km west of the deformation front, where deformation is actively ongoing as the Pacific plate subducts beneath the Australian plate (Fig 6.1). LWD measurements were recorded to a maximum depth of 600mbsf, and an observatory was installed within the well for future monitoring of seismic activity along the fault (Pecher et al., 2019; Wallace et al., 2019)(Fig 6.3). This site samples a major west-dipping thrust fault, the Pāpaku fault,which is thought to accommodate a large amount of the plate convergence and possibly slow slip events (SSEs) (Pecher et al., 2019; Wallace et al., 2019), with a dip-slip displacement of ∼6km (Fagereng et al., 2019b). Site U1520 is the most seaward LWD site, located in the offshore Hikurangi Trough on the Pacific plate, between the deformation front and the Tuūranganui Knoll seamount complex (Fig 6.1);LWD data were recorded down to 750mbsf and wireline logging data down to 947mbsf (Fig 6.4 (Pecher et al., 2019; Wallace et al., 2019). This site was chosen for drilling in order to characterise the state of the sediments seaward of the deformation front which have undergone little or no tectonic deformation, and represents the inputs into the subduction zone (Wallace et al., 2019).

6.3.3 Core Data

During IODP Expedition 375 core samples were collected at five drill sites along 05CM-04, however I will not be using one of the sites, U1526, in this study due to the shallow depths (∼85m) and the proximity of the drill site to the edge of the FWI model. Core was recovered to depths of 1054.1mbsf at site U1520, 494mbsf at site U1518 and at discrete intervals down to 640mbsf at site U1519 (Pecher et al., 2019; Wallace et al., 2019). Cores were taken from two boreholes at site U1520,

with 58% core recovery at site U1520C and 62% recovery at site U1520D (Fig 6.4). Cores taken from two boreholes at site U1518, U1518E and U1518F had 87% and 43% core recovery respectively (Fig 6.3), and core recoveries at sites U1519C, D and E were 55%, 101% and 103% respectively (for core recovery > 100%, core is recovered outside of the cored interval) , however these were taken at discrete intervals (spot-cored), leaving much of the borehole at U1519 unsampled (Fig 6.2). All sites, particularly site U1519, contained large coring gaps, zones of poor recovery, and pervasive coring disturbance (Wallace et al., 2019).

Core samples were analysed to identify the lithostratigraphic units at all three sites. Two lithostratigraphic units were identified at site U1519 (Unit I and II in Fig 6.2), however there were large coring gaps at this site due to poor core recovery and pervasive coring disturbances. The main lithologies in the recovered core were found to be mud(stone), silt(stone) and sand(stone). Three main lithostratigraphic units were identified at site U1518 (Fig 6.3), and contained a background of silty clay(stone) or mud(stone) alternating with thin beds of silt(stone) to silty sand(stone), although some of the original stratigraphic section may be missing due to submarine slides/ mass wasting after frontal accretion based on higher than expected porosities (Wallace et al., 2019). The main fault zone is between 315.3-322.4mbsf, and a second, subsidiary fault located in the footwall between 351.2 and 361.7mbsf. Six different lithostratigraphic units were defined at site U1520 (Fig 6.4), representing the incoming section, including hemipelagic muds down to 509.82mbsf, pelagic carbonate facies from 509.82-848.45mbsf, volcaniclastics from 848.45-1016.24mbsf and a blend of volcaniclastics, mudstone, limestone and siltstone down to 1045.75mbsf (Pecher et al., 2019; Wallace et al., 2019). The recovered cores showed that rocks at site U1520 were generally undeformed.

Physical property measurements were also taken at discrete locations along the recovered core, and include porosity, moisture and density (MAD), natural gamma ray, gamma ray attenuation (GRA) bulk density, P-wave velocity, undrained shear strength, compressional strength, magnetic susceptibility, thermal conductivity and gamma ray attenuation.

6.4 Method

In this study we firstly calculate the difference in Vp between undeformed basin sediments at the location of U1520 and velocities within the rest of the incoming section and accretionary wedge. We do this to investigate what happens to the sedimentary rocks as they approach the accretionary wedge. Then, the drilling data are used to derive relationships between various recovered physical properties. These derived relationships are then used to transform the FWI Vp model into models of velocity difference, porosity, Vs, Vp/Vs, bulk modulus and shear modulus. As the FWI model is constrained to ∼2kmbsf and the drilling data reaches depths of ∼1kmbsf, the transformed FWI physical property models are restricted to depths of <∼2kmbsf. As clastic, pelagic and volcaniclastic lithologies are found in the Hikurangi Trough (Fig 6.4), different relationships are found for the different lithologies and applied to the appropriate parts of the model. Note that picked horizons

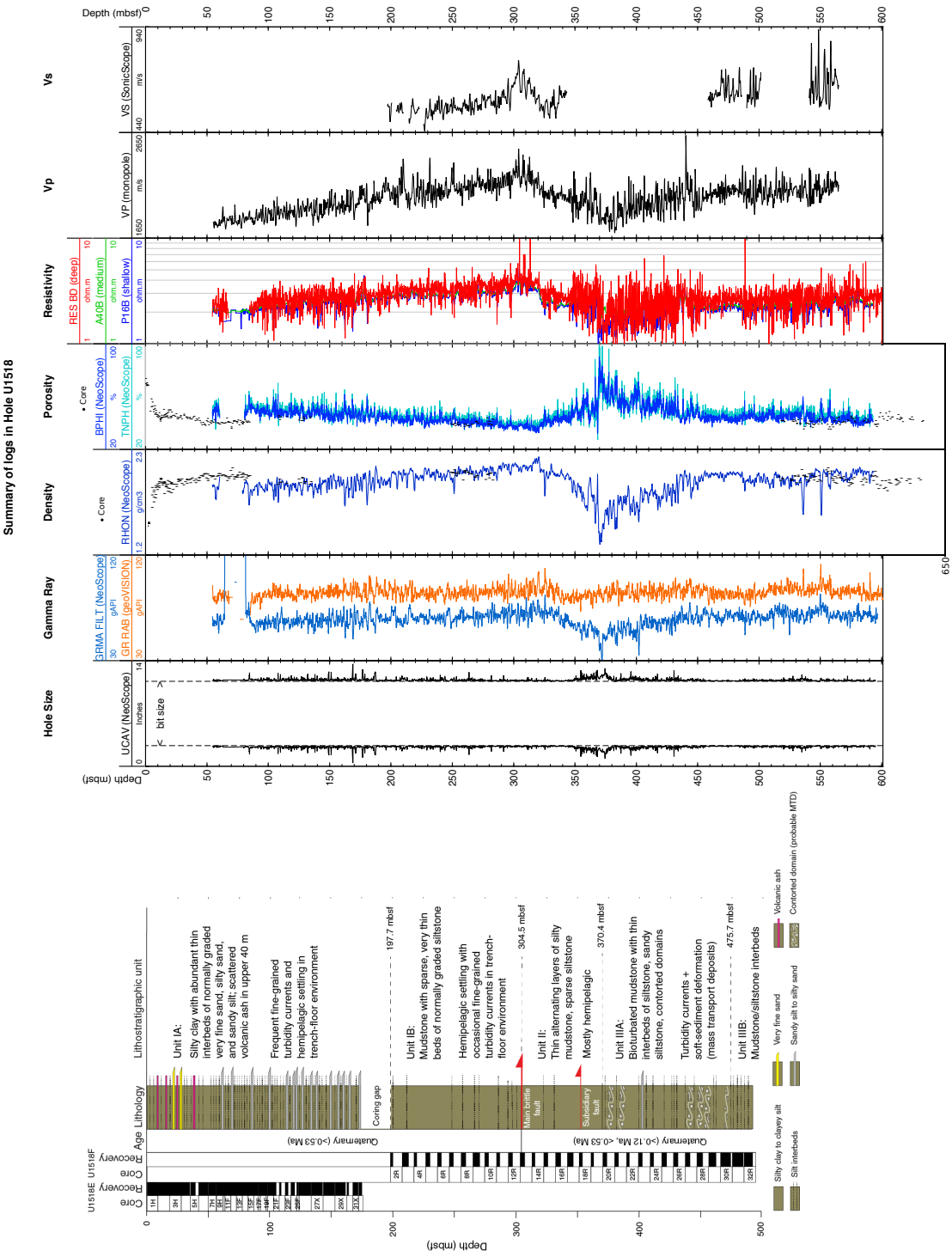


Figure 6.2: LWD and core data recovered at site U1519 on the overriding plate. Images from Wallace et al. (2019).

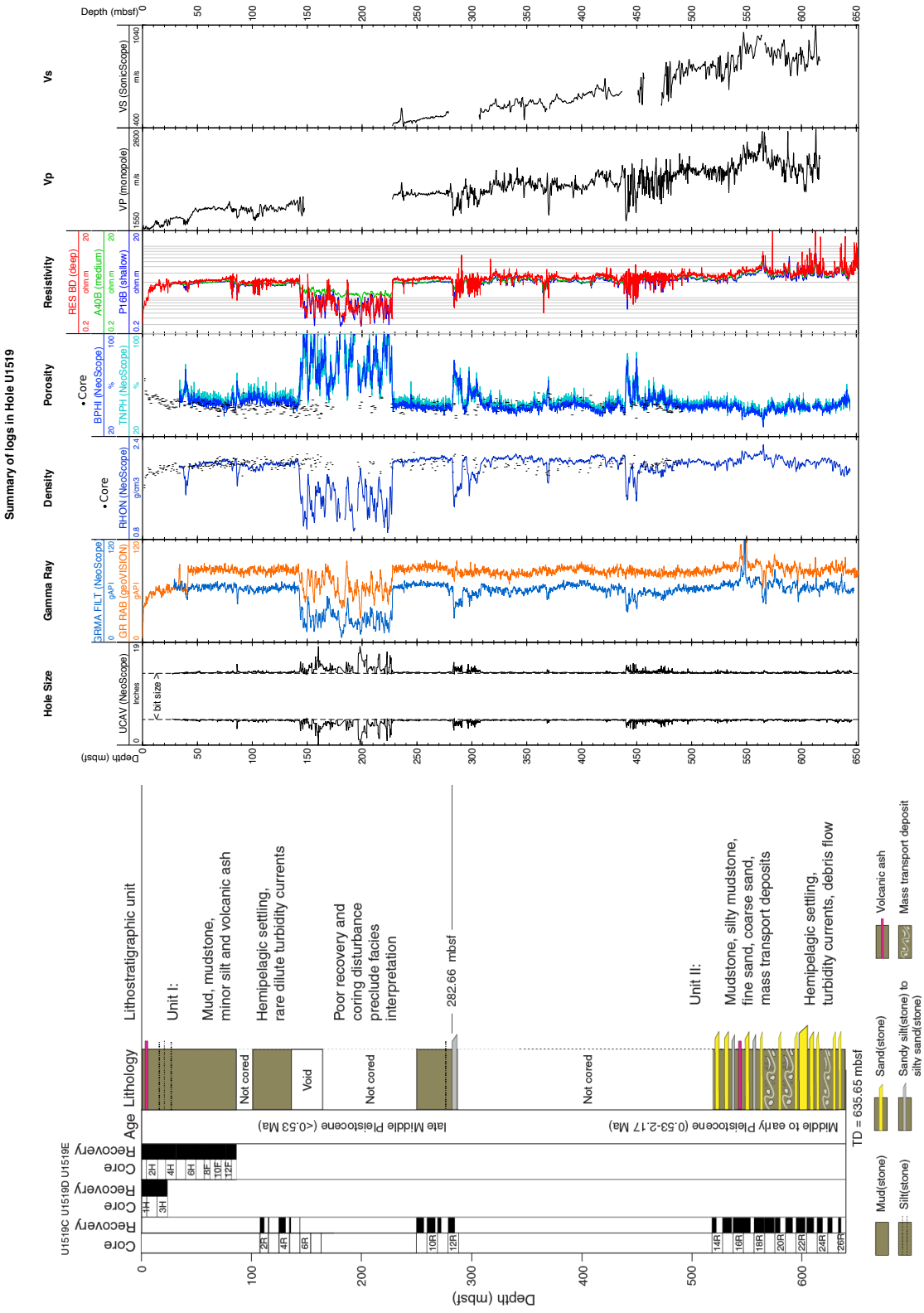


Figure 6.3: LWD and core data recovered at site U1518 near the trench.Images from Wallace et al. (2019).

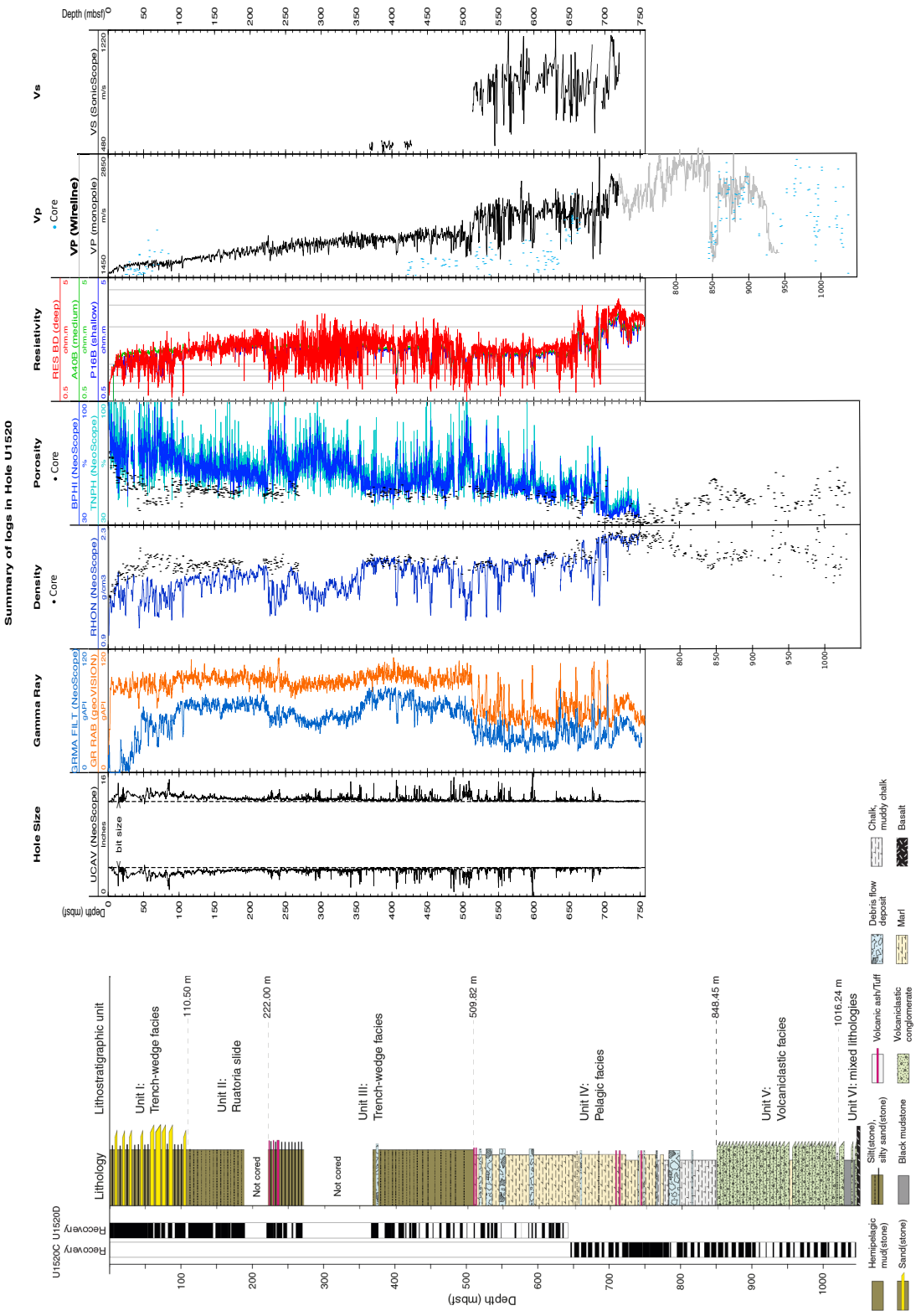


Figure 6.4: LWD and core data recovered at site U1520 in the Hikurangi Trough.Images from Wallace et al. (2019).

for the top of the pelagics and top of the volcaniclastics are after Barnes et al. (in review) and are mapped as a continuous boundary across faults in order to create distinct separate packages for the application of each velocity-porosity relationship, hence not precisely honouring the true geometry of the faults. While plausible estimates of Vs, Vp/Vs, elastic modulii and porosity are derived, it should be noted that the analysis does not provide independent constraints on these parameters.

6.4.1 Vp difference model

Based on relationships between porosity and velocity by Gardner et al. (1974); Hamilton (1978); Nafe and Drake (1957), velocity is strongly correlated with porosity, thus velocity can be used to investigate changes in compaction. Here, I followed the method of Bangs et al. (1990) which was applied in a study of the Barbados ridge complex. Bangs et al. (1990) plot the difference in velocity between their velocity model and a reference curve of velocity versus depth of undeformed sediments of the same thickness. The velocity difference plot is then used to identify regions that have higher or lower velocities than expected for their depth. Regions with reduced velocities for their depth are interpreted to have higher porosities and be under-compacted, which may indicate that pore fluid pressures are high and that pore fluids support the overburden load (Bangs et al., 1990). In contrast, regions which have a higher velocity than expected for their depth are interpreted as being over-compacted, with greater fluid loss. For this study, I have obtained the reference velocity profiles from undeformed sediments in the incoming section at site U1520. The profiles are based on the Vp recorded during LWD and core measurements for the clastic and pelagic sediments as well as the velocity profile extracted at the well site from the FWI Vp model (Fig 6.5). The volcaniclastic unit is suspected to be deeper than the resolved FWI velocity model in the west so I did not consider volcaniclastic sediments in the reference profile based on the core and LWD measurements (Barnes et al., (in review)). Relationships between Vp and depth for both clastic and pelagic lithologies were modelled as a best fit linear regression using data sampled every 0.1524m (0.5ft). While the regression led to a profile for the clastics lying in the range of Vp for clastic rock of 2-3.5km/s for porous and saturated sandstones (Bourbié et al., 1992), the pelagic velocity profile rapidly increased to unrealistic values of ∼7km/s at depths of ∼2.5kmbsf and the gradient of the line seems to have been biased by a large scatter of Vp values at depth (Fig 6.5). To address this, I first averaged the pelagic velocities over 15m intervals to remove anomalous data points, and then computed the best-fit linear regression. This produced a more reasonable velocity-depth profile for the pelagic unit. The equations for the velocity-depth profiles used as reference profiles in this study are shown in Table 6.1.

These two velocity-depth reference profiles were then subtracted from the FWI Vp model, and the resulting velocity difference plotted down to 2kmbsf. The differences between the velocities of undeformed sediments within the Hikurangi Trough and deformed sediments within the wedge are expected to reflect differences in consolidation, fluids and lithology.

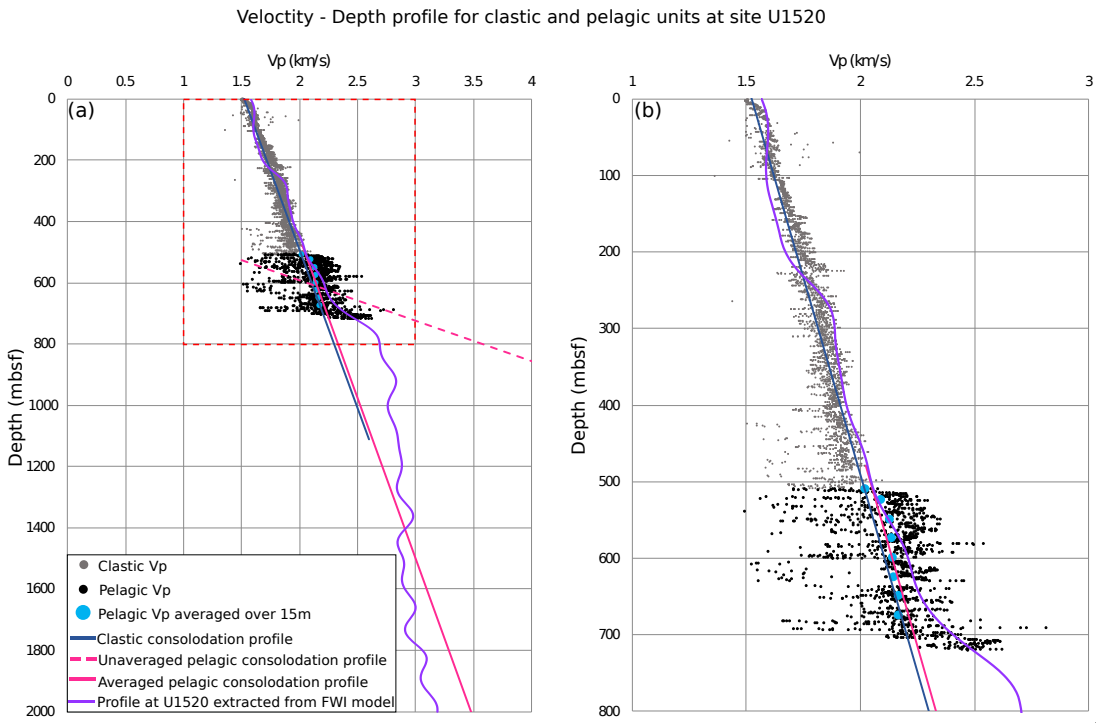


Figure 6.5: General velocity vs depth trend based on LWD measurements through undeformed clastic (grey points) and pelagic sediments (black points) in the Hikurangi trough ever 0.1524m (0.5ft). Blue points represent the velocity of pelagic sediments averaged over 15m intervals. The blue line represents the clastic velocity-depth profile and the pink lines represent best-fit pelagic velocity-depth profiles for the unconstrained (dashed) and averaged (solid) pelagic values. The purple line shows the velocity profile extracted from the FWI model at the location of U1520 (b) shows a zoomed-in version of the area in (a) denoted by the red box

Table 6.1: Velocity-depth profiles used for modelling velocity differences between undeformed sediments in the Hikurangi Trough, and deformed sediments in the wedge.

Unit	**Velocity-depth profile**	$\mathbf{R^2}$
Clastic	$V_P = (z - 1575.9)/1034$	0.782
Pelagic (averaged every 15m)	$V_P = (z - 1634.9)/1044.6$	0.739

6.4.2 Porosity Model

In order to create a porosity model, I used physical property measurements from LWD and core data to derive a velocity-porosity relationship, which I then applied to my Vp FWI model to transform velocities into porosities. While the LWD logs give a direct measurement for porosity, the neutron porosity tool is sensitive to the average hydrogen density, and the conversion to porosity assumes that all hydrogen in the formation is in the form of pore-filling liquid of a certain density (Wiley and Patchett, 1990)). This can cause porosity to be either over- or under-estimated, since water may be bound (e.g. within clay) and gas (instead of water) lowers the hydrogen density. Porosity measured on core samples, however were taken by measuring the wet and dry mass and volume, calculating the porosity and bulk density as

$$\rho_b = \frac{M_{wet}}{V_{wet}}, \tag{6.1}$$

and

$$\phi = \frac{V_f}{V_{wet}}, \tag{6.2}$$

Where M_{wet} is the total mass of the wet sample, V_{wet} is the bulk volume of the wet sample, ϕ is the porosity and V_f is the calculated volume of the pore fluid (Blum, 1997; Wallace et al., 2019). This is an accurate measure of the interconnected and isolated porosity, excluding clay-bound water (Blum, 1997), however there are fewer core porosity readings than there are LWD measurements. In order to calculate porosity from the more extensive, but less accurate LWD porosity measurements I used the core data to create a cross-plot of porosity vs density. From this plot I extracted a relationship between porosity and density at each well, detailed in Table 6.2, and then applied these relationships to the density LWD log, to obtain a better estimate of LWD porosity (Fig 6.6).

The porosities calculated from the density LWD logs using this relationship were generally 1-5% lower and less scattered than the neutron porosity LWD measurements (Fig 6.6 (d)-(f), see appendix for log comparisons). Porosity-velocity relationships have been investigated in detail in a number of studies including Wyllie et al. (1958) based on experimental investigation on natural and synthetic porous media, Hamilton (1978) based on deep sea drilling and velocity data for

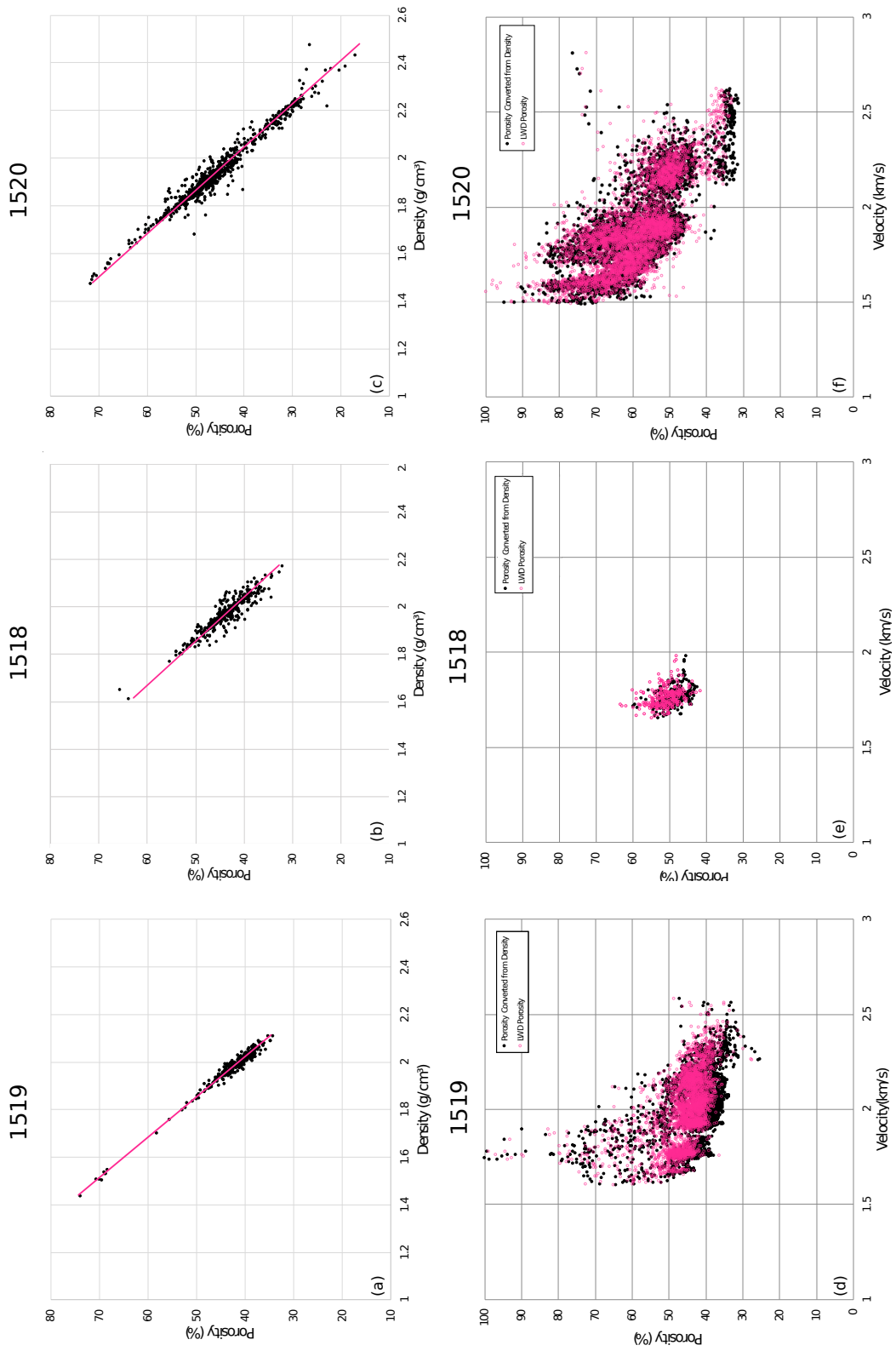


Figure 6.6: Cross-plots of porosity vs density from core data for U1519 (a), U1518(b) and U1520 (c), and corresponding density LWD data converted to porosity (black points) directly compared to porosity LWD data (pink points), for U1519 (d), U1518 (e), and U1520 (f).

Table 6.2: Best-fit porosity-density relationships using core data at each well.

Well	**Relationship**	$\mathbf{R^2}$
U1519	$\phi = -58.859\rho + 159.06$	0.976
U1518	$\phi = -53.627\rho + 149.49$	0.857
U1520	$\phi = -55.036\rho + 152.55$	0.958

sea-floor sediments and marine rocks, (Hyndman et al., 1993) based on core, log and seismic data from the Nankai accretionary prism, and Erickson and Jarrard (1998) based on statistical analysis of ocean drilling data for water-saturated siliciclastic sediments. The Erickson and Jarrard (1998) study presents two equations for normal and high consolidation, the high-consolidation equation was chosen in this study as it produced a better fit to the Hikurangi data before parameter fitting (see Appendix). As all of the porosity-velocity equations described above relate the two properties inversely, I also investigated the application of a simple reciprocal relationship between porosity and velocity of the form:

$$\phi = \frac{av}{b+v}, \tag{6.3}$$

where ϕ is porosity, v is velocity and a and b are constants (Table 6.3). I employed an inversion algorithm to find the parameter values in the various velocity-porosity equations mentioned above that best fit the Hikurangi data (see Table 6.3). Separate relationships between velocity and porosity were derived for the different lithologies: clastics (Fig 6.7(a)), pelagics (Fig 6.7(b)) and volcaniclastics (Fig 6.7(c)). Pelagic and volcaniclastic lithologies were, however, only identified in the Hikurangi Trough at site U1520 (Fig 6.4).

The resulting best-fit parameters obtained using a non-linear least squares algorithm for each of the studied relationships are shown in Table 6.3. As the algorithm could chose numbers in the range -infinity-infinity, some of the parameters do appear to be unrealistic. For example, using the Wyllie equation to fit the clastic data results in unrealistic values for fluid velocity (v_f) and matrix velocity (v_m), however the units of properties used as input are different to the literature and the resulting equation produces a porosity model from the velocity model which gives realistic porosity values.

Each of the empirical relationships between porosity and velocity from Table 6.3 were then used to convert the FWI velocity model into a porosity model. Each porosity model is slightly different due to the different equations used (Fig 6.7, Table 6.3), however differences between the calculated porosity for each relationship are small. Fig 6.8 clips porosities at $+/-\Delta 20\%$. High % differences (>10%) between porosity values calculated with different models only occur in the pelagic zone (Fig 6.8 (a), (c), (e) and (f)). Based on Fig 6.7(b), this appears to be due to a difference in measurements between core and converted LWD data. The core measurements (filled circles in

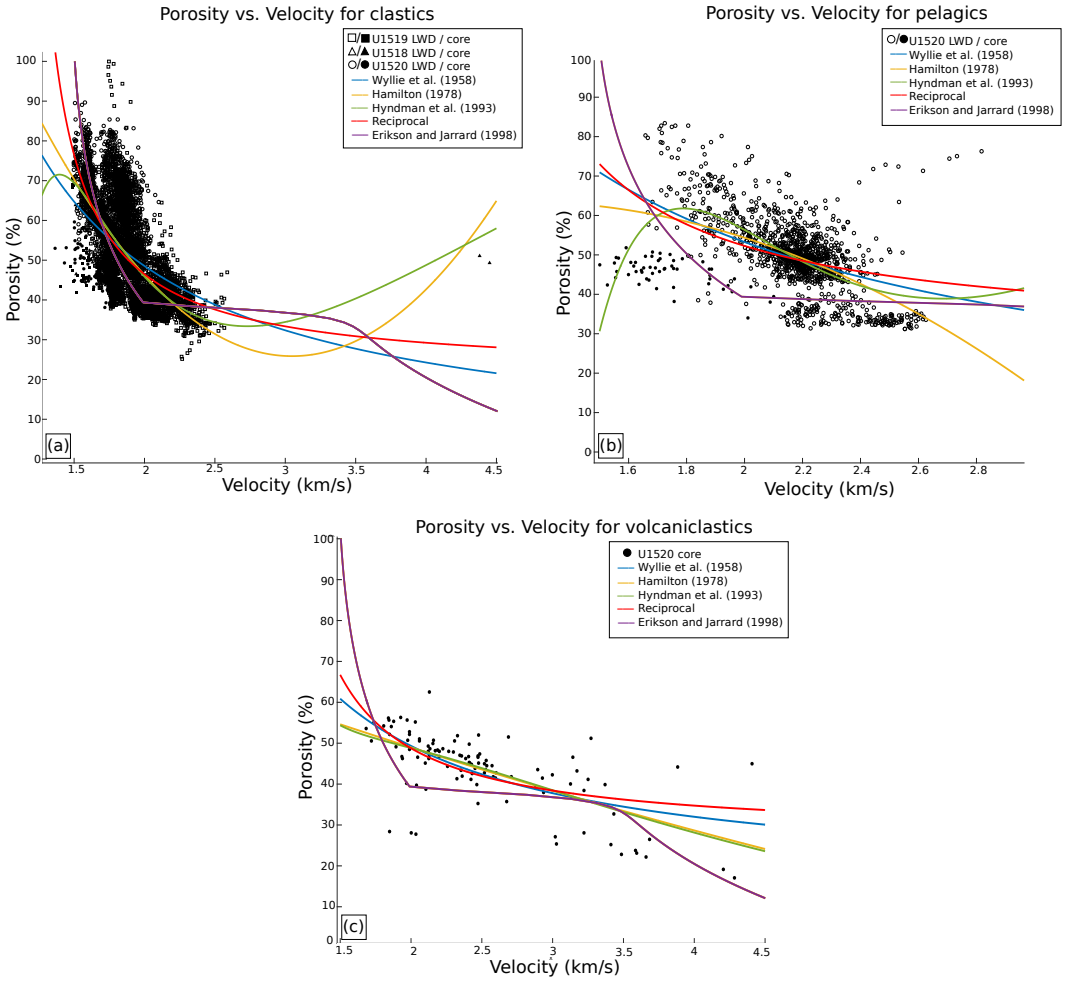


Figure 6.7: Cross-plot of porosity converted from density LWD data (detailed in Fig 6.6), vs velocity from LWD data for all three wells U1518-1520. Five best-fit relationships to the data based on different porosity-velocity models are plotted as coloured lines, for each lithology: clastic (a), pelagic (b), and volcaniclastic (c).

Table 6.3: Porosity-velocity equations used in a linear least-squares best fit algorithm, and the associated best-fit parameters.

Publication	**True equation**	**Best-fit clastic**	**Best-fit pelagic**	**Best-fit volcaniclastic**
Wyllie et al. (1958)	$\frac{1}{v} = \frac{\phi}{v_f} + \frac{1-\phi}{v_m}$	$v_f = -97.06$ $v_m = 3.419 \times 10^5$	$v_f = -87.15$ $v_m = 488.3$	$v_f = -4.42$ $v_m = 4.721$
Hamilton (1978)	$\phi = \frac{(\rho-\rho_m}{(\rho_f-\rho_m}$ $\rho = a + bV + cV^2$ a=0.917, b=0.744, c=0.08	$\rho_m = 2.714$, $\rho_f = 1.05$ (from logs) a=-327 b=188.1 c=-30.85	$\rho_m = 2.714$, $\rho_f = 1.05$ (from logs) a=-67.28 b=-59.31 c=24.54	$\rho_m = 2.714$, $\rho_f = 1.05$ (from logs) a=-118.4 b=21.26 c=-0.7245
Hyndman et al. (1993)	$\phi = A + \frac{B}{V} + \frac{C}{V^2} + \frac{D}{V^3}$ A=-1.180, B=8.607 C=-17.89, D=13.94	A=245.6 B=-1397 C=2884 D=-1776	A=669.5 B=-4355 C=9743 D=-6973	A=-40.07 B=417 C=-674.8 D=392
Reciprocal (unpublished)	$\phi = \frac{av}{b+v}$	a=21.33 b=-1.082	a=28.22 b=-0.9205	a=26.97 b=-0.8594
Erickson and Jarrard (1998)	$V_P = 1.11 + 0.178\phi + \frac{0.305}{[(\phi+0.135)+0.0775]}$ $+0.61(v_{sh} - 1)[X_2]$ Where $X_2 = \tanh[20(\phi - \phi_C)]$ $-\lvert\tanh[20(\phi - \phi_C)\rvert$ (high consolidation)	$v_{sh} = 0.8629$ $phi_C = 0.2191$	$v_{sh} = 0.424$ $\phi_C = 0.5381$	$v_{sh} = 0.7304$ $\phi_C = 0.8594$

Fig 6.7(b)) at velocities between 1.5-2km/s have lower associated porosities (40-50%), than the converted LWD data which have porosities of 50-85% for the same velocity range of 1.5-2km/s. The converted LWD data clusters at 45-60% porosity with associated velocities between 2.1-2.4 km/s, while core data is not recorded above 2.1 km/s, with the majority of the core data (70% of all data points) lying between 1.5 and 1.8km/s. This causes an apparent divergence in the best-fit trends based on the different models (Erickson and Jarrard, 1998; Hamilton, 1978; Hyndman et al., 1993; Wyllie et al., 1958). Specifically, fits based on models by Hamilton (1978) and Hyndman et al. (1993) display large % differences to the other models. There appears to be much smaller difference between models in the clastic region, and very little difference in the volcaniclastic region, which is likely due to this layer containing the least amount of data points (Fig 6.7(c)).

My preferred model is the reciprocal model as it gives a simple relationship between velocity and porosity within the constrained region up to 2kmbsf, and produces a model with small differences compared to the other porosity models produced with the other relationships. The porosity values predicted by this model at specific areas of interest such as within faults will be discussed in sections 6.5.1.3 and 6.5.1.4.

6.4.3 Vs, Vp/Vs, bulk modulus and shear modulus

Due to washouts, poor core recovery and poor borehole conditions in some parts of the drilling data acquisition, limited measurements of Vs were taken on Expeditions 372 and 375 (Pecher et al., 2019; Wallace et al., 2019). To convert my Vp FWI model into a Vs model, I used the Vs and Vp data recorded at the same location to derive a relationship between Vs and Vp. At well U1520, LWD data were acquired down to 720.8mbsf, wireline logging Vp measurements down to 947mbsf and core measurements down to 1045.6mbsf, while Vs measurements were only recorded by LWD tool between 368.5 and 720.8mbsf, with several gaps in the measurements. At site U1519, Vs measurements were taken between 227.7 and 617.1mbsf with four small (<30m) gaps in recording, while Vp measurements were recorded down to 617.1mbsf from the seafloor with a gap in recording between 147.7 and 227.7mbsf due to washouts. Site U1518 recorded Vs values between 214.7 and 564.9mbsf, with fours gaps in recording of up to 114.5m, with continuous Vp measurements from 55.1mbsf to the base of the well at 564.9mbsf (Pecher et al., 2019; Wallace et al., 2019). The Vp and Vs logs are shown in detail in section 6.5.3. By cross-plotting recorded Vp and Vs measurements at the depths at which they are both recorded, I extracted a linear relationship based on Castagna et al. (1985) for the clastic lithologies:

$$V_P = aV_S + b, \tag{6.4}$$

and quadratic relationship based on Greenberg and Castagna (1992) for pelagic lithologies (Fig 6.9, Tables 6.4, 6.5):

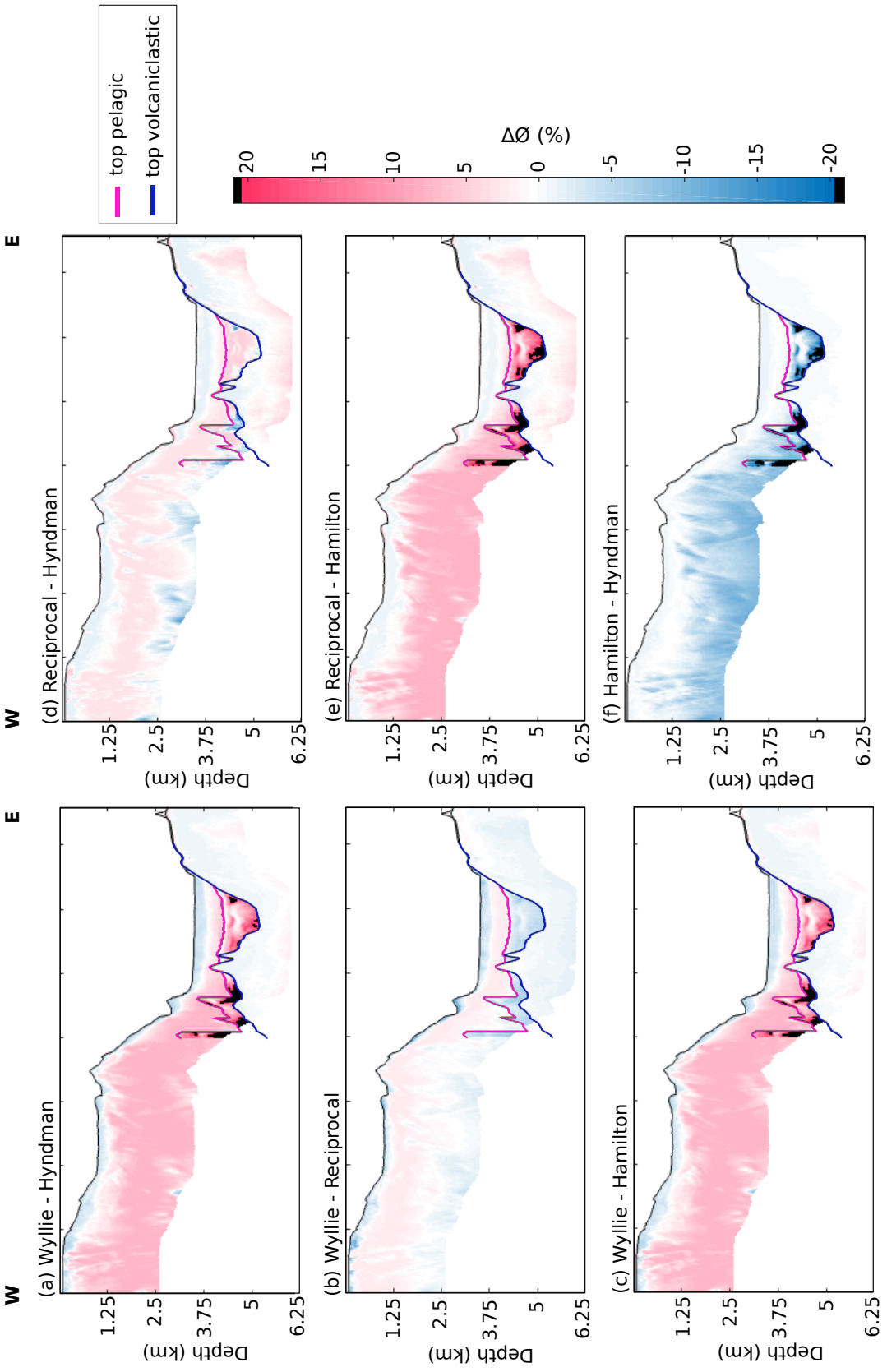


Figure 6.8: Differences between porosity models based on different best fit relationships between porosity and velocity data outlined in Fig 6.7 and Table 6.3.

Table 6.4: Parameters used by Castagna et al. (1985) to relate Vp to Vs, and the associated parameters found in this study.

Dataset/ equation	**a**	**b**	**R^2**
Castagna et al. (1985)	1.16	1.36	
U1519 Clastic	0.8803	1.5	0.7881
U1518 Clastic	1.0283	1.5	0.09918
U1520 Clastic	0.7467	1.5	0.31883
All clastic	0.9222	1.5	0.53347

Table 6.5: Parameters used by Greenberg and Castagna (1992) to relate Vp to Vs, and the associated parameters found in this study.

Dataset/ equation	**a**	**b**	**c**	**R^2**
Greenberg and Castagna (1992) (Limestone)	-0.05508	1.01677	-1.03049	
U1520 Pelagic	-0.2058	1.5188	-1.4431	0.54009

$$V_S = aV_P^2 + bV_P + c. \tag{6.5}$$

The two studies used for modelling focus on different lithologies, with Castagna et al. (1985) focussing on clastic rock and Greenberg and Castagna (1992) focussing on a range of porous sedimentary rock including pelagic limestones and shales. The best fit relationship for clastics was constrained to give Vs=0 when Vp=1.5km/s, as fluids contain no shear strength.

As no Vs measurements were taken in the region of volcaniclastic lithologies, I did not transform this region within the Vs model.

These relationships were used to convert the Vp model into a Vs model. The resulting Vs model could then be used to calculate a Vp/Vs model, bulk modulus model and shear modulus model, based on standard equations:

$$K = \rho(V_P^2 - \frac{4}{3}V_S^2), \tag{6.6}$$

where K is the bulk modulus, ρ is the density, V_P is the P-wave velocity and V_S is the S-wave velocity; and

$$\mu = V_S^2\rho^2, \tag{6.7}$$

where μ is the shear modulus.

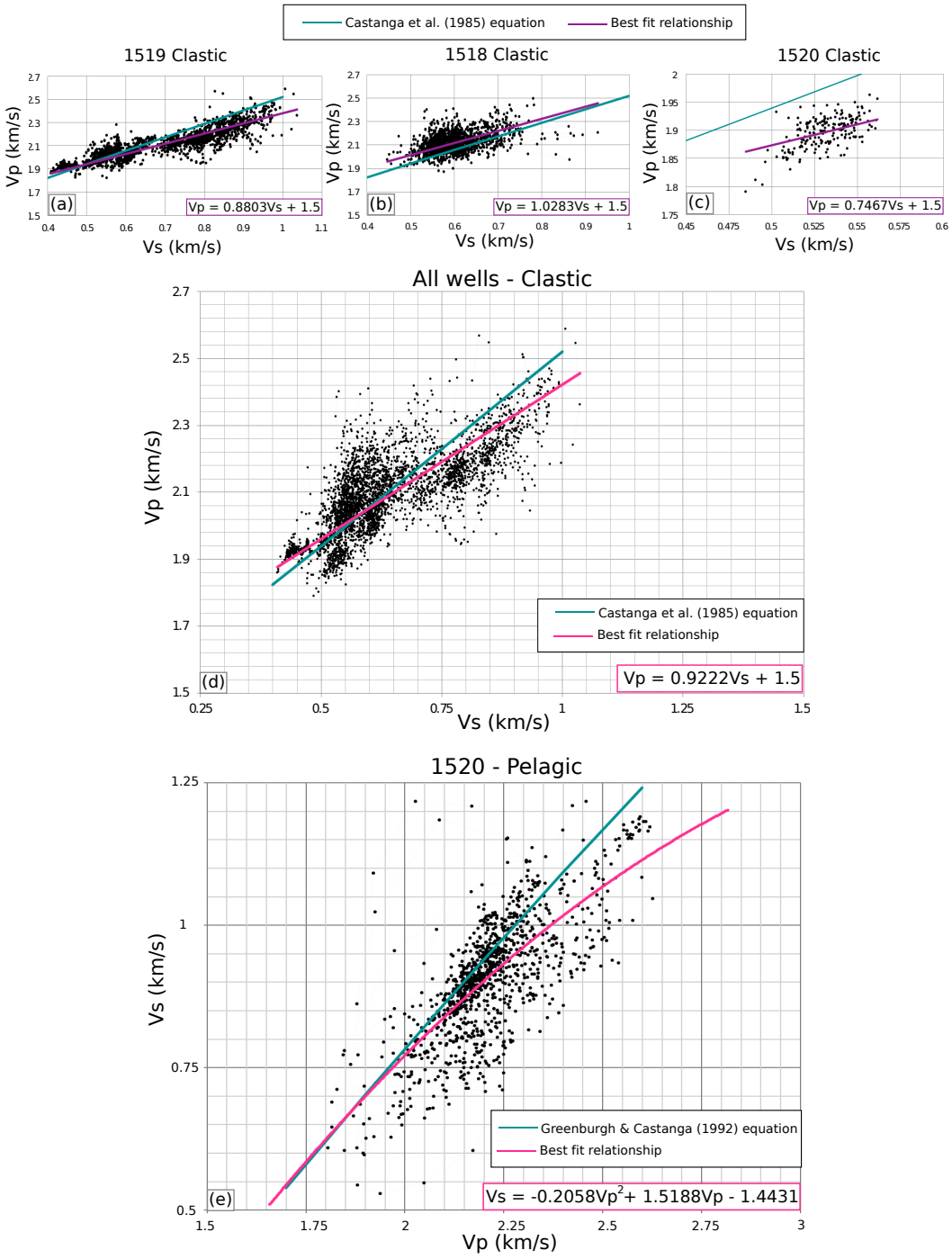


Figure 6.9: Vp vs Vs measurements for clastic lithology taken from LWD data for (a) U1519, (b) U1518, (c) U1520, (d) all sites and (d) U1520. (e) Shows Vs vs Vp for pelagic lithology at 1520. Note the axes are reversed in order to fit relationships based on Greenberg and Castagna (1992). Standard equations from Castagna et al. (1985) and Greenberg and Castagna (1992) are shown in green while best fit relationships based on data are shown in purple (a, b and c) and pink (d and e). The relationships derived in (d) and (e) (equations displayed on graphs and shown in Tables 6.4 and 6.5) were used to convert Vp to Vs in the models.

The bulk modulus, K, describes the ability of a material to withstand volumetric stress, and the shear modulus, μ, describes the rigidity of a material, or its ability to withstand shear strain or angular distortions.

As the FWI code uses Gardners Law (for density in kg/m^3 and V_P in m/s) (Gardner et al., 1974),

$$\rho = 310 V_P^{0.25}, \tag{6.8}$$

for density calculation during inversion, I used this relationship to convert Vp to density during model calculation of bulk and shear modulii. During error analysis, however, I compared the results to calculations using direct density, Vp and Vs measurements at the wells to understand if the choice of density affected results significantly (see section 6.5.3).

6.5 Results

6.5.1 Velocity difference and porosity models

6.5.1.1 Velocity difference model

Subtracting the velocity-depth profiles shown in Fig 6.5 from the final FWI velocity model in Fig 6.10(a) produces two models of the velocity differences between the shallow part (upper 2000mbsf) of the incoming section and wedge compared to undeformed sediments at site U1520 (Fig 6.10(c)). Fig 6.10(c) shows velocity anomalies based on the profiles extracted from the core and LWD data, while Fig 6.10(d) shows velocity anomalies based on the profile extracted at U1520 from the FWI model. Both models are considered in order to determine whether systematic differences between sensitivities of FWI and LWD Vp profiles affect the conclusions drawn from these models. Velocity anomalies are in the range +/- 1000m/s. Given the limited well penetration to characterise the volcaniclastics, and the fact that volcaniclastic sediments to the west of the deformation front are likely deeper than 2000mbsf based on interpretation of the PSDM image (Barnes, (inreview)), we restrict our analysis to only compare velocity anomalies for clastic and pelagic lithologies. This also explains the large positive velocity anomalies at the Tūranganui seamount complex in Fig 6.10(d).

The differences in velocity presented in Figs 6.10(c) and (d) can be caused by different compaction rates of the rock (Bangs et al., 1990; Han et al., 2017). If a rock is over-compacted for its present depth, porosity will be reduced and velocity difference will be high compared to undeformed sediment. If a rock is under-compacted, porosities will remain higher than undeformed sediment at the same depth, and hence velocity differences will be negative. This is, of course, based on the assumption that the rock is the same lithology as the undeformed sediments. By using the FWI profile through both lithologies as well as two velocity-depth profiles for undeformed rock-one for

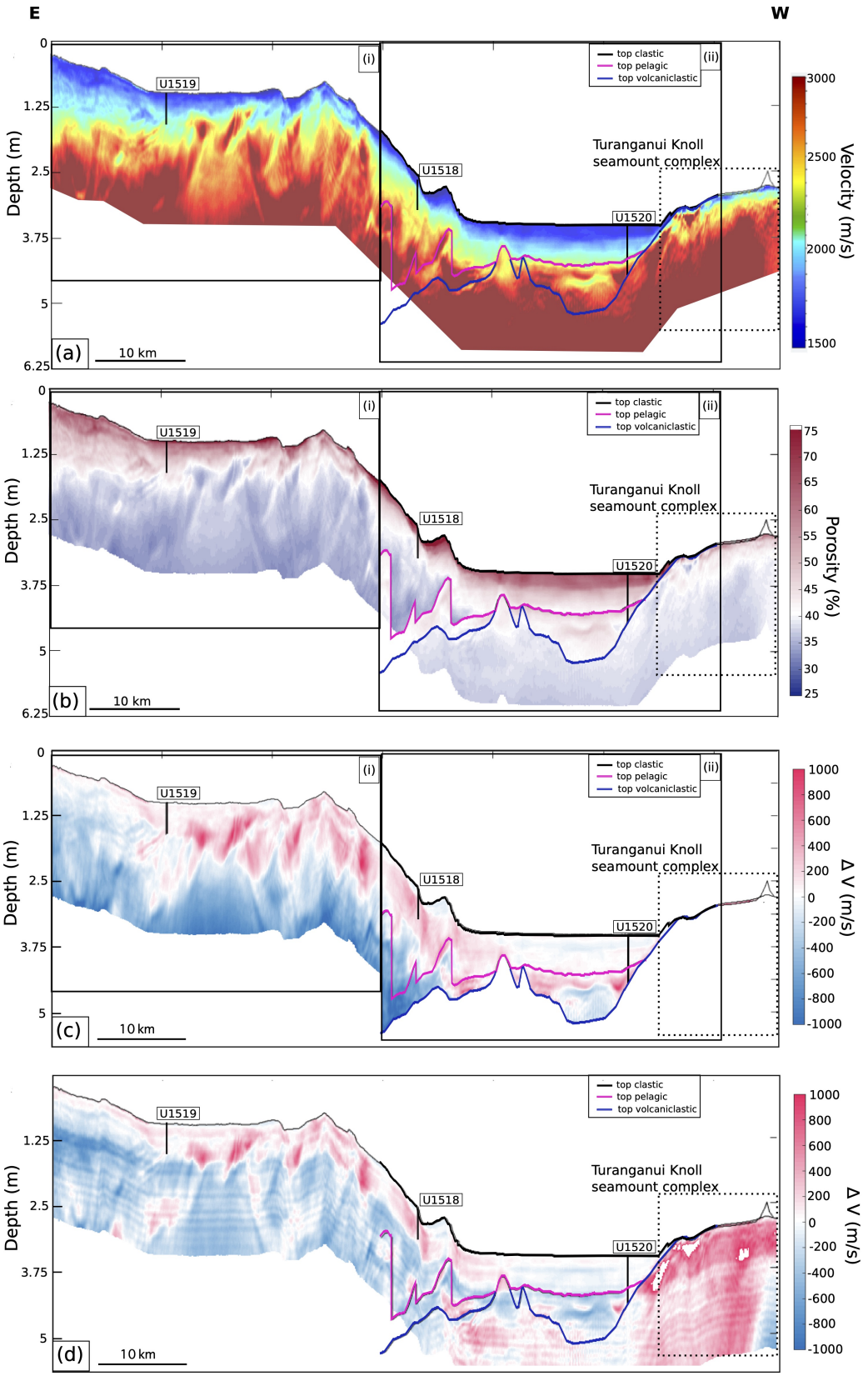


Figure 6.10: (a) Vp model (from chapter 4), (b) porosity model across 05CM-04 based on the reciprocal relationship between Vp and porosity (Fig 6.7, Table 6.3) (c) Velocity anomaly model based on difference between (a) and the velocity vs depth trend for undeformed clastic and pelagic sediments from LWD and core data (Fig 6.5) (d) Velocity anomaly model based on difference between (a) and the velocity vs depth trend for undeformed sediments from the FWI model extracted at site U1520 (Fig 6.5).

clastics and one for pelagics (Fig 6.5)-I have attempted to ensure the velocity difference profile represents under- or over-compaction of rocks of the same lithology, however any errors in the picked lithological boundaries (top pelagic and top volcaniclastic) may cause errors in the model by displaying velocity differences due to different rock types. Both models show similar patterns of positive and negative velocity anomalies within the wedge and incoming section.

As expected, velocity differences are low (∼+/- 50m/s) in the clastic layer of the Hikurangi Trough, where sediments are generally undeformed (Figs 6.10(c) and (d)). Velocity differences in the pelagic layer range from +/-50m/s to ∼+350m/s moving landward towards the volcaniclastic cone. The model based on the FWI profile shows less defined positive velocity anomalies in the upper part of the Hikurangi Trough, but shows a similar pattern of increasing velocity anomalies moving eastwards towards the trench. A very large positive velocity difference of +800m/s is present near the bottom of well U1520. In chapter 4 it was determined that this feature is likely real, however it has anomalously high Vp compared to the surrounding rock. This feature may be influencing the velocity-depth profile by causing a large scatter in the measurements (Fig 6.5, which already contain fewer values than for the clastic layer, causing the velocity-depth curve to be more complicated than the linear approximation made in section 6.4.1. Features in the incoming section and toe of the wedge will be discussed in more detail in section 6.5.1.4.

Within the wedge, positive velocity differences are identified in the upper ∼1000mbsf across the model, with a ∼+50m/s difference from the undeformed sediment profile, increasing to higher values of up to ∼+800m/s in the hanging walls of faults identified in the wedge. The most landward part of the wedge, near U1519 shows smaller differences of +/- 50m/s. Below ∼1000mbsf, the model shows more negative velocity differences, decreasing from ∼-50m/s at ∼1000mbsf down to -600-800m/s at depths of ∼2000mbsf. This part of the profile based on 6.10(c)will be discussed in more detail in section 6.5.1.3.

6.5.1.2 Porosity model

The porosity model (Fig 6.10(b)) was created using the preferred reciprocal relationship derived between porosity and velocity (Table 6.7, Table 6.3). Based on Nur et al. (1998) the critical porosity-where the modulus-porosity trend abruptly changes from stiffness being determined by the framework of contacting grains to the stiffness being determined by the pore fluid-is 40% for sandstones, limestones and dolomites. I therefore present the porosity model in terms of this critical porosity, with red values representing porosities above this critical porosity, and blue values below.

Across the model, high porosities of ∼65-75% are seen in the upper ∼500mbsf, gradually decreasing with depth as rocks become more compacted. Very high porosities (∼75%) at the surface are likely due to unconsolidated sediment deposited on the seafloor. To the far east of the model, at the Tūranganui seamount, there is a much more abrupt lateral change in porosity than the rest of the model due to a sharp reduction in porosity between pelagic and volcaniclastic rocks (Fig 6.10(b)).

Small-scale porosity anomalies exist in the porosity model, including the volcaniclastic cones within the Hikurangi trough, splay faults at the deformation front, and faults in the upper plate, detailed in sections 6.5.1.3and 6.5.1.4 (Figs 6.11 and 6.12). These anomalies mirror the Vp velocity anomalies described in chapter 4, which is expected as the porosity has been derived directly from the FWI Vp model (section 6.4.2).

6.5.1.3 Porosity and velocity differences on the overriding plate

Fig 6.11 shows a close-up of the overriding plate, ∼10-40km west of the deformation front (see Fig 6.10 for location). The largest velocity differences in this area are seen in the footwalls and hanging walls of faults 1, 2 and 3 (Fig 6.11(c)). Some of the most significant anomalies are large positive velocity differences within the hanging wall of fault 2 of up to +900m/s compared to the same depth within the undeformed sedimentary section (Fig 6.10). Given our velocity-porosity relationship, the velocities within the hanging wall of fault 2 indicate porosities of ∼35% compared to porosities of ∼45% at the same depth at well U1519. In contrast, within the fault zones, negative velocity differences are seen, modelled up to -500m/s, most prominently within the fault zone and footwall of fault 2, which have porosities of 40-45%. These observations may indicate that the hanging walls of these faults are over-compacted compared to normally compacting sediments in the Hikurangi Trough, while higher porosity in fault zones and the upper footwalls suggest under-compaction. These changes in porosity across fault 2 are also seen at fault 3, but less so at fault 1 (Fig 6.11).

Areas of isolated low porosity in the model, indicated by the dashed circles, also correlate with areas of high-velocity differences near the faults and further east on the slope (Fig 6.11). Small scale features a, b and c have been identified as shallow gas anomalies associated with the bottom simulating reflector (BSR) (chapter 4) (Navalpakam et al., 2012) and correspond to high porosity and negative velocity difference features in the models.

6.5.1.4 Porosity and velocity differences in the Hikurangi Trough and toe of the wedge

Within the Hikurangi Trough, east of the volcaniclastic domes, sediments are undergoing normal compaction, with a gradual increase in porosity with depth and little velocity difference from the extracted profile (Fig 6.5) in the clastic layer. Within the pelagics, however, the velocity difference model shows more variability, suggesting over-compaction from ∼750-1000mbsf, and under-compaction below ∼1000mbsf. Some key features are visible, including a sharp transition from positive to negative velocity difference, and a feature showing very high velocity difference of ∼+800m/s near the base of well U1520 labelled d and e respectively in chapter 4 Fig 4.11. In chapter 4 I stated that I believed these features to be real, and that these features may be associated with the Hikurangi basement sequence (HKB). These features are also visible as lower porosity anomalies in the porosity model (Fig 6.12(b)). The proximity of these features to site

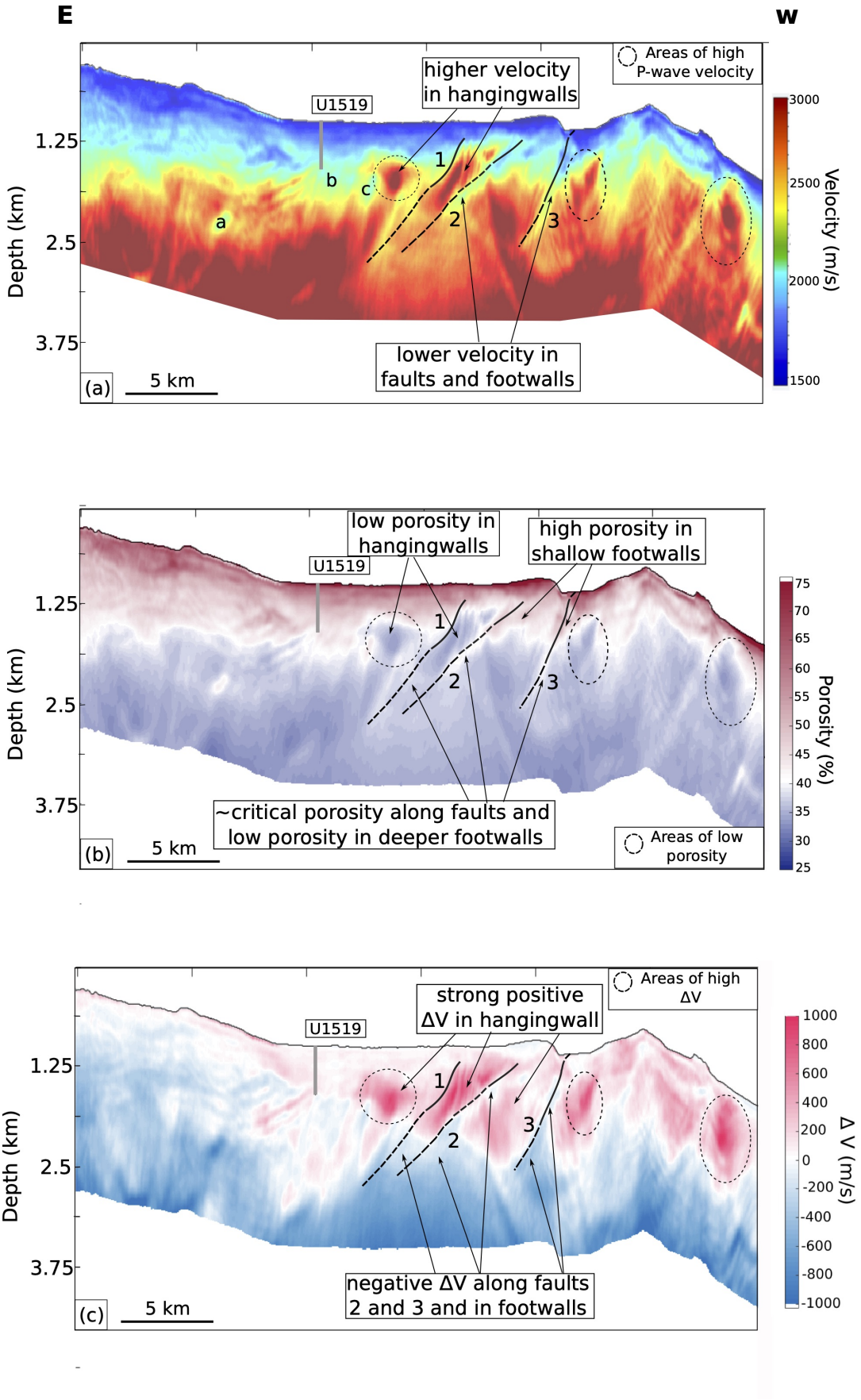


Figure 6.11: Detailed models of P-wave velocity overlying PSDM seismic image (from chapter 4) (a), porosity (b) and velocity anomaly (c) of the overriding plate (Fig 6.10(i)). This part of the model contains three faults (faults 1, 2 and 3) with strong variations in properties between footwalls, hanging walls and along faults.

U1520 may have affected the velocity-depth profile based on LWD data, causing the pelagic layer to show such variable velocity differences. Chapter 4 also shows that the lower limit (>700mbsf) of the wireline data collected on Expedition 372 does not correlate as well with the FWI model as the upper 700mbsf, which may affect the velocity difference modelling.

Landward of the volcaniclastic domes, at ∼5.3km east of the trench, larger velocity anomalies on the incoming plate become apparent in the model, with positive velocity differences occurring to depths of ∼500mbsf of ∼+100m/s and anomalies getting larger, up to ∼+300m/s moving towards the trench, within both the clastic and pelagic packages (Fig 6.12(c)). Porosities are also lower landward of the domes, with porosities of ∼50% east of the domes, and ∼40% west of the domes at ∼450mbsf in the clastics. Similarly in the pelagics, porosities decrease from ∼45% east of the domes to ∼40% west of the domes at depths of ∼950bsf.

At the trench, porosity appears to vary within the different lithologies. In the hanging walls of faults 4, 5 and the Pāpaku fault (fault 6), porosities are lower, with values of ∼35%, while porosities in the pelagic unit remain higher at ∼45% (Fig 6.12). This is reflected in the velocity difference model where the pelagic unit has a negative velocity difference of ∼-400m/s in the hanging wall of the Pāpaku fault, and even lower values of ∼ -850m/s in the hanging wall of fault 5. The velocity difference model also shows a negative velocity anomaly along the Pāpaku fault itself in the pelagic layer. While lower porosities in the hanging wall of fault 5 should suggest over-compaction and a higher velocity difference, at depths of <950mbsf the clastic sediment appears to be under-compacted based on negative (-60-300m/s) velocity differences. This effect is not seen in the hanging wall of the Pāpaku fault, where lower velocities produce positive (+100-250m/s) velocity differences.

6.5.2 Vs, Vp/Vs, shear and bulk modulii calculations

Fig 6.13 shows the results for the Vp, Vs, Vp/Vs, bulk modulus and shear modulus models along line 05CM-04, which were transformed from the Vp model using relationships derived in section 6.4.3. It is important to note the different scales, especially between the two velocity models. As all of these models were calculated using relationships based on Vp, it is no surprise that the models reflect the patterns seen in the Vp FWI model. The lack of independent constraints on Vs, Vp/Vs and elastic parameters means these models reflect plausible estimates of these parameters.

The model of the Vp/Vs ratio (Fig 6.13(c)) is derived simply by dividing the Vp model by the transformed Vs model. Vp/Vs ratios are a good indicator of fluid presence as Vs is sensitive to fluids, therefore a high Vp/Vs ratio may indicate fluids are present. Extremely high values of ∼15-25 are present in the upper ∼20m of the model, but these high values are attributed to unconsolidated, fluid rich sediment. In the Hikurangi Trough values >8 exist in the upper ∼250mbsf, with values decreasing uniformly in the clastic layer to ∼2.7 at ∼700mbsf. Values in the pelagic layer are

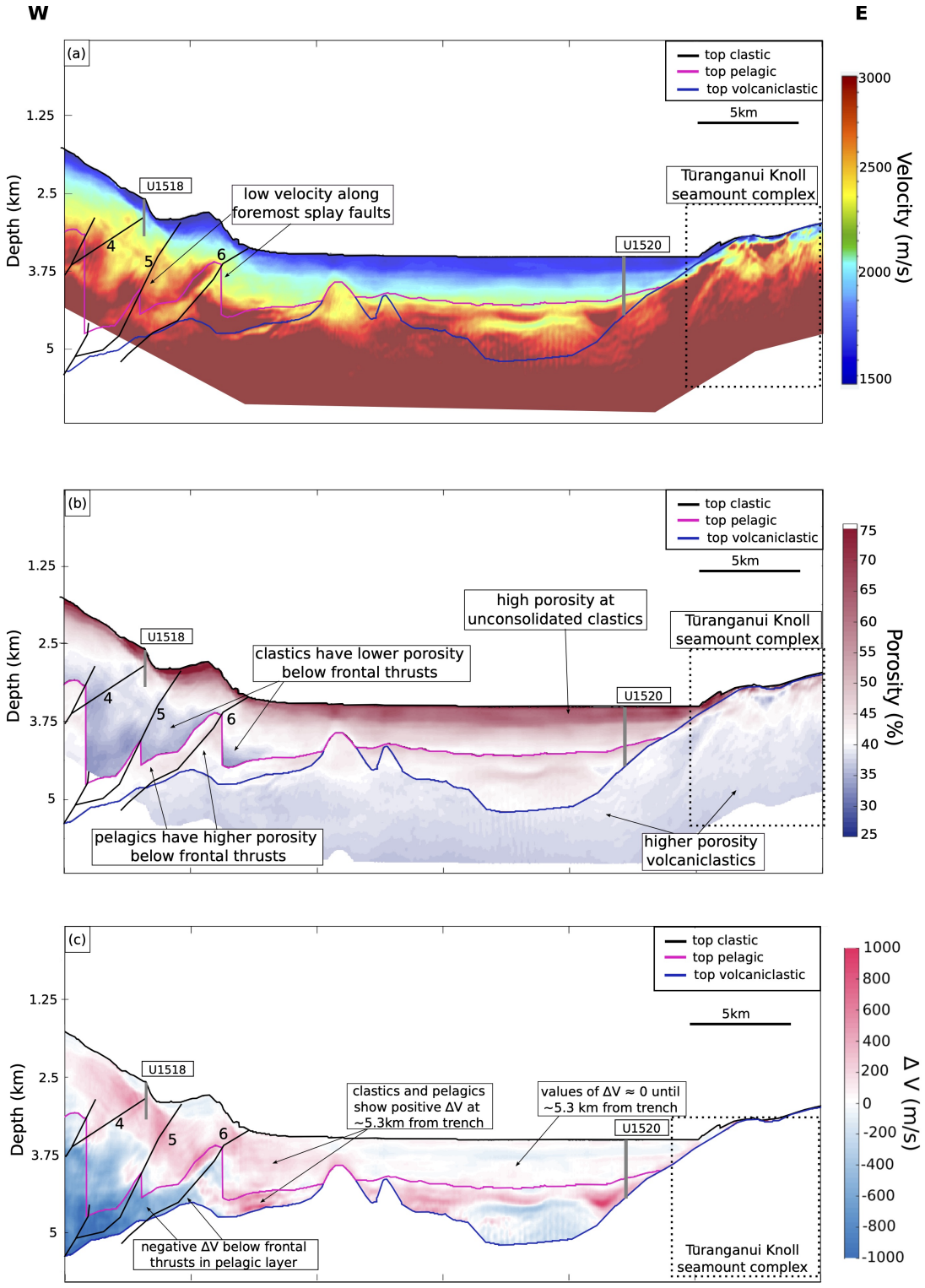


Figure 6.12: Detailed models of P-wave velocity overlying PSDM seismic image (from chapter 4) (a), porosity (b) and velocity anomaly (c) of Hikurangi trough and trench (Fig 6.10(ii)). This part of the model contains three faults (faults 4, 5 and 6) with the Pāpaku fault (fault 6) the frontalmost thrust fault at the trench, and fault 4 which was drilled by well U1518.

more constant, lying at 2.3-2.4 within the trough. Values in the wedge are more variable, but are generally higher (>3) in the upper 400mbsf. Values below 400mbsf range from ∼2 to 1.5 in the deeper parts of the model ∼2kmbsf. Vp/Vs is also higher (∼2-3) in footwalls and along faults (2.7-4) in the wedge, and lower (∼1.8) in the hanging walls.

Fig 6.13(d) shows the bulk modulus model, calculated using equation 6.6, which is dependent on the Vs and Vp models (equations 6.6 and 6.8). A high bulk modulus indicates that the material is able to withstand more pressure, and therefore is more difficult to compress. The model shows bulk modulus generally increases with depth, with values starting at ∼5Gpa near the surface (Fig 6.13(d)). The undeformed sediments in the Hikurangi trough around well U1520 have lower bulk moduli within the clastic layers, with values of ∼8.5Gpa near the top-pelagics, increasing to ∼10GPa closer to the trench. The pelagic layer has higher values of ∼10-14GPa. Higher values of bulk modulus (∼12GPa) can be found in the hanging walls of faults within the wedge, with lower values of ∼7-8GPa along faults and ∼8-8.5Gpa in footwalls. The lower parts of the overriding plate between 1000-2000mbsf have bulk modulus in the range 10-13GPa.

Finally, the model of shear stress (Fig 6.13(e)) is more dependent on Vs than Vp (equation 6.7) and therefore regions of low Vs near the surface will control these surface shear modulus values. Low shear modulus values indicate that the material is not very resistant to shear strain or angular distortions, i.e. it is not very rigid. This could be the case for unconsolidated sediments and areas with high fluid content. The model shows low values of 0-0.15GPa in the shallowest <375mbsf of the model increasing to 7.5Gpa at a depth of ∼600mbsf. The sediments in the Hikurangi Trough have lower shear modulus values of ∼0.02-1.4GPa in the clastic layer and ∼1.8-3.5GPa in the pelagic layer (Fig 6.13(e)). Moving landward, higher values of shear modulus are found within the wedge of around ∼4GPa at depths of 1000mbsf. Higher shear modulus (∼6GPa) can be seen in the hanging walls of faults on the overriding plate, with lower values of ∼0.8 -1.7GPa along the faults themselves. Deeper parts of the overriding plate, between 1000-2000mbsf have variable shear modulus values but in general are 3-5GPa, with some features as low as 1.5GPa and as high as 12GPa.

The models reveal most variations in elastic properties around the faults. For example, fault 2 shows strong contrasts between the fault zone and the hanging wall for Vs, Vp/Vs, bulk and shear modulus models. While the hanging wall of fault 2 shows high Vs values of ∼1500-2000m/s, along the fault zone Vs values range from ∼520m/s at 350mbsf to ∼900m/s at ∼850mbsf, with velocity contrasts of ∼850-1000m/s across the fault. This is reflected in the Vp/Vs ratio, which is ∼1.7 in the hanging wall of the fault, and from ∼3.7 at ∼350mbsf to ∼2.5 at ∼850mbsf within the fault zone. The shear modulus is ∼5-6GPa in the hanging wall and ranges from ∼0.5GPa at ∼350mbsf to ∼1.7GPa at ∼850mbsf within the fault zone, and the bulk modulus model also shows a significant drop from ∼12.75GPa in the hanging wall, to ∼7.5 GPa at ∼350mbsf and ∼9.25 GPa at ∼850mbsf within the fault zone. This higher Vp/Vs ratio alongside lower shear modulus values in the fault

zone may suggest that while the hanging wall is consolidated and rigid, the fault itself appears less consolidated and unable to withstand shear strain. Alongside the lowered Vs values, lower shear modulus could be indicative of fluid presence along fault 2 as fluid presence would reduce Vs, emphasised by the high Vp/Vs ratio. A similar analysis can be made for fault 3 as similar contrast in parameters also occurs between the hanging wall and fault itself. These contrasts in rock properties are also visible along faults 1 and 3, which could indicate that these faults are acting in a similar way.

Within the Hikurangi Trough, Vs values in the clastic layer are relatively low nearest the seafloor in the upper 50mbsf, modelled at ∼80m/s, and increase at a constant rate to ∼200m/s at ∼250mbsf. Vs values then increase steadily at a more rapid rate, from ∼200 to ∼400m/s over the next 100mbsf, and then steadily increase again to ∼850m/s at ∼700mbsf where the clastic layer ends. These variations, including the jump between 250-350mbsf are mirrored in the Vp/Vs, bulk modulus and shear modulus properties. The pelagic layer is more variable, with the features relating to the HKB described in section 6.5.1.4 showing variations in Vs, bulk modulus and shear modulus, but less so in the Vp/Vs model. This is to be expected based on the Vp and Vs models which both show these features, which therefore get cancelled out when taking the ratio.

Of particular note are the properties surrounding the Pāpaku fault (fault 6), the frontal most splay fault at the trench wedge. Along this fault there is a variation in elastic properties. Vs values are ∼900-1000m/s within the fault zone itself with values of ∼1200m/s in the surrounding pelagic footwall and hanging wall. These low Vs values correspond to a lower shear modulus of ∼2.3-4GPa along the fault compared to ∼7-10GPa in surrounding pelagic footwall and hanging wall, and higher Vp/Vs ratios of 1.8-2 within the fault compared to ∼1.4 in the surrounding pelagics. The bulk modulus has only a small contrast across the fault, with values of ∼8.6GPa in the fault zone compared to ∼9.5GPa in the surrounding pelagics. These results are similar to those found along faults 1, 2 and 3, which were identified as possible fluid conduits (see chapter 4).

6.5.3 Error analysis

As I am using cross-plots to find best fit relationships between properties, and using these relations to convert between different rock properties using equations 6.6, 6.7, and 6.8, errors will be present in the calculations. For example, the cross-plot between Vp and Vs for clastics has a mean percentage error of ∼10% between predicted and observed values (Fig 6.9(d)). This error would propagate into the calculation of Vp/Vs, bulk modulus and shear modulus.

e.g. for Vp = 2km/s,
Vs=0.569km/s +/-0.057km/s (10% error),
Vp/Vs = 3.515 +/- 0.35 (10% error),
K = 7.386 +/- 1.62GPa (22% error),

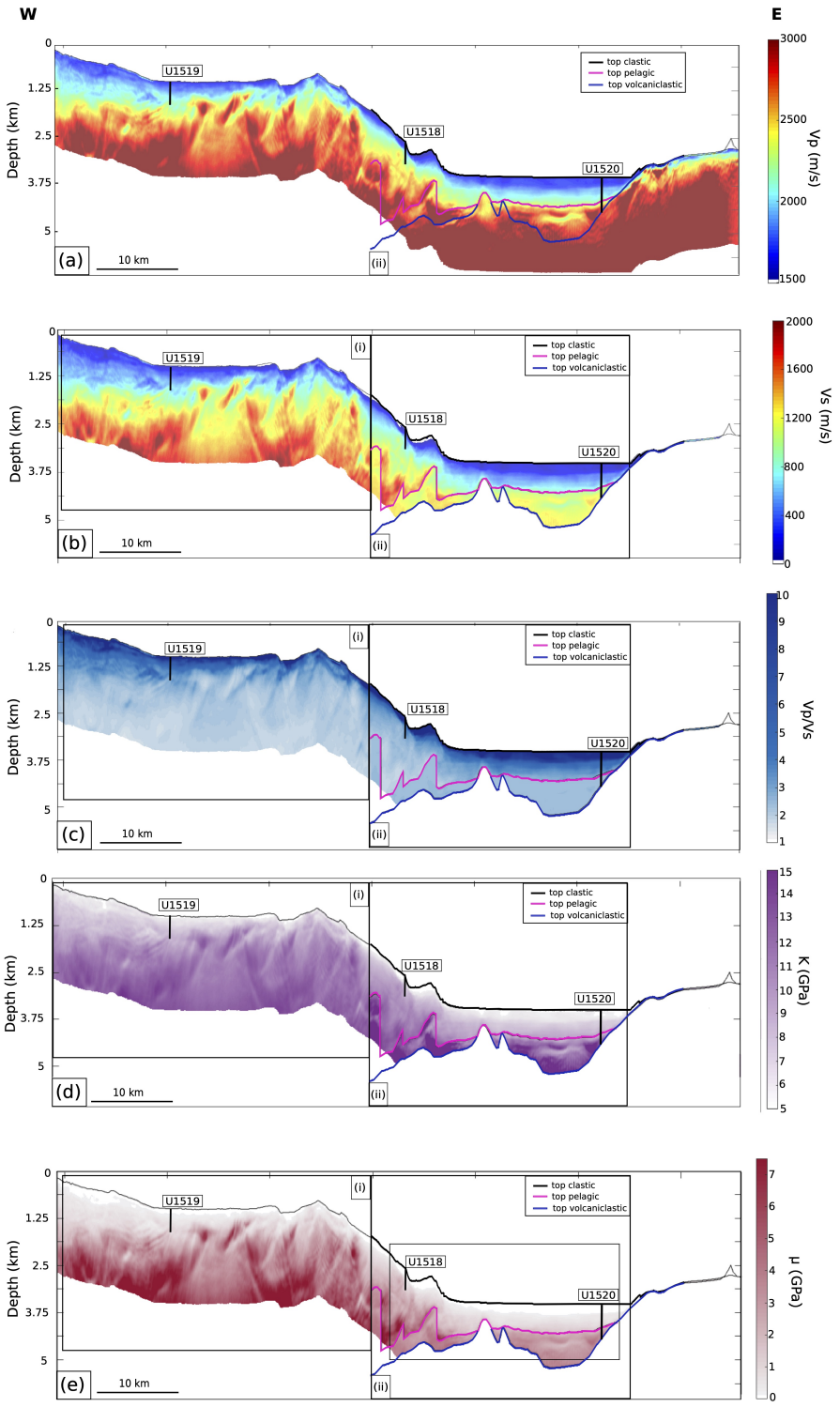


Figure 6.13: (a) Final FWI Vp model (from chapter 4), (b) Vs model based on linear equation from Vp vs Vs cross-plots of wells U1519 and U1520 (Fig 6.9). (c) Vp/Vs ratio calculated by dividing (a) by (b), (d) Bulk modulus and (e) shear modulus models calculated using equations 6.6 and 6.7 respectively.

μ = 1.39 +/- 0.3GPa (22% error).

The mean percentage error for the pelagic Vp to Vs calculations is ∼10%. This is based on an error only in the Vs value.

Comparing LWD, wireline and core values of density, Vp, Vs, porosity and elastic moduli to values extracted from the transformed model at the well locations can help to understand how well the transforms recover elastic properties (Figs 6.14, 6.15, and 6.16). The relationships chosen for converting Vp to Vs, outlined in the methods chapter (section 6.4.3, Fig 6.9, Tables 6.4 and 6.5), are used to convert Vp measurements from LWD, wireline and core data to Vs. Vs logs, both directly measured by the LWD tool and converted from Vp can then be used to calculate Vp/Vs, bulk modulus and shear modulus, using LWD density measurements from the same drill sites.

As stated in chapter 4, when comparing LWD P-wave velocities with velocities produced by FWI modelling, the LWD tool is most sensitive to vertical changes in velocity while FWI, determined by refracted turning waves, is more sensitive to horizontal velocities. This means it is not a straightforward comparison between the LWD data and the velocity data produced by FWI. As the full-waveform inversion is isotropic, any anisotropy in the subsurface geology will not be accounted for, so logs may not match exactly, however general trends should still be recovered by the models, and values should be in the same range, even if high-frequency features cannot be resolved (see chapter 4 for more detail).

(a) Density comparisons

Density is another important factor to consider. Figs 6.14, 6.15, and 6.16(a) shows the variation in densities at the three drill sites. The black dots represent the LWD density data, purple dots the core density data, and the grey dots the predicted density using Gardners law applied to the Vp LWD data measurements (Gardner et al., 1974). Site U1520 shows the greatest difference in densities, the values differ significantly until ∼700mbsf. Density calculated using Gardners law and Vp values taken from the FWI model at the well location, however, match very well with the predicted density from LWD Vp. This is because the Vp values fit well between the FWI and reality as in Figs 6.14, 6.15, and 6.16(b), but it seems that Gardners law may not be appropriate in the upper 700m at site U1520. Core density measurements, shown as purple dots, are also very variable, but match slightly better with both Gardner predicted densities in the shallow subsurface between 50-75mbsf, and are in the range of the FWI predicted density below ∼860mbsf. Such a high variability between measured and calculated density may affect accuracy of the models by introducing further errors than those calculated above for Vs alone. The mean percentage difference between the LWD densities and densities predicted using Gardners law from LWD velocities is ∼15%. Using the

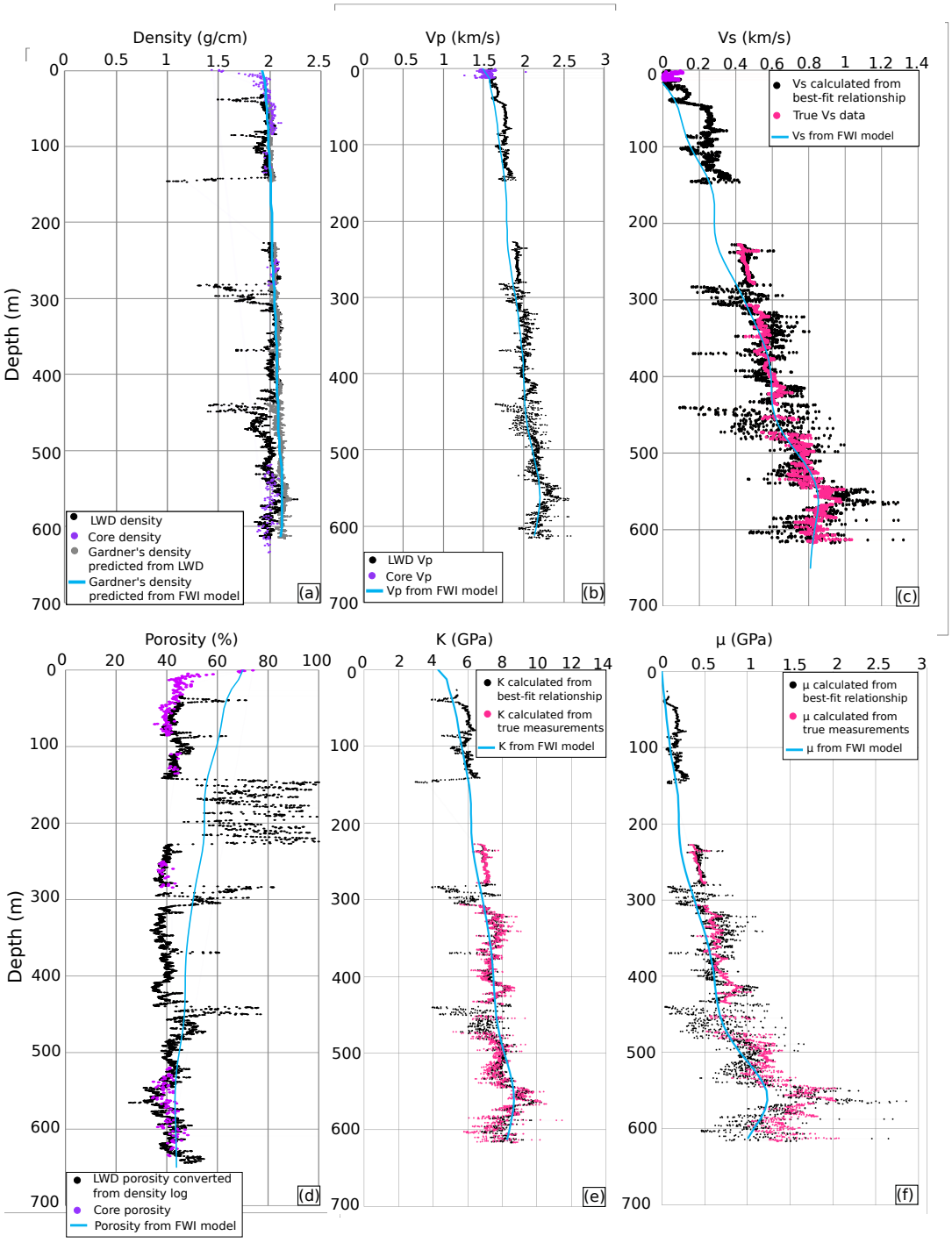


Figure 6.14: Site U1519. (a) Differences is possible density values. Black dots represent LWD density measurements, purple dots represent core density measurements, grey dots represent density values calculated from velocity LWD using Gardners relationship (equation 6.8). The blue line shows the density extracted from the P-wave FWI model converted to density using Gardners law. (b) shows the Vp measurements from LWD while the blue line shows Vp from the FWI model extracted at the drill site. (c) Black dots show Vs values calculated from Vp LWD measurements shown in (b) using the best-fit relationships derived in section 6.4.3 (Tables 6.4 and 6.5), as well as LWD Vs data shown in pink. The blue line shows the Vs profile extracted from the Vs model at the drill site. (d) Shows the porosity converted to desity from the LWD log as outlined in Section 6.3.2. Purple dots show the porosty from core measurements and the blue line shows the porosity profile extracted from the model at the well site. (e) and (f) show calculated bulk and shear modulii using density, Vp and Vs values from the logs shown using both calculated (black) and true (pink) Vs. Also shown in (d) and (e) are the calculated values of elastic modulii from well U1519 location in the models shown in Fig 6.13 using Gardners density, FWI derived Vp and Vs calculated from equations in Tables 6.4 and 6.5.

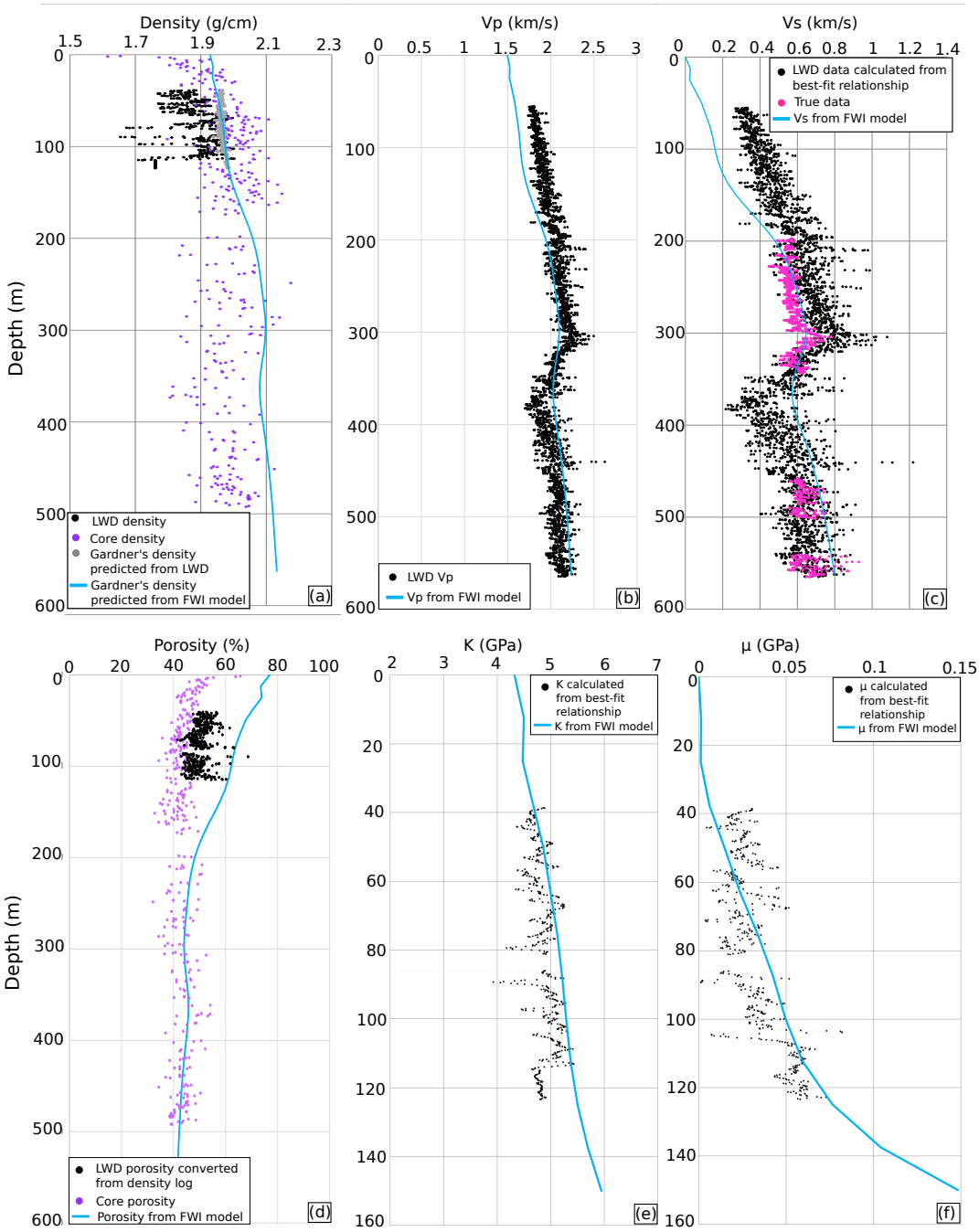


Figure 6.15: Site U1518. (a) Differences is possible density values. Black dots represent LWD density measurements, purple dots represent core density measurements, grey dots represent density values calculated from velocity LWD using Gardners relationship (equation 6.8). The blue line shows the density extracted from the P-wave FWI model converted to density using Gardners law. (b) Shows the Vp measurements from LWD in black and core in purple, while the blue line shows Vp from the FWI model extracted at the drill site. (c) Black and purple dots show Vs values calculated from Vp LWD and core measurements respectively shown in (b) using the best-fit relationships derived in section 6.4.3 (Tables 6.4 and 6.5), as well as LWD Vs data shown in pink. The blue line shows the Vs profile extracted from the Vs model at the drill site. (d) Shows the porosity converted to density from the LWD log as outlined in Section 6.3.2. Purple dots show the porosty from core measurements and the blue line shows the porosity profile extracted from the model at the well site. (e) and (f) show calculated bulk and shear modulii using density, Vp and Vs values from the logs shown. Also shown in (d) and (e) are the calculated values of elastic modulii from well U1518 location in the models shown in Fig 6.13 using Gardners density, FWI derived Vp and Vs calculated from equations in Tables 6.4 and 6.5.

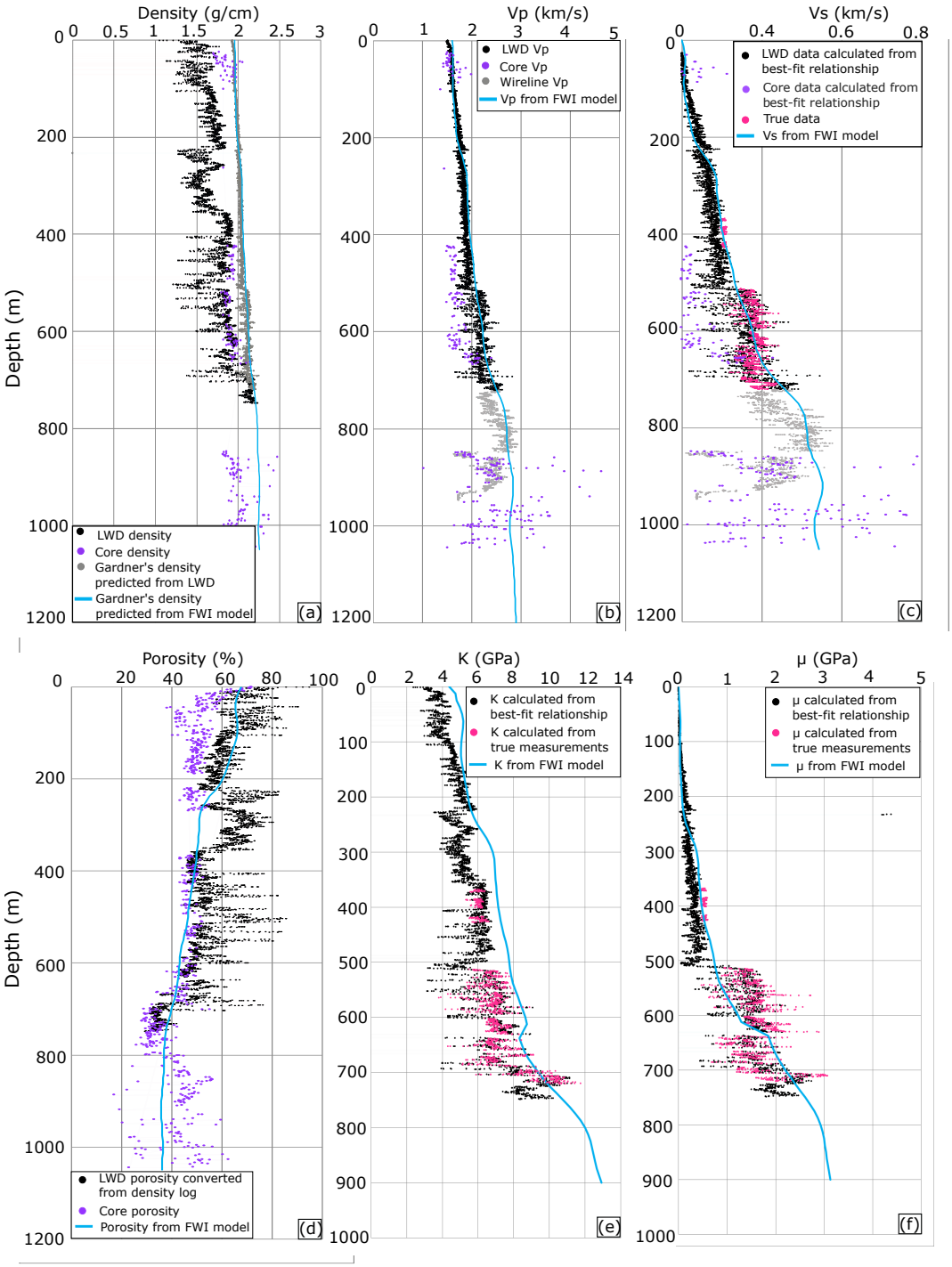


Figure 6.16: Site U1520. (a) Differences is possible density values. Black dots represent LWD density measurements, purple dots represent core density measurements, grey dots represent density values calculated from velocity LWD using Gardners relationship (equation 6.8). The blue line shows the density extracted from the P-wave FWI model converted to density using Gardners law. (b) Shows the Vp measurements from LWD, purple dots show core Vp values, and grey dots show wireline Vp values, while the blue line shows Vp from the FWI model extracted at the drill site. (c) Black, purple, and grey dots show Vs values calculated from Vp LWD, core, and wireline measurements respectively shown in (b) using the best-fit relationships derived in section 6.4.3 (Tables 6.4 and 6.5), as well as LWD Vs data shown in pink. The blue line shows the Vs profile extracted from the Vs model at the drill site. (d) Shows the porosity converted to desity from the LWD log as outlined in Section 6.3.2. Purple dots show the porosty from core measurements and the blue line shows the porosity profile extracted from the model at the well site. (e) and (f) show calculated bulk and shear modulii using density, Vp and Vs values from the logs shown using both calculated (black) and true (pink) Vs. Also shown in (d) and (e) are the calculated values of elastic modulii from well U1519 location in the models shown in Fig 6.13 using Gardners density, FWI derived Vp and Vs calculated from equations in Tables 6.4 and 6.5.

same example as above, this would increase errors in the calculation of bulk and shear modulii to:

K = 7.386 +/- 1.9GPa (26% error),
μ = 1.39 +/- 0.5GPa (37% error).

These percentage errors, were calculated using LWD and core data which is highly variable at shallow depths due to washouts, poor core recovery and poor borehole conditions(Pecher et al., 2019; Wallace et al., 2019), and so are used as an estimate of the model percentage error rather than a concrete value. Variations at sites U1518 and U1519 are less significant, however these sites contain less data than site U1520. Using borehole density instead in the model would require extracting a velocity-density relationship from the borehole data and applying it to the whole model. This will introduce more uncertainties in extracting the relationship and applying it to the entire model including unsampled parts.

(b) Porosity comparisons

The reliability of the FWI model transformed to porosity can be considered by comparing porosity values extracted from the model to LWD, wireline and core values at the well locations (Figs 6.14, 6.15, and 6.16(d)). Using the density-porosity relationships extracted in section 6.4.2(Fig 6.6, Table 6.2), density LWD logs were converted to porosity logs for comparison. Data extracted from the model at the well locations can then be compared to the drilling data to assess similarities between the two. I expect the match to be good as the LWD and core data were used to derive the relationship between velocity and porosity, however, the relationship I derived is very simple compared to the true variations in porosity that are seen in the well data, and the LWD tool is more sensitive to vertical changes and measures at higher frequencies (1-20kHz) compared to the FWI model which is more sensitive to horizontal structure and lower frequencies (3-8Hz) (see chapter 4).

At well U1519 porosities appear to be overestimated in our model until ∼450mbsf (Fig 6.14(d)). LWD porosities are highly variable between ∼35-250mbsf and these values were not included in the cross-plot (Fig 6.7) that was used to derive the preferred velocity-porosity relationship due to the lack of Vp data at these depths (Fig 6.2 and shown in chapter 4). Below 250mbsf model porosities gradually trend towards the LWD and core values, until ∼450mbsf where they begin to match well. Similarly at well U1518, porosities in our model appear to be overestimated shallower than ∼200mbsf (Fig 6.15(d)). Despite the limited LWD data at this site (Fig 6.3), porosity measured from core data align well with our predicted model porosities. At well U1520, predicted model porosities align well with LWD porosities converted from density logs, but overestimate porosity derived from core (Fig 6.16(d)). Between ∼260-360mbsf, where there is a gap in the core data (Fig 6.4, the predicted model porosities underestimate the porosity calculated from the LWD measurements, but match with core values from ∼360-500mbsf. At the lower end of the log, between 800 and 1050mbsf, predicted

model porosities lie within the bounds of the measured values from cores.

(c) Vs comparisons

At well U1519, it can be noted that the Vs values calculated from Vp LWD data, match well with the recorded Vs LWD data (Figs 6.14, 6.15, and 6.16(c)) which indicates that our equations for estimating Vs from Vp work well (Tables 6.4 and 6.5, Fig 6.9). The Vs model created using these equations from tables 6.4 and 6.5, to transform the FWI model also works well, with the Vs values from our transformed FWI Vp model, shown by the red line, extracted at the well location showing a good match to the real data, albeit slightly underestimating true Vs recorded by LWD. This is expected based on the good match between Vp LWD data and Vp from the FWI model (chapter 4), and the fact that we use the Vp and Vs LWD data to derive the relationships used to transform the model. As no Vs data was available in any of the wells to derive a relationship between Vp and Vs at depths shallower than 150mbsf, an imperfect match in this region is expected, and an underestimation of model Vs vs LWD converted Vs occurs (Figs 6.14, 6.15, and 6.16). Core Vp data converted to Vs, match well with predicted Vs values from the transformed FWI Vp model at shallow depths. LWD Vp values calculated at site U1518 had a larger variance than at the other wells, which resulted in a more poorly constrained Vp-Vs relationship with a lower R^2 value (Table 6.4). While the match between true Vs and Vs converted from Vp LWD logs is again a good fit below 450mbsf at U1518, the shallower values appear to overestimate Vs between 200-350mbsf (Fig 6.15(c)). The Vs extracted from the transformed FWI model does, however capture the velocity inversion shown by the Vp converted LWD data between 300-400mbsf, but with reduced amplitudes. At site U1520 transformed model Vs values match relatively well from ∼225-600mbsf, lying between converted LWD data and true Vs measurements, which are slightly higher than the predicted values at around 400mbsf and between ∼520-620mbsf (Fig 6.16(c)). True Vs measurements and those converted from Vp logs match more closely between ∼620-720mbsf, however the transformed Vs model overestimates Vs from ∼600mbsf. The transformed model Vs values does not capture the velocity inversion at ∼850mbsf recorded by the wireline tool.

(d) Elastic modulii comparisons

By using density and velocity measurements from the LWD tool, equations 6.6 and 6.7 were applied to calculate the bulk and shear modulii at the well sites in order to compare the results with the transformed models of bulk and shear modulus. Figs 6.14, 6.15, and 6.16(e) and (f) show logs for bulk and shear moduli respectively, calculated from LWD Vp, Vs and density data, and equations 6.6 and 6.7. Wireline data from the bottom of well U1520 was not included in bulk and shear moduli calculations due to a lack of corresponding density data, and core data was not included due to a lack of both density and Vp measurements at the same discrete depths. Depths at which a density log was recorded with no corresponding Vp log for the same depths were discarded, and vice versa when calculating bulk and shear moduli. The density, Vp and Vs logs were then used to calculate the bulk modulus, K, and

shear modulus, μ. The results of these direct calculations were then compared to the values extracted from the transformed FWI models at the well locations, shown by the blue line in Figs 6.14, 6.15, and 6.16(e) and (f). For the bulk modulus at site 1520, we see that the results calculated using the predicted and true Vs match well, but the model overestimates bulk modulus, while for the shear modulus, the results calculated using the predicted and true Vs values match well at depths >500mbsf, but the predicted Vs values underestimate the true shear modulus between ∼350-450mbsf. The shear modulus model shows a better match to the shear modulus calculated from the LWD data than the bulk modulus at U1520, which is unexpected based on the error analysis presented in section 6.5.3. The model also shows a good match to the bulk and shear modulii calculated at wells U1519 and U1518, although limited density data at site U1518 means the comparisons are made of a small, shallow interval from 38.6-123.5mbsf.

6.6 Discussion

6.6.1 How far from the trench do incoming sediments first feel the effects of compression?

Away from the deformation front, in the Hikurangi Trough, sediments will be compacting normally due to the vertical weight of sediments being deposited above them. As the deformation front approaches, however, a component of lateral compaction is introduced as the Pacific plate subducts. The magnitude of this lateral force and the distance over which it has an effect is not well known, however the velocity difference model produced in this chapter may be able to constrain this force (Carbotte et al., 2012; Cochrane et al., 1994; Han et al., 2017; Yuan et al., 1994)

The velocity difference at 200mbsf (Fig 6.17) shows a sharp increase at ∼8km from the trench in both models where velocity difference estimates rise from ∼ -70m/s and ∼ -30m/s at 8km from the trench to ∼ +60m/s and ∼+80m/s at ∼6.2km from the trench for the model based on LWD and core data and the model based on FWI data respectively. The profile then dips to ∼0-20m/s velocity difference directly above the volcaniclastic cones between 5.3-6km from the trench in both models before increasing steadily from ∼5.3km from the trench to a maximum velocity difference of ∼300m/s and ∼250m/s at ∼500m from the trench for the model based on LWD and core data and the model based on FWI data respectively. The increase in velocity difference and therefore potential onset of sediment compaction between ∼5.3-8km from the trench may be due to the effect of lateral compression caused by subduction. Compression due to overburden alone should not produce large velocity differences in the model as these have been accounted for in the velocity-depth profile used to create the model (Fig 6.5). The incoming section begins to feel the effect of the deformation front at ∼5.3km seaward from the trench, where the profiles from both models begin a constant increase in velocity anomaly, as it becomes more and more compacted approaching

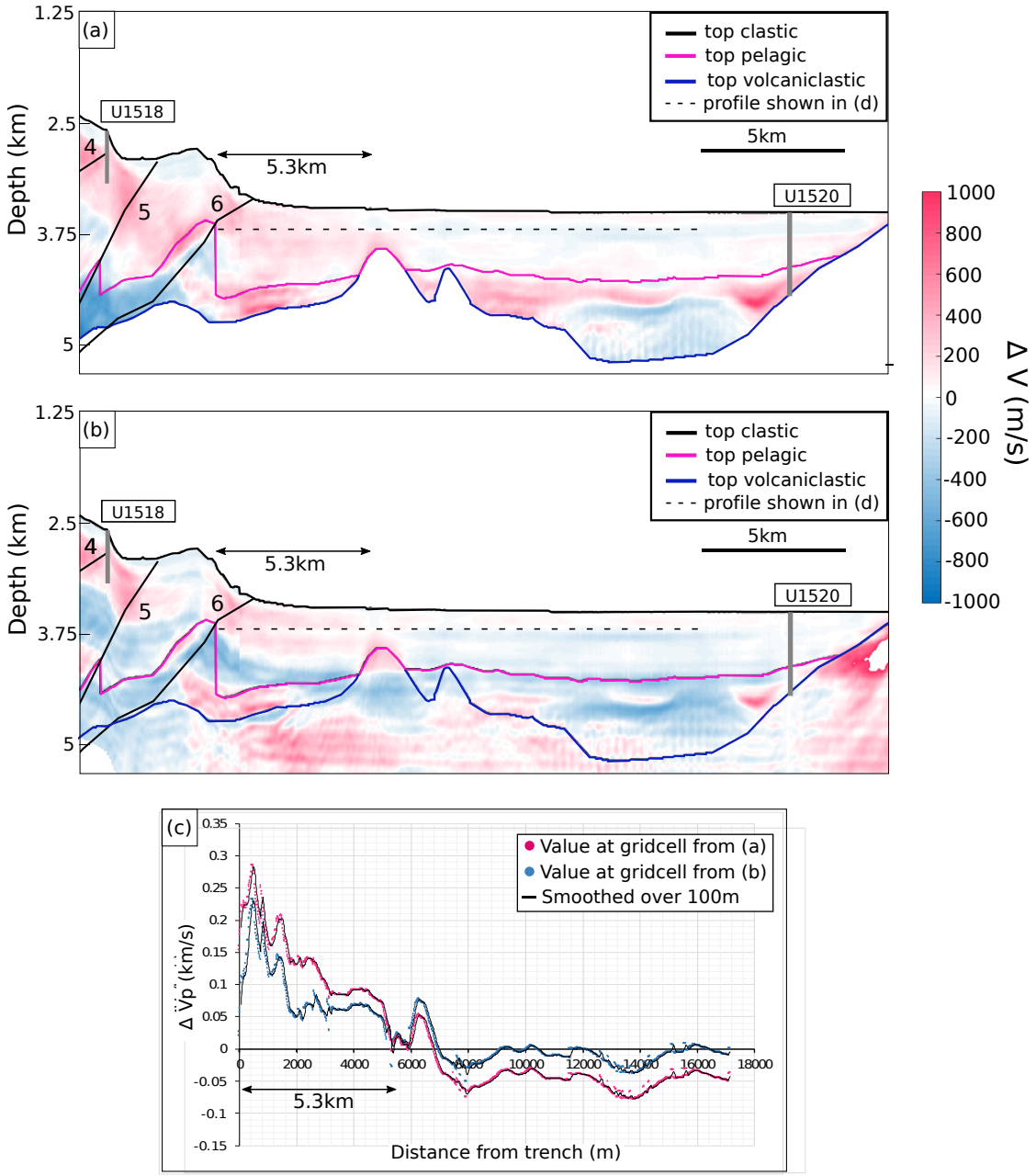


Figure 6.17: (a) shows the velocity difference model in the Hikurangi Trough based on velocity profiles extracted from LWD and core data. (b) Shows the velocity difference model in the Hikurangi Trough based on the velocity profile extracted at U1520 from the FWI model.The dashed lines show the location where the profile in (c) was extracted, at 200mbsf.

the Pāpaku fault, and may feel these effects all the way to ∼8km from the trench, although the presence of the volcaniclastic cones and potential differential compaction around the more rigid cones could also play a role. The velocity difference detected between 5.3-8km from the trench, around the volcaniclastic cones may also be due to seismic interpretation errors with the top of the cone not being picked shallow enough, and so the velocity difference profile around the top of the cone may be responding to a change in lithology rather than compaction. Overall based on the velocity difference modelling, it is apparent that the incoming section begins to feel lateral compaction due to subduction between 5.3-8km from the trench.

These results are consistent with the lower end of values in the analysis by Barnes et al. (2018) who found the onset of deformation, or proto-thrust zone (PZT) to range from <5km-25km at the southern Hikurangi margin based on interpretations of protothrust faults in high-quality geophysical and bathymetric images. Such proto-thrust faults are not seen in seismic reflection data from the north Hikurangi margin (e.g. Fig 6.10(a)). The velocity difference within the incoming sedimentary section which we observe (Fig 6.12, 6.17) suggests that sub-seismic scale deformation and compression is occurring at distances up to 8km from the deformation front. This proto-thrust zone width is narrower than in the most southern parts of Hikurangi where the PTZ extends to ∼25km (Barnes et al., 2018). This may be related to the incoming sediment thickness, which decreases from almost 5km near the Cook Strait which separates the North and South Islands, ∼3-4km near Hawkes Bay, and down to ∼1km off the Raukumara peninsula at the tip of the North Island (Barnes et al., 2010). The much smaller sediment supply at northern Hikurangi, and the fact that the northern part of the margin is experiencing subduction erosion rather than accretionary erosion as in the southern margin (Barker et al., 2009; Barnes et al., 2010; Fagereng, 2011) may be why proto-thrusts are not prominent on seismic images as seen in the south by Barnes et al. (2018). The velocity difference models presented here may indicate that sub-seismic scale deformation related to lateral compaction will also not extend more than 8km from the deformation front in the north.

Comparably, at Cascadia the PTZ has been estimated at 5-10 km using similar velocity estimates from multi-channel seismic data as well as kinematic modelling of strain based on stratal thicknesses and porosity (Morgan and Karig, 1995; Wang et al., 1994), and at Nankai the PTZ ranges 2.5-4.5km characterized by thickening and seaward tilting of the trench wedge sediments within multichannel seismic data (Moore et al., 1990). A proto-thrust is also imaged at the Makran subduction zone ∼10km from the trench (Minshull and White, 1989), which has an extremely high sediment input of ∼7km (Kopp et al., 2000), however there is little evidence of a wide proto-thrust zone at Makran as is found at southern Hikurangi and Nankai (Minshull and White, 1989).

The pelagic layer, at depths of ∼1000mbsf also shows an increase in velocity difference trenchward of the volcanic cones, ∼5km from the deformation front. Below faults 5 and the Pāpaku fault (fault 6), however, at similar depths of ∼1000mbsf, large negative velocity differences of ∼-500m/s

are present in the pelagic layer (Fig 6.12(c)). This could indicate that pelagics, are maintaining higher porosities as they subduct and are therefore under-compacted. As pelagics generally have lower permeabilities than hemipelagic and clastic sediments (Spinelli et al., 2004), it is possible that they are more liable to experience higher fluid pressure due to a high rate of increase in overburden pressure during subduction on relatively undeformed rock containing limited permeability pathways to expel fluid (Bangs et al., 1990).

Han et al. (2017) suggests that the consolidation state of the sediments near the deformation front is a key factor contributing to megathrust slip behaviour and may influence the deformation style of the wedge. The study found that offshore Washington, the Cascadia margin starts to experience over-consolidation based on a positive Vp difference from undeformed sediment at ∼20km seaward of the wedge. The decollement here is deep, near the basement, and the entire sedimentary section is subject to horizontal compression from the accretionary wedge 10-15km seaward from the trench. This suggests over-consolidated sediments are incorporated into a strong wedge, little fluid-rich sediment is subducted and the Washington megathrust is likely to be mechanically strong (Han et al., 2017). On the other hand offshore central Oregon, sediments are over-compacted in the upper 1.5-1.7kmbsf of the incoming sediment, with lower sediments showing evidence of under-compaction (negative velocity differences compared to undeformed sediment) indicating higher porosity and lower effective stress. The decollement at Central Oregon is shallower , incoming sediment below ∼1.7mbsf maintains high porosity, likely due to trapped fluid from rapid burial and low permeability, and this likely facilitates elevated pore pressure on the plate interface potentially weakening the megathrust (Han et al., 2017). This is similar to the results at Hikurangi which show the under-consolidated pelagic sediment at the trench lying below the over-consolidated clastic sediment. Hikurangi too could therefore be subject to elevated pore pressure on the plate interface, however deeper imaging is necessary to determine whether the pelagic sediment is subducted or accreted.

Analysis at Nankai based on porosity measurements at three wells, one within the undeformed trench and two near the frontal thrusts also indicated under-consolidation of pelagic sediment beneath the frontal thrusts (Screaton et al., 2002). This lead to estimates of overpressure based on pore pressure calculations within hemipelagic sediments, and an interpretation of lateral stress within the accretionary prism, leading to greater stress above the décollement than below (Morgan and Karig, 1995; Screaton et al., 2002). Fluids trapped in these underthrust sediments will escape primarily through fractures and/or other conduits (Screaton et al., 2002). Saffer and McKiernan (2005) also attribute higher porosities at Costa Rica to higher permeability based on flow through testing of hemipelagic ODP samples, with the key implication of this high porosity and therefore high permeability contributing to rapid compaction, high fluid volume expulsion, improved drainage and higher strength at the wedge base for thin incoming sections compared to thicker incoming sediments. Although possible fluid conduits along faults have been identified at Hikurangi based on FWI modelling (chapter 4), and there is some evidence presented here for over-pressured pelagic

sediment, neither the drilling data nor the FWI model constrain the physical properties of the décollement or underthrust section. Currently it is uncertain whether the pelagic sediment at Hikurangi is being subducted, and if so whether the margin is behaving similarly to Nankai or Costa Rica, however the deeper penetrating 3D seismic data and further laboratory measurements of permeability and pore pressure may be able to provide more detail in the future.

6.6.2 How much fluid is expelled across the margin?

The calculation of porosities (Fig 6.10(b)) can allow an estimation of fluid expelled in the wedge, using the same method presented by Bangs et al. (1990). The improved resolution of the Vp model produced using FWI has also enabled this analysis to be conducted for the first time at the scale of individual fault blocks. In order to calculate fluid expulsion I assume that the lithology at a particular depth in the wedge is the same lithology as at the equivalent depth in the undeformed section. At the present time a direct correlation between individual seismic units mapped at U1520 and U1518 has not been published to do a more detailed analysis, however both cores recover clastic lithologies at the depths I am considering (U1520 recovers clastics to 509.82mbsf-Figs 6.2, 6.3, 6.4), and the velocity difference model (Fig 6.10(c)) shows a velocity difference of ∼0m/s around well U1519.

6.6.2.1 Dewatering estimates within the wedge

At 8km seaward of the trench within the Hikurangi Trough, unconsolidated porosities are 58.7% at 250mbsf, while at 5km into the wedge, porosities at 250mbsf drop to 44.1%. If $\phi_{58.7}$ is the fluid volume at 58.7% porosity and s is the rock volume, then:

$$\frac{\phi_{58.7}}{(s+\phi_{58.7})} = 0.587. \tag{6.9}$$

The solid volume of rock is conserved after porosity reduction due to fluid expulsion, so a decrease in porosity to 44.1% will give:

$$\phi_{44.1} = 0.55\phi_{58.7}, \tag{6.10}$$

meaning that the remaining pore fluid at 5km landward of the trench is 55% of the pore fluid within the undeformed sediment 8km seaward of the trench. This implies that 45% of pore fluid is removed by 5km landward the trench within the accretionary wedge at depths of ∼250mbsf.

In the more landward part of the wedge, 25km landward from the trench, where over-compacted sediments are overthrust around faults 1 and 2, hanging wall porosities decrease to an average of 35% at depths of 250mbsf. Following the same calculation, this gives:

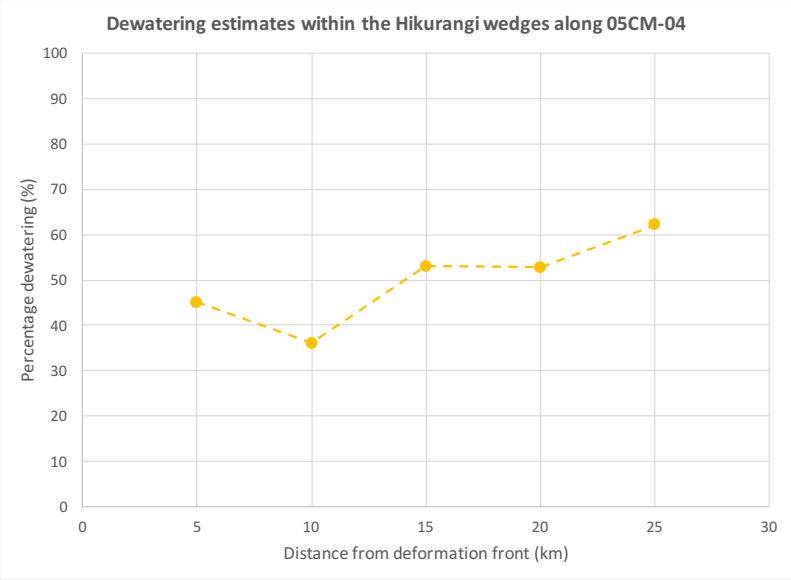


Figure 6.18: Estimates of fluid released at 5km intervals landward of the trench at a depth of 250mbsf using porosity taken form the transformed model.

$$\phi_{35} = 0.36\phi_{58.7}, \tag{6.11}$$

indicating that 64% of the initial pore fluids in the unconsolidated region of the Hikurangi Trough have now been expelled.

By calculating estimates of fluid expulsion in this way, I was able to create a profile of percentages of fluid expelled at 5km intervals landward of the wedge at 250mbsf (Fig 6.18). The data I have used comes from porosity measurements over ∼100m at 250mbsf at 5km intervals from the trench until 25km from the trench. Beyond 25km from the trench the FWI model images perched basins rather than buried and exhumed sediments at these depths and so will not give an accurate estimate of expelled fluid.

Results show that initially ∼55% of fluid is released in the leading 5km from the trench, where three frontal thrust faults exist (Pāpaku fault 6 and faults 4 and 5). Fluid expulsion estimates then decrease at 10km landward from the trench. This measurement lies in the low porosity anomaly identified to the most eastern part of Fig 6.11(b). Fluid expelled estimates then steadily increase to ∼62% of initial fluid expelled at ∼25km landward from the trench in the vicinity of faults 1,2 and 3.

6.6.2.2 Dewatering estimates across individual faults

Figs 6.10(c), 6.11(c) and 6.12(c) show that shallow sediments in the hanging walls of faults have higher velocities than the equivalent stratigraphic intervals in the undeformed Hikurangi Trough, which indicates that they are likely over-compacted for their present depth. In general, deeper

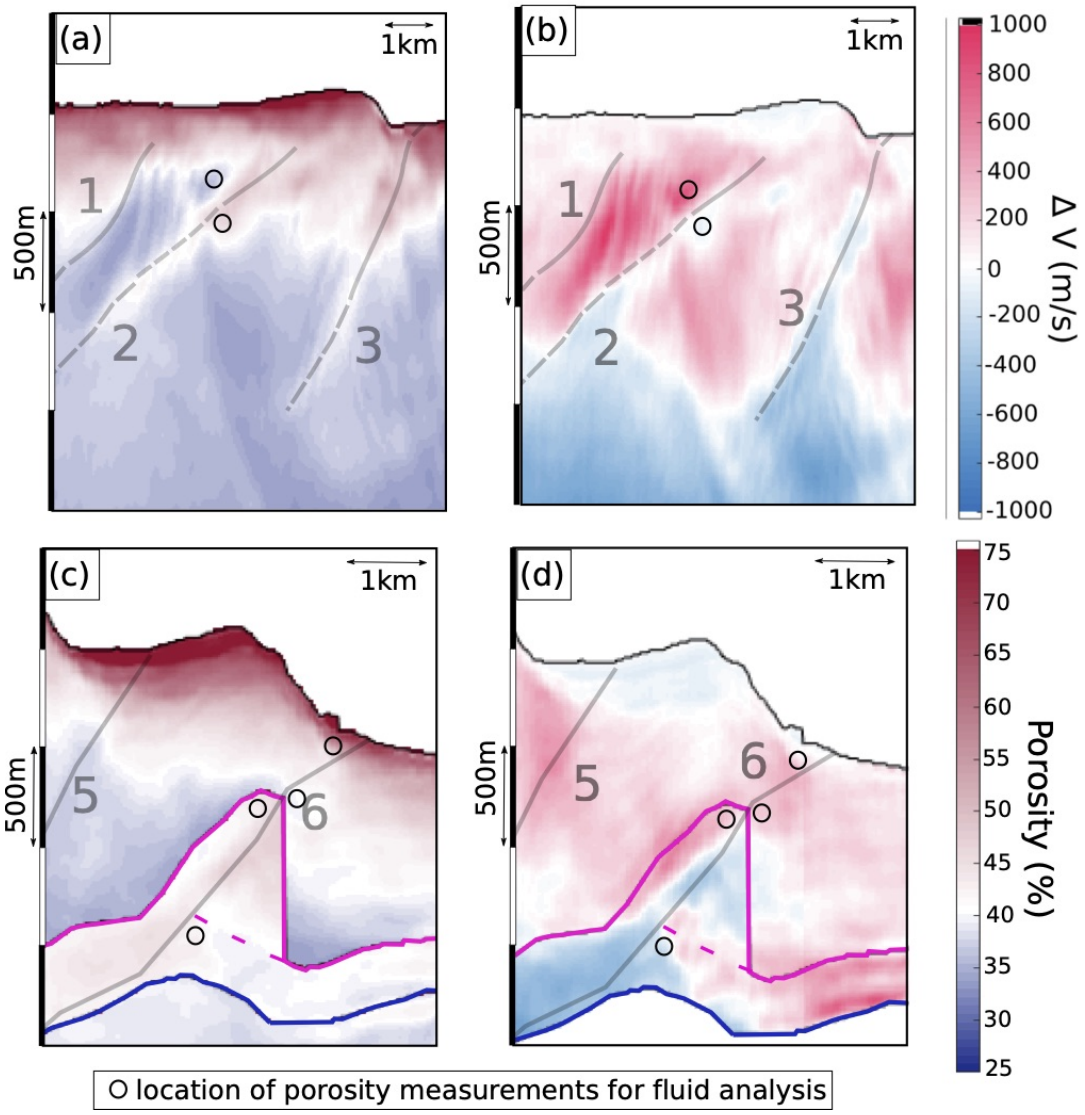


Figure 6.19: Zoom in of faults 1, 2, 3,5 and 6 in porosity model (a), (c) and velocity difference model (b), (d), highlighting where porosity measurements were taken for use in calculation of expelled fluid.

sediments, particularly in the footwalls of faults, notably the footwalls of faults 1,2,3 and 6 are potentially under-compacted due to negative velocity differences and higher porosities, and lower shear modulii (Fig 6.10, 6.13). As hanging wall sediments are likely to have been buried and then exhumed, it makes sense that they will appear over-compacted for their current depth in the velocity difference model.

In order to calculate fluid expulsion across faults I compare the porosity of the same approximate stratigraphic interval in the hanging wall and footwall. At the Pāpaku faults, I have chosen to make measurements just below the mapped Top pelagic horizon for pelagic measurements, and just above the mapped Top pelagic horizon for clastic measurements in order to calculate estimates for the individual lithologies (Fig 6.19).

The fault showing the largest porosity difference between footwall and hanging wall is fault 2 (Fig. 6.11(b), 6.19(b)). At ∼650mbsf the footwall of fault 2 has modelled porosities of ∼47.5% while

the hanging wall has modelled porosities of ∼35.3% at ∼350mbsf, the assumed same stratigraphic unit (Fig 6.19). This would indicate a fluid loss of 40% for a horizon which exists at a depth of ∼650mbsf in the footwall of fault 2. Locations where these porosity measurements were taken are shown in Fig 6.19(a).

The porosity contrast across the Pāpaku fault (fault 6) within the clastic layer shows the footwall modelled as having porosity of ∼39% at ∼500mbsf, which has a ∼10% lower porosity than in the corresponding location in the hanging wall before faulting (∼49%) (Fig 6.19(c)), resulting in ∼33% of fluids being lost across the fault. Within the pelagic unit, porosities across fault 6 decrease from ∼44% to ∼39% at locations estimated to be part of the same stratigraphic interval before faulting (Fig 6.19(c)). This suggests ∼20% of initial fluid is lost across the Pāpaku fault in the pelagic layer. This indicates more fluid is expelled from the clastic lithology than from the pelagic.

6.6.2.3 Comparison of fluid expelled at other subduction zones

At the Barbados accretionary complex, Bangs et al. (1990) found that 33% of the initial fluid within undeformed sediment was expelled within the leading 25km of the wedge, and 71% is expelled within the midportion of the wedge (∼40km from the trench), calculated using a porosity model derived from seismic velocity and the equations presented in section 6.6.2.1. At Nankai, 70.66% of initial fluid is estimated to escape out of the top of the accretionary wedge via diffuse flow within 30km of the trench, and 0-5% of fluid escapes along the décollement, with ∼1.33% being subducted based on compaction and flow transport modelling (Saffer and Bekins, 1998). At the Alaskan margin it is estimated that most rapid dewatering (∼65%) occurs in the leading 10km of the wedge and a total of ∼85% of fluid is lost by ∼20km into the wedge based on a residual porosity model produced using interval velocities from a PSDM seismic section and velocity-porosity relations derived from drill holes in both the trench and the wedge. Signs of vigorous fluid venting near the deformation front also indicate potentially high pore-fluid pressures at the Alaskan margin(Suess et al., 1998; Von Huene et al., 1998).

Comparing these dewatering measurements to those calculated at the Hikurangi margin in section 6.6.2.1 indicates that Hikurangi lies within the general dewatering trend of other subduction zones, dewatering at a slightly lower rate than Alaska, and higher rate than Barbados (Fig 6.20). Many published studies that present dewatering estimates do not explain the depths at which the measurements were made, therefore, it is difficult to compare them with our results directly.

One key influencing factor on release of fluids at subduction zones may be incoming sediment composition. Pelagic incoming sediment will likely not undergo a reduction in porosity consistent with depth due to low permeability inhibiting the release of porewater (Spinelli et al., 2004; Westbrook, 1991), as at the Barbados ridge complex, which is also mostly pelagic (Bangs et al., 1990). At the Nankai complex, where incoming sediments are also mostly homogeneous hemipelagic mudstones and claystones (Moore et al., 2001), underthrust sediment also remain undrained with high pore

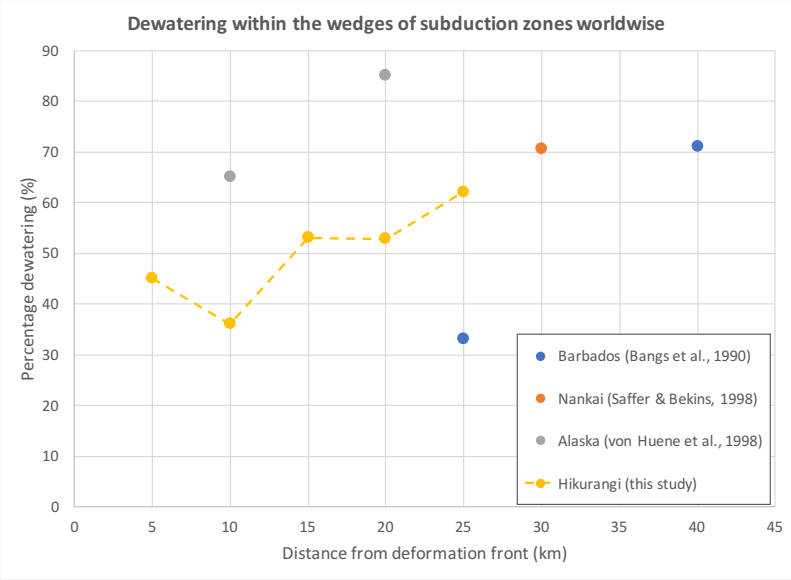


Figure 6.20: Comparison of fluid release at various subduction zones.

fluid pressures (Saffer et al., 2000; Screaton et al., 2002). This process is also observed at the Costa Rican subduction margin where low permeability in the pelagic incoming section inhibits pore-water drainage, and the result is under-consolidated underthrust sediment due to sustained pore-fluid pressures above hydrostatic (Saffer et al., 2000; Spinelli et al., 2004). Inferred pore fluid pressures in the underthrust hemipelagic layers at Costa Rica indicate better drainage than underthrust pelagic sediments at Barbados and Nankai (Saffer, 2002), likely due to slightly higher permeabilities in hemipelagic sediment compared to pelagic (Spinelli et al., 2004), allowing upper hemipelagic sediments at Costa Rica to be partially drained while pelagic carbonates remain largely undrained (Saffer, 2003).

While at Hikurangi, we unfortunately do not penetrate the underthrust sediment with drilling data, pelagic sediment is found in the Hikurangi Trough, and pelagic sediments are thought to be incorporated within the wedge based on interpretation of seismic reflection data (Barnes et al., (in review)). The models presented here indicate that the pelagic sediment may, in the same way as at Costa Rica, Nankai and Barbados, remain undrained, and may therefore also experience an increase in pore pressure with increased overburden. This is also plausible in relation to the under-compaction of the pelagics inferred from the velocity difference model in the shallow part of the wedge, as described in section 6.6.1.

At the Makran, Alaskan, and Vancouver wedges, where the incoming section consists of clastic sediment, data indicates an over-compacted sedimentary section relative to undeformed sediments in the trough, which implies rapid fluid loss from the accreted section (Davis et al., 1990; Fowler et al., 1985; Minshull and White, 1989). As the input sequence of the Alaskan margin is primarily clastic sediment from the glacial erosion of Alaska (Dobson and O'Leary, 2019; Scholl, 1974), this may explain the much higher rate of dewatering compared to other margins in Fig 6.20. Similarly

at the Makran margin, high amounts of dewatering are experienced across the frontal fold, with very little change in porosity-depth gradients across the next 50km of the prism. The incoming clastic sands at the Makran margin leads to assumptions that the highly permeable nature of sand causes most fluid loss to occur during preaccretionary normal compaction, allowing the Makran margin to remain at hydrostatic pressure throughout (Fowler et al., 1985; Fruehn et al., 1997).

At Hikurangi, calculations across the Pāpaku fault (section 6.6.2.2) suggest more fluid is expelled from the clastic layer compared to the pelagic layer. This could indicate that similar to Alaska and Makran, the clastic sediment undergoes more fluid expulsion across the initial thrust faults, while the pelagic sediment may be retaining more fluids during accretion as at Nankai, Barbados and Costa Rica (Saffer, 2003; Saito and Goldberg, 2001; Screaton et al., 2002; Zhao et al., 1998). Unfortunately the IODP expeditions did not drill through the décollement to compare sediment properties above and below the plate interface to investigate which lithologies are subducted and if any subducting pelagics are under-compacted. Planned laboratory experiments will provide evidence on the potential differences in the compaction behaviour of pelagics and volcaniclastic during subduction.

The volcaniclastic section and volcaniclastic domes, which may be subducted at Hikurangi, could also be playing a role in fluid behaviour, similar to the Barbados accretionary complex, where there is a volcaniclastic dome present seaward of the trench which has been interpreted at Barbados to cause pore fluid to diffuse towards the east-seaward from the trench-along stratigraphic horizons rather than being released directly to the surface (Westbrook and Smith, 1983). Overall, it is apparent that the incoming lithology plays an important role in fluid inputs into the subduction zone.

6.6.3 Can models of estimated elastic moduli improve modelling of tsunami generation?

While the models of elastic properties produced in this chapter do not provide independent constraints on Vs, Vp/Vs and bulk and shear moduli, they do produce plausble estimates of these parameters. So discussion of elastic properties in this section are based on these plausible estimates rather than fully constrained models.

Hamilton (1979) did a study on Vp/Vs ratios in the upper 1kmbsf of in-situ water-saturated silt clays, turbidites and mudstones based on drilling data from the Indian Ocean, the Japan and Bering Seas, the Atlantic Ocean, Caribbean Sea, and Gulf of Mexico. The study found values between 7 and 13 in the upper 20mbsf, which are lower than values in the upper 20mbsf at Hikurangi, modelled at 15-25. Modelled Vp/Vs values in the pelagics of the Hikurangi Trough of 2.3-2.4 between 700-1000mbsf are slightly lower than values of 2.6-3 found by Hamilton (1979) at the same depths, and values modelled in the hanging walls of faults (∼1.8) ∼300-400mbsf and below

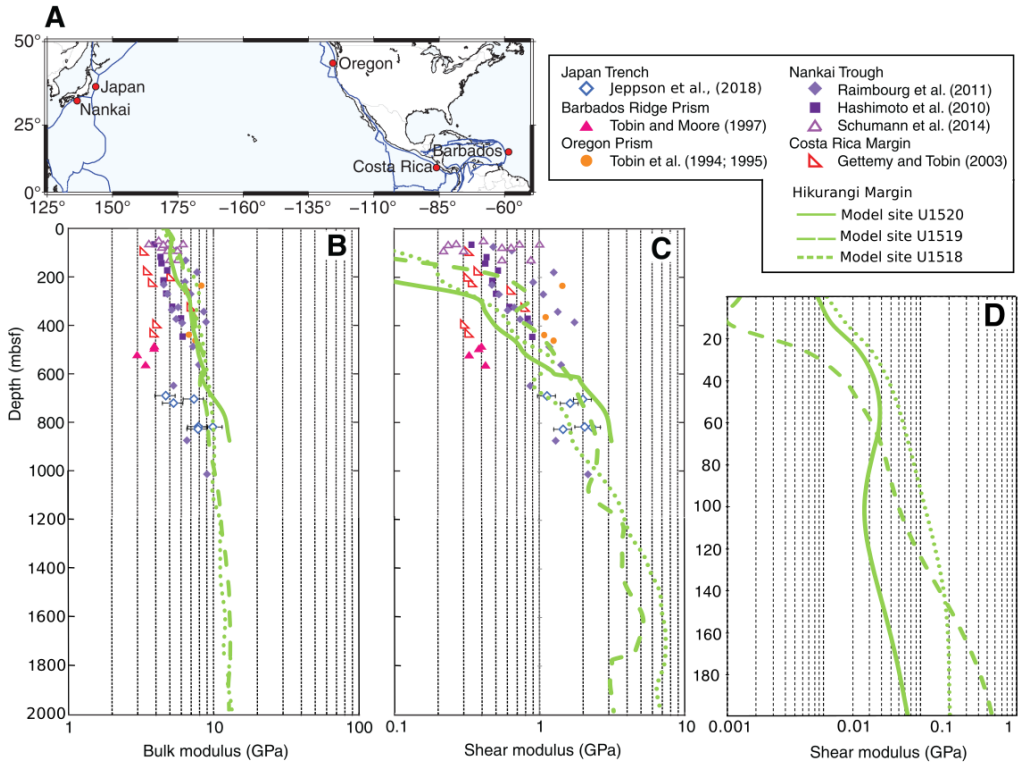


Figure 6.21: (A) Map showing where data from prism sediments are taken to compare to the Hikurangi transformed models. Blue lines show plate boundaries. Comparison between (B) bulk modulus and (C) shear modulus from margins shown in (A) calculated by Jeppson et al. (2018) using measured (open symbols) and calculated (closed symbols) S-waves, and profiles extracted from well locations from the transformed models shown in Fig 6.13(d) and (e).(D) shows bulk modulus from models above 100m which are too low for (C) (<0.1GPa)

400mbsf in the wedge (∼1.5 to 2) are lower than found by Hamilton (1979) which are lowest at 1kmbsf with a value of 2.58. Other studies in New Zealand have found similar lower values, such as Reyners et al. (2006) which found Vp/Vs ratios of 1.6-1.9 with an average value of 1.75 beneath the central North Island by inverting earthquake data from the trench to 300kmbsf. Eberhart-Phillips and Reyners (1999); Eberhart-Phillips and Chadwick (2002) also modelled Vp/Vs ratios at the Hikurangi margin using passive seismic data and found Vp/Vs values from 1.675-1.95, with values ∼1.7 at depths of 0-3km. Both these studies give results which are consistent with hanging walls and lower parts of the wedge modelled in this chapter, however the resolution of these studies are much lower (>10km grid spacing), and targets were much deeper, so small-scale variations, such as along fault zones are not determined by the passive seismic studies. Overall it appear that the Hikurangi wedge has lower Vp/Vs values than expected by Hamilton (1979).

Bulk and shear moduli at Hikurangi extracted from the models at the three well sites match well with results from drilling at accretionary wedges around the globe, fitting the general depth trends of the Japan trench (Jeppson et al., 2018), Barbados Ridge prism (Tobin and Moore, 1997), Oregon prism (Tobin et al., 1994, 1995), Nankai Trough (Hashimoto et al., 2010; Raimbourg et al., 2011; Schumann et al., 2014) and Costa Rica margin (Gettemy and Tobin, 2003) (Fig 6.21). Bulk modulus at Hikurangi is on the higher end of the sampled margins, and is most similar to the

Nankai trough and Oregon prism, while the shear modulus above 100m is extremely low (0.01-0.1GPa) (Fig 6.21D), and below 100m values are on the lower end of the sampled margins, again most closely matching samples from the Nankai trough. Jeppson et al. (2018) stipulates that differences in elastic-modulii depth trends at the various margins are controlled by differences in composition, grain size and history; for example, at the same depths, samples from the prism toe are less compliant than from the upper prism. This can be seen in the differences between the modelled values from the 3 Hikurangi drill sites taken in the trough (U1520), toe (U1518) and within the wedge (U1519) (Fig 6.21).

Geist and Bilek (2001), have shown how estimates of tsunami size generated by subduction zone earthquakes are significantly affected by the choice of shear modulus at shallow depths. As most studies which estimate shear modulus with depth use earthquake data (Bilek and Lay, 1998, 1999b,a, 2000; Dziewonski and Anderson, 1981), shear modulus estimates are distinctly lacking in the upper 5km of subduction zones. This means that shallow shear modulus variations remain poorly constrained in megathrust studies and are often ignored. Analysis of tsunami generated by tsunami earthquakes point to a reduction in shear modulus at shallow depth, with values of 10-20GPa most often used to match tsunami amplitudes (Heinrich et al., 1998; Satake and Tanioka, 1995, 1999; Tanioka and Sataka, 1996). Geist and Bilek (2001) compared tsunami tide gauge record to numerical tide gauge estimates of the 1992 Nicaragua tsunami earthquake using both a constant shear modulus of 30GPa, and a shear modulus which varied logarithmically with depth from ∼85GPa at ∼30kmbsf to ∼3.6GPa at the seafloor. Results showed that using a constant shear modulus of 30GPa under-predicted the amplitude of the tsunami, while using a depth-dependent shear-modulus caused an increase in the initial tsunami amplitude near the up-dip edge of rupture and fitted the recorded tide gauge of the tsunami much better. Direct measurements of core data by Jeppson et al. (2018) found even lower values of shear modulus (1.0-2.3GPa) within the Tohoku-Oki accretionary wedge, and found that these values correlated well with values from shallow subduction zone drill core samples from accretionary prisms at Barbados (Tobin and Moore, 1997), Oregon (Tobin et al., 1994, 1995), Nankai (Hashimoto et al., 2010; Raimbourg et al., 2011; Schumann et al., 2014) and Costa Rica (Gettemy and Tobin, 2003) (Fig 6.21). Low shear modulus values also correlate well with numerical simulations by Lotto et al. (2017) who show that local enhancement of shallow slip is amplified with shear modulus values of ∼2GPa. Comparing the core values to the values used by (Geist and Bilek, 2001) derived from earthquake data, as well as the preliminary earth reference model (PREM) (Dziewonski and Anderson, 1981) suggest that shear modulus values at the surface may be underestimated by up to 20GPa (Jeppson et al., 2018).

The shear modulus model presented here (Fig 6.13(e)) within the same depth range (<855mbsf) as in Jeppson et al. (2018), 5km landward from the trench show shear modulus values in the range 1.91-2.44GPa, and low shear modulus values are also modelled along faults 1, 2 and 3, ranging from ∼2.5GPa at 1.4kmbsf, to ∼0.4GPa at ∼100mbsf. The frontal Pāpaku fault also has low shear modulus, specifically in the pelagic layer, with values of 2-3.8GPa. This indicates that these

faults lack rigidity and may also allow rupture to propagate up-dip over large areas during seismic events. These lower shear modulus values may have been an influence on the March and May 1947 tsunami earthquakes offshore Gisborne (Fig 6.1). Tsunami height modelling for the 1947 earthquakes at Hikurangi used shear modulus values as low as 7GPa yet could not simulate the recorded tsunami wave heights of ∼6m and ∼10m (Bell et al., 2014; Bilek and Lay, 1999b; Downes, 2001; Pelayo and Wiens, 1992; Power et al., 2008). The shear modulus from the models shown in this study, however, are much lower (∼1-3GPa), which would correspond to an overall increase in the amount of average slip, generating enhanced tsunami amplitudes (Geist and Bilek, 2001). Modelling of tsunami amplitudes generated by tsunami earthquakes can vary by a factor of three or more with the same seismic moment and location due to rupture complexity Geist and Bilek (2001), and therefore accurate knowledge of varying shear modulus and heterogeneous slip distribution is extremely important. The new 3D data acquired in 2017-2018 (chapter 5) will allow elastic moduli to be constrained to depths of 10kmbsf within the tsunami earthquake rupture zone.

The shear modulus model presented in this chapter is able to resolve shear modulus values within individual fault blocks and within important fault zones, which is a great improvement in shear modulus models at subduction margins (e.g. Jeppson et al. (2018)). Models such as these may be able to help explain where and how the largest tsunami are generated, not just at margins which experience tsunami earthquakes such as Hikuranagi, but also at margins which experience shallow coseismic slip all the way to the trench during large-magnitude earthquakes such as at the Japan trench (e.g. Fujii et al. (2011); Kodaira (2012); Lay et al. (2011), Peru-Chile trench (Yue, 2014), Nankai (Sakaguchi et al., 2011) and Cascadia (Satake, 2003). It is becoming increasingly apparent that the complex nature of large subduction earthquakes and tsunami generation require heterogeneous models of elastic properties, which vary laterally and with depth for more accurate hazard modelling. The use of FWI shows great potential to advance understanding of the mechanics of tsunami and tsunamigenic earthquakes.

6.7 Conclusions

The following conclusions have been made based on the models of porosity, compaction, Vs, Vp/Vs bulk modulus and shear modulus presented in this chapter.

(a) The incoming section begins to undergo deformation due to subduction at a distance of ∼5.3-8km from the trench based on the velocity anomalies between undeformed basin sediment and sediments closer to the trench. There also appears to be an element of differential compaction between ∼6-8km from the trench related to the presence of volcaniclastic domes. If this velocity anomaly reflects the width of the proto-thrust zone, it is shorter than PTZs at southern Hikurangi which are as large as 25km. I suggest that limited incoming sediment thickness at southern Hikurnagi may discourage proto-thrust faulting on the same scale as at the southern margin, where many proto-thrusts are identified in seismic images. Instead, at the northern

part of the margin these proto-thrusts may be at sub-seismic scales.

(b) Shallow sediments that have been over-thrust in fault hanging walls are under-compacted and indicate 45% of fluid is removed by 5km from the trench. This is higher than at the Barbados accretionary complex where calculations find 33% of fluid is expelled in the leading 25km of the wedge, but lower than the Alaskan margin. The amount of expelled fluid is likely related to the lithologies of the incoming section, with the interpreted pelagic layer retaining more pore-fluid and the clastic layer expelling the majority of fluid as it subducts.

(c) Deeper sediments across the model, particularly in footwalls of faults are under-compacted and have porosities of around 40%, which is ∼10% lower than surrounding rock, which is to be expected for buried and exhumed sediments at these depths.

(d) Pelagics which have been incorporated into the wedge are under-compacted, likely due to low permeability, which may indicate they are undrained, while clastics appear over compacted which could indicate that they are drained.

(e) The improved resolution of elastic moduli along line 05CM-04 is one of the few studies which models properties within the upper 2km of a subduction zone, and the elastic properties modelled here could provide an improvement to tsunami hazard modelling in the region. We find that values of rigidity are lower (∼1-3GPa), than previously used to model tsunami in North Hikurangi (7GPa).

6.A Appendix

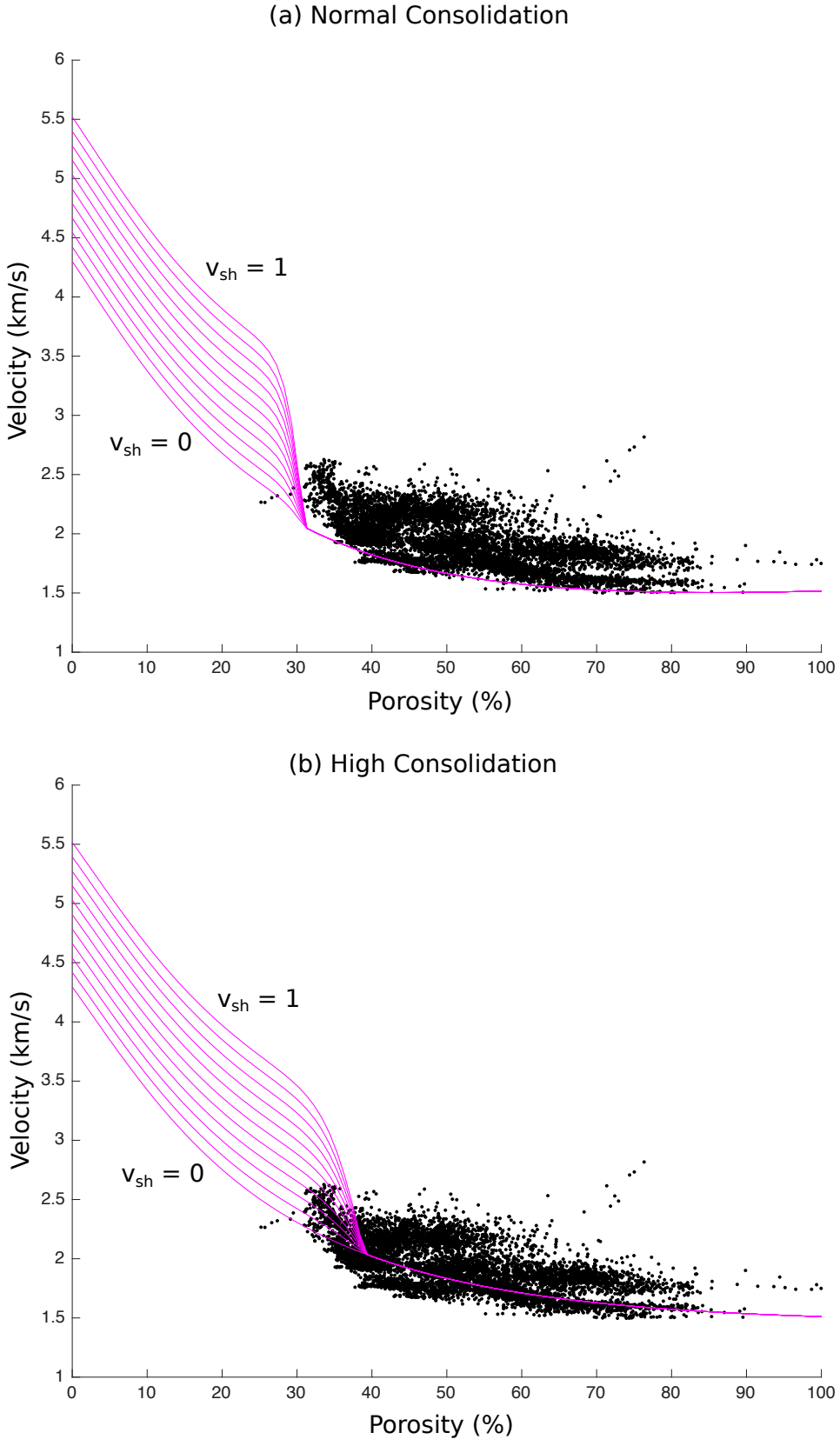


Figure 6.22: Comparison of the standard Erickson and Jarrard equations with data collected at Hikurangi from all three well sites.

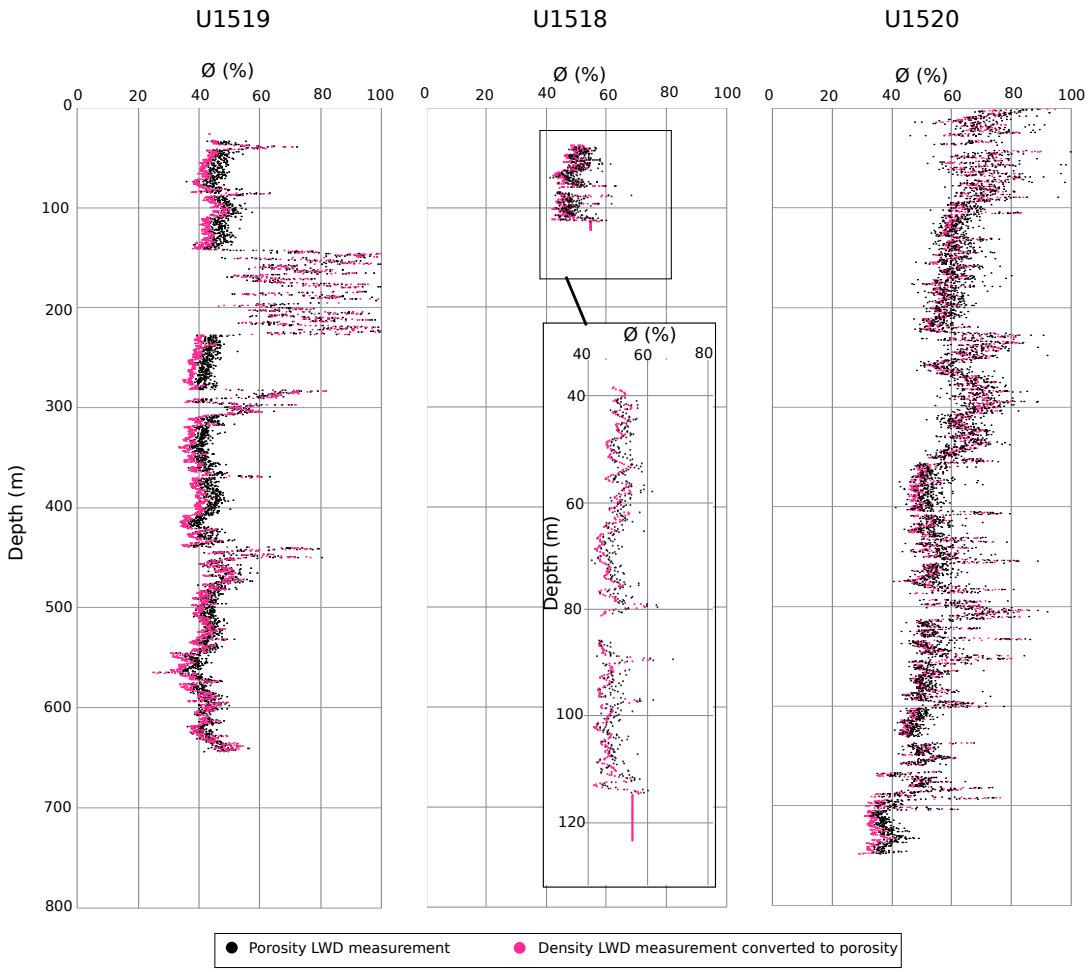


Figure 6.23: Comparison between porosity LWD measurements and porosity measurements converted from density LWD recordings. As the porosity LWD tool measures free hydrogen in the rock and assumes this is all within pores, the tool often overestimates density.

Chapter 7

Conclusions

This thesis has tested the feasibility of conducting FWI at subduction margins using streamer data. The model produced using 2D FWI on 2D streamer data along line 05CM-04 is a great improvement to previous tomographic models. The results were integrated with drilling data to transform the model into various other physical properties at the Hikurangi margin. This included models of potential compaction, porosity, Vs, Vp/Vs bulk modulus and shear modulus. Synthetic full-waveform inversion results were also used to optimally design a new 3D experiment, which was conducted in 2017-2018. This work offers new contributions to scientific knowledge in terms of the use of FWI at subduction zones, as well as the recovery of detailed models of a range of physical properties. In this final chapter the major conclusions and contributions drawn from this study are outlined. These conclusions are arranged in terms of the two main aims and associated objectives proposed in chapter 1 (section 1.6). I will then discuss future work which can possibly be undertaken to further the knowledge obtained from this study.

7.1 Aim 1: To determine whether the application of FWI is feasible at subduction zones

7.1.1 Objective 1.1: To apply 2D FWI to line 05CM-04

I have shown in chapter 4 that 2D FWI can be used with 2D streamer data across Hikurangi to produce a detailed velocity model. Despite the fact that the dataset used, line 05CM-04 collected in May 2005, was not obtained with optimal acquisition parameters for FWI, and raytracing showed that depth was constrained to ∼2kmbsf, the data were able to be used to produce a reliable and detailed Vp model of the shallow structure of the margin.

While adjusting the velocity of the water column, depth to the seabed and smoothness of the initial PSTM starting model was challenging (chapter 3), the technique worked well in recovering plau-

sible velocity features to a resolution of ∼140m in material with P-wave velocities of ∼2200m/s at frequencies up to 8Hz (chapter 4). Extensive quality assurance methods were carried out to determine the reliability of the model (chapter 4). The features recovered in the model match well with features recovered using PSDM migration, synthetic waveforms computed through the model match well with real data, and velocity-depth profiles at well locations match with sonic data recovered from LWD and wireline tools. Compared to tomographic modelling, the features recovered are less blocky and more geologically realistic, and individual faults can be easily discerned. Overall the technique works well.

7.1.2 Objective 1.2: To use synthetic 3D FWI to optimise the 3D survey

A new 3D experiment was designed in chapter 5 optimally to image a slow slip zone using 3D FWI. The acquisition geometry contained land geophones and OBS receivers with long offsets and wide azimuths over an area of ∼60 x 15km surface area. Ray-tracing in chapter 5 along a 2D slice of a larger 3D synthetic model using the NZ3D-FWI acquisition geometry suggested the data would allow imaging down to ∼19km, which is a great improvement on the ∼2kmbsf I was able to image using the streamer dataset. Incorporating land receivers allows for imaging beyond the source region, as shown in checkerboard testing in chapter 5. These checkerboard tests also indicated that imaging will be possible along the decollement, across the proposed subducting seamount, at the downdip location of changing plate coupling behaviour, and in the origination zone of SSEs.

Using the optimal geometry described in chapter 5, the experiment was carried out successfully in January and February 2018. The data acquisition went smoothly and preliminary processing of land receiver data shows coherent arrivals across the experimental geometry. The marine data is now being conventionally processed to produce long-wavelength P-wave velocity models, and future research projects have been funded to apply 3D FWI to the dataset.

7.2 Aim 2: To investigate the physical properties of the incoming section and overriding plate and interpret them in terms of the seismic behaviour of the north Hikurangi margin

7.2.1 Objective 2.1: To assess the geological significance of high-resolution P-wave velocity anomalies.

Low velocity features recovered along faults at the toe of the decollement and within the accretionary wedge could be an indicator of fluid. Velocities recovered along some faults are ∼500m/s lower than the surrounding rock and may indicate that these are zones of high porosity, which

may be maintained by fluid throughput from depth. The interpretation of fluid flow at Hikurangi, potentially along faults, is supported by elevated heatflow (Antriasian et al., 2018) and the observation of a number of fluid flow features in the vicinity of seismic line 05CM04 near the frontal thrust, including pockmarks, flares, and mounds. These features are similar to low velocity anomalies of ∼500-1000m/s along faults identified using waveform tomography at Nankai, identified by Kamei et al. (2012) as potential fluid conduits. The potential for these faults for conduits of fluid flow are also emphasised by higher porosity and Vp/Vs rations along these faults in transformed models in chapter 6. Velocities recovered within the Hikurangi Trough near IODP site U1520 display distinct velocity changes with depth. These depths are consistent with results from cores recovered at the site which find turbidites, mass transport deposits, and hemipelagic muds down to 509.82mbsf, pelagic carbonate facies from 509.82 to 848.45mbsf, volcaniclastics from 848.45 to 1,016.24mbsf and a blend of volcaniclastics, mudstone, limestone, and siltstone down to 1,045.75mbsf (Wallace et al., 2019). Using the FWI model it is possible to track these lithological boundaries away from the drill site towards the trench, indicating that both clastic and pelagic sediment are accreted at Hikurangi. Aside from the low velocities along faults in the wedge potentially indicating conduits for fluid, there are other notable interpretations that can be made from the P-wave FWI model. Velocity contrasts between the footwall and hanging wall of some faults in the wedge (e.g., Faults 3 and the upper part of Fault 7 between 900 and 1,200mbsf, chapter 4) likely indicate under-consolidated, lower velocity sediments in the footwall compared to the hanging wall, which is now over-consolidated at its current depth, causing velocities to be higher. This is in agreement with velocity differences within the footwalls and hanging walls of faults compared to undeformed sediment in the Hikurangi Trough (chapter 6). In addition, some isolated low velocity features appear to correlate with shallow gas anomalies associated with the bottom simulating reflection as interpreted by Navalpakam et al. (2012).

7.2.2 Objective 2.2: To use IODP drilling measurements be used to transform the model into other physical properties

I was able to apply different relationships between Vp and various physical properties for pelagic and clastic packages, allowing a detailed model of these physical properties to be produced (chapter 6). Deriving relationships of undeformed sediment compaction rates with depth and Vp vs porosity relationships from data obtained on IODP expeditions 372 and 375 have also provided estimates on sediment compaction rates as material in the Hikurangi Trough approaches the trench. Lateral compaction due to subduction begins between ∼5.3 - 8km from the trench. This is similar to the lower end of the proto-thrust zone width measured by Barnes et al. (2018) who found proto-thrusts between 5-25km from the trench at southern Hikurnagi. The lack of proto-thrusts at northern Hikurangi suggests the lateral deformation here is occurring at sub-seismic scale.

The model of difference between the velocities of sediment with depth in the wedge compared to

the Hikurangi Trough emphasised that the hanging-walls are indeed over-compacted and footwalls under-compacted, assuming the same lithologies. These results are emphasised by lower modelled porosities in hanging walls and higher porosities in footwalls.

The porosity model also allowed for fluid expulsion estimation across faults within the wedge and estimated indicate ∼40% of fluid is lost between the footwall and hanging wall of fault 2 in the first ∼400mbsf (chapter 6). Porosities suggest that the clastic sediment dewaters quickly, with ∼30% of initial fluid lost across the Pāpaku fault and ∼45% within the first 8km landward of the trench. The pelagic layer, on the other hand, appears to retain more fluid, only releasing ∼20% of initial fluid in comparison. Moving further landward I estimate ∼62% of initial fluid is lost by 25km landward of the wedge.

Shear and bulk modulii are also lower along the faults in the wedge indicating they are compressible and lack rigidity. Tsunami earthquakes recorded in 1947 were modelled with rigidities of ∼7GPa, but this was unable to match recorded run-up heights, which were modelled lower than observed (Bell et al., 2014). IODP measurements from LWD and core have allowed me to create a model of shear modulus, which shows much lower values of 1-4GPa in the upper 2km. Lower shear modulus will likely result in a higher tsunami run-up height model, as in Geist and Bilek (2001). These models may allow for more accurate tsunami modelling, especially due to limited studies of shear modulus at subduction zones at <5km. The model shows just how variable shear modulus can be laterally and with depth at these complex subduction zones, and by using more detailed, heterogeneous rigidity models it may be possible to more accurately estimate tsunami hazards at the margin. The new 3D data from the NZ3D-FWI experiment which I helped to design and carry out (chapter 5) will also be critical for recovering this important parameter at depth in the future.

The input sequence at Hikurangi may play an important role in subduction zone behaviour. Unlike the Nankai, Barbados, Costa Rica and Cascadia margins, the input sequence at Hikurangi does not contain purely pelagic and hemipelagic sediments. Neither are the inputs purely clastic such as at Alaska, Vancouver and the Makran margins. At Hikurangi, the input sequence is a clastic layer overlying a pelagic layer, and so the combination of these two lithologies on the input to the subduction zone may have an effect. For example, subduction zones with clastic input sequences tend to dewater at a high rate during subduction, while pelagics tend to retain water due to limited permeability. Therefore at Hikurangi a combination of these behaviours may be taking place, with rapid dewatering from the clastic layer, and high fluid input from the pelagic layer.

Several indications of fluid presence manifest themselves as low Vp, Vs and shear modulus features, as well as higher porosity at depth. The models presented in this thesis indicate that fluid is present in the wedge at Hikurangi, and fluid conduits presence is possible along faults. Fault frictional properties and fluid presence are believed to influence seismic behaviour at subduction zones, so evidence of fluid is promising in furthering these theories.

7.3 Future Work

In chapter 5 I have demonstrated how the new NZ3D-FWI data has the potential to image deeper, including the key slow slip zone target at a depth of 2-10km below sea surface. Recovery of physical properties to these depths at Hikurangi would provide important new insights into slip processes and seismicity. As outlined in chapter 4, the main obstacle in the models produced in this thesis is the fact that a 3D world is modelled in 2D. Using 3D data will hopefully allow for accurate models of the plate interface, subducting seamount, deeper fault network and SSE source origination zones to be recovered.

While this future work is very promising, I do not expect it to be straightforward. As shown in the methods chapter (chapter 3), having an accurate seafloor bathymetry and water column velocity to produce an appropriate starting model is extremely challenging for the 2D streamer dataset, which will only be more challenging to produce in 3D. Fortunately the 2D model produced in chapter 4 in this work not only shows the feasibility of FWI at Hikurangi, but also provides an excellent starting point for creating a 3D starting model and highlighting some of the features we may expect to resolve in 3D.

Chapter 6 shows how the 2D model was used in conjunction with in-situ measurements from two IODP expeditions. The models of Vs, porosity, velocity difference form undeformed basin sediments, Vp/Vs, bulk modulus and shear modulus are extremely promising for future work. Similar methods could be applied to a 3D model at Hikurangi to extend conclusions made in this thesis to greater depths and lateral variations. Aside from offshore measurements, the onshore data collected from geophones, examples of which are shown in chapter 5, show that we can extend imaging beyond source regions and perhaps learn more about the mud volcano system, which is also directly related to the subduction zone.

IODP drilling across fault 4 allows for future analysis of key differences in the footwall and hanging wall of one frontal thrust faults, however, the physical properties produced by FWI models presented in this thesis are very different across fault 4 compared to the Pāpaku fault (the true frontal thrust). The low velocity fault zone is much more prominent across the Pāpaku fault as well has displaying higher porosities and lowered elastic properties, which may indicate the fault is acting as a conduit for fluid flow. It would therefore be useful to drill into this fault to investigate these properties with in situ measurements, and compare results to the drilling across fault 4 at site U1518. IODP pre-proposal 959 (Fagereng et al., 2019a) has been submitted to IODP to propose this drilling, using the results of my work to justify site selection. IODP has recommended that this pre-proposal be developed into a full proposal.

Finally, FWI modelling at other locations at subduction margins would be an interesting advancement to this work. On a regional scale, using FWI modelling at the southern Hikurangi margin, which does not experience slow-slip events would be useful. This would allow comparisons between

velocity structure and physical property modelling in regions with and without SSE occurrence. This could help to pin-point key properties within the wedge, incoming section and at frontal thrusts which may be encouraging slow slip at Hikurangi. Globally, Carrying out FWI at a range of subduction zones which do and do not experience SSEs could help create a large database of the different physical properties, which in the long term may help categorize the slip mechanisms at subduction zones worldwide.

Bibliography

Abercrombie, R. E., Antolik, M., Felzer, K., and Ekström, G. (2001). The 1994 java tsunami earthquake: Slip over a subducting seamount. *Journal of Geophysical Research: Solid Earth*, 106(B4):6595–6607.

Agudo, Ò. C., da Silva, N. V., Warner, M., and Morgan, J. (2018). Acoustic full-waveform inversion in an elastic world. *Geophysics*, 83(3):R257–R271.

Ammon, C. J., Kanamori, H., Lay, T., and Velasco, A. A. (2006). The 17 july 2006 java tsunami earthquake. *Geophysical Research Letters*, 33(24).

Anderson, R. N. (1989). Methods for monitoring temperature-vs-depth characteristics in a borehole during and after hydraulic fracture treatments. US Patent 4,832,121.

Ando, R., Takeda, N., and Yamashita, T. (2012). Propagation dynamics of seismic and aseismic slip governed by fault heterogeneity and newtonian rheology. *Journal of Geophysical Research: Solid Earth*, 117(B11).

Antriasian, A., Harris, R. N., Trhu, A. M., Henrys, S. A., Phrampus, B. J., Lauer, R., Gorman, A. R., Pecher, I. A., and Barker, D. (2018). Thermal regime of the northern hikurangi margin, new zealand. *Geophysical Journal International*, 216(2):1177–1190.

Asnaashari, A., Brossier, R., Garambois, S., Audebert, F., Thore, P., and Virieux, J. (2013). Regularized seismic full waveform inversion with prior model information. *Geophysics*, 78(2):R25–R36.

Audet, P., Bostock, M. G., Boyarko, D. C., Brudzinski, M. R., and Allen, R. M. (2010). Slab morphology in the cascadia fore arc and its relation to episodic tremor and slip. *Journal of Geophysical Research: Solid Earth*, 115(B4).

Audet, P., Bostock, M. G., Christensen, N. I., and Peacock, S. M. (2009). Seismic evidence for overpressured subducted oceanic crust and megathrust fault sealing. *Nature*, 457(7225):76–78.

Audet, P. and Kim, Y. (2016). Teleseismic constraints on the geological environment of deep episodic slow earthquakes in subduction zone forearcs: A review. *Tectonophysics*, 670:1–15.

Audet, P. and Schwartz, S. Y. (2013). Hydrologic control of forearc strength and seismicity in the costa rican subduction zone. *Nature Geoscience*, 6(10):852.

Baeten, G., De Maag, J. W., Plessix, R.-E., Klaassen, R., Qureshi, T., Kleemeyer, M., Ten Kroode, F., and Rujie, Z. (2013). The use of low frequencies in a full-waveform inversion and impedance inversion land seismic case study. *Geophysical Prospecting*, 61(4):701–711.

Bangs, N., Moore, G., Gulick, S., Pangborn, E., Tobin, H., Kuramoto, S., and Taira, A. (2009). Broad, weak regions of the nankai megathrust and implications for shallow coseismic slip. *Earth and Planetary Science Letters*, 284(1):44–49.

Bangs, N. L., McIntosh, K. D., Silver, E. A., Kluesner, J. W., and Ranero, C. R. (2014). Fluid accumulation along the costa rica subduction thrust and development of the seismogenic zone. *Journal of Geophysical Research: Solid Earth*, 10(1002):JB011265–JB011265.

Bangs, N. L., Shipley, T. H., Gulick, S. P. S., Moore, G. F., Kuromoto, S., and Nakamura, Y. (2004). Evolution of the nankai trough decollement from the trench into the seismogenic zone: Inferences from three-dimensional seismic reflection imaging. *Geology*, 32(4):273–276.

Bangs, N. L., Shipley, T. H., Moore, J. C., and Moore, G. F. (1999). Fluid accumulation and channeling along the northern barbados ridge decollement thrust. *Journal of Geophysical Research: Solid Earth*, 104(B9):20399–20414.

Bangs, N. L. B., Westbrook, G. K., Ladd, J. W., and Buhl, P. (1990). Seismic velocities from the barbados ridge complex: Indicators of high pore fluid pressures in an accretionary complex. *Journal of Geophysical Research: Solid Earth*, 95(B6):8767–8782.

Barker, D. H., Henrys, S., Caratori Tontini, F., Barnes, P. M., Bassett, D., Todd, E., and Wallace, L. (2018). Geophysical constraints on the relationship between seamount subduction, slow slip and tremor at the north hikurangi subduction zone, new zealand. *Geophysical Research Letters*.

Barker, D. H. N., Sutherland, R., Henrys, S., and Bannister, S. (2009). Geometry of the hikurangi subduction thrust and upper plate, north island, new zealand. *Geochemistry, Geophysics, Geosystems*, 10(2).

Barnes, P., Pecher, I., and LeVay, L. (2017). Expedition 372 scientific prospectus: Creeping gas hydrate slides and lwd for hikurangi subduction margin. *Int. Ocean Discov. Program*.

Barnes, P. M. and de Lpinay, B. M. (1997). Rates and mechanics of rapid frontal accretion along the very obliquely convergent southern hikurangi margin, new zealand. *Journal of Geophysical Research: Solid Earth*, 102(B11):24931–24952.

Barnes, P. M., Ghisetti, F. C., Ellis, S., and Morgan, J. K. (2018). The role of protothrusts in frontal accretion and accommodation of plate convergence, hikurangi subduction margin, new zealand. *Geosphere*, 14(2):440–468.

Barnes, P. M., Lamarche, G., Bialas, J., Henrys, S., Pecher, I., Netzeband, G. L., Greinert, J., Mountjoy, J. J., Pedley, K., and Crutchley, G. (2010). Tectonic and geological framework for

gas hydrates and cold seeps on the hikurangi subduction margin, new zealand. *Marine Geology*, 272(1-4):26–48.

Bartlow, N. M., Wallace, L. M., Beavan, R. J., Bannister, S., and Segall, P. (2014). Timedependent modeling of slow slip events and associated seismicity and tremor at the hikurangi subduction zone, new zealand. *Journal of Geophysical Research: Solid Earth*, 119(1):734–753.

Bell, R., Holden, C., Power, W., Wang, X., and Downes, G. (2014). Hikurangi margin tsunami earthquake generated by slow seismic rupture over a subducted seamount. *Earth and Planetary Science Letters*, 397:1–9.

Bell, R., Sutherland, R., Barker, D. H. N., Henrys, S., Bannister, S., Wallace, L., and Beavan, J. (2010). Seismic reflection character of the hikurangi subduction interface, new zealand, in the region of repeated gisborne slow slip events. *Geophysical Journal International*, 180(1):34–48.

Ben-Hadj-Ali, H., Operto, S., and Virieux, J. (2008). Velocity model building by 3d frequency-domain, full-waveform inversion of wide-aperture seismic data3d full-waveform tomography. *Geophysics*, 73(5):VE101–VE117.

Bentham, H., Morgan, J., and Angus, D. (2018). Investigating the use of 3-d full-waveform inversion to characterize the host rock at a geological disposal site. *Geophysical Journal International*, 215(3):2035–2046.

Berryman, K., Wallace, L., Hayes, G., Bird, P., Wang, K., Basili, R., Lay, T., Pagani, M., Stein, R. S., Sagiya, T., et al. (2015). *The GEM faulted earth subduction interface characterisation project*. GNS Science.

Beydoun, W. B. and Tarantola, A. (1988). First born and rytov approximations: Modeling and inversion conditions in a canonical example. *The Journal of the Acoustical Society of America*, 83(3):1045–1055.

Bijwaard, H., Spakman, W., and Engdahl, E. R. (1998). Closing the gap between regional and global travel time tomography. *Journal of Geophysical Research: Solid Earth*, 103(B12):30055–30078.

Bilek, S., Phillips, W., Walter, J., Schwartz, S., Peng, Z., and Rotman, H. (2014). Temporal and spatial variations of earthquake source parameters within the 2012 nicoya, costa rica mw= 7.6 earthquake rupture zone. In *AGU Fall Meeting Abstracts*.

Bilek, S. L. and Lay, T. (1998). Variation of interplate fault zone properties with depth in the japan subduction zone. *Science*, 281(5380):1175–1178.

Bilek, S. L. and Lay, T. (1999a). Comparison of depth dependent fault zone properties in. In *the Japan Trench and Middle America Trench, Pure Appl. Geophys.* Citeseer.

Bilek, S. L. and Lay, T. (1999b). Rigidity variations with depth along interplate megathrust faults in subduction zones. *Nature*, 400(6743):443.

Bilek, S. L. and Lay, T. (2000). Depth dependent rupture properties. *GeoComplexity and the Physics of Earthquakes*, (120):165.

Bilek, S. L. and Lay, T. (2002). Tsunami earthquakes possibly widespread manifestations of frictional conditional stability. *Geophysical Research Letters*, 29(14).

Bilek, S. L., Schwartz, S. Y., and DeShon, H. R. (2003). Control of seafloor roughness on earthquake rupture behavior. *Geology*, 31(5):455–458.

Bilham, R. (2004). Urban earthquake fatalities: A safer world, or worse to come? *Seismological Research Letters*, 75(6):706–712.

Blum, P. (1997). Physical properties handbook: a guide to the shipboard measurement of physical properties of deep-sea cores.

Bourbié, T., Coussy, O., Zinszner, B., and Junger, M. C. (1992). Acoustics of porous media.

Boyer, T. P., Antonov, J. I., Baranova, O. K., Coleman, C., Garcia, H. E., Grodsky, A., Johnson, D. R., Locarnini, R. A., Mishonov, A. V., O'Brien, T. D., et al. (2013). World ocean database 2013.

Brossier, R., Operto, S., and Virieux, J. (2009). Seismic imaging of complex onshore structures by 2d elastic frequency-domain full-waveform inversion. *Geophysics*, 74(6):WCC105–WCC118.

Bunks, C., Saleck, F. M., Zaleski, S., and Chavent, G. (1995). Multiscale seismic waveform inversion. *Geophysics*, 60(5):1457–1473.

Bürgmann, R. (2018). The geophysics, geology and mechanics of slow fault slip. *Earth and Planetary Science Letters*, 495:112–134.

Calderón Agudo, Ò., Vieira da Silva, N., Warner, M., Kalinicheva, T., and Morgan, J. (2018). Addressing viscous effects in acoustic full-waveform inversion. *Geophysics*, 83(6):R611–R628.

Calvert, A. J., Preston, L. A., and Farahbod, A. M. (2011). Sedimentary underplating at the cascadia mantle-wedge corner revealed by seismic imaging. *Nature Geoscience*, 4(8):545.

Canales, L. L. (1984). Random noise reduction. In *SEG Technical Program Expanded Abstracts 1984*, pages 525–527. Society of Exploration Geophysicists.

Carbotte, S., Canales, J., Carton, H., Nedimovic, M., Han, S., Marjanovic, M., Gibson, J., Janiszewski, H., Horning, G., Delescluse, M., et al. (2012). Evolution and hydration of the juan de fuca crust and uppermost mantle: A plate-scale seismic investigation from ridge to trench. In *AGU Fall Meeting Abstracts*.

Carter, L., Manighetti, B., Elliot, M., Trustrum, N., and Gomez, B. (2002). Source, sea level and circulation effects on the sediment flux to the deep ocean over the past 15 ka off eastern new zealand. *Global and Planetary Change*, 33(3-4):339–355.

Castagna, J. P., Batzle, M. L., and Eastwood, R. L. (1985). Relationships between compressional-wave and shear-wave velocities in clastic silicate rocks. *Geophysics*, 50(4):571–581.

Chester, F. M., Rowe, C., Ujiie, K., Kirkpatrick, J., Regalla, C., Remitti, F., Moore, J. C., Toy, V., Wolfson-Schwehr, M., Bose, S., et al. (2013). Structure and composition of the plate-boundary slip zone for the 2011 tohoku-oki earthquake. *Science*, 342(6163):1208–1211.

Christeson, G., Gulick, S., Morgan, J., Gebhardt, C., Kring, D., Le Ber, E., Lofi, J., Nixon, C., Poelchau, M., and Rae, A. (2018). Extraordinary rocks from the peak ring of the chicxulub impact crater: P-wave velocity, density, and porosity measurements from iodp/icdp expedition 364. *Earth and Planetary Science Letters*, 495:1–11.

Christeson, G. L., Morgan, J. V., and Warner, M. R. (2012). Shallow oceanic crust: Full waveform tomographic images of the seismic layer 2a/2b boundary. *Journal of Geophysical Research: Solid Earth*, 117(B5).

Cloos, M. (1992). Thrust-type subduction-zone earthquakes and seamount asperities: A physical model for seismic rupture. *Geology*, 20(7):601–604.

Cochrane, G., Moore, J., MacKay, M., and Moore, G. (1994). Velocity and inferred porosity model of the oregon accretionary prism from multichannel seismic reflection data: Implications on sediment dewatering and overpressure. *Journal of Geophysical Research: Solid Earth*, 99(B4):7033–7043.

Collot, J.-Y., Lewis, K., Lamarche, G., and Lallemand, S. (2001). The giant ruatoria debris avalanche on the northern hikurangi margin, new zealand: Result of oblique seamount subduction. *Journal of Geophysical Research: Solid Earth*, 106(B9):19271–19297.

da Silva, N., Yao, G., Warner, M., Umpleby, A., and Debens, H. (2017). Global visco-acoustic full waveform inversion. In *79th EAGE Conference and Exhibition 2017*.

da Silva, N. V., Yao, G., and Warner, M. (2018). Semi-global inversion of vp to vs ratio for elastic wavefield inversion. *Inverse Problems*, 34(11):115011.

da Silva, N. V., Yao, G., and Warner, M. (2019). Semiglobal viscoacoustic full-waveform inversion. *Geophysics*, 84(2):R271–R293.

Davis, E., Hyndman, R., and Villinger, H. (1990). Rates of fluid expulsion across the northern cascadia accretionary prism: Constraints from new heat row and multichannel seismic reflection data. *Journal of Geophysical Research: Solid Earth*, 95(B6):8869–8889.

Davy, B., Hoernle, K., and Werner, R. (2008). Hikurangi plateau: Crustal structure, rifted formation, and gondwana subduction history. *Geochemistry, Geophysics, Geosystems*, 9(7).

Davy, B. and Wood, R. (1994). Gravity and magnetic modelling of the hikurangi plateau. *Marine geology*, 118(1-2):139–151.

Debens, H. A. (2015). *Three-dimensional anisotropic full-waveform inversion*. PhD thesis, Imperial College London.

Delescluse, M., Nedimović, M. R., and Louden, K. E. (2011). 2d waveform tomography applied to long-streamer mcs data from the scotian slope. *Geophysics*, 76(4):B151–B163.

DeMets, C., Gordon, R. G., Argus, D. F., and Stein, S. (1994). Effect of recent revisions to the geomagnetic reversal time scale on estimates of current plate motions. *Geophysical research letters*, 21(20):2191–2194.

Dixon, T. H., Jiang, Y., Malservisi, R., McCaffrey, R., Voss, N., Protti, M., and Gonzalez, V. (2014). Earthquake and tsunami forecasts: Relation of slow slip events to subsequent earthquake rupture. *Proceedings of the National Academy of Sciences*, 111(48):17039–17044.

Dmowska, R. (2006). *Advances in Geophysics: Advances in Wave Propagation in Heterogeneous Earth*. Elsevier.

Dobson, M. R. and O'Leary, D. (2019). Sediment delivery and depositional processes along the eastern aleutian trench. *Journal of the Geological Society*, pages jgs2019–034.

Dominguez, S., Lallemand, S. E., Malavieille, J., and von Huene, R. (1998). Upper plate deformation associated with seamount subduction. *Tectonophysics*, 293(3):207–224.

Doser, D. I. and Webb, T. H. (2003). Source parameters of large historical (19171961) earthquakes, north island, new zealand. *Geophysical Journal International*, 152(3):795–832.

Douglas, A., Beavan, J., Wallace, L., and Townend, J. (2005). Slow slip on the northern hikurangi subduction interface, new zealand. *Geophysical Research Letters*, 32(16).

Downes, G. (2001). The 26 march and 17 may 1947 gisborne earthquakes and tsunami: implications for tsunami hazard for the east coast, north island, new zealand, international tsunami workshop" tsunami risk assessment beyond 2000: Theory. *Practice and Plans", Moscow, Russia*.

Dragert, H., Wang, K., and James, T. S. (2001). A silent slip event on the deeper cascadia subduction interface. *Science*, 292(5521):1525–1528.

Dragert, H., Wang, K., and Rogers, G. (2004). Geodetic and seismic signatures of episodic tremor and slip in the northern cascadia subduction zone. *Earth, planets and space*, 56(12):1143–1150.

Dziewonski, A. M. and Anderson, D. L. (1981). Preliminary reference earth model. *Physics of the earth and planetary interiors*, 25(4):297–356.

Eberhart-Phillips, D. and Bannister, S. (2015). 3-d imaging of the northern hikurangi subduction zone, new zealand: variations in subducted sediment, slab fluids and slow slip. *Geophysical Journal International*, 201(2):838–855.

Eberhart-Phillips, D. and Chadwick, M. (2002). Threedimensional attenuation model of the shallow hikurangi subduction zone in the raukumara peninsula, new zealand. *Journal of Geophysical Research: Solid Earth*, 107(B2).

Eberhart-Phillips, D. and Reyners, M. (1997). Continental subduction and threedimensional crustal structure: The northern south island, new zealand. *Journal of Geophysical Research: Solid Earth*, 102(B6):11843–11861.

Eberhart-Phillips, D. and Reyners, M. (1999). Plate interface properties in the northeast hikurangi subduction zone, new zealand, from converted seismic waves. *Geophysical Research Letters*, 26(16):2565–2568.

Ellis, S., Fagereng, ., Barker, D., Henrys, S., Saffer, D., Wallace, L., Williams, C., and Harris, R. (2015). Fluid budgets along the northern hikurangi subduction margin, new zealand: The effect of a subducting seamount on fluid pressure. *Geophysical Journal International*, 202(1):277–297.

Erickson, S. N. and Jarrard, R. D. (1998). Velocity-porosity relationships for water-saturated siliciclastic sediments. *Journal of Geophysical Research: Solid Earth*, 103(B12):30385–30406.

Fagereng, Å., Bassett, D., Bell, R., Savage, H., Wallace, L., Arai, R., Bangs, N., Barker, D., Barnes, P., Crutchley, G., Harris, R., Henrys, S., Ikari, M., Kitajima, H., Kodaira, S., Moore, G., Saffer, D., Solomon, E., Ujiie, K., and Underwood, M. (2019a). Probing the physical controls on a locked vs. creeping megathrust with ocean drilling, hikurangi subduction margin, nz. IODP pre-proposal.

Fagereng, Å., Savage, H., Morgan, J., Wang, M., Meneghini, F., Barnes, P., Bell, R., Kitajima, H., McNamara, D., Saffer, D., et al. (2019b). Mixed deformation styles observed on a shallow subduction thrust, hikurangi margin, new zealand. *Geology*.

Fagereng, Å. and Sibson, R. H. (2010). Melange rheology and seismic style. *Geology*, 38(8):751–754.

Fagereng, . (2011). Wedge geometry, mechanical strength, and interseismic coupling of the hikurangi subduction thrust, new zealand. *Tectonophysics*, 507(1-4):26–30.

Fei, T. and Larner, K. (1995). Elimination of numerical dispersion in finite-difference modeling and migration by flux-corrected transport. *Geophysics*, 60(6):1830–1842.

Ferrara, E., Cowan, C., and Grant, P. (1985). Frequency-domain adaptive filtering. *Adaptive filters*, 145.

Fowler, S. R., White, R. S., and Louden, K. E. (1985). Sediment dewatering in the makran accretionary prism. *Earth and Planetary Science Letters*, 75(4):427–438.

Fruehn, J., White, R., and Minshull, T. (1997). Internal deformation and compaction of the makran accretionary wedge. *Terra nova*, 9(3):101–104.

Fu, Y. and Freymueller, J. T. (2013). Repeated large slow slip events at the southcentral alaska subduction zone. *Earth and Planetary Science Letters*, 375:303–311.

Fujii, Y., Satake, K., Sakai, S., Shinohara, M., and Kanazawa, T. (2011). Tsunami source of the 2011 off the pacific coast of tohoku earthquake. *Earth, planets and space*, 63(7):55.

Gardner, G., Gardner, L., and Gregory, A. (1974). Formation velocity and densitythe diagnostic basics for stratigraphic traps. *Geophysics*, 39(6):770–780.

Gauthier, O., Virieux, J., and Tarantola, A. (1986). Two-dimensional nonlinear inversion of seismic waveforms: Numerical results. *Geophysics*, 51(7):1387–1403.

Geist, E. L. and Bilek, S. L. (2001). Effect of depth-dependent shear modulus on tsunami generation along subduction zones. *Geophysical Research Letters*, 28(7):1315–1318.

GeoNet. www.geonet.org.nz.

Gettemy, G. and Tobin, H. J. (2003). Tectonic signatures in centimeter-scale velocity-porosity relationships of costa rica convergent margin sediments. *Journal of Geophysical Research: Solid Earth*, 108(B10).

Ghisetti, F. C., Barnes, P. M., Ellis, S., PlazaFaverola, A. A., and Barker, D. H. (2016). The last 2 myr of accretionary wedge construction in the central hikurangi margin (north island, new zealand): Insights from structural modeling. *Geochemistry, Geophysics, Geosystems*, 17(7):2661–2686.

Gomberg, J., Wech, A., Creager, K., Obara, K., and Agnew, D. (2016). Reconsidering earthquake scaling. *Geophysical Research Letters*, 43(12):6243–6251.

Graeber, F. M. and Asch, G. (1999). Threedimensional models of p wave velocity and ptos velocity ratio in the southern central andes by simultaneous inversion of local earthquake data. *Journal of Geophysical Research: Solid Earth*, 104(B9):20237–20256.

Graves, R. W. (1996). Simulating seismic wave propagation in 3d elastic media using staggered-grid finite differences. *Bulletin of the Seismological Society of America*, 86(4):1091–1106.

Gray, M., Bell, R., Morgan, J., Henrys, S., Barker, D., teh IODP Expedition 372, and science parties, . (2019). Imaging the shallow subsurface structure of the north hikurangi subduction zone, new zealand, using 2d fullwaveform inversion. *JGR: Solid Earth*.

Greenberg, M. and Castagna, J. (1992). Shear-wave velocity estimation in porous rocks: theoretical formulation, preliminary verification and applications. *Geophysical Prospecting*, 40(2):195–209.

Greinert, J., Lewis, K., Bialas, J., Pecher, I. A., Rowden, A., Bowden, D., De Batist, M., and Linke, P. (2010). Methane seepage along the hikurangi margin, new zealand: Overview of studies in 2006 and 2007 and new evidence from visual, bathymetric and hydroacoustic investigations. *Marine Geology*, 272(1-4):6–25.

Guasch, L. (2012). 3d elastic full-waveform inversion.

Guasch, L., Warner, M., and Ravaut, C. (2019). Adaptive waveform inversion: Practice. *Geophysics*, 84(3):R447–R461.

Gulanay, N.

Gulunay, N. (1986). Fxdecon and complex wiener prediction filter. In *SEG Technical Program Expanded Abstracts 1986*, pages 279–281. Society of Exploration Geophysicists.

Hamilton, E. L. (1978). Sound velocity–density relations in sea-floor sediments and rocks. *The journal of the Acoustical Society of America*, 63(2):366–377.

Hamilton, E. L. (1979). V p/v s and poissons ratios in marine sediments and rocks. *The Journal of the Acoustical Society of America*, 66(4):1093–1101.

Hamling, I. J., Hreinsdóttir, S., Clark, K., Elliott, J., Liang, C., Fielding, E., Litchfield, N., Villamor, P., Wallace, L., Wright, T. J., et al. (2017). Complex multifault rupture during the 2016 mw 7.8 kaikōura earthquake, new zealand. *Science*, 356(6334):eaam7194.

Han, S., Bangs, N. L., Carbotte, S. M., Saffer, D. M., and Gibson, J. C. (2017). Links between sediment consolidation and cascadia megathrust slip behaviour. *Nature Geoscience*, 10(12):954.

Hansen, R. T., Bostock, M. G., and Christensen, N. I. (2012). Nature of the low velocity zone in cascadia from receiver function waveform inversion. *Earth and Planetary Science Letters*, 337:25–38.

Hashimoto, Y., Tobin, H., and Knuth, M. (2010). Velocity-porosity relationships for slope apron and accreted sediments in the nankai trough seismogenic zone experiment, integrated ocean drilling program expedition 315 site c0001. *Geochemistry, Geophysics, Geosystems*, 11(12).

Heinrich, P., Schindele, F., Guibourg, S., and Ihmlé, P. F. (1998). Modeling of the february 1996 peruvian tsunami. *Geophysical Research Letters*, 25(14):2687–2690.

Heki, K. and Kataoka, T. (2008). On the biannually repeating slow-slip events at the ryukyu trench, southwestern japan. *Journal of Geophysical Research: Solid Earth*, 113(B11).

Heuret, A. and Lallemand, S. (2005). Plate motions, slab dynamics and back-arc deformation. *Physics of the Earth and Planetary Interiors*, 149(1-2):31–51.

Heuret, A., Lallemand, S., Funiciello, F., Piromallo, C., and Faccenna, C. (2011). Physical characteristics of subduction interface type seismogenic zones revisited. *Geochemistry, Geophysics, Geosystems*, 12(1).

Hicks, S. P., Rietbrock, A., Haberland, C. A., Ryder, I. M., Simons, M., and Tassara, A. (2012). The 2010 mw 8.8 maule, chile earthquake: Nucleation and rupture propagation controlled by a subducted topographic high. *Geophysical Research Letters*, 39(19).

Hirose, H., Hirahara, K., Kimata, F., Fujii, N., and Miyazaki, S. (1999). A slow thrust slip event following the two 1996 hyuganada earthquakes beneath the bungo channel, southwest japan. *Geophysical Research Letters*, 26(21):3237–3240.

Hoernle, K., Hauff, F., Van den Bogaard, P., Werner, R., Mortimer, N., Geldmacher, J., Garbe-Schönberg, D., and Davy, B. (2010). Age and geochemistry of volcanic rocks from the hikurangi and manihiki oceanic plateaus. *Geochimica et Cosmochimica Acta*, 74(24):7196–7219.

Hoffman, N. W. (2004). *Physical Properties of Sediments in the Nanki Trough Accretionary Prism.* PhD thesis, New Mexico Institute of Mining and Technology Socorro.

Hole, J. (1992). Nonlinear high-resolution three-dimensional seismic travel time tomography. *Journal of Geophysical Research: Solid Earth*, 97(B5):6553–6562.

Houbiers, M., Mispel, J., Knudsen, B., and Amundsen, L. (2013). Fwi with obc data from the mariner field, uk-the impact on mapping sands at reservoir level. In *75th EAGE Conference & Exhibition incorporating SPE EUROPEC 2013*.

Howe, B. M., Worcester, P. F., and Spindel, R. C. (1987). Ocean acoustic tomography: Mesoscale velocity. *Journal of Geophysical Research: Oceans*, 92(C4):3785–3805.

Husen, S., Kissling, E., and Quintero, R. (2002). Tomographic evidence for a subducted seamount beneath the gulf of nicoya, costa rica: The cause of the 1990 mw= 7.0 gulf of nicoya earthquake. *Geophysical Research Letters*, 29(8):79–1.

Husen, S., Quintero, R., Kissling, E., and Hacker, B. (2003). Subduction-zone structure and magmatic processes beneath costa rica constrained by local earthquake tomography and petrological modelling. *Geophysical Journal International*, 155(1):11–32.

Hyndman, R., Moore, G., and Moran, K. (1993). 17. velocity, porosity, and pore-fluid loss from the nankai subduction zone accretionary prism1.

Hyndman, R., Wang, K., and Yamano, M. (1995). Thermal constraints on the seismogenic portion of the southwestern japan subduction thrust. *Journal of Geophysical Research: Solid Earth*, 100(B8):15373–15392.

Ide, S., Beroza, G. C., Shelly, D. R., and Uchide, T. (2007). A scaling law for slow earthquakes. *Nature*, 447(7140):76.

Ikari, M. J., Marone, C., Saffer, D. M., and Kopf, A. J. (2013). Slip weakening as a mechanism for slow earthquakes. *Nature geoscience*, 6(6):468.

Ikari, M. J. and Saffer, D. M. (2011). Comparison of frictional strength and velocity dependence between fault zones in the nankai accretionary complex. *Geochemistry, Geophysics, Geosystems*, 12(4).

Ito, Y., Asano, Y., and Obara, K. (2009). Verylowfrequency earthquakes indicate a transpressional stress regime in the nankai accretionary prism. *Geophysical Research Letters*, 36(20).

Jeppson, T. N., Tobin, H. J., and Hashimoto, Y. (2018). Laboratory measurements quantifying elastic properties of accretionary wedge sediments: Implications for slip to the trench during the 2011 m w 9.0 tohoku-oki earthquake. *Geosphere*, 14(4):1411–1424.

Jiang, Y., Wdowinski, S., Dixon, T. H., Hackl, M., Protti, M., and Gonzalez, V. (2012). Slow slip events in costa rica detected by continuous gps observations, 2002–2011. *Geochemistry, Geophysics, Geosystems*, 13(4).

Johnson, J. M. and Satake, K. (1997). Estimation of seismic moment and slip distribution of the april 1, 1946, aleutian tsunami earthquake. *Journal of Geophysical Research: Solid Earth*, 102(B6):11765–11774.

Jones, C., Evans, M., Ratcliffe, A., Conroy, G., Jupp, R., Selvage, J., and Ramsey, L. (2013). Full waveform inversion in a complex geological setting-a narrow azimuth towed streamer case study from the barents sea. In *75th EAGE Conference & Exhibition incorporating SPE EUROPEC 2013*.

Kalinicheva, T., Warner, M., Ashley, J., and Mancini, F. (2017). Two-vs three-dimensional full-waveform inversion in a 3d world. In *SEG technical program expanded abstracts 2017*, pages 1383–1387. Society of Exploration Geophysicists.

Kamei, R., Pratt, R. G., and Tsuji, T. (2012). Waveform tomography imaging of a megasplay fault system in the seismogenic nankai subduction zone. *Earth and Planetary Science Letters*, 317-318:343–353.

Kanamori, H. (1972). Mechanism of tsunami earthquakes. *Physics of the earth and planetary interiors*, 6(5):346–359.

Katsumata, A. and Kamaya, N. (2003). Low-frequency continuous tremor around the moho discontinuity away from volcanoes in the southwest japan. *Geophysical Research Letters*, 30(1):20–1.

Katz, H.-R. (1981). Probable gas hydrate in continental slope east of the north island, new zealand. *Journal of petroleum geology*, 3(3):315–324.

Kitajima, H. and Saffer, D. M. (2012). Elevated pore pressure and anomalously low stress in regions of low frequency earthquakes along the nankai trough subduction megathrust. *Geophysical Research Letters*, 39(23).

Kodaira, S., Iidaka, T., Kato, A., Park, J.-O., Iwasaki, T., and Kaneda, Y. (2004). High pore fluid pressure may cause silent slip in the nankai trough. *Science*, 304(5675):1295–1298.

Kodaira, S No, T. N. Y. F. T. K. Y. M. S. T. N. K. Y. T. A. (2012). Coseismic fault rupture at the trench axis during the 2011 tohoku-oki earthquake. *Nature Geoscience*, 5(9):646.

Kopp, C., Fruehn, J., Flueh, E., Reichert, C., Kukowski, N., Bialas, J., and Klaeschen, D. (2000). Structure of the makran subduction zone from wide-angle and reflection seismic data. *Tectonophysics*, 329(1-4):171–191.

Kopp, H., Hindle, D., Klaeschen, D., Oncken, O., Reichert, C., and Scholl, D. (2009). Anatomy of the western java plate interface from depth-migrated seismic images. *Earth and Planetary Science Letters*, 288(3-4):399–407.

Kostoglodov, V., Singh, S. K., Santiago, J. A., Franco, S. I., Larson, K. M., Lowry, A. R., and Bilham, R. (2003). A large silent earthquake in the guerrero seismic gap, mexico. *Geophysical Research Letters*, 30(15).

Lailly, P. (1983). The seismic inverse problem as a sequence of before stack migrations. In *Conference on Inverse Scattering–Theory and Application*, volume 11, page 206. Siam.

Lauer, R. M. and Saffer, D. M. (2012). Fluid budgets of subduction zone forearcs: The contribution of splay faults. *Geophysical Research Letters*, 39:L13604–L13604.

Lavier, L. L., Bennett, R. A., and Duddu, R. (2013). Creep events at the brittle ductile transition. *Geochemistry, Geophysics, Geosystems*, 14(9):3334–3351.

Lay, T. (2009). Long range science plan for seismology workshop. In *Seismological Grand Challenges in Understanding Earth's Dynamic Systems*.

Lay, T., Ammon, C. J., Kanamori, H., Xue, L., and Kim, M. J. (2011). Possible large near-trench slip during the 2011 m w 9.0 off the pacific coast of tohoku earthquake. *Earth, planets and space*, 63(7):32.

Lei, J. and Zhao, D. (2005). P-wave tomography and origin of the changbai intraplate volcano in northeast asia. *Tectonophysics*, 397(3-4):281–295.

Levander, A. R. (1988). Fourth-order finite-difference p-sv seismograms. *Geophysics*, 53(11):1425–1436.

Lewis, K. and Pettinga, J. (1993). The emerging, imbricate frontal wedge of the hikurangi margin. *Sedimentary basins of the world*, 2:225–250.

Lewis, M., Ben-Zion, Y., and McGuire, J. J. (2007). Imaging the deep structure of the san andreas fault south of hollister with joint analysis of fault zone head and direct p arrivals. *Geophysical Journal International*, 169(3):1028–1042.

Li, Y.-G., Ellsworth, W. L., Thurber, C. H., Malin, P. E., and Aki, K. (1997). Fault-zone guided waves from explosions in the san andreas fault at parkfield and cienega valley, california. *Bulletin of the Seismological Society of America*, 87(1):210–221.

Liu, Y. and Rice, J. R. (2005). Aseismic slip transients emerge spontaneously in threedimensional rate and state modeling of subduction earthquake sequences. *Journal of Geophysical Research: Solid Earth*, 110(B8).

Liu, Y. and Rice, J. R. (2007). Spontaneous and triggered aseismic deformation transients in a subduction fault model. *Journal of Geophysical Research: Solid Earth*, 112(B9).

Lotto, G. C., Nava, G., and Dunham, E. M. (2017). Should tsunami simulations include a nonzero initial horizontal velocity? *Earth, Planets and Space*, 69(1):117.

Lowry, A. R., Larson, K. M., Kostoglodov, V., and Bilham, R. (2001). Transient fault slip in guerrero, southern mexico. *Geophysical Research Letters*, 28(19):3753–3756.

Lu, R., Lazaratos, S., Wang, K., Cha, Y., Chikichev, I., and Prosser, R. (2013). High-resolution elastic fwi for reservoir characterization. In *75th EAGE Conference & Exhibition incorporating SPE EUROPEC 2013*.

Luo, Y. and Schuster, G. T. (1991). Wave-equation traveltime inversion. *Geophysics*, 56(5):645–653.

Marfurt, K. J. (1984). Accuracy of finite-difference and finite-element modeling of the scalar and elastic wave equations. *Geophysics*, 49(5):533–549.

Marone, C. (1998). Laboratory-derived friction laws and their application to seismic faulting. *Annual Review of Earth and Planetary Sciences*, 26(1):643–696.

Marone, C. and Scholz, C. (1988). The depth of seismic faulting and the upper transition from stable to unstable slip regimes. *Geophysical Research Letters*, 15(6):621–624.

Marone, C. J., Scholtz, C., and Bilham, R. (1991). On the mechanics of earthquake afterslip. *Journal of Geophysical Research: Solid Earth*, 96(B5):8441–8452.

Matsubara, M., Obara, K., and Kasahara, K. (2009). High-vp/vs zone accompanying non-volcanic tremors and slow-slip events beneath southwestern japan. *Tectonophysics*, 472(1-4):6–17.

Mazengarb, C. and Speden, I. (2000). *GEOLOGY OF THE RAUKUMARA AREA*.

McCaffrey, R. and Goldfinger, C. (1995). Forearc deformation and great subduction earthquakes: Implications for cascadia offshore earthquake potential. *Science*, 267(5199):856–859.

McCaffrey, R., Wallace, L. M., and Beavan, J. (2008). Slow slip and frictional transition at low temperature at the hikurangi subduction zone. *Nature Geoscience*, 1(5):316.

McIntosh, K. D., Silver, E. A., Ahmed, I., Berhorst, A., Ranero, C. R., Kelly, R. K., and Flueh, E. R. (2007). The nicaragua convergent margin: Seismic reflection imaging of the source of a tsunami earthquake.

Medwin, H. (1975). Speed of sound in water: A simple equation for realistic parameters. *The Journal of the Acoustical Society of America*, 58(6):1318–1319.

Mendoza, C. and Hartzell, S. (1999). Fault-slip distribution of the 1995 colima-jalisco, mexico, earthquake. *Bulletin of the Seismological Society of America*, 89(5):1338–1344.

Miller, M. M., Melbourne, T., Johnson, D. J., and Sumner, W. Q. (2002). Periodic slow earthquakes from the cascadia subduction zone. *Science*, 295(5564):2423–2423.

Minshull, T. and White, R. (1989). Sediment compaction and fluid migration in the makran accretionary prism. *Journal of Geophysical Research: Solid Earth*, 94(B6):7387–7402.

Moore, G. F., Shipley, T., Stoffa, P., Karig, D., Taira, A., Kuramoto, S., Tokuyama, H., and Suyehiro, K. (1990). Structure of the nankai trough accretionary zone from multichannel seismic reflection data. *Journal of Geophysical Research: Solid Earth*, 95(B6):8753–8765.

Moore, G. F., Taira, A., Klaus, A., Becker, L., Boeckel, B., Cragg, B. A., Dean, A., Fergusson, C. L., Henry, P., Hirano, S., et al. (2001). New insights into deformation and fluid flow processes in the nankai trough accretionary prism: Results of ocean drilling program leg 190. *Geochemistry, Geophysics, Geosystems*, 2(10).

Moore, J. C. (1989). Tectonics and hydrogeology of accretionary prisms: role of the décollement zone. *Journal of Structural Geology*, 11(1-2):95–106.

Mora, P. (1988). Elastic wave-field inversion of reflection and transmission data. *Geophysics*, 53(6):750–759.

Morgan, J. and Karig, D. (1995). Kinematics and a balanced and restored cross-section across the toe of the eastern nankai accretionary prism. *Journal of Structural Geology*, 17(1):31–45.

Morgan, J., Warner, M., Arnoux, G., Hooft, E., Toomey, D., VanderBeek, B., and Wilcock, W. (2016). Next-generation seismic experimentsii: wide-angle, multi-azimuth, 3-d, full-waveform inversion of sparse field data. *Geophysical Journal International*, 204(2):1342–1363.

Morgan, J., Warner, M., Bell, R., Ashley, J., Barnes, D., Little, R., Roele, K., and Jones, C. (2013). Next-generation seismic experiments: wide-angle, multi-azimuth, three-dimensional, full-waveform inversion. *Geophysics Journal International*, 195(3):1657–1678.

Morgan, J., Warner, M., Collins, G., Grieve, R., Christeson, G., Gulick, S., and Barton, P. (2011). Full waveform tomographic images of the peak ring at the chicxulub impact crater. *Journal of Geophysical Research: Solid Earth*, 116(B6).

Mothi, S., Schwarz, K., and Zhu, H. (2013). Impact of full-azimuth and long-offset acquisition on full waveform inversion in deepwater gulf of mexico. In *SEG Technical Program Expanded Abstracts 2013*, pages 924–928. Society of Exploration Geophysicists.

Mountjoy, J. J. and Barnes, P. M. (2011). Active upper plate thrust faulting in regions of low plate interface coupling, repeated slow slip events, and coastal uplift: Example from the hikurangi margin, new zealand. *Geochemistry, Geophysics, Geosystems*, 12(1).

Multiwave (2005). 05cm 2d seismic survey, offshore east coast–north island. *New Zealand unpublished open file petroleum report 3136*.

Nafe, J. E. and Drake, C. L. (1957). Variation with depth in shallow and deep water marine sediments of porosity, density and the velocities of compressional and shear waves. *Geophysics*, 22(3):523–552.

Nangoo, T., Warner, M., Morgan, J., Umpleby, A., Stekl, I., and Bertrand, A. (2012). Full-waveform seismic inversion at reservoir depths. In *74th EAGE Conference and Exhibition incorporating EUROPEC 2012*.

Navalpakam, R. S., Pecher, I. A., and Stern, T. (2012). Weak and segmented bottom simulating reflections on the hikurangi margin, new zealandimplications for gas hydrate reservoir rocks. *Journal of Petroleum Science and Engineering*, 88:29–40.

Nedimović, M. R., Hyndman, R. D., Ramachandran, K., and Spence, G. D. (2003). Reflection signature of seismic and aseismic slip on the northern cascadia subduction interface. *Nature*, 424(6947):416.

Nishimura, T. (2014). Short-term slow slip events along the ryukyu trench, southwestern japan, observed by continuous gnss. *Progress in Earth and Planetary Science*, 1(1):22.

Nolet, G. (1987). Seismic wave propagation and seismic tomography. In *Seismic tomography*, pages 1–23. Springer.

Nur, A., Mavko, G., Dvorkin, J., and Galmudi, D. (1998). Critical porosity: A key to relating physical properties to porosity in rocks. *The Leading Edge*, 17(3):357–362.

Obara, K. (2002). Nonvolcanic deep tremor associated with subduction in southwest japan. *Science*, 296(5573):1679–1681.

Obara, K., Hirose, H., Yamamizu, F., and Kasahara, K. (2004). Episodic slow slip events accompanied by non-volcanic tremors in southwest japan subduction zone. *Geophysical Research Letters*, 31(23).

Obara, K. and Ito, Y. (2005). Very low frequency earthquakes excited by the 2004 off the kii peninsula earthquakes: A dynamic deformation process in the large accretionary prism. *Earth, Planets and Space*, 57(4):321–326.

Ohta, Y., Freymueller, J. T., Hreinsdóttir, S., and Suito, H. (2006). A large slow slip event and the depth of the seismogenic zone in the south central alaska subduction zone. *Earth and Planetary Science Letters*, 247(1-2):108–116.

Oleskevich, D., Hyndman, R., and Wang, K. (1999). The updip and downdip limits to great subduction earthquakes: Thermal and structural models of cascadia, south alaska, sw japan, and chile. *Journal of Geophysical Research: Solid Earth*, 104(B7):14965–14991.

Operto, S., Ravaut, C., Improta, L., Virieux, J., Herrero, A., and DellAversana, P. (2004). Quantitative imaging of complex structures from dense wide-aperture seismic data by multiscale traveltime and waveform inversions: A case study. *Geophysical prospecting*, 52(6):625–651.

Operto, S., Virieux, J., Dessa, J.-X., and Pascal, G. (2006). Crustal seismic imaging from multifold ocean bottom seismometer data by frequency domain full waveform tomography: Application to the eastern nankai trough. *Journal of Geophysical Research: Solid Earth*, 111(B9).

Outerbridge, K. C., Dixon, T. H., Schwartz, S. Y., Walter, J. I., Protti, M., Gonzalez, V., Biggs, J., Thorwart, M., and Rabbel, W. (2010). A tremor and slip event on the cocos-caribbean subduction zone as measured by a global positioning system (gps) and seismic network on the nicoya peninsula, costa rica. *Journal of Geophysical Research: Solid Earth*, 115(B10).

Ozawa, S., Miyazaki, S., Hatanaka, Y., Imakiire, T., Kaidzu, M., and Murakami, M. (2003). Characteristic silent earthquakes in the eastern part of the boso peninsula, central japan. *Geophysical Research Letters*, 30(6).

Ozawa, S., Murakami, M., Kaidzu, M., Tada, T., Sagiya, T., Hatanaka, Y., Yarai, H., and Nishimura, T. (2002). Detection and monitoring of ongoing aseismic slip in the tokai region, central japan. *Science*, 298(5595):1009–1012.

P, B. (in review). *in review.*

Park, J.-O., Fujie, G., Wijerathne, L., Hori, T., Kodaira, S., Fukao, Y., Moore, G. F., Bangs, N. L., Kuramoto, S., and Taira, A. (2010). A low-velocity zone with weak reflectivity along the nankai subduction zone. *Geology*, 38(3):283–286.

Park, J.-O., Tsuru, T., Kodaira, S., Cummins, P. R., and Kaneda, Y. (2002). Splay fault branching along the nankai subduction zone. *Science*, 297(5584):1157–1160.

Peacock, S. M. (2009). Thermal and metamorphic environment of subduction zone episodic tremor and slip. *Journal of Geophysical Research: Solid Earth*, 114(B8).

Pecher, I., Barnes, P., LeVay, L., , and the Expedition 372A Scientists, editors (2019). *Creeping Gas Hydrate Slides.*, College Station, TX (International Ocean Discovery Program).

Pecher, I., Barnes, P., LeVay, L., Bourlange, S., Brunet, M., Cardona, S., Clennell, M., Cook, A., Dugan, B., and Elger, J. (2018). International ocean discovery program expedition 372 preliminary report: Creeping gas hydrate slides and hikurangi lwd.

Pedley, K. L. (2010). Modelling submarine landscape evolution in response to subduction processes, northern hikurangi margin, new zealand.

Pelayo, A. M. and Wiens, D. A. (1992). Tsunami earthquakes: Slow thrust-faulting events in the accretionary wedge. *Journal of Geophysical Research: Solid Earth*, 97(B11):15321–15337.

Peng, Z. and Gomberg, J. (2010). An integrated perspective of the continuum between earthquakes and slow-slip phenomena. *Nature Geoscience*, 3(9):599–607.

Pettinga, J. R. (2003). Mud volcano eruption within the emergent accretionary hikurangi margin, southern hawke's bay, new zealand. *New Zealand Journal of Geology and Geophysics*, 46(1):107–121.

PlazaFaverola, A., Henrys, S., Pecher, I., Wallace, L., and Klaeschen, D. (2016). Splay fault branching from the hikurangi subduction shear zone: Implications for slow slip and fluid flow. *Geochemistry, Geophysics, Geosystems*, 17(12):5009–5023.

PlazaFaverola, A., Klaeschen, D., Barnes, P., Pecher, I., Henrys, S., and Mountjoy, J. (2012). Evolution of fluid expulsion and concentrated hydrate zones across the southern hikurangi subduction margin, new zealand: An analysis from depth migrated seismic data. *Geochemistry, Geophysics, Geosystems*, 13(8).

Plessix, R.-E. (2006). A review of the adjoint-state method for computing the gradient of a functional with geophysical applications. *Geophysical Journal International*, 167(2):495–503.

Plessix, R.-E. (2008). Introduction: Towards a full waveform inversion. *Geophysical Prospecting*, 56(6):761–763.

Plessix, R.-É. (2009). Three-dimensional frequency-domain full-waveform inversion with an iterative solver. *Geophysics*, 74(6):WCC149–WCC157.

Polet, J. and Kanamori, H. (2000). Shallow subduction zone earthquakes and their tsunamigenic potential. *Geophysical Journal International*, 142(3):684–702.

Power, W., Wallace, L., and Reyners, M. (2008). *Tsunami hazard posed by earthquakes on the Hikurangi subduction zone interface*. GNS Science.

Pratt, R. G. (1999). Seismic waveform inversion in the frequency domain, part 1: Theory and verification in a physical scale model. *Geophysics*, 64(3):888–901.

Pratt, R. G. and Goulty, N. R. (1991). Combining wave-equation imaging with traveltime tomography to form high-resolution images from crosshole data. *Geophysics*, 56(2):208–224.

Pratt, R. G. and Worthington, M. (1990). Inverse theory applied to multi-source cross-hole tomography. part 1: Acoustic wave-equation method. *Geophysical prospecting*, 38(3):287–310.

Raimbourg, H., Hamano, Y., Saito, S., Kinoshita, M., and Kopf, A. (2011). Acoustic and mechanical properties of nankai accretionary prism core samples. *Geochemistry, Geophysics, Geosystems*, 12(4).

Reyners, M., Eberhart-Phillips, D., Stuart, G., and Nishimura, Y. (2006). Imaging subduction from the trench to 300 km depth beneath the central north island, new zealand, with vp and vp/vs. *Geophysical Journal International*, 165(2):565–583.

Ridd, M. (1970). Mud volcanoes in new zealand. *AAPG Bulletin*, 54(4):601–616.

Robein, E. (2010). *Seismic imaging: a review of the techniques, their principles, merits and limitations*. EAGE publications.

Rogers, G. and Dragert, H. (2003). Episodic tremor and slip on the cascadia subduction zone: The chatter of silent slip. *Science*, 300(5627):1942–1943.

Rondenay, S., Abers, G. A., and Van Keken, P. E. (2008). Seismic imaging of subduction zone metamorphism. *Geology*, 36(4):275–278.

Rowe, C. D., Moore, J. C., Remitti, F., and Scientists, I. E. T. (2013). The thickness of subduction plate boundary faults from the seafloor into the seismogenic zone. *Geology*, 41(9):991–994.

Rubin, A. M. (2008). Episodic slow slip events and rate-and-state friction. *Journal of Geophysical Research: Solid Earth*, 113(B11).

Saffer, D. (2002). Differences in taper angle along strike of the nankai accretionary complex: A consequence of lithostratigraphy? In *AGU Fall Meeting Abstracts*.

Saffer, D. and Bekins, B. (1998). Fluid budgets and pore pressures in the shallow subduction zone: A comparison of the nankai and cascadia accretionary systems. *Eos Trans. AGU*, 79(45).

Saffer, D. M. (2003). Pore pressure development and progressive dewatering in underthrust sediments at the costa rican subduction margin: Comparison with northern barbados and nankai. *Journal of Geophysical Research: Solid Earth*, 108(B5).

Saffer, D. M. and McKiernan, A. W. (2005). Permeability of underthrust sediments at the costa rican subduction zone: Scale dependence and implications for dewatering. *Geophysical research letters*, 32(2).

Saffer, D. M., Silver, E. A., Fisher, A. T., Tobin, H., and Moran, K. (2000). Inferred pore pressures at the costa rica subduction zone: implications for dewatering processes. *Earth and Planetary Science Letters*, 177(3-4):193–207.

Saffer, D. M. and Tobin, H. J. (2011). Hydrogeology and mechanics of subduction zone forearcs: Fluid flow and pore pressure. *Annual Review of Earth and Planetary Sciences*, 39:157–186.

Saffer, D. M. and Wallace, L. M. (2015). The frictional, hydrologic, metamorphic and thermal habitat of shallow slow earthquakes. *Nature Geoscience*, 8(8):594.

Sahling, H., Masson, D. G., Ranero, C. R., Hhnerbach, V., Weinrebe, W., Klaucke, I., Brk, D., Brckmann, W., and Suess, E. (2008). Fluid seepage at the continental margin offshore costa rica and southern nicaragua. *Geochemistry, Geophysics, Geosystems*, 9(5).

Saito, S. and Goldberg, D. (2001). Compaction and dewatering processes of the oceanic sediments in the costa rica and barbados subduction zones: estimates from in situ physical property measurements. *Earth and Planetary Science Letters*, 191(3-4):283–293.

Saito, T., Ujiie, K., Tsutsumi, A., Kameda, J., and Shibazaki, B. (2013). Geological and frictional aspects of very-low-frequency earthquakes in an accretionary prism. *Geophysical Research Letters*, 40(4):703–708.

Sakaguchi, A., Chester, F., Curewitz, D., Fabbri, O., Goldsby, D., Kimura, G., Li, C.-F., Masaki, Y., Screaton, E. J., Tsutsumi, A., et al. (2011). Seismic slip propagation to the updip end of plate boundary subduction interface faults: Vitrinite reflectance geothermometry on integrated ocean drilling program nantro seize cores. *Geology*, 39(4):395–398.

Satake, K. (1993). Depth distribution of coseismic slip along the nankai trough, japan, from joint inversion of geodetic and tsunami data. *Journal of Geophysical Research: Solid Earth*, 98(B3):4553–4565.

Satake, K. and Tanioka, Y. (1995). Tsunami generation of the 1993 hokkaido nansei-oki earthquake. *Pure and applied geophysics*, 144(3-4):803–821.

Satake, K. and Tanioka, Y. (1999). Sources of tsunami and tsunamigenic earthquakes in subduction zones. *Pure and Applied Geophysics*, 154(3-4):467–483.

Satake, K Wang, K. A. B. (2003). Fault slip and seismic moment of the 1700 cascadia earthquake inferred from japanese tsunami descriptions. *Journal of Geophysical Research: Solid Earth*, 108(B11).

Savage, J. (1983). A dislocation model of strain accumulation and release at a subduction zone. *Journal of Geophysical Research: Solid Earth*, 88(B6):4984–4996.

Scholl, D. W. (1974). Sedimentary sequences in the north pacific trenches. In *The geology of continental margins*, pages 493–504. Springer.

Scholz, C. H. and Small, C. (1997). The effect of seamount subduction on seismic coupling. *Geology*, 25(6):487–490.

Schumann, K., Stipp, M., Behrmann, J. H., Klaeschen, D., and Schulte-Kortnack, D. (2014). P and s wave velocity measurements of water-rich sediments from the nankai trough, japan. *Journal of Geophysical Research: Solid Earth*, 119(2):787–805.

Screaton, E., Saffer, D., Henry, P., and Hunze, S. (2002). Porosity loss within the underthrust sediments of the nankai accretionary complex: Implications for overpressures. *Geology*, 30(1):19–22.

Segall, P. and Bradley, A. (2009). Numerical models of slow slip and dynamic rupture including dilatant stabilization and thermal pressurization. In *AGU Fall Meeting Abstracts*.

Seno, T. (2002). Tsunami earthquakes as transient phenomena. *Geophysical research letters*, 29(10).

Shaddox, H. R. and Schwartz, S. Y. (2019). Subducted seamount diverts shallow slow slip to the forearc of the northern hikurangi subduction zone, new zealand. *Geology*, 47(5):415–418.

Shelly, D. R., Beroza, G. C., Ide, S., and Nakamula, S. (2006). Low-frequency earthquakes in shikoku, japan, and their relationship to episodic tremor and slip. *Nature*, 442(7099):188–191.

Shibazaki, B. and Iio, Y. (2003). On the physical mechanism of silent slip events along the deeper part of the seismogenic zone. *Geophysical Research Letters*, 30(9).

Shipp, R. M. and Singh, S. C. (2002). Two-dimensional full wavefield inversion of wide-aperture marine seismic streamer data. *Geophysical Journal International*, 151(2):325–344.

Silver, E. A. and Reed, D. L. (1988). Backthrusting in accretionary wedges. *Journal of Geophysical Research: Solid Earth*, 93(B4):3116–3126.

Silverton, A. (2015). *Applied 3D Full-Waveform Inversion: Increasing the Resolution and Depth Penetration*. PhD thesis, Imperial College London.

Sirgue, L., Barkved, O., Dellinger, J., Etgen, J., Albertin, U., and Kommedal, J. (2010). Thematic set: Full waveform inversion: The next leap forward in imaging at valhall. *First Break*, 28(4):65–70.

Sirgue, L., Barkved, O., Van Gestel, J., Askim, O., and Kommedal, J. (2009). 3d waveform inversion on valhall wide-azimuth obc. In *71st EAGE Conference and Exhibition incorporating SPE EUROPEC 2009*.

Sirgue, L., Etgen, J., and Albertin, U. (2007). 3d full-waveform inversion: Wide-versus narrow-azimuth acquisitions. In *SEG Technical Program Expanded Abstracts 2007*, pages 1760–1764. Society of Exploration Geophysicists.

Sirgue, L. and Pratt, R. G. (2004). Efficient waveform inversion and imaging: A strategy for selecting temporal frequencies. *Geophysics*, 69(1):231–248.

Skarbek, R. M., Rempel, A. W., and Schmidt, D. A. (2012). Geologic heterogeneity can produce aseismic slip transients. *Geophysical Research Letters*, 39(21).

Smithyman, B., Pratt, R. G., Hayles, J., and Wittebolle, R. (2009). Detecting near-surface objects with seismic waveform tomography. *Geophysics*, 74(6):WCC119–WCC127.

Solomon, E. A., Torres, M., and Harris, R. (2018). Probing the nature of the hikurangi margin hydrogeologic system.

Song, T.-R. A., Helmberger, D. V., Brudzinski, M. R., Clayton, R. W., Davis, P., Prez-Campos, X., and Singh, S. K. (2009). Subducting slab ultra-slow velocity layer coincident with silent earthquakes in southern mexico. *Science*, 324(5926):502–506.

Spakman, W., Stein, S., van der Hilst, R., and Wortel, R. (1989). Resolution experiments for nw pacific subduction zone tomography. *Geophysical Research Letters*, 16(10):1097–1100.

Spinelli, G. A., Giambalvo, E. R., and Fisher, A. T. (2004). Sediment permeability, distribution, and influence on fluxes in oceanic basement. *Hydrogeology of the oceanic lithosphere*, pages 151–188.

Spinelli, G. A., Saffer, D. M., and Underwood, M. B. (2006). Hydrogeologic responses to three-dimensional temperature variability, costa rica subduction margin. *Journal of Geophysical Research: Solid Earth*, 111(B4).

Stockwell, J. and Cohen, J. K. (2002). The new su users manual. *Center for Wave Phenomena, Colorado School of Mines, Golden, USA*, 3.

Suess, E., Bohrmann, G., von Huene, R., Linke, P., Wallmann, K., Lammers, S., Sahling, H., Winckler, G., Lutz, R. A., and Orange, D. (1998). Fluid venting in the eastern aleutian subduction zone. *Journal of Geophysical Research: Solid Earth*, 103(B2):2597–2614.

Tanioka, Y. and Sataka, K. (1996). Fault parameters of the 1896 sanriku tsunami earthquake estimated from tsunami numerical modeling. *Geophysical Research Letters*, 23(13):1549–1552.

Tarantola, A. (1984). Inversion of seismic reflection data in the acoustic approximation. *Geophysics*, 48(8):1259–1266.

Tarantola, A. (2005). *Inverse problem theory and methods for model parameter estimation*, volume 89. siam.

Thurber, C., Roecker, S., Ellsworth, W., Chen, Y., Lutter, W., and Sessions, R. (1997). Two-dimensional seismic image of the san andreas fault in the northern gabilan range, central california: Evidence for fluids in the fault zone. *Geophysical Research Letters*, 24(13):1591–1594.

Thurber, C., Roecker, S., Zhang, H., Baher, S., and Ellsworth, W. (2004). Fine-scale structure of the san andreas fault zone and location of the safod target earthquakes. *Geophysical Research Letters*, 31(12).

Tobin, H., Vannucchi, P., and Meschede, M. (2001). Structure, inferred mechanical properties, and implications for fluid transport in the dcollement zone, costa rica convergent margin. *Geology*, 29(10):907–910.

Tobin, H. J. and Moore, J. C. (1997). Variations in ultrasonic velocity and density with pore pressure in the decollement zone, northern barbados ridge accretionary prism. In *Proceedings of the Ocean Drilling Program. Scientific results*, volume 156, pages 125–135. Ocean Drilling Program.

Tobin, H. J., Moore, J. C., and Moore, G. F. (1994). Fluid pressure in the frontal thrust of the oregon accretionary prism: Experimental constraints. *Geology*, 22(11):979–982.

Tobin, H. J., Moore, J. C., and Moore, G. F. (1995). Laboratory measurement of velocity versus effective stress in thrust faults of the oregon accretionary prism: Implications for fault zone overpressure. *Prediction and Effects of Fluid Pressure in Active Accretionary Prism Fault Systems*, page 20.

Tobin, H. J. and Saffer, D. M. (2009). Elevated fluid pressure and extreme mechanical weakness of a plate boundary thrust, nankai trough subduction zone. *Geology*, 37(8):679–682.

Todd, E. K. (2017). *Interplay between modes of strain release along the shallow northern Hikurangi subduction zone, New Zealand*. Thesis.

Todd, E. K., Schwartz, S. Y., Mochizuki, K., Wallace, L. M., Sheehan, A. F., Webb, S. C., Williams, C. A., Nakai, J., Yarce, J., Fry, B., et al. (2018). Earthquakes and tremor linked to seamount subduction during shallow slow slip at the hikurangi margin, new zealand. *Journal of Geophysical Research: Solid Earth*, 123(8):6769–6783.

Toomey, D. R., Purdy, G., Solomon, S. C., and Wilcock, W. S. (1990). The three-dimensional seismic velocity structure of the east pacific rise near latitude 9 30 n. *Nature*, 347(6294):639.

Treitel, S. (1974). The complex wiener filter. *Geophysics*, 39(2):169–173.

USGS (2014). Earthquake glossary. last modified 2014, https://earthquake.usgs.gov/learn/glossary/?term=interplate

Vallée, M., Nocquet, J.-M., Battaglia, J., Font, Y., Segovia, M., Regnier, M., Mothes, P., Jarrin, P., Cisneros, D., Vaca, S., et al. (2013). Intense interface seismicity triggered by a shallow slow slip event in the central ecuador subduction zone. *Journal of Geophysical Research: Solid Earth*, 118(6):2965–2981.

Vigh, D., Jiao, K., Watts, D., and Sun, D. (2014). Elastic full-waveform inversion application using multicomponent measurements of seismic data collection. *Geophysics*, 79(2):R63–R77.

Vigh, D., Starr, E. W., and Kapoor, J. (2009). Developing earth models with full waveform inversion. *The Leading Edge*, 28(4):432–435.

Virieux, J. and Operto, S. (2009). An overview of full-waveform inversion in exploration geophysics. *Geophysics*, 74(6):WCC1–WCC26.

Von Huene, R., Klaeschen, D., Gutscher, M., and Fruehn, J. (1998). Mass and fluid flux during accretion at the alaskan margin. *Geological Society of America Bulletin*, 110(4):468–482.

Walcott, R. (1984). The kinematics of the plate boundary zone through new zealand: A comparison of shortand longterm deformations. *Geophysical Journal of the Royal Astronomical Society*, 79(2):613–633.

Walcott, R. I. (1987a). Geodetic strain and the deformational history of the north island of new zealand during the late cainozoic. *Philosophical Transactions of the Royal Society of London. Series A, Mathematical and Physical Sciences*, 321(1557):163–181.

Walcott, R. I. (1987b). Geodetic strain and the deformational history of the north island of new zealand during the late cainozoic. *Philosophical Transactions of the Royal Society of London. Series A, Mathematical and Physical Sciences*, 321(1557):163–181.

Wallace, L., Saffer, D., Barnes, P., Pecher, I., Petronotis, K., LeVay, L., , and the Expedition 372/375 Scientists, editors (2019). *Hikurangi Subduction Margin Coring, Logging and Observatories*, volume 372B/375, college Station, TX (International Ocean Discovery Program). International Ocean Discovery Program.

Wallace, L. M., Bartlow, N., Hamling, I., and Fry, B. (2014). Quake clamps down on slow slip. *Geophysical Research Letters*, 41(24):8840–8846.

Wallace, L. M. and Beavan, J. (2006). A large slow slip event on the central hikurangi subduction interface beneath the manawatu region, north island, new zealand. *Geophysical Research Letters*, 33(11).

Wallace, L. M. and Beavan, J. (2010). Diverse slow slip behavior at the hikurangi subduction margin, new zealand. *Journal of Geophysical Research: Solid Earth*, 115(B12).

Wallace, L. M., Beavan, J., Bannister, S., and Williams, C. (2012). Simultaneous long-term and short-term slow slip events at the hikurangi subduction margin, new zealand: Implications for processes that control slow slip event occurrence, duration, and migration. *Journal of Geophysical Research: Solid Earth*, 117(B11).

Wallace, L. M., Beavan, J., McCaffrey, R., and Darby, D. (2004). Subduction zone coupling and tectonic block rotations in the north island, new zealand. *Journal of Geophysical Research: Solid Earth*, 109(B12).

Wallace, L. M., Kaneko, Y., Hreinsdóttir, S., Hamling, I., Peng, Z., Bartlow, N., DAnastasio, E., and Fry, B. (2017). Large-scale dynamic triggering of shallow slow slip enhanced by overlying sedimentary wedge. *Nature Geoscience*, 10(10):765.

Wallace, L. M., Reyners, M., Cochran, U., Bannister, S., Barnes, P. M., Berryman, K., Downes, G., Eberhart-Phillips, D., Fagereng, A., Ellis, S., et al. (2009). Characterizing the seismogenic zone

of a major plate boundary subduction thrust: Hikurangi margin, new zealand. *Geochemistry, Geophysics, Geosystems*, 10(10).

Wallace, L. M., Webb, S. C., Ito, Y., Mochizuki, K., Hino, R., Henrys, S., Schwartz, S. Y., and Sheehan, A. F. (2016). Slow slip near the trench at the hikurangi subduction zone, new zealand. *Science*, 352(6286):701–704.

Wang, C.-y., Hwang, W.-t., and Cochrane, G. R. (1994). Tectonic dewatering and mechanics of protothrust zones: example from the cascadia accretionary margin. *Journal of Geophysical Research: Solid Earth*, 99(B10):20043–20050.

Wang, H., Crutchley, G., and Stern, T. (2017). Gas hydrate formation in compressional, extensional and un-faulted structural settingsexamples from new zealand's hikurangi margin. *Marine and Petroleum Geology*, 88:69–80.

Wang, K. and Bilek, S. L. (2011). Do subducting seamounts generate or stop large earthquakes? *Geology*, 39(9):819–822.

Wang, K. and Bilek, S. L. (2014). Invited review paper: Fault creep caused by subduction of rough seafloor relief. *Tectonophysics*, 610:1–24.

Wang, K. and Dixon, T. (2004). coupling semantics and science in earthquake research. *Eos, Transactions American Geophysical Union*, 85(18):180–180.

Wannamaker, P. E., Evans, R. L., Bedrosian, P. A., Unsworth, M. J., Maris, V., and McGary, R. S. (2014). Segmentation of plate coupling, fate of subduction fluids, and modes of arc magmatism in c ascadia, inferred from magnetotelluric resistivity. *Geochemistry, Geophysics, Geosystems*, 15(11):4230–4253.

Warner, M., Morgan, J., Umpleby, A., Stekl, I., and Guasch, L. (2012). Which physics for full-wavefield seismic inversion? In *74th EAGE Conference and Exhibition incorporating EUROPEC 2012*.

Warner, M., Ratcliffe, A., Nangoo, T., Morgan, J. V., Umpleby, A., Shah, N., Vinje, V., tekl, I., Guasch, L., Win, C., Conroy, G., and Bertrand, A. (2013). Anisotropic 3d full-waveform inversion. *Geophysics*, 78(2):R59–R80.

Warner, M., Umpleby, A., and Stekl, I. (2010). 3d full-wavefield tomography: imaging beneath heterogeneous overburden. In *72nd EAGE Conference and Exhibition-Workshops and Fieldtrips*.

Wech, A. G., Creager, K. C., and Melbourne, T. I. (2009). Seismic and geodetic constraints on cascadia slow slip. *Journal of Geophysical Research: Solid Earth*, 114(B10).

Wei, M., McGuire, J. J., and Richardson, E. (2012). A slow slip event in the south central alaska subduction zone and related seismicity anomaly. *Geophysical Research Letters*, 39(15).

Wesson, R. L. (1988). Dynamics of fault creep. *Journal of Geophysical Research: Solid Earth*, 93(B8):8929–8951.

Westbrook, G. (1991). Geophysical evidence for the role of fluids in accretionary wedge tectonics. *Philosophical Transactions of the Royal Society of London. Series A: Physical and Engineering Sciences*, 335(1638):227–242.

Westbrook, G. and Smith, M. (1983). Long decollements and mud volcanoes: Evidence from the barbados ridge complex for the role of high pore-fluid pressure in the development of an accretionary complex. *Geology*, 11(5):279–283.

Wiley, R. and Patchett, J. (1990). Cnl neutron porosity modelinga step forward. *The Log Analyst*, 31(3):133–149.

Williamson, P. R. (1991). A guide to the limits of resolution imposed by scattering in ray tomography. *Geophysics*, 56(2):202–207.

Wu, R.-S. and Toksöz, M. N. (1987). Diffraction tomography and multisource holography applied to seismic imaging. *Geophysics*, 52(1):11–25.

Wyllie, M., Gregory, A., and Gardner, G. (1958). An experimental investigation of factors affecting elastic wave velocities in porous media. *Geophysics*, 23(3):459–493.

Yilmaz, O. (1987). Seismic data processing. *Investigations in geophysics*.

Yilmaz, . (2001). *Seismic data analysis*, volume 1. Society of Exploration Geophysicists Tulsa.

Yuan, T., Spence, G., and Hyndman, R. (1994). Seismic velocities and inferred porosities in the accretionary wedge sediments at the cascadia margin. *Journal of Geophysical Research: Solid Earth*, 99(B3):4413–4427.

Yue, H Lay, T. R. L. A. C. V. C. T. X. S. J. (2014). Localized fault slip to the trench in the 2010 maule, chile mw= 8.8 earthquake from joint inversion of highrate gps, teleseismic body waves, insar, campaign gps, and tsunami observations. *Journal of Geophysical Research: Solid Earth*, 119(10):7786–7804.

Zhao, C., Hobbs, B., and Mühlhaus, H. (1998). Finite element modelling of temperature gradient driven rock alteration and mineralization in porous rock masses. *Computer Methods in Applied Mechanics and Engineering*, 165(1-4):175–187.

Zhao, D., Huang, Z., Umino, N., Hasegawa, A., and Kanamori, H. (2011). Structural heterogeneity in the megathrust zone and mechanism of the 2011 tohoku-oki earthquake (mw 9.0). *Geophysical Research Letters*, 38(17).

Zoback, M., Hickman, S., Ellsworth, W., et al. (2011). Scientific drilling into the san andreas fault zone–an overview of safod's first five years. *Scientific Drilling*, 11:14–28.